Modelling of floating fish cage dynamics with computational fluid dynamics

Chen, Hao

Publication date:
2016

Document Version
Publisher's PDF, also known as Version of record

Modelling of floating fish cage dynamics with computational fluid dynamics

PhD Thesis

$$(EIv'')'' = q - \rho A\ddot{v}$$

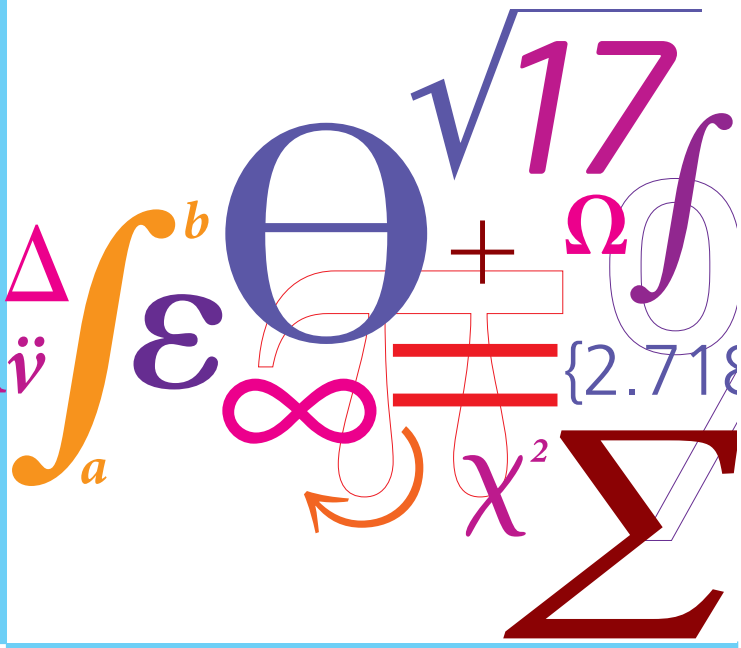

Hao Chen
December 2016

DTU Mechanical Engineering
Department of Mechanical Engineering

Modelling of floating fish cage dynamics with computational fluid dynamics

Hao Chen

Technical University of Denmark
Department of Mechanical Engineering
Section of Fluid Mechanics, Coastal and Maritime Engineering

December 23, 2016

Modelling of floating fish cage dynamics with computational fluid dynamics

PhD Thesis
Font: Computer Modern typeset with LaTeX 2_ε

DTU Mechanical Engineering
Section of Fluid Mechanics, Coastal and Maritime Engineering
Technical University of Denmark

Nils Koppels Allé, Bld. 403
DK-2800 Kongens Lyngby
Denmark
www.mek.dtu.dk

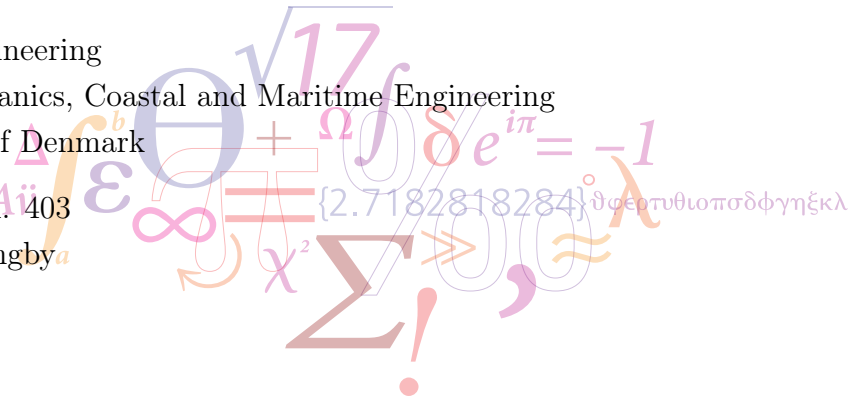

Dedicated to my girlfriend Yang Lv,
for her love, support and understanding

Preface

The present thesis is submitted as a partial fulfillment of the requirements for the degree of Philosophiae Doctor (Ph.D.) at the Technical University of Denmark (DTU).

The thesis was completed at the Section of Fluid mechanics, Coastal and Maritime Engineering, Department of Mechanical Engineering. This work was carried out from September 2013 to December 2016, under the supervision of Professor Erik Damgaard Christensen.

An external research stay was undertaken from September 2016 to October 2016 at the Department of Marine Technology, Norwegian University of Science and Technology, under the supervision of Professor Trygve Kristiansen.

The Ph.D. study was funded by the Technical University of Denmark and the FP7-OCEAN-2011 project "Innovative Multi-purpose offshore platforms: planning, design and operation", MERMAID, 288710, under the call "Ocean of Tomorrow". Financial support was also received from the Otto Mønsted A/S Fond for the attendance of the 36th International Conference on Ocean, Offshore and Arctic Engineering (OMAE) in Busan, Korea.

The thesis is written as a collection of journal articles and conference papers, which were produced in the time frame of the present research study.

Hao Chen
Kgs. Lyngby, December 23rd 2016

Acknowledgements

First and foremost I would like to express my gratitude to my supervisor Prof. Erik Damgaard Christensen. During the past three years, he provided me a lot of guidance and suggestions on this project. Without him, this thesis would never have been completed or written. A clear goal was set up by him for this Ph.D. study, while I still have a lot of freedom to carry out research that I am interested in within the scope of the project.

Then I would like to thank my colleges in the Section of Fluid mechanics, Coastal and Maritime Engineering. We have had very good communications and discussions on some common topics at the breakfast meeting on Monday every week. Special thanks go to Bjarne Jensen, Sina Saremi and Pietro Danilo Tomaselli for their help in model setup and simulation in OpenFOAM. In addition, Mostafa Amini Afshar and Assistant Prof. Yanlin Shao are acknowledged for their help on potential theory on wave-structure interaction.

Prof. Trygve Kristiansen is appreciated for hosting me in NTNU for a short stay. We had some in depth discussions on the fish farming related topics. Furthermore, a special thanks should go to the Ph.D. student Peng Li and Mohsen Bardestani for their help and discussions.

I am also grateful to Prof. Yunpeng Zhao, Chunwei Bi and Xiaodong Bai from Dalian University of Technology. They are the predecessors on CFD modelling of fish cages. From the talk and discussions with them, I gained a lot of experiences and inspirations.

Finally many thanks go to my families and my girlfriend for their encourages, understanding and support during the time I studied abroad. I will forever be indebted for their sacrifices in supporting me.

Abstract

The present thesis considers modelling of the dynamic response of floating fish cages in current and wave conditions. The numerical model was developed based on the computational fluid dynamic (CFD) approach. The modelling framework is OpenFOAM, an open source CFD toolbox. A two-phase flow solver provided in official OpenFOAM software has been adopted as the foundation of the present numerical model. The solver treats the water and air as a mixture fluid, and solves mass and momentum conservation equations for the whole mixture system. The volume of fluid (VOF) method was applied to track the free surface.

A floating fish cage usually contains a net cage, a floater, a sinker and mooring lines. The focus of the present work is on modelling of the floater and the net cage. The sinker and the mooring lines were not explicitly modelled. Only the constant forces were added to the relative equations for the motion/deformation of the floater and the net cage.

A net cage contains a large number of twines and knots. Therefore, a detailed modelling of the geometry of the net cage is not possible yet. In the present work, it was modelled as a sheet of porous media with very thin thickness. Volume averaged Navier-Stokes equations were applied as the governing equations for the porous media flow. Due to the volume averaging process, a resistance term appears in the governing equations, representing the viscous force of the net cage on the fluid flow. The force was usually expressed as the sum of a linear drag force and a quadratic drag force. But it was found that for a net cage, the quadratic drag force completely dominated over the linear drag force. Therefore, the linear component was neglected. An analytical expression was derived to relate the quadratic force coefficients with the physical parameters of the net cage, e.g. the length of the mesh bar, the solidity ratio, the drag force coefficient for the twins etc. The derivation indeed was based on the transformation from Morison type load model. Two new parameters were introduced to account for the interaction effects between the

twines, and they were calibrated based on the available experimental data. The proposed expression was validated against model test results for current and wave interaction with fixed plane net panels and circular net cages.

Considering the flexibility of the net cage in response to the current and waves, the porous media model was further coupled with a lumped mass structural model. A new coupling scheme was implemented in the numerical model. The coupling scheme was based on the static mesh, therefore the mesh does not need to conform the deformed geometry of the net cage. Instead, the geometry of the deformed net cage was approximated by several dynamic porous media zones, corresponding to the panel elements in the lumped mass model. At every time step, the cells in the porous media zones were updated based on the transferred nodal positions from the structural model. This coupling scheme was validated against experiments for top fixed and bottom weighted plane net panels and circular cages in current and waves.

In general, for a fish cage in steady current flow, the net cage is the main part to stand the drag force on it. However, when modelling the floating fish cage in wave conditions, the motion of the floater is the main contributor to the forces on the net cage. Hereby in the numerical model it should be considered. Presently a body-fitted computational mesh was applied, and the geometry of the floater was resolved by the mesh. A six degree of freedom motion solver was applied to solve the motion equations of the floater with different motion integration methods. Careful validations were performed first on wave loads on the fixed floater, and motion responses of the floating floater. It was decided to apply the explicit-implicit Adams-Bashforth-Moulton scheme as the motion integration scheme for the floater. This floater model was successfully coupled with the above described model for the net cage, hereby is capable to model the responses of the whole floating fish cage system. This integrated numerical model was validated against the experimental data on snap loads of the net cage in regular waves, which is due to the relative motion between the sinker and the floater, and the mooring loads in combined current and wave conditions.

Resumé

Denne PhD afhandling omhandler modellering af laste og påvirkning af flydende fiskebure i udsat for strøm og bølger. Den numeriske model blev udviklet baseret på open source CFD-biblioteket OpenFOAM. Der er taget udgangspunkt i en to-fase strømningsløser, som er en del af OpenFOAM. Løseren behandler luft og vand i en blanding fluid, og løser masse- og impuls bevarelses ligningerne. "Volume of fluid" (VOF) metoden blev anvendt til at finde den frie overflade.

Et flydende fiskebur indeholder sædvanligvis en net-bur, en flyder, lodder og fortøjningstrosser. Studiet fokuserede på modellering af flyderen og net-buret, mens lodderne og fortøjninger ikke blev modelleret direkte. I stedet blev kræfterne fra f.eks. lodderne medtaget som konstante tyngdekræfter i ligningerne for bevægelsen / deformation af flyderen og net-bur.

En net-bur indeholder et stort antal af liner og knuder. Derfor er en detaljeret modellering af geometrien af net-buret ikke muligt endnu. I det foreliggende arbejde blev det modelleret som et flade af et tyndt porøst medie. De volumen-midlede Navier-Stokes ligninger blev anvendt som de styrende ligninger for strømningen i vand og i det porøse medie. På grund af midlingsprocessen medtages strømningsmodstanden fra bl.a. viskoseeffekter i de styrende ligninger. Kraften blev udtrykt som summen af et lineært bidrag, og et ikke-lineært, kvadratisk, bidrag. Det viste sig, at for en net-bur, dominerer den kvadratiske modstandskraft sammenlignet med den lineære modstandskraft. Derfor blev der efterfølgende set bort fra den lineære komponent. Et analytisk udtryk blev udledt, som relaterede den kvadratiske kraftkoefficient med de fysiske parametre af net- buret, f.eks længden af net bar, soliditetsgrad, kraftkoefficienterne for linerne etc.

Udledningen var baseret på en transformation af Morison last model til en porøs lastmodel. To nye parametre blev indført for at tage hensyn til vekselvirkningseffekter mellem forskellige dele af nettet, og de blev kalibreret baseret på tilgængelige forsøgsdata. De foreslåede udtryk blev valideret mod resultater fra fysiske model

test for strøm og bølge vekselvirkning med faste plane net-paneler og cirkulære net-bure.

For at medtage fleksibiliteten af net-buret i strøm og bølger, blev modellen for det porøse medie yderligere koblet med en punkt masse struktur-model. En ny koblingsmetode blev implementeret i den numeriske model. Koblingsmetoden er baseret på det faste beregningsnet, hvilket betød at beregningsnetten ikke behøvede at svare til den deformerede geometri af net-buret. I stedet blev geometrien af det deformerede net-bur tilnærmet med flere dynamiske porøse medier zoner svarende til de panelelementer i punkt masse modellen. I hvert tids skridt blev zonerne i de porøse medier opdateret på baggrund af de overførte positioner fra den strukturelle model. Denne koblingsmetode blev valideret mod eksperimenter af plane net kun fastgjort i toppen og mod cirkulære bure i strøm og bølger.

Generelt for et fiskebur i konstant strøm, udgør net-buret den vigtigste del af modstandskraften på det. For flydende fiskebure udsat for bølger er bevægelsen af flyderen den største bidragyder til lastene på net-buret. I dette studie opløste beregningsnettet geometrien af flyderen direkte. En seks frihedsgraders bevægelsesløser blev anvendt til at løse bevægelsesligningerne for flyderen med forskellige integrationsmetoder. Valideringer blev udført først af bølgebelastninger på den faste flyder og dernæst af bevægelserne fra den flydende flyder. Det blev besluttet at anvende den eksplicitte-implicitte Adams-Bashforth-Moulton skema til tidsintegration af bevægelsen af flyderen. Denne flydermodel blev succesfuldt kombineret med den ovenfor beskrevne model for net-buret. Herved er metoden i stand til at modellere bevægelsen fra hele det flydende fiskebur. Denne integrerede numeriske model blev valideret mod eksperimentelle data af net-buret i regelmæssige bølger, der skyldes den relative bevægelse mellem lodderne og flyderen, og fortøjningsbelastninger i kombineret bølger og strøm.

List of publications

This thesis consists of a chapter on introduction and four papers, which are listed hereafter. In addition, some papers and reports refer to the studies that are not directly related to the work presented in this thesis. However, they were carried out in the last three years, and for this reason they are listed under *Other publications* to give the reader a full view of the publications produced in the time frame of the Ph.D. project, but they will not be included in the thesis.

1. **Chen, H.** & Christensen, E.D., 2016. Investigations on the porous resistance coefficients for fishing net structures. Journal of Fluids and Structures, 65.

2. **Chen, H.** & Christensen, E.D., 2017. Development of a numerical model for fluid-structure interaction analysis of flow through and around aquaculture net cages. Submitted for publication.

3. **Chen, H.** & Christensen, E.D., 2017. On the wave generation and interaction with fixed fish cage floaters in OpenFOAM. To be submitted.

4. **Chen, H.** & Christensen, E.D., 2017. Simulating the responses of floating fish cages in current and waves. To be submitted.

Other publications

Peer-reviewed Conference Papers

1. **Chen, H.** & Christensen, E.D., 2015. Numerical Simulation of Wave Interaction with Moving Net Structures. in Proceedings of the ASME 34th International Conference on Ocean, Offshore and Arctic Engineering, OMAE2015-41598, American Society of Mechanical Engineers.

2. **Chen, H.** & Christensen, E.D., 2016. Computation of added mass and damping coefficients of a horizontal circular cylinder in OpenFOAM. in Proceedings of the ASME 35th International Conference on Ocean, Offshore and Arctic Engineering, OMAE2016-54429, American Society of Mechanical Engineers.

Peer-reviewed Reports

1. Christensen, E.D., Sumer, B.M., Schouten, J-J, Kirca, Ö., Petersen, O., Jensen, B., Carstensen, S., Baykal, C., Tralli, A., **Chen, H.**, Tomaselli, P.D., Petersen, T.U., Fredsøe, J., Raaijmakers, T.C., Kortenhaus, A., Hjelmager Jensen, J., Saremi, S., Bolding, K. & Burchard, H. 2015, MERMAID project report: D5.3 Interaction between currents, wave, structure and subsoil.

Contents

Preface **v**

Acknowledgements **vii**

Abstract (English/Dansk) **ix**

List of publications **xiii**

Contents **xvi**

1 Introduction **1**

1.1 Background and motivation 1

1.1.1 Status and trend on the development of aquaculture 1

1.1.2 Different design concepts for fish cages 2

1.1.3 Open circular fish cage 3

1.1.4 Motivation for the current project 5

1.2 Literature Review 6

1.2.1 Floater 7

1.2.2 Net cage 9

1.2.3 Global analysis on the floating fish cage system 11

1.3 The present model 12

1.4 Thesis Outlines 14

1.5 Recommendations on the future work 15

1.6 References 16

2 Investigations on the porous resistance coefficients for fishing net structures 25

3 Development of a numerical model for fluid-structure interaction analysis of flow through and around aquaculture net cages 65

4 On the wave generation and interaction with fixed fish cage floaters in OpenFOAM 93

5 Simulating the responses of floating fish cages in current and waves 125

A Applied discretization schemes for the numerical simulations 157

A.1 Momentum equation 158

A.1.1 Time derivative operator 158

A.1.2 Divergence operator 161

A.1.3 Surface normal gradient operator 167

A.1.4 Laplacian operator 168

A.2 Transport equation for volume fraction 168

A.2.1 Applied schemes in the predictor step 168

A.2.2 Applied schemes in the corrector steps 169

A.3 References 170

1 Introduction

1.1 Background and motivation

1.1.1 Status and trend on the development of aquaculture

The production from capture fisheries and aquaculture has been an important food resource for human beings. According to [1], capture fisheries and aquaculture supplied the world with about 148 million tonnes of fish in 2010 (with a total value of 217.5 billion US dollars), of which about 128 million tonnes was utilized as food for people. Considering that the number of population is expected to reach 9 billion all over the world in 2050, the capture fisheries and aquaculture is expected to continue playing an important role and making contributions towards the food security and nutrition supplement.

However, it has been reported that the capture fishery production keeps relatively static since the late 1980s, while aquaculture is growing fast. Aquatic food production has transitioned from being primarily based on capture of wild fish to culture of increasing numbers of farmed species. In 2014, the aquaculture sector's contribution to the supply of fish for human consumption overtook that of wild-caught fish for the first time [4]. The main reason is that the oceans can not support additional landings for the wild-caught species. Overfishing has already been a major threat for many species. Therefore, aquaculture has been chosen as a sustainable way to meet the demand for the food, just like the transition from hunting and gathering to agriculture for land based food production systems.

Aquaculture has a long and well established tradition in Denmark, which is ranking sixth in the world's leading exporters of fish products [31]. The development of

Danish aquaculture started in the middle of the 1950s with fish farms established along Danish river systems. Since 1970s, land based marine aquaculture units were also developed.

The main aquatic product in Denmark from both mariculture and land based systems is the rainbow trout, which completely dominates other species. Besides that, eel is farmed in recirculated freshwater tank systems; mussels and oysters are produced in minor quantities and turbot fry is exported for further ongrowing [31].

However, during the past years there has been limited development in Danish marine aquaculture. Currently there are 18 marine fish farms in Denmark, and in 2010 they produced approximately 10 000 tonne fish [3]. This is mainly due to the restrictions imposed by the Ministry of Environment and Energy, (Now it is merged into the new section called the Ministry of Environment and Food of Denmark, where the energy section was detached.) including a provisional stop for extensions and new establishments [16]. Nowadays following the recommendations from advisory committees, adjustments to the regulations are being considered for both marine and freshwater farming and to some extent new optimism is growing in the industry [31].

1.1.2 Different design concepts for fish cages

There have been many conceptual designs for fish cages. Except the commonly used open fish cage systems with plastic collar and flexible nets (usually made of Nylon), some new concepts were also proposed and applied during the past years. Metal frame fish cage system is among one of them that has already been used, particularly in sheltered areas. The stable frame and extra wide walkways allow full flexibility of operation and easy access from cage to cage. This is becoming essential for good husbandry and maintenance in some of the sites [2]. However if it is applied for offshore aquaculture, the frame needs to be remarkably robust, to prevent damage from e.g. storm and ice collisions [55]. In addition, submersible or semi-submersible fish cage system has also been an option. This system has advantages that it could avoid the storm by submerging below surface. However it has not been widely used all over the world, due to e.g. high investment cost, the relative impracticality of feeding and handling the fish, and potential problems with fish welfare [55].

Recently in Norway, SINTEF fisheries and aquaculture has been very active on

investigations of closed flexible fish cages (CFFC). This kind of fish cage uses closed membrane structures to control the interactions between the fish cage and the surrounding environment. The analysis of loads and deformation of CFFC under sea conditions have been presented in e.g. [45] and [28].

1.1.3 Open circular fish cage

In the present work, we will limit the study within the scope of traditional open fish cages that are commonly used in offshore areas. A sketch of such fish cage is given in Fig. 1.1. This kind of fish cage typically consists of the following main components: a floater or floating collar, a net cage, a weight system and mooring lines.

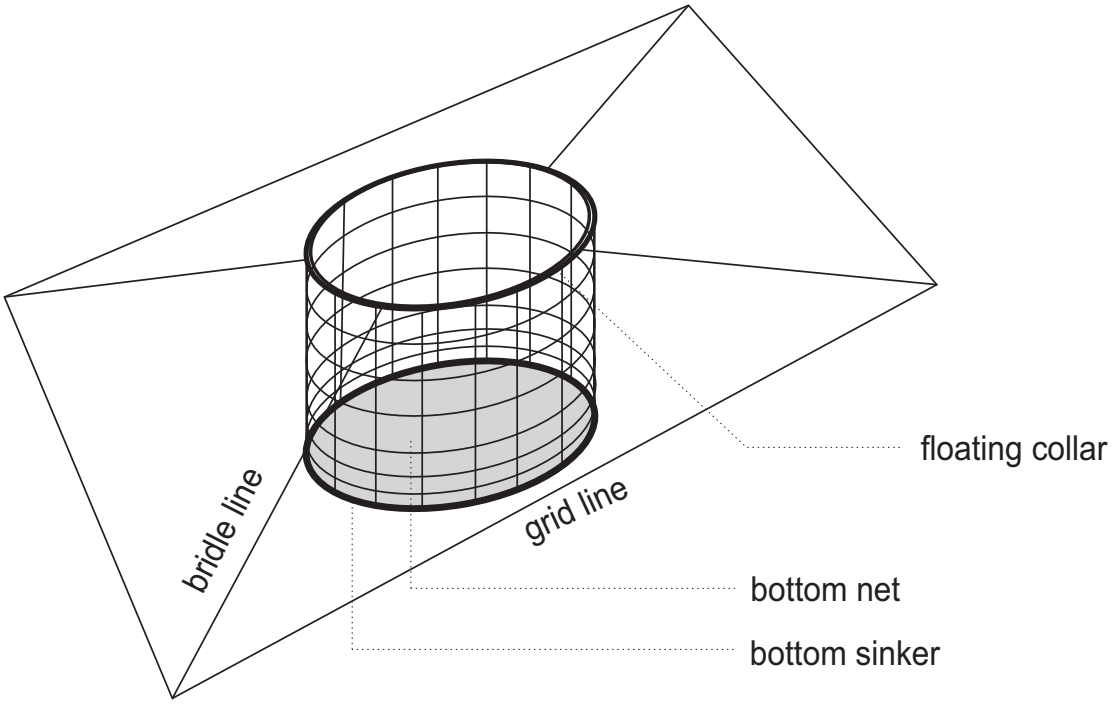

Figure 1.1 – Illustration of the fish cage and its main components.

The floater has usually one to three torus depending on the dimension of the fish cage [15]. It is usually made from high-density polyethylene (HDPE) pipe, filling with expanded polystyrene. This ensures the easy fabrication and repair. In addition, the plastic has outstanding corrosion characteristics, and the material is compliant and (historically) inexpensive [17]. However, HDPE to some degree behaves like viscoelastic material. The loading rate may affect deformation of the

structure. The Young's modulus of elasticity for this material was measured to be around 800 MPa [56], and the yield stress is about 25 MPa.

The netting material is usually Nylon, and the net cage could be constructed as either knotted or knotless nettings. The knotless nettings are usually produced of knitted bundles of multifilament, while the knotted nettings are made of twines of twisted multifilament bundles that are connected by knots. Knotless Nylon netting is by far the dominating material in aquaculture net cages. In [42], tests have been performed to investigate the tensile properties of the netting materials. It was found that under static loading, the netting material has linear material properties for relatively small stain. However under large stain, nonlinear material properties become important. A third degree polynomial has been proposed to fit the stress-strain curve. Furthermore, under dynamic loading condition, creep property was also observed in [41].

Marine growth is an important issue for net cages. Fouling can decrease the product value of farmed species by up to 90%, and about 5% - 10% of the industry value is used for dealing with biofouling and its related problems on a yearly basis [14]. The main impact of fouling is that with fouled nettings, dissolved oxygen levels in the cage drop dramatically, leading to stress on the fish. Furthermore, fouling significantly increases the weight and drag force of the cage, which affects cage structure and behaviour in rough seas and high current conditions [47]. Different anti-fouling strategies have been proposed, e.g. use of anti-fouling paints and coatings, automatic cleaners etc. Presently in the thesis we only consider clean nets. However, the methodologies used in the study can easily be extended to nets with fouling. But this is recommended as future works.

The shape of the net cage is maintained by either distributed weights, or by a heavy bottom ring/sinker tube. This is essentially important in order to maintain the capacity of the cage and prevent from large volume reductions, which may affect the welfare of the fish. In addition maintaining the shape could also prevent predators, e.g. seals, from pushing against the net wall in order to attack the fish inside.

A marine fish farm may contain several cages that are arranged in arrays. The mooring system is used to keep them at the desired position. It is made of a number of cables which are attached to the cages with their lower ends of the cables anchored at the sea bed. There have been different options for the geometry of the mooring systems. One typical arrangement is the multi-directional anchor

lines for the rectangular array cages, as shown in Fig. 1.2. This could be in general cost effective, and it can stand loads from multi-directions. But one should also care about e.g. disease transmission of the fish in-between the cages.

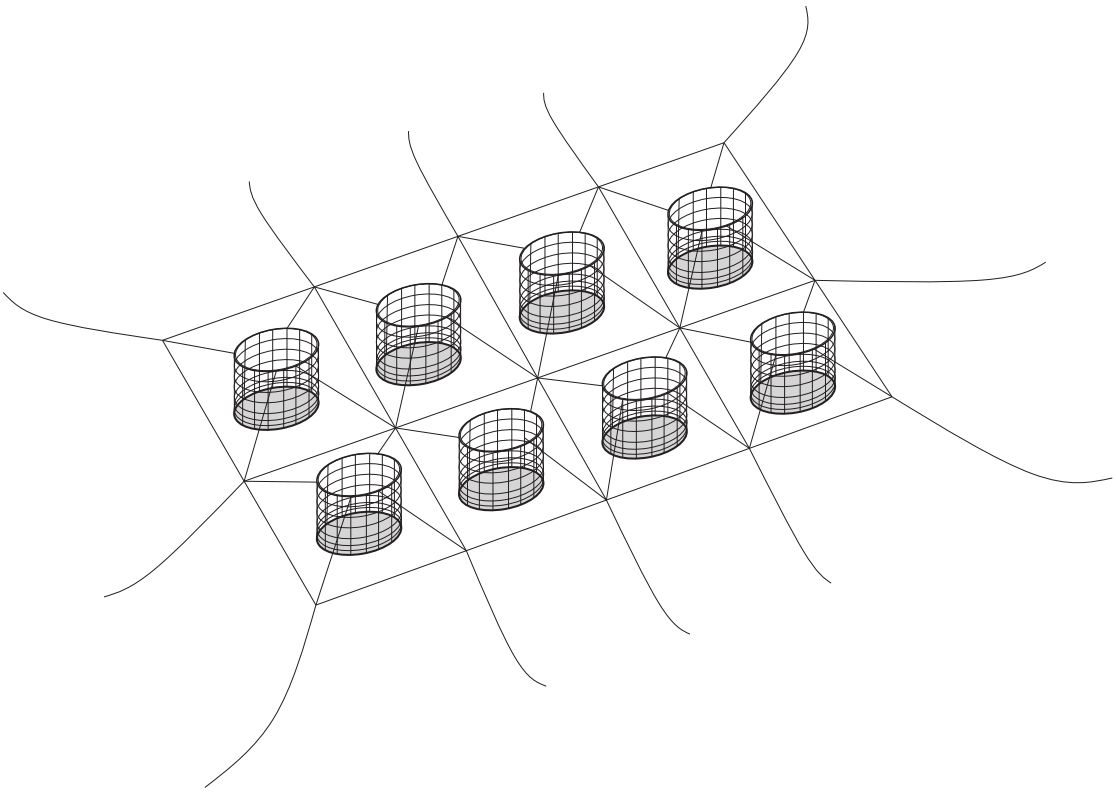

Figure 1.2 – A sketch for general configuration of marine fish farms.

1.1.4 Motivation for the current project

Generally, inshore mariculture production is well established in protected coastal locations, in shallow waters with low hydrodynamic energy, and in areas that are in close proximity to supporting infrastructures. For instance, a study of spacial distribution of fish cages and pens has been carried out in [50] among 16 countries in the Mediterranean. It shows that 80 percent of these installations were within 1 km of the coast and that the maximum distance offshore was about 7 km. However, globally the rapid growth of aquaculture faces some limitations in the availability of suitable inshore sites and in the ecological carrying capacity of these existing sites. Hereby offshore aquaculture is being promoted to overcome such limitations [49].

A number of definitions have been proposed for offshore aquaculture. For instance in [13], offshore aquaculture is defined as *taking place in the open sea with significant exposure to wind and wave action, and where there is a requirement for equipment and servicing vessels to survive and operate in severe sea conditions from time to time. The issue of distance from the coast or from a safe harbour or shore base is often but not always a factor.* This means that the cage will be installed and operated in more exposed areas under larger current and wave conditions. In [24], the status and potential for offshore aquaculture development are measured and estimated from a spatial perspective. The technical limits they set for the near future development of offshore aquaculture are within the water depth of 25 - 100 m and current speeds of 10 - 100 cm/s. The cost effective area for development of offshore aquaculture is within the distance of 46 km from the shore to offshore installations. Therefore, in order to install fish cages in such kind of exposed area, better understanding and prediction on the environmental loading and the responses of fish cages are necessary, and this forms the motivation of the present work.

1.2 Literature Review

Modelling of floating fish cage dynamics in current and waves is in general very challenging. This is due to several reasons as summarized below:

- The net cage itself has a large number of twines and knots, which makes it difficult to model. In the real world, the diameter of the fish cage is usually in the order of ten meters, while the mesh size for a net cage is in the order of ten millimetres. Therefore, the number of knots and twines for a full scale fish cage may reach million or even higher. This makes a detailed modelling of each twine and knot very expensive.

- The problem of current and wave interaction with floating fish cage has multi-scale characteristics. The fish cage floater has a diameter of 0.5 m - 1 m, while as mentioned above, the twine diameter of the net is in the order of ten millimetres. Furthermore, the wake behind the fish cage is suppose to be turbulent, which has also strong multi-scale characteristics. Therefore, a numerical model which covers all the scale ranges is not feasible.

- Both the floater and the net cage are kind of flexible structures. In relatively

exposed sea condition, large motion/deformation of both the floater and the net cage may occur. Hereby this is a hydroelastic problem, which involves both the structural mechanics and hydrodynamics.

In order to resolve the above issues, different modelling methodologies and strategies have been proposed. This section gives an overview on the previous related works on modelling of the floating fish cage dynamics, which includes modelling the dynamics of the floater, the net cage, and more or less the complete fish cage system. Hereby one could have a general picture on the current state-of-the-art model.

1.2.1 Floater

Fish cage floater is a kind of slender structure floating at the free surface, whose diameter is smaller than the wave length. Wave induced loads on a floater and the motion response of it is a traditional marine hydrodynamic problem. In 2D case where the floater is simplified as an infinite horizontal cylinder floating at the free surface, the solution of the problem can be dated back to 1940s, when Ursell provided the analytical solution for the radiation problem in [52], [53], [54] using classic potential theory. The solution of the linear diffraction problem is given in e.g. [39]. However, if the diffraction effects are neglected, i.e. the incoming wave is believed to be undisturbed due to sufficiently long wave length, the wave loads on the floater can be calculated based on Morison equation. This method has been applied in [35] where the optimal inertia and drag coefficients are given for a partially submerged floater.

With increasing computer resources, solutions based on computational fluid dynamic approach have been presented in the recent years for this 2D problem. The advantages of these solvers are that they are capable to handle highly nonlinear wave system and viscous effects simultaneously. This is important when e.g. overtopping occurs. In [25] a Navier-Stokes solver was implemented to address this problem. The solver combines the finite difference discretization and constrained interpolation profile (CIP). An immerse boundary method was applied to describe the boundary patch of the floater, and one-fluid method with colour function was adopted to capture the interface. In addition, a fraction step approach was used to solve the incompressible Navier-Stokes equations. Extensive validation cases were performed under different wave conditions for both fixed and floating floater,

and the agreement is in general very good. Furthermore, in [10] and [43], CFD results have also been presented for wave interaction with fixed partially submerged horizontal cylinder. In [43], the open source toolbox REEF3D was used, which is also a finite difference code with immerse boundary method. Specifically, Weighted Essentially Non-Oscillatory (WENO) scheme was applied for the convective term, which reaches up to 5th-order accurate for a smooth solution. But in [10], results from another set of code with finite element method was presented. The special ingredient of this solver is to use a Lagrangian–Eulerian advection remap algorithm, known as the CLEAR-VOF model [5]. The idea of this algorithm is to move the fluid portion of an element in a Lagrangian sense, and redistribute it locally in the Eulerian fixed mesh. The fraction step technique presented in [23] was applied for solving Navier-Stokes equations.

When the problem is extended to fully 3D case, no direct CFD solution has been provided in the open literature. Instead, solutions from potential theory or Morison equation have been given in several publications. In [12], an analytical method was proposed for motion and elastic deformation of the floater in waves. By using the curved beam theory, the deformation of the floater was obtained. Modal superposition method was applied where the deformation was expressed as a weighted sum of eigenmodes. The wave forces were predicted by Morison equation, while the diffraction effects were fully neglected. This model was further extended in [59], where damping of the structure was considered.

An extended 3D hydroelastic theory was developed in [20] to predict the hydroelastic response of flexible floating interconnected structures. Later on, it was applied in [19] to predict dynamic responses of the fish farm floaters in waves. Hinge modes in two directions and flexible torsional modes were all considered in the analyses. The dry and wet resonant natural frequencies were also calculated for each rigid relative motion and the flexible modes. Some numerical examples were given on the dynamic response of 5 by 2 fish cage floaters in regular wave conditions for a specific open ocean fish farm.

In [33], a derivation of vertical added mass, damping and wave excitation loads on an elastic semi-submerged torus is presented based on 3D long wave length theory. The final expression was given by matching the near field solution and far field solution. It was revealed that the strip theory may not correctly predict them, indicating the importance of 3D effects. Series of model tests on regular deep water wave interaction with the floater were further performed in [32]. The study

was focused on the longitudinal motions and vertical accelerations as well as wave motion inside it. A nearly rigid floater was used, therefore they could also apply a second order potential flow solver without considering the deformation of the floater. The importance of nonlinearity was emphasized, where third and fourth order of harmonics may concern. Viscous effects are secondary for small amplitude waves, but in steep waves where flow separation occurs, it is important. A fully nonlinear 3D CFD method that accounts for hydroelasticity effect is required to consider all the effects, but in principle it is computationally expensive.

1.2.2 Net cage

As mentioned in Section 1.2, net cage is a kind of compliant structure with large amount of knots and twines, which makes direct modelling of the flow field around it and the hydrodynamic load on it rather difficult. Previous works, and also the present thesis, are seeking a so-called "rational method" to model it.

In [36] a wake model for flow through a net panel was developed. The wake model was based on the sum of wake behind each individual net twine, which is governed by simplified linear differential equations. Then this "sum of the cylinder" model was modified afterwards in order to give correct asymptotic value in the far field. A force model was also included where the force coefficients for the net panel were given as a function of solidity ratio S_n and angle for a limited range of S_n (0.13 - 0.317). This lays the foundation for the screen type force model. This force model was directly applied in current and waves to study the influence of different parameters on the behaviour of the net [29]. Further generalization of this model is presented in [26] to account for a wider range of solidity ratios S_n up to 0.5. In addition, the effect of Reynolds number was also considered.

Screen type force model is based on the concept of "super element", i.e. each net panel element has the same properties with the net structures that are being simulated. Besides this force model, another type of force model is the Morison type force model, which models the net as individual elements. The forces on each twine are calculated based on Morison equation. The cross-flow principle should be applied in case that the flow is ambient, which assumes that the current could be separated into flow tangential and normal to the element axis. This model has been applied in e.g. [40], [34] and [51].

Alternatively, in some previous publications, the potential wave theory was com-

bined with Darcy's law to describe the effects of the net cage on the flow. This modelling strategy was first proposed in [11], where a porous wavemaker theory was developed. Then it has been used in e.g. [38] and [46] for analysis of wave past the net cage. In this set of formulation, the wave field was described by the potential theory, where the governing equation is the Laplace equations plus the linearised kinematic and dynamic boundary conditions. The key point of this method is to modify the kinematic boundary condition based on Darcy's law when wave past the porous membrane, where a porous-effect parameter was introduced. Via this way, the effect of net cage on the fluid domain was taken into account.

Besides the hydrodynamic model, one also needs a structural model to model the deformation of the net cage due to the hydrodynamic load. In general there are three types of structural model. The simplest model is the so-called lumped mass model, which is actually a mechanical model. By application of this model, the net cage is represented as a set of lumped mass points which are connected by the springs without mass. By solving the displacement of each lumped mass point based on Newton's second law, the shape of the net cage is obtained. This kind of method has been applied in e.g. [62] and [63]. More advanced structural models usually involve finite element methods, where the elements with different shape functions could be applied. However, in the perspective of modelling strategies, the finite element models for modelling of the net cage deformation can be broadly divided into two groups. The first group uses truss or beam elements to model the twines of the net cage. This is similar to the lumped mass model, but each element can have higher degree of freedom considering e.g. tension and bending stiffness of the twines. This has been applied in e.g. [40] and [51]. Alternatively, surface membrane elements can be applied to model the net deformation. Therefore, the net cage is represented by a sheet of deformable membrane. Highly nonlinear relation needs to be applied between external forces and node displacements, as shown in [30].

Although as mentioned above, direct modelling of the geometry of the net cage is not feasible, there have been investigations on combing a computational fluid dynamic (CFD) solver with a porous media model to model the flow field around net. One could either model the net as a surface boundary patch across which the pressure drops. Alternatively a volume region could be applied to represent the net structures, where a resistance was added as a source term due to presence of the net. The magnitude of the resistance can be determined by fitting the

experimental data. The latter method gains more popularity in recent years, and it has been applied in e.g. [44], [60] and [61] for current flow through plane net panel and circular net cages fixed in a frame. Deformation of the net could also be incorporated by coupling a porous media model with a lumped mass structural model. In [7] and [8] this has been achieved for steady current flow through plane net panel and circular net cages.

1.2.3 Global analysis on the floating fish cage system

From previous works, investigations have been performed on the net-floater system in current and waves in both 2D and 3D cases, by both numerical simulation and model test. In [18], [37] and [6] focus has been given on the interactions between the net cage and the floater in 2D cases. A thoroughly investigation was performed in [6] on the snap load of the fish cage in regular waves by both numerical simulations and experiments. The snap load is generated due to the relative motion between the floater and the bottom sinker, and the magnitude of it could be several times larger than the weight of the bottom. The numerical model in [6] is a combination of the screen type load model for the net panel and potential flow code in time domain for the motion of floater. In [18] systematic experiments have been performed in a towing tank to identify the contribution of the net and the floater on the total forces. Based on the data from the experiments, a hybrid empirical-numerical method was proposed for hydroelastic analysis of a floater-net system [37].

State-of-the-art numerical model for simulating 3D fish cages are mainly based on the coupling between an analytical model for the floater motion and a lumped mass/truss bar model for the net cages. In [62] series of simulations have been performed for the response of fish cage under combined current and wave conditions. The interaction between current and waves was neglected. The floater was treated as a rigid body and its motion was calculated based on the force and moment balance. The deformation of the net cage was modelled by a lumped mass model where the load on it was calculated by Morison type load model. This model was further applied for simulating fish cages under many other different environmental loads, e.g. for multiple fish cages in a single line in [58], which was focused on the comparison between the twin mooring system and the orthogonal mooring system.

The dual pontoon floating cage was also looked into in [48], where a novel dual pontoon was applied as the floater. A fully nonlinear numerical wave tank was set

up to compute the wave forces on the floater based on boundary element method. The forces on the net cage were also calculated based on Morison equation. But the deformation of the cage was neglected. Furthermore, in order to consider the damping effect due to viscosity, an uncoupled damping matrix was incorporated to reduce the motion of the floater near the resonance frequency.

Until now one of the most advanced numerical model was developed in [27], which considers most of the important factors. The screen type force model developed in [26] was applied in unsteady flows for the hydrodynamic forces on the net cage. Regarding the floater, elasticity of the floater was taken into account. Further, the diffraction forces were also considered together with nonlinear Froude–Kriloff forces, restoring forces, added mass and damping forces and viscous drag force. The mooring lines were treated in the same manner as the net cage, i.e. they were modelled as trusses. All parts of the system were solved simultaneously. This gave a strong coupling between the floater, net cage and moorings. Dedicated experiments have also been performed to validate the numerical model under a variety of wave conditions.

1.3 The present model

In the present work we developed a CFD model to simulate the responses of floating fish cages, where the modeling framework is the open source toolbox OpenFOAM. Different versions of OpenFOAM have been used in the project, but finally all the codes were ported into OpenFOAM-3.0.x, which is a bug fix version and was regularly updated until OpenFOAM-4.0 was released. This allowed the author to stay the most up-to-date possible of OpenFOAM's latest source code through gitHub during the Ph.D. project.

The fish cage itself is a highly complex system with a large number of moving components where all components behave under mutual influence [27]. In the numerical model each part of the fish cage was simplified to some degree. Below the assumptions and simplifications introduced in the numerical model are given together with the methodology used to model each component.

Regarding the net cage, the porous media model was applied, where the net cage was modelled as a sheet of porous media layer. This method has been used several times for modelling net cages, as shown in Section 1.2.2. In [22] the formulation of the porous media model was revised and it was applied in the model. This

formulation was derived by volume averaging the Navier-Stokes equations. Besides the resistance term, the added mass term and the porosity were also considered in the formulation. However, one should note that by using the porous media model, the flow details at pore scale, e.g. the boundary layers around each knot and twine, were not modelled. Only an added mass force and a drag force were added to the Navier-Stokes equations. In addition, in 3D cases for modelling of circular cages, the bottom net was not considered. In order to resolve the deformation of the net cage, a lumped mass model was implemented, and it was coupled with the porous media model to achieve the fluid-structure interaction (FSI) analysis for the net cage.

In steady current flow, only the net cage was considered in the numerical model. However, in wave condition the motion of the floater is important, and it is the main contributor to the force on the net cage [29]. Hereby in the present work motion of the floater was also taken into account under wave condition. The floater was resolved by a body-fitted computational mesh, but the geometry of the floater was simplified to a cylinder with circular cross section. In the vicinity of the free surface and the floater, the mesh was properly refined. A six degree of freedom motion solver was applied to resolve the motion status of the floater under wave conditions.

The weight system for the net cage was not resolved by the mesh, instead the mean forces acting on the weight system were directly added to the lumped mass points connecting the weight system. This includes the sum of the buoyancy and gravity force. In addition, in steady current flow, the mean drag force was also added based on Morison equation, but the lift force was neglected, since it is time varying and has a zero mean value. Under wave condition, the mean drag force was also neglected, considering the rather weak orbital motion of the water particles at that depth. The mooring lines were neither modelled explicitly, but treated as a linear spring, and the restoring force was added to the equation of motion for the floater.

Furthermore, an additional issue is the swimming fish effects on the hydrodynamic behaviour of the cage. There have been rather limited publications on this topic. [9] examined the effects of locomotor activity on water dispersion within the cage in lentic conditions. In [21] the fish effect on the mooring load of a fish cage was investigated both numerically and experimentally. As reported in [21], the total volume of fish is typically about 2.5% of the volume of the fish cage at rest. From the artificial fish experiments, where nine artificial fish were put in the cage

occupying the same volume, i.e. 2.5%, the result shows that the influence of the artificial fish on the mooring load is insignificant and less than 3% of the no fish case. However, for live fish experiments, the influence is not negligible. The mooring load for the cage with fish in current is between 10% and 28% larger than the loads without fish, but this is due to the contact between the fish and the back cone part of the net cage. Presently the swimming fish induced effects were fully neglected in the numerical model. It is recommended as future works.

1.4 Thesis Outlines

The present thesis consists of several papers. Each one forms an individual chapter and deals with a specific topic related to CFD modelling of floating fish cage dynamics. Below the main content of each chapter is outlined with its contributions to the current state-of-the-art models.

In Chapter 2 and Chapter 3, the main focus is on the simulation of flow through and around pure net cage, without occurrence of floater. Chapter 2 presents a new method to calculate the porous resistance coefficients for the net cage. Previously the coefficients were obtained by fitting the measured data via e.g. least square method. However for a specific net, the measured data could be very limited or even non-existing. Therefore this limits the application of porous media model. In this chapter, a new formula was derived to calculate the coefficients. The formula relates the porous resistance coefficients with the physical parameters of the net cage e.g. the twine diameter, the mesh size etc. Therefore, as long as the net cage is given, one can easily obtain the resistance coefficients without any measured data. This eases direct application of the porous media model for the net cage.

Due to flexibility of the net cage, its deformation should not be neglected. As mentioned above in Section 1.2.2, there have been limited publications that successfully achieve the FSI analysis for the net cage in steady current flow. In Chapter 3, a new scheme was proposed and implemented for the coupling between the porous media model and the lumped mass model for the net cage. The scheme ensures an efficient data exchange at every time step, and is applicable in both steady and unsteady flow conditions. Therefore the FSI analysis for the net cage can also be applied in wave and combined current and wave conditions.

Chapter 4 presents an in-depth discussion on the existing multiphase flow solver and the so-called Weller volume of fluid (VOF) scheme in OpenFOAM, and its

application in wave generation and interaction with fixed horizontal cylinder that serves as a fish cage floater in 2D case. By application of the VOF method, one needs to solve an extra advection equation for the volume fraction field. However, there are several issues for solving this equation. One needs to maintain the boundness of the solution, since the volume fraction field is always between zero and one. Meanwhile the numerical diffusion should be minimized, otherwise the free surface will be smeared. Chapter 4 illustrates how Weller-VOF scheme resolves these issues. In addition, previously it has been reported that near-surface kinematics can not be correctly reproduced in many Navier-Stokes solvers including OpenFOAM, e.g. in [57]. That is due to the large density ratio between the air and water which generates unbalanced forces. In this chapter we conducted series of numerical experiments to identify the best combination of schemes and parameters that could minimize this effect and generate the best quality waves. This set of parameters and schemes were further used for validation of wave loads on a fixed fish cage floater.

Finally in Chapter 5, the six degree of freedom motion solver was applied in the numerical model to solve the motion equation for the floater. Different motion integration methods were implemented and tested, and it was decided to use the explicit-implicit Adams-Bashforth-Moulton scheme as the motion integration scheme for the floater. Then the newly developed model for the net cage was combined with this model to form a complete framework for CFD modelling of floating fish cage dynamics. This allows one to conduct integrated analysis for the whole net-floater system. A variety of experiments were reproduced by the numerical model, where the snap load of the net cage on the floater, and the mooring forces were compared with the experimental data. However the validation of the model was restricted to 2D cases, and 3D validations and applications are recommended as future work.

1.5 Recommendations on the future work

Several topics on the future work have been mentioned in the above sections to overcome the limitation of the present study. In this section they are summarized with some relevant comments and suggestions.

The investigations on the floater and the whole fish cage system have been limited to 2D cases in the present work. Future work can be in relation to 3D modelling

of them. The first step will be 3D modelling of the floater without the net cage. Comparison can be made with the experimental and numerical results presented in [32], to investigate if improvements are reached by applying a CFD solver comparing with linear and nonlinear potential solvers. Furthermore, for a flexible floater, either an analytical model or a numerical model could be incorporated to obtain the deformation of the floater. However, a fully coupled CFD/FEM analysis on the floater will be extremely time consuming. The analytic model based on curved beam theory might be a better option, depending on the accuracy of the results.

The numerical model can also be further developed to take into consideration the marine growth. This mainly concerns the choice of the porous resistance coefficients for fouled net panels. Systematic experiments needs to be done to investigate the drag force on the fouled net panel, and the flow field behind and around it.

Swimming fish effects on the hydrodynamic field of the fish cage can also be a research topic in the future. Directly modelling of the geometry of the fish itself is not straight-forward in the CFD model, due to its complex geometry of the body shape, and simultaneous modelling of its moving and interaction between the fish is nearly impossible. One possible way to consider the fish effects is to add some extra resistances in the numerical model. Maybe a fixed path of movement could be assigned to the resistances to mimic the schooling of the fish. But the schooling path depends mostly on the species of fish.

1.6 References

[1] The State of World Fisheries and Aquaculture 2012 / Food and Agriculture Organization of the United Nations. Rome, 2012. – Forschungsbericht. – ISBN 9789251091852

[2] Cage farming aquaculture 2014-2015 / AKVA group. 2015. – Forschungsbericht

[3] *Marine fish farms*. 2016. – URL http://eng.mst.dk/topics/industry/aquaculture/marine-fish-farms/. – Accessed: 2016-10-18

[4] The State of World Fisheries and Aquaculture 2016 / Food and Agriculture Organization of the United Nations. Rome, 2016. – Forschungsbericht. – ISBN 9789251091852

[5] Ashgriz, Nasser ; Barbat, Tiberiu ; Wang, Gang: A computational

Lagrangian–Eulerian advection remap for free surface flows. In: *International Journal for Numerical Methods in Fluids* 44 (2004), Nr. 1, S. 1–32. – URL http://dx.doi.org/10.1002/fld.620. – ISSN 1097-0363

[6] Bardestani, Mohsen ; Faltinsen, Odd M.: A two dimensional approximation of a floating fish farm in waves and current with the effect of snap loads. In: *Proceedings of the ASME 2013 32nd International Conference on Ocean, Offshore and Arctic Engineering*. Nantes, France, 2013

[7] Bi, Chun-Wei ; Zhao, Yun-Peng ; Dong, Guo-Hai ; Xu, Tiao-Jian ; Gui, Fu-Kun: Numerical simulation of the interaction between flow and flexible nets. In: *Journal of Fluids and Structures* 45 (2014), jan, S. 180–201. – URL http://linkinghub.elsevier.com/retrieve/pii/S0889974613002594. – ISSN 08899746

[8] Bi, Chun-Wei ; Zhao, Yun-Peng ; Dong, Guo-Hai ; Zheng, Yan-Na ; Gui, Fu-Kun: A numerical analysis on the hydrodynamic characteristics of net cages using coupled fluid-structure interaction model. In: *Aquacultural Engineering* 59 (2014), mar, S. 1–12. – URL http://linkinghub.elsevier.com/retrieve/pii/S014486091400003Xhttp://www.sciencedirect.com/science/article/pii/S014486091400003X. – ISSN 01448609

[9] Chacon-Torres, A. ; Ross, L. G. ; Beveridge, M. C M.: The effects of fish behaviour on dye dispersion and water exchange in small net cages. In: *Aquaculture* 73 (1988), Nr. 1-4, S. 283–293. – ISSN 00448486

[10] Chen, Bing ; Lu, Lin ; Greated, Clive a. ; Kang, Haigui: Investigation of wave forces on partially submerged horizontal cylinders by numerical simulation. In: *Ocean Engineering* 107 (2015), S. 23–31. – URL http://linkinghub.elsevier.com/retrieve/pii/S002980181500339X. – ISSN 00298018

[11] Chwang, Allen T.: A porous-wavemaker theory. In: *Journal of Fluid Mechanics* 132 (1983), S. 395–406

[12] Dong, Guo-Hai ; Hao, Shuang-Hu ; Zhao, Yun-Peng ; Zong, Zhi ; Gui, Fu-Kun: Elastic responses of a flotation ring in water waves. In: *Journal of Fluids and Structures* 26 (2010), jan, Nr. 1, S. 176–192. – URL http://linkinghub.elsevier.com/retrieve/pii/S0889974609001145. – ISSN 08899746

[13] Drumm, A: Evaluation of the promotion of offshore aquaculture through a technology platform (OATP) / Marine Institute. Galway, Ireland, 2010. – Forschungsbericht

[14] Dürr, Simone ; Watson, Douglas I.: Biofouling and Antifouling in Aquaculture. In: Dürr, Simone (Hrsg.) ; Thomason, Jeremy C. (Hrsg.): *Biofouling*. Oxford, UK : Wiley-Blackwell, 2009, Kap. 19

[15] Endresen, Per C.: *Vertical Wave Loads and Response of a Floating Fish Farm with Circular Collar*, Norwegian University of Science and Technology, Master Thesis, 2011

[16] Fernandes, T. F. ; Miller, K. L. ; Read, P. A.: Monitoring and regulation of marine aquaculture in Denmark. In: *Journal of Applied Ichthyology* 16 (2000), Nr. 4-5, S. 138–143. – ISBN 01758659

[17] Fredriksson, David W. ; DeCew, Judson C. ; Tsukrov, Igor: Development of structural modeling techniques for evaluating HDPE plastic net pens used in marine aquaculture. In: *Ocean Engineering* 34 (2007), nov, Nr. 16, S. 2124–2137. – URL http://linkinghub.elsevier.com/retrieve/pii/S0029801807001333. – ISSN 00298018

[18] Fu, Shi-Xiao ; Xu, Yu-Wang ; Hu, Ke ; Zhong, Qian ; Li, Run-Pei: Experimental Investigation on Hydrodynamics of a Fish Cage Floater-net System in Oscillatory and Steady Flows by Forced Oscillation Tests. In: *Journal of Ship Research* 58 (2014), mar, Nr. 1, S. 20–29. – URL http://www.ingentaselect.com/rpsv/cgi-bin/cgi?ini=xref{&}body=linker{&}reqdoi=10.5957/JOSR.58.1.130022. – ISSN 00224502

[19] Fu, Shixiao ; Moan, Torgeir: Dynamic analyses of floating fish cage collars in waves. In: *Aquacultural Engineering* 47 (2012), mar, S. 7–15. – URL http://linkinghub.elsevier.com/retrieve/pii/S0144860911000835. – ISSN 01448609

[20] Fu, Shixiao ; Moan, Torgeir ; Chen, Xujun ; Cui, Weicheng: Hydroelastic analysis of flexible floating interconnected structures. In: *Ocean Engineering* 34 (2007), Nr. 11-12, S. 1516–1531. – ISBN 0047735511

[21] He, Zhao ; Faltinsen, Odd M. ; Fredheim, Arne ; Kristiansen, Trygve: The influence of fish on the mooring loads of a floating fish farm. In: *Proceeding*

of 7th International Conference on Hydroelasticity in Marine Technology. Split, Croatia, 2015

[22] Jensen, Bjarne ; Jacobsen, Niels G. ; Christensen, Erik D.: Investigations on the porous media equations and resistance coefficients for coastal structures. In: *Coastal Engineering* 84 (2014), feb, S. 56–72. – URL http://linkinghub.elsevier.com/retrieve/pii/S0378383913001816. – ISSN 03783839

[23] Jiang, Chun B. ; Kawahara, Mutsuto ; Kashiyama, Kazuo: A Taylor–Galerkin-based finite element method for turbulent flows. In: *Fluid Dynamics Research* 9 (1992), Nr. 4, S. 165. – URL http://stacks.iop.org/1873-7005/9/i=4/a=A03

[24] Kapetsky, James M. ; Aguilar-Manjarrez, José ; Jenness, Jeff: *A global assessment of offshore mariculture potential from a spatial perspective*. Food and Agriculture Organization of the United Nations, 2013. – 181 S. – ISBN 978-92-5-107584-5

[25] Kristiansen, David: *Wave Induced Effects on Floaters of Aquaculture plants*, Norwegian University of Science and Technology, Ph.D. thesis, 2010

[26] Kristiansen, Trygve ; Faltinsen, Odd M.: Modelling of current loads on aquaculture net cages. In: *Journal of Fluids and Structures* 34 (2012), oct, S. 218–235. – URL http://linkinghub.elsevier.com/retrieve/pii/S0889974612000783. – ISSN 08899746

[27] Kristiansen, Trygve ; Faltinsen, Odd M.: Experimental and numerical study of an aquaculture net cage with floater in waves and current. In: *Journal of Fluids and Structures* 54 (2015), apr, S. 1–26. – URL http://linkinghub.elsevier.com/retrieve/pii/S0889974614002114. – ISSN 08899746

[28] Lader, Pål ; Fredriksson, David W. ; Volent, Zsolt ; DeCew, Jud ; Rosten, Trond ; Strand, Ida M.: Drag Forces on, and Deformation of, Closed Flexible Bags. In: *Journal of Offshore Mechanics and Arctic Engineering* 137 (2015), Nr. 4, S. 041202

[29] Lader, Pål F. ; Fredheim, Arne: Dynamic properties of a flexible net sheet in waves and current-A numerical approach. In: *Aquacultural Engineering* 35 (2006), oct, Nr. 3, S. 228–238. – URL http://linkinghub.elsevier.com/retrieve/pii/S0144860906000161. – ISSN 01448609

[30] Larsen, Carl M. ; Tronstad, Harald: NFEM approaches for calculating fishing gear as a system of flexible lines. In: *Proceedings of the International Conference on Offshore Mechanics and Arctic Engineering* Bd. 1, 1997, S. 101–108

[31] Larsen, K: National Aquaculture Sector Overview. Denmark / National Aquaculture Sector Overview Fact Sheets. Rome, 2005. – Forschungsbericht

[32] Li, Peng ; Faltinsen, Odd M. ; Lugni, Claudio: Nonlinear vertical accelerations of a floating torus in regular waves. In: *Journal of Fluids and Structures* 66 (2016), S. 589–608. – URL http://linkinghub.elsevier.com/retrieve/pii/S0889974615302383. – ISSN 08899746

[33] Li, Peng ; Faltinsen, Odd M.: Wave-induced vertical response of an elastic circular collar of a floating fish farm. In: *Proceedings of 10th International Conference on Hydrodynamics*, 2012

[34] Li, Yu-Cheng ; Zhao, Yun-Peng ; Gui, Fu-Kun ; Teng, Bin: Numerical simulation of the hydrodynamic behaviour of submerged plane nets in current. In: *Ocean Engineering* 33 (2006), dec, Nr. 17-18, S. 2352–2368. – URL http://linkinghub.elsevier.com/retrieve/pii/S0029801806000370. – ISSN 00298018

[35] Li, Yucheng ; Gui, Fukun ; Teng, Bin: Hydrodynamic behavior of a straight floating pipe under wave conditions. In: *Ocean Engineering* 34 (2007), mar, Nr. 3-4, S. 552–559. – URL http://linkinghub.elsevier.com/retrieve/pii/S0029801806000989. – ISSN 00298018

[36] Løland, Geir: Current forces on, and water flow through and around, floating fish farms. In: *Aquaculture International* 1 (1993), Nr. 1, S. 72–89. – ISBN 8271192698, 9788271192693

[37] Ma, Lei-Xin ; Hu, Ke ; Fu, Shi-Xiao ; Moan, Torgeir ; Li, Run-Pei: A Hybrid Empirical-Numerical Method for Hydroelastic Analysis of a Floater-and-Net System. In: *Journal of Ship Research* 60 (2016), Nr. 1, S. 14–29

[38] Mandal, S. ; Sahoo, T.: Gravity wave interaction with a flexible circular cage system. In: *Applied Ocean Research* 58 (2016), S. 37–48. – URL http://dx.doi.org/10.1016/j.apor.2016.03.005. – ISBN 0141-1187

[39] Martin, P. A. ; Dixon, A. G.: The scattering of regular surface waves by a fixed, half-immersed, circular cylinder. In: *Applied Ocean Research* 5 (1983), Nr. 1, S. 13–23. – ISSN 01411187

[40] Moe, H. ; Fredheim, A. ; Hopperstad, O. S.: Structural analysis of aquaculture net cages in current. In: *Journal of Fluids and Structures* 26 (2010), apr, Nr. 3, S. 503–516. – URL http://linkinghub.elsevier.com/retrieve/pii/S0889974610000289. – ISSN 08899746

[41] Moe, Heidi ; Hopperstad, Odd S. ; Olsen, Anna ; Jensen, Østen ; Fredheim, Arne: Temporary-creep and post-creep properties of aquaculture netting materials. In: *Ocean Engineering* 36 (2009), Nr. 12-13, S. 992–1002. – URL http://dx.doi.org/10.1016/j.oceaneng.2009.05.009. – ISBN 978-0-7918-5535-5

[42] Moe, Heidi ; Olsen, Anna ; Hopperstad, Odd S. ; Jensen, Østen ; Fredheim, Arne: Tensile properties for netting materials used in aquaculture net cages. In: *Aquacultural Engineering* 37 (2007), nov, Nr. 3, S. 252–265. – URL http://linkinghub.elsevier.com/retrieve/pii/S0144860907000763. – ISSN 01448609

[43] Ong, Muk C. ; Kamath, Arun ; Bihs, Hans ; Afzal, Mohammad S.: Numerical simulation of free-surface waves past two semi-submerged horizontal circular cylinders in tandem. In: *Marine Structures* 52 (2017), S. 1–14. – URL http://dx.doi.org/10.1016/j.marstruc.2016.11.002. – ISSN 09518339

[44] Patursson, Øystein ; Swift, M. R. ; Tsukrov, Igor ; Simonsen, Knud ; Baldwin, Kenneth ; Fredriksson, David W. ; Celikkol, Barbaros: Development of a porous media model with application to flow through and around a net panel. In: *Ocean Engineering* 37 (2010), feb, Nr. 2-3, S. 314–324. – URL http://linkinghub.elsevier.com/retrieve/pii/S0029801809002406. – ISSN 00298018

[45] Strand, I. M. ; Sørensen, A. J. ; Volent, Z. ; Lader, P.: Experimental study of current forces and deformations on a half ellipsoidal closed flexible fish cage. In: *Journal of Fluids and Structures* 65 (2016), S. 108–120. – URL http://dx.doi.org/10.1016/j.jfluidstructs.2016.05.011. – ISSN 10958622

[46] Su, Wei ; Zhan, Jie-min ; Huang, Hua: Analysis of a porous and flexible cylinder in waves. In: *China Ocean Engineering* 29 (2015), Nr. 3, S. 357–

368. – URL http://link.springer.com/10.1007/s13344-015-0025-z. – ISBN 1334401500

[47] Swift, M. R. ; Fredriksson, David W. ; Unrein, Alexander ; Fullerton, Brett ; Patursson, Oystein ; Baldwin, Kenneth: Drag force acting on biofouled net panels. In: *Aquacultural Engineering* 35 (2006), Nr. 3, S. 292–299. – ISBN 0144-8609

[48] Tang, Hung-Jie ; Huang, Chai-Cheng ; Chen, Wei-Ming: Dynamics of dual pontoon floating structure for cage aquaculture in a two-dimensional numerical wave tank. In: *Journal of Fluids and Structures* 27 (2011), oct, Nr. 7, S. 918–936. – URL http://linkinghub.elsevier.com/retrieve/pii/S0889974611001034. – ISSN 08899746

[49] Troell, Max ; Joyce, Alyssa ; Chopin, Thierry ; Neori, Amir ; Buschmann, Alejandro H. ; Fang, Jian G.: Ecological engineering in aquaculture — Potential for integrated multi-trophic aquaculture (IMTA) in marine offshore systems. In: *Aquaculture* 297 (2009), dec, Nr. 1-4, S. 1–9. – URL http://linkinghub.elsevier.com/retrieve/pii/S0044848609007856. – ISSN 00448486

[50] Trujillo, Pablo ; Piroddi, Chiara ; Jacquet, Jennifer: Fish farms at Sea: The ground truth from Google Earth. In: *PLoS ONE* 7 (2012), Nr. 2, S. 1–4. – ISSN 19326203

[51] Tsukrov, Igor ; Eroshkin, Oleg ; Fredriksson, David ; Swift, M. R. ; Celikkol, Barbaros: Finite element modeling of net panels using a consistent net element. In: *Ocean Engineering* 30 (2002), Nr. 2, S. 251–270

[52] Ursell, F: On the heaving motion of a circular cylinder on the surface of a fluid. In: *The Quarterly Journal of Mechanics and Applied Mathematics* (1949), Nr. April 1948, S. 218–231. – URL http://qjmam.oxfordjournals.org/content/2/2/218.short

[53] URSELL, F.: water waves generated by oscillating bodies. In: *The Quarterly Journal of Mechanics and Applied Mathematics* (1954)

[54] Ursell, F.: The decay of the free motion of a floating body. In: *Journal of Fluid Mechanics* 19 (1964), Nr. 02, S. 305–319. – URL http://journals.cambridge.org/article{_}S0022112064000738. – ISSN 0022-1120

[55] Vielma, J ; Kankainen, M: Offshore fish farming technology in Baltic Sea production conditions / Aquabest. 2013. – Forschungsbericht

[56] Vikestad, K ; Lien, E: Bending stiffness of a clamps-connected 2-rings PE fish cage collar. In: *Maritime Transportation and Exploitation of Ocean and Coastal Resources, Two Volume Set*. Taylor & Francis, aug 2006, S. 1293–1301. – URL http://dx.doi.org/10.1201/9781439833728.ch159. – ISBN 978-0-415-39036-1

[57] Wroniszewski, Paweł A. ; Verschaeve, Joris C. ; Pedersen, Geir K.: Benchmarking of Navier–Stokes codes for free surface simulations by means of a solitary wave. In: *Coastal Engineering* 91 (2014), S. 1–17. – URL http://linkinghub.elsevier.com/retrieve/pii/S0378383914000842. – ISSN 03783839

[58] Xu, Tiao-Jian ; Zhao, Yun-Peng ; Dong, Guo-Hai ; Li, Yu-Cheng ; Gui, Fu-Kun: Analysis of hydrodynamic behaviors of multiple net cages in combined wave–current flow. In: *Journal of Fluids and Structures* 39 (2013), may, S. 222–236. – URL http://linkinghub.elsevier.com/retrieve/pii/S088997461300042X. – ISSN 08899746

[59] Zhao, Yun-Peng ; Bai, Xiao-Dong ; Dong, Guo-Hai ; Bi, Chun-Wei ; Gui, Fu-Kun: Numerical analysis of the elastic response of a floating collar in waves. In: *Ocean Engineering* 95 (2015), S. 175–182. – URL http://linkinghub.elsevier.com/retrieve/pii/S0029801814004727. – ISSN 00298018

[60] Zhao, Yun-Peng ; Bi, Chun-Wei ; Dong, Guo-Hai ; Gui, Fu-Kun ; Cui, Yong ; Guan, Chang-Tao ; Xu, Tiao-Jian: Numerical simulation of the flow around fishing plane nets using the porous media model. In: *Ocean Engineering* 62 (2013), apr, S. 25–37. – URL http://linkinghub.elsevier.com/retrieve/pii/S0029801813000243. – ISSN 00298018

[61] Zhao, Yun-Peng ; Bi, Chun-Wei ; Dong, Guo-Hai ; Gui, Fu-Kun ; Cui, Yong ; Xu, Tiao-Jian: Numerical simulation of the flow field inside and around gravity cages. In: *Aquacultural Engineering* 52 (2013), jan, S. 1–13. – URL http://linkinghub.elsevier.com/retrieve/pii/S0144860912000593. – ISSN 01448609

[62] Zhao, Yun-Peng ; Li, Yu-Cheng ; Dong, Guo-Hai ; Gui, Fu-Kun ; Teng, Bin: A numerical study on dynamic properties of the gravity cage in combined

wave-current flow. In: *Ocean Engineering* 34 (2007), dec, Nr. 17-18, S. 2350–2363. – URL http://linkinghub.elsevier.com/retrieve/pii/S0029801807001400. – ISSN 00298018

[63] Zhao, Yun-Peng ; Li, Yu-Cheng ; Dong, Guo-Hai ; Gui, Fu-Kun ; Wu, Hao: An experimental and numerical study of hydrodynamic characteristics of submerged flexible plane nets in waves. In: *AQUACULTURAL ENGINEERING* 38 (2008), Nr. 1, S. 16–25. – ISSN 01448609, 18735614

2 Investigations on the porous resistance coefficients for fishing net structures

---

Originally published as:
Chen, H. & Christensen, E.D., 2016. Investigations on the porous resistance coefficients for fishing net structures. Journal of Fluids and Structures, 65.

Investigations on the porous resistance coefficients for fishing net structures

Hao Chen[a,*], Erik Damgaard Christensen[a]

[a]*Section of Fluid Mechanics, Coastal and Maritime Engineering, Department of Mechanical Engineering, Technical University of Denmark, DK-2800 Kgs. Lyngby, Denmark*

Abstract

The porous media model has been successfully applied to numerical simulation of current and wave interaction with traditional permeable coastal structures such as breakwaters. Recently this model was employed to simulate flow through and around fishing net structures, where the unknown porous resistance coefficients were adjusted by fitting the available experimental data. In the present paper, a new approach was proposed to calculate the porous resistance coefficients based on the transformation of Morison type load model. The transformation follows the principle that the total forces acting on a net panel from Morison type load model should be equal to the forces obtained from the porous media model. In order to account for the interaction effects in-between the twines, two coefficients were introduced, and they were calibrated by minimizing the least square error function. Extensive validation cases were carried out to examine the performance of the numerical model. This includes steady current flow through plane net panels and circular fish cages, and wave interaction with plane net panels. A variety of fishing nets with different solidity ratios were used in the validation cases, from which it was seen that the overall agreement between the numerical and experimental results is fair.

Keywords: porous media model, resistance coefficients, fishing nets, Navier-Stokes equations

1. Introduction

Porous structures are widely used in coastal engineering, *e.g.* breakwaters for sea defense. A number of studies have been carried out on numerical simulation of flow through and around such structures, *e.g.* Jensen et al. (2014), Hsu et al. (2002), Liu et al. (1999), Losada et al. (2008), del Jesus et al. (2012), Higuera et al. (2014a) and Higuera et al. (2014b). Among these works, the effect of porous structures on the fluid was taken into account without resolving the exact geometry of them. Instead, they were treated as one continuum from a macroscopic point of view. By volume averaging the Navier-Stokes equations over a representative elementary volume, the effect of porous structures was included via a resistance term. This term was usually described by the extended Darcy-Forchheimer equation, which includes linear and nonlinear forces as well as inertia forces to account for accelerations.

Recently this approach was applied to simulate flow through fishing nets. In Patursson et al. (2010), Zhao et al. (2013a) and Zhao et al. (2013b), the porous media model was applied to simulate steady flow through a single net panel with different attack angles, multiple net panels and gravity cages, respectively. Furthermore, in Bi et al. (2014a) and Bi et al. (2014b), the porous media model was coupled with a lumped mass structural model to account for fluid-structure interaction effect. An iterative scheme was set up between these two models and the steady solution of the flow field and net deformation was obtained after several iterations. Similar work was also performed in Devilliers et al. (2016), where advanced adaptive mesh refinement technique was developed to increase the mesh resolution and improve the accuracy of the numerical results. Bi et al. (2015) and Zhao et al. (2014) further applied the porous media model for wave

*Corresponding author, tel.: (45) 50302416; e-mail address: hchen@mek.dtu.dk; fax (45) 45251961.

Nomenclature

γ_p	empirical coefficient in the expression of added mass coefficient
λ	mesh bar length of the fishing net
$\langle \bar{p}^f \rangle$	volume averaged ensemble averaged pore pressure
$\langle \bar{u'} \rangle$	volume averaged ensemble averaged turbulent fluctuating velocity field
$\langle \bar{u} \rangle$	volume averaged ensemble averaged velocity field
$\langle \mu_t \rangle$	volume averaged eddy viscosity
$\langle k \rangle$	volume averaged specific turbulent kinetic energy
μ	dynamic viscosity of the fluid
ν	kinematic viscosity of the fluid
ω	wave angular frequency
ρ	density of the fluid
θ	attack angle, where $\theta = 90°$ indicates the flow is aligned with the normal direction of the net panel
a	interaction coefficient in the expression of normal quadratic drag resistance coefficient
A_{net}	outlined area of the net panel
b	interaction coefficient in the expression of tangential quadratic drag resistance coefficient
C	quadratic porous drag resistance coefficient
C_m	added mass coefficient of the porous media
$C_{d,net}$	drag force coefficient of the net
$C_{d,twine}$	drag force coefficient of the net twines
$C_{I,twine}$	inertia force coefficient of the net twines
$C_{l,net}$	lift force coefficient of the net
D	linear porous drag resistance coefficient
d	twine diameter of the fishing nets
F	hydrodynamic forces acting on the porous media based on the Morison type load model
$F_{d,net}$	drag force of the net
$F_{d,twine}$	drag force of the net twines
$F_{I,twine}$	inertia force of the net twines
$F_{l,net}$	lift force of the net
g	gravitation acceleration
KC	Keulegan-Carpenter number
n	porosity of the fishing net
P	total pressure
p	excess pressure, where the hydrostatic pressure is subtracted
Q	hydrodynamic forces acting on the porous media based on the porous media model
R	transformation matrix from local coordinate system to global coordinate system
Re	Reynolds number
S	porous drag resistance
S_1	total projected area for in-plane twines of the considered net panel
S_2	total projected area for out-of-plane twines of the considered net panel
S_n	solidity ratio of the fishing net, defined as complement of porosity
T	wave period
u	velocity field
U_∞	magnitude of the velocity at infinity for current flow
U_m	magnitude of the maximum velocity in one period for the considered wave
V	volume of the porous media zone

interaction with net structures. The transmission coefficients obtained from CFD simulations were compared with laboratory tests under different wave conditions.

As described above, porous media model has already been used in several papers to simulate current and wave interaction with fishing nets. The net was modeled as a sheet of porous media with very thin thickness,

usually between 10 mm - 50 mm. Unlike the model used in breakwater design, anisotropy was taken into account in porous media flow for fishing nets, due to the difference between the exerted resistances in tangential and normal directions. Darcy-Forchheimer formula was applied to calculate the porous resistance forces, where constant resistance coefficients were obtained by optimizing the fit between the measured drag and lift forces from experiments and computed drag and lift forces at different flow velocities and attack angles. This approach has advantages that it avoids direct modeling of the fishing nets geometry, which is usually unrealistic since a single net panel may have tens of thousands of twins and knots. From the validation of the numerical model provided in the above mentioned works, the predicted forces and wake velocities from the porous media model in general agreed well with laboratory experiments, which demonstrates the feasibility of this approach.

However, there remains one issue for direct application of porous media model on flow through fishing nets, i.e. finding the porous resistance coefficients in Darcy-Forchheimer equation. Fitting procedure requires that for each individual net panel, measured drag and lift forces must be available for a variety of incoming velocities and attack angles, which limits its application in practical design. The present work provides an alternative approach to calculate the porous resistance coefficients, which expresses them as a function of physical parameters of the fishing net. These parameters are easily obtained from a given net panel, therefore the resistance coefficients are directly determined without any need of experimental data. Hereby this eases the application of the numerical model.

The remainder of the paper is organized as follows. In Section 2, a brief description is given on the numerical model, where the volume averaged Reynolds averaged Navier-Stokes equations proposed in Jensen et al. (2014) are employed as the governing equations. Section 3 gives the derivation and calibration of the expressions for porous resistance coefficients, followed by summary and discussion on the overall numerical model in Section 4. In Section 5, preliminary tests are run for the general setup and convergence analysis of the numerical model, while in Section 6 extensive validation cases are performed against laboratory tests. Series of experiments conducted in Patursson (2007), Zhan et al. (2006), Lader et al. (2007a) and Lader et al. (2007b) are reproduced by the numerical model to examine its accuracy and performance. Furthermore, sensitivity analysis is performed to test the influences of uncertainties in calculation of the porous resistance coefficients in Section 7. Finally conclusions of the paper are given in Section 8.

2. Description of the numerical model

The numerical model was set up within the framework of the open source computational fluid dynamics toolbox OpenFOAM with the version of extend-3.1. It uses finite volume discretization method with a collocated variable arrangement on unstructured grid. The solvers employed in the present work solve the volume averaged Reynolds averaged Navier-Stokes (VARANS) equations. For single phase porous media flow, e.g. net panel in current, a transient single phase flow solver was employed. For two phase porous media flow where waves were involved in, the solver solves VARANS equations for two incompressible, isothermal and immiscible fluids where volume of fluid (VOF) approach (see Hirt and Nichols (1981)) was used to capture the interface.

2.1. Governing equations

The VARANS equations proposed in Jensen et al. (2014) are the governing equations in the present work. Start from the general form of the incompressible Navier-Stokes equations:

$$\frac{\partial u_i}{\partial x_i} = 0 \tag{1}$$

$$\frac{\partial \rho u_i}{\partial t} + \frac{\partial \rho u_i u_j}{\partial x_j} = -\frac{\partial p}{\partial x_i} - g_j x_j \frac{\partial \rho}{\partial x_i} + \frac{\partial}{\partial x_j}\mu\left(\frac{\partial u_i}{\partial x_j} + \frac{\partial u_j}{\partial x_i}\right) \tag{2}$$

where $x_i = (x, y, z)$ is the global Cartesian coordinate system.

If free surface is involved in the numerical model for handling cases of wave propagation and interaction with fishing nets, an additional advection equation needs to be solved for local water volume fraction α:

$$\frac{\partial \alpha}{\partial t} + \frac{\partial}{\partial x_i}(u_i \alpha) = 0 \tag{3}$$

However, solving Eq. (3) introduces a number of difficulties with respect to boundness of the solution and prevention of a smeared interface. In OpenFOAM, an artificial compression term was added where the advection equation becomes:

$$\frac{\partial \alpha}{\partial t} + \frac{\partial}{\partial x_i}(u_i \alpha) + \frac{\partial}{\partial x_i}(u_i^r \alpha(1-\alpha)) = 0 \tag{4}$$

where u^r is the compressive velocity field. By introducing this term, smear of the interface was effectively prevented. Boundness of the volume fraction was guaranteed by a special designed solver called multi-dimensionsal limiter for explicit solution (MULES) solver, where the bounded solution was achieved by using flux from first order upwind scheme plus a limited portion of flux from high order scheme. Detailed discretization method of Eq. (4) can be found in e.g. Berberović et al. (2009) and Márquez Damián (2013). In Gopala and van Wachem (2008) it was concluded that this VOF scheme is completely mass conservative, and as long as the Courant number is kept low, the interface can be captured sharply.

In order to obtain the equations for porous media flow, Eq. (1 - 2) and Eq. (4) were ensemble averaged and volume averaged over a representative elementary volume (REV). The size of REV was much smaller than the size of the entire domain but much larger than the pore size. Therefore the volume averaged property was not dependent on the size of REV. Detailed derivation of the volume averaged equations is presented in Jensen et al. (2014) and here only the final equations are given:

$$\frac{\partial \langle \bar{u}_i \rangle}{\partial x_i} = 0 \tag{5}$$

$$(1+C_m)\frac{\partial}{\partial t}\frac{\rho\langle \bar{u}_i\rangle}{n} + \frac{1}{n}\frac{\partial}{\partial x_j}\frac{\rho\langle \bar{u}_i\rangle\langle \bar{u}_j\rangle}{n} = -\frac{\partial \langle \bar{p}\rangle^f}{\partial x_i} - g_j x_j \frac{\partial \rho}{\partial x_i} + \frac{1}{n}\frac{\partial}{\partial x_j}\mu\left(\frac{\partial \langle \bar{u}_i\rangle}{\partial x_j} + \frac{\partial \langle \bar{u}_j\rangle}{\partial x_i}\right) - \frac{1}{n}\frac{\partial}{\partial x_j}\rho\langle \overline{u_i' u_j'}\rangle + S_i \tag{6}$$

$$\frac{\partial \alpha}{\partial t} + \frac{1}{n}\frac{\partial}{\partial x_i}(\langle \bar{u}_i\rangle \alpha) + \frac{1}{n}\frac{\partial}{\partial x_i}(\langle \bar{u}_i^r\rangle \alpha(1-\alpha)) = 0 \tag{7}$$

In Eq. (6), the resistance force exerted by the porous media was represented by two terms, namely the added mass coefficient C_m, which accounts for the inertial effect due to the presence of the porous skeleton, and the drag resistance S. The formulation of these two forces are given below in Section 2.2. In addition, it should be mentioned that no turbulence model was applied in the present work, therefore $\rho\langle \overline{u_i' u_j'}\rangle = 0$. The detailed reason will be illustrated in Section 4, after we introduce the expressions for porous resistance coefficients in Section 3.

2.2. Porous resistance force due to fishing nets

In this section, description is given to the flow resistance force due to presence of the fishing nets. As mentioned above the resistance force was represented by two terms in Eq. 6, namely C_m and S. In van Gent (1995) C_m was expressed as:

$$C_m = \gamma_p \frac{1-n}{n} \tag{8}$$

where γ_p is a nondimensional empirical coefficient, and takes value of 0.34. This value was adopted in the present work. In the following part, we keep the main focus of the work on the drag force of the fishing net structures, and the inertia force will not be discussed until in Section 4.

The porous drag resistance was usually described by Darcy-Forchheimer equation:

$$S_i = -\left(\mu D_{ij}\langle\bar{u}_j\rangle + \frac{1}{2}\rho C_{ij}\sqrt{\langle\bar{u}_k\rangle\langle\bar{u}_k\rangle}\langle\bar{u}_j\rangle\right) \tag{9}$$

where D and C are the prescribed porous resistance coefficient matrix. In local $x^*y^*z^*$ coordinate where x^* is normal to the net plane panel, y^* and z^* are in plane with the net panel but perpendicular to each other, they are of the following form:

$$D^*_{ij} = \begin{bmatrix} D_1 & 0 & 0 \\ 0 & D_2 & 0 \\ 0 & 0 & D_3 \end{bmatrix} \quad C^*_{ij} = \begin{bmatrix} C_1 & 0 & 0 \\ 0 & C_2 & 0 \\ 0 & 0 & C_3 \end{bmatrix} \tag{10}$$

The first term in Eq. (9), proposed in Darcy (1856), addresses a linear relation between the resistance and the volume averaged ensemble averaged velocity. The second term was added by Forchheimer (1901) to consider a nonlinear relation between them. From the porous media point of view, the relative importance of these two terms is dependent on the flow regime, which is defined based on the pore Reynolds number:

$$Re = \frac{\langle\bar{u}\rangle d}{n\nu} \tag{11}$$

In general the flow regimes are denoted as Darcy flow regime, Forchheimer flow regime, transitional flow regime and fully turbulent flow regime. For a very low Reynolds number, the linear term dominates the resistance and the quadratic term will not influence the total resistance to a very high degree. When the Reynolds number is increasing from Forchheimer regime to fully turbulent regime, the quadratic term is gaining importance. A detailed description of different flow regimes is given in Burcharth and Andersen (1995). For flow through fishing nets, in general $Re \sim \mathcal{O}(10^2 \sim 10^3)$. This most probably corresponds to the fully turbulent flow regime, where the linear term is negligible and the quadratic term completely dominates over the linear term. Therefore it was reasonable to assume $D^* = 0$. This assumption was further justified by the physical explanation: Fishing nets are composed of twines with very small diameters, typical in the order of millimeters, the quadratic drag force is the dominant force for such kind of marine structures. Inertia and other forces are secondary. (This will be illustrated in detail in Section 4). The linear term is not physical for flow through such structures, since the force should not be related to the dynamic viscosity of water. Therefore in the present numerical model, the linear drag term was completely neglected and the porous resistance force was calculated purely based on the quadratic drag term:

$$S_i = -\frac{1}{2}\rho C_{ij}\sqrt{\langle\bar{u}_k\rangle\langle\bar{u}_k\rangle}\langle\bar{u}_j\rangle \tag{12}$$

If the local $x^*y^*z^*$ coordinate system of the porous media is not aligned with the global xyz coordinate system, the coefficient matrix needs to be transformed from local to global coordinate system. In Zhao et al. (2013a) and Patursson et al. (2010), two different methods were applied for the transformation. It was found the transformation approach in Zhao et al. (2013a) has relatively simple mathematical formulation, but it is valid only if the flow is unidirectional and the direction of the flow is aligned with x axis. Patursson et al. (2010) applied a tensor transformation matrix, which is more complex but has universal applicability. The details of these two approaches are presented in Appendix A, and in the present work, the latter one was adopted.

2.3. Forces on the net

The instantaneous force on the net is one of the most important output from the numerical simulations. Normally for simulation of flow around ships or other offshore structures, the geometry of the structure is resolved as a boundary patch of the fluid domain, and the forces acting on them are obtained by integrating the pressure and viscous force over the boundary patch. However, when it comes to the forces acting on the porous media, the situation becomes more complex. The geometry of the structure is not resolved, therefore

it is not possible to integrate the pressure and viscous stress on it. Patursson (2008) proposed a method based on conservation of the linear momentum in a control volume. The control volume should enclose the porous media, but the porous media does not have to fill the control volume. Furthermore the porous media could be oriented arbitrarily. So the forces acting on the fluid from the porous media is equal to the momentum loss in the control volume. The detailed derivation is illustrated in Appendix B and only the final result is presented here:

$$Q_i = -\frac{\partial}{\partial t}\left(\int_{CV} \rho u_i \, \mathrm{d}V\right) - \int_{CS} \rho u_i u_j \mathrm{n}_j \, \mathrm{d}S - \int_{CS} p\mathrm{n}_i \, \mathrm{d}S + \int_{CS} \tau_{ij}\mathrm{n}_j \, \mathrm{d}S + \int_{CV} \rho g_i \, \mathrm{d}V \tag{13}$$

where τ_{ij} is the viscous stress tensor, CV is the control volume and CS is the control surface.

This method requires that in the numerical simulation, each term on the right-hand side of Eq. (13) must be found at every time step. In the present work another method was applied. As shown in Section 2.1 and Section 2.2, the resistance force is the force acting on the fluid from the porous media. This resistance force includes inertia and quadratic drag forces. Therefore the forces acting on the porous media should be the reaction forces of them. In the numerical model, the inertia force was neglected for the output of the forces, only the quadratic drag term was retained. This is primarily due to its difficulty to output time derivative of the velocity at run time. However in general this is acceptable since this term has minor influence in most of the cases, which will be discussed in detail in Section 4. The final expression for the output of the instantaneous force is given as:

$$Q_i = \frac{1}{2}\rho \int_{PV} C_{ij}\sqrt{\langle \bar{u}_k \rangle \langle \bar{u}_k \rangle}\langle \bar{u}_j \rangle \, \mathrm{d}V \tag{14}$$

The quadratic drag term in Eq. (14) should be exactly integrated on the instantaneous wet volume of the porous media zone PV. In addition, the quadratic coefficient matrix C may vary inside the porous media zone, therefore in Eq. (14) it should not be regarded as a constant and separated from the integrand. This usually occurs in the simulation of flow through circular gravity cages, where cylindrical coordinate system needs to be introduced as shown in Section 6.3. In local cylindrical coordinate system C^* has the same value everywhere in the porous media zone. However after transformation into global Cartesian coordinate system, each cell has its unique value of C.

3. Calculation of the quadratic drag resistance coefficients

This section presents new formulas to calculate the quadratic coefficient matrix C in Eq. (12) for flow through fishing nets. The expressions were derived based on the available rational load model. The derivation indeed reflects a transformation process from the rational load model to the porous media model, and the transformation follows the principle that the force acting on the porous media zone should be equal to the force obtained from the rational load model.

The first issue here is to choose an appropriate rational load model for the transformation. Mainly two types of load models were proposed in the existing literature. The first is Morison type load model. In this kind of model, each twine of the net is treated as an individual cylinder, and the force acting on it is calculated by Morison equation. Due to relatively high porosity for fishing nets, the interaction effects between twines are neglected. So the total forces acting on the net panel is obtained by summing up the force on each twine. This type of force model has been extensively applied in e.g. Moe et al. (2010), Xu et al. (2013a), Xu et al. (2013b) and Huang et al. (2006).

Another kind of force model is the so-called screen type force model. This model was first introduced in Løland (1993), where drag and lift force coefficients on a flat net panel were given as a function of solidity ratio and attack angle. The formulas were based on curve fitting experimental data in Rudi et al. (1988), and were suggested to be used for net panels with solidity ratio in between 0.13 and 0.317. It was further extended in Kristiansen and Faltinsen (2012) and Kristiansen and Faltinsen (2015) to cover a wider range of solidity ratios, and the effect of Reynolds number was accounted for.

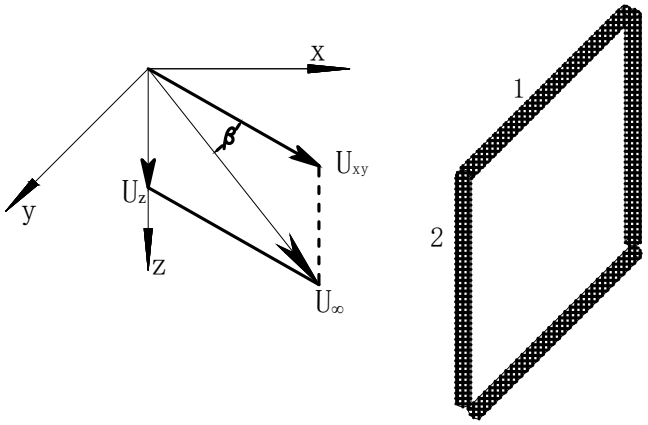

Figure 1: Left: illustration of the decomposition of the velocity vector in 3D. Right: simplification of net panel into twines without knots.

Actually both load models could be transformed to obtain the quadratic drag resistance coefficients, but with different complexities. The theory behind screen type force model is more reasonable, since the interaction effects in-between the net twines are naturally accounted for, while in Morison type load model they are neglected. However, the mathematical expressions obtained from Morison type force model have similarities with the quadratic drag force. This could greatly ease the transformation process, and lead to simple mathematical formulations. In addition, it was found that one could still obtain reasonable results by properly dropping the attack angle dependence of the derived coefficients from Morison type force model. But this will result in constant quadratic drag resistance coefficients, which is expected by the authors. This concerns the following reason: Time and space independent porous resistance coefficients could be applied in most of the open source or commercial CFD code without any modification of the code itself, as long as they support solvers for Darcy-Forchheimer type porous media flow. Therefore the derived formulas could be easily applied in most of the softwares. So it was decided to use a Morison type load model in the present paper. In order to eliminate the side effects of the assumption made in Morison type force model, i.e. there is no interaction in-between twines due to the high porosity, two new interaction coefficients a and b were introduced in the expressions for normal and tangential quadratic drag resistance coefficients. Physically they represent a compensation due to the above mentioned assumption. The details will be given in the following.

3.1. Derivation

Below in this section a generalized 3D derivation is given on the transformation of the quadratic drag resistance coefficients from Morison type load model. Assume that a fishing net panel is in steady current and only composed of twines without knots. The panel is within y-z plane and the normal direction of the net is aligned with x direction, so transformation of the coefficient is not needed. The flow is ambient in 3D and is decomposed into components in x-y plane and z axis. Fig. 1 illustrates the decomposition of the velocity vector and simplification of the net panel into small twines without knots. The purpose of such a decomposition is to simplify the 3D case into 2D where $U_{xy} = U_\infty \cos\beta$ and $U_z = U_\infty \sin\beta$. We now focus on the forces acting on net twine 1 and net twine 2.

First we consider the velocity vector in x-y plane, namely U_{xy} and its induced forces on net twines, as shown in Fig. 2. According to the cross flow principle (see e.g. Hoerner (1965)), the forces acting on twine 1 and twine 2 are different. For twine 2 the incoming flow is fully normal, and the generated force is in the

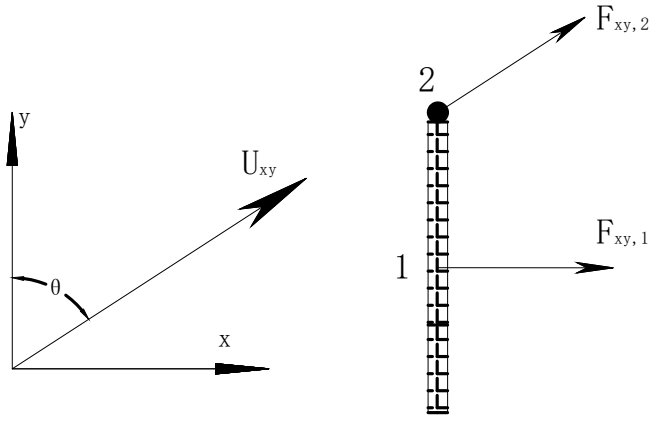

Figure 2: The projected velocity and its induced forces in x-y plane

same direction with the flow and its magnitude is equal to:

$$F_{x,2} = \frac{1}{2} C_{d,twine} \rho A_2 U_{xy}^2 \sin\theta \tag{15}$$

$$F_{y,2} = \frac{1}{2} C_{d,twine} \rho A_2 U_{xy}^2 \cos\theta \tag{16}$$

where A_2 is the projected area of twine 2.

However, for twine 1, the current velocity is decomposed into the tangential and normal components to the twine. The tangential component does not generate any forces (the friction force is small and neglected). The normal velocity generates a force aligned with x direction:

$$F_{x,1} = \frac{1}{2} C_{d,twine} \rho A_1 U_{xy}^2 \sin^2\theta \tag{17}$$

$$F_{y,1} = 0 \tag{18}$$

where A_1 is the projected area of twine 1.

Then we consider the forces generated by U_z. since it is fully parallel to twine 2, no force is generated on that twine. Meanwhile it is fully perpendicular to twine 1, so generates a force aligned with z direction:

$$F_{z,1} = \frac{1}{2} C_{d,twine} \rho A_1 U_z^2 \tag{19}$$

Then the total forces acting on a fishing net panel are simply superposition of the drag force for each twine:

$$F_x = \frac{1}{2} C_{d,twine} \rho U_{xy}^2 \left(\sin\theta \sum_{i=1}^{M} A_{2,i} + \sin^2\theta \sum_{j=1}^{N} A_{1,j} \right) \tag{20}$$

$$F_y = \frac{1}{2} C_{d,twine} \rho U_{xy}^2 \cos\theta \sum_{i=1}^{M} A_{2,i} \tag{21}$$

$$F_z = \frac{1}{2} C_{d,twine} \rho U_z^2 \sum_{j=1}^{N} A_{1,j} \tag{22}$$

$$\tag{23}$$

where M is the number of twines parallel to twine 2, or the so-called out-of-plane twin. N is the number of twines parallel to twine 1, which is the in-plane twine.

On the other hand, according to Section 2.3, the forces acting on the porous media Q were obtained by applying Eq. (14):

$$Q_x = \frac{1}{2}\rho C_1 V U_\infty U_{xy} \sin\theta \tag{24}$$

$$Q_y = \frac{1}{2}\rho C_2 V U_\infty U_{xy} \cos\theta \tag{25}$$

$$Q_z = \frac{1}{2}\rho C_3 V U_\infty U_z \tag{26}$$

Here it was assumed that the unknown volume averaged velocity $\langle\bar{u}\rangle$ is equal to the undisturbed velocity. This is a reasonable assumption since fishing net is kind of porous structure with very high porosity, and the velocity reduction is not significant, as shown in Bi et al. (2013a). Therefore the volume averaged ensemble averaged velocity $\langle\bar{u}\rangle$ inside the porous media should be very close to the undisturbed velocity.

Since the fishing nets were approximated by a sheet of porous media, the forces acting on the porous media should be equal to the superposition of forces from each twine, i.e. $F = Q$. By substituting the expression of F and Q into the equilibrium relation, the following relations were obtained for C_1, C_2 and C_3:

$$C_1 = \frac{1}{V} C_{d,twine} \cos\beta \left(\sum_{i=1}^{M} A_{2,i} + \sin\theta \sum_{j=1}^{N} A_{1,j} \right) \tag{27}$$

$$C_2 = \frac{1}{V} C_{d,twine} \cos\beta \sum_{i=1}^{M} A_{2,i} \tag{28}$$

$$C_3 = \frac{1}{V} C_{d,twine} \sin\beta \sum_{j=1}^{N} A_{1,j} \tag{29}$$

As mentioned at the beginning of this section, two coefficients a and b were introduced to account for the interaction effects in-between twines in tangential and normal direction, respectively. In addition, the derived expressions for C as shown above have attack angle dependence, indicating time and space varying quadratic drag resistance coefficients in unsteady flow. However, in traditional porous media theory, C was applied as a constant for all the attack angles. Angle dependence of porous resistance was merely handled by transformation from local to global coordinate system, while porous resistance coefficients were kept the same. Recalling that in the literature survey in Section 1, almost all the paper applied constant porous resistance coefficients, but still obtained good agreement between numerical and experimental results. This indicates that angle dependence of the porous resistance coefficients might have minor effects on the final results. Therefore in the present work, it was directly dropped, and constant drag resistance coefficients were applied throughout the paper. Actually this further indicated that an averaged value of C against different attack angles was employed, and this contribution was implicitly included in the parameters of a and b. This leads to the final expressions for the coefficients:

$$C_1 = \frac{1}{V} a C_{d,twine} \left(S_1 + S_2\right) \tag{30}$$

$$C_2 = \frac{1}{V} b C_{d,twine} S_2 \tag{31}$$

$$C_3 = \frac{1}{V} b C_{d,twine} S_1 \tag{32}$$

where S_1 is the total projected area for in-plane twines where $S_1 = \sum_{j=1}^{N} A_{1,j}$, S_2 is the total projected area for out-of-plane twines where $S_2 = \sum_{i=1}^{M} A_{2,i}$. Given Eq. (30 - 32), the forces acting on the porous media

were expressed as:

$$Q_x = \frac{1}{2}\rho a C_{d,twine} U_\infty^2 (S_1 + S_2)\cos\beta \sin\theta \tag{33}$$

$$Q_y = \frac{1}{2}\rho b C_{d,twine} U_\infty^2 S_2 \cos\beta \cos\theta \tag{34}$$

$$Q_z = \frac{1}{2}\rho b C_{d,twine} U_\infty^2 S_1 \sin\beta \tag{35}$$

A few additional comments are given here on the interaction coefficients a and b: (1) When considering flow through nets, mainly two interaction effects should be accounted for, namely the shading effect of the downstream twines from the upstream twines for large inflow angles, and the local speed-up of the flow in-between the twines. This has been explained in detail in Kristiansen and Faltinsen (2012). Both of them are affected by the solidity ratio, therefore a and b were believed to be functions of solidity ratio. (2) The parameter a, which is in the expression for the normal quadratic drag resistance coefficient C_1, is strongly influenced by the local speed-up interaction effect. Therefore it is expected that when $S_n \to 0$, where the distance between the twines is infinitely large, the flow should not speed up and $a \to 1$. (3) Both tangential porous resistance coefficients C_2 and C_3 share the same interaction coefficient b. This is reasonable since for most of the fishing nets, the material properties in y and z direction, (i.e. within the net panel plane) are the same. Therefore the interaction effects in both directions should be the same. Indeed for most of the fishing nets, especially the nets used in aquaculture industry, $C_2 \approx C_3$ since they usually have symmetric mesh patterns. In previous works, they were usually represented by a single tangential resistance coefficient called C_t. (4) For parameter b, which accounts for the flow interaction effects for tangential porous resistance coefficient, both interaction effects may play important roles. Shading effect will result in a reduction of the force on the downstream twine due to decrease of the incoming velocity. But the local speed-up effect will lead to an increase of the force on the twine. (5) By comparison of the results between CFD simulations and experiments, it was found that for nets with small solidity ratios, b was almost kept as a constant. Meanwhile, it started to increase for nets with intermediate to high solidity ratios. This indicated that both effects are equally important for nets with small solidity ratios but the local speed-up effect is gaining importance when solidity ratio increases.

3.2. Calibration of the parameters

In this section, the unknown interaction coefficients a and b were calibrated for nets with different solidity ratios. The reference values for three specific nets were determined first based on the selected experimental data in Rudi et al. (1988). The principle for determination of a and b is that the error between the drag and lift forces obtained from Eq. (33 - 34) and from laboratory tests should be minimized. (The out-of-plane lift force Q_z was not considered here due to 2D flow in Rudi et al. (1988), i.e. $\beta = 0°$.) The error function E was defined based on the least square normalized error:

$$E = \sum_{p=1}^{P}\left(\frac{F_{x,p}^M - Q_{x,p}}{F_{x,p}^M}\right)^2 + \sum_{k=1}^{K}\left(\frac{F_{y,k}^M - Q_{y,k}}{F_{y,k}^M}\right)^2 \tag{36}$$

where F^M is the measured force with different incoming velocities and attack angle for one specific net. P and K are the number of data used in calibration for forces in x and y direction, respectively. Substituting Eq. (33) and Eq. (34) into Eq. (36) reads:

$$E = \sum_{p=1}^{P}\left(1 - \frac{1}{2F_{x,p}^M}\rho a C_{d,twine}^p U_{\infty,p}^2 \sin\theta_p (S_1 + S_2)\right)^2 + \sum_{k=1}^{K}\left(1 - \frac{1}{2F_{y,k}^M}\rho b C_{d,twine}^k U_{\infty,k}^2 \cos\theta_k S_2\right)^2 \tag{37}$$

As mentioned above, the incoming velocity U_∞, attack angle θ and drag coefficient $C_{d,twine}$ are varying with index of the experimental data p and k. By taking derivative of E with respect to a, and equaling it

to zero, a was expressed as:

$$a = \frac{A_{net} \sum_{p=1}^{P} \left(\frac{C_{d,twine}^{p} \sin\theta_p}{C_{d,net}^{p}} \right)}{(S_1 + S_2) \sum_{p=1}^{P} \left(\frac{\sin^2\theta_p (C_{d,twine}^{p})^2}{(C_{d,net}^{p})^2} \right)} \tag{38}$$

By the same manipulation b was obtained:

$$b = \frac{A_{net} \sum_{k=1}^{K} \left(\frac{C_{d,twine}^{k} \cos\theta_k}{C_{l,net}^{k}} \right)}{S_2 \sum_{k=1}^{K} \left(\frac{\cos^2\theta_k (C_{d,twine}^{k})^2}{(C_{l,net}^{k})^2} \right)} \tag{39}$$

where the drag and lift force coefficients of the net panel were defined as

$$C_{d,net} = \frac{F_{d,net}}{1/2\rho A_{net} U_{\infty}^2} \tag{40}$$

$$C_{l,net} = \frac{F_{l,net}}{1/2\rho A_{net} U_{\infty}^2} \tag{41}$$

In Rudi et al. (1988) series of experiments were conducted under a variety of velocities and attack angles for nets with different solidity ratios. The experimental data for three net cases were selected to calibrate the formula and their geometrical characteristics are listed in Table 1. The reason to select these three nets is that extensive experiments have been done in Rudi et al. (1988) for these three net panels, and plenty of data are available. In addition the solidity ratio of these three nets are distributed from low to high, providing the reference value of a and b in a wide range of net panels. The calculated reference values of the interaction coefficients are also presented in Table 1.

Table 1: The geometric parameters of the three nets in Rudi et al. (1988) and the calibrated reference values of the interaction coefficients

Net case no.	1	2	3
Solidity ratio	0.13	0.243	0.317
Twine diameter (mm)	1.83	1.83	1.83
Bar length (mm)	29.0	15.5	12
a	1.31	1.45	1.85
b	0.92	0.85	1.50

Linear interpolation was applied to obtain the interaction coefficients for nets with other solidity ratios. This considers the boundness property of linear interpolation, i.e. for a net panel with solidity ratio in-between the solidity ratios for the reference nets, the interaction coefficients a and b should also remain in-between the values of the coefficients for the reference nets. Polynomial fit may introduce unexpected extroplative behavior. For $0 < S_n < 0.13$, asymptotic value of a was used while b was kept constant. This has been explained in Section 3.1. The final expression of a and b is given in Eq. (42) and Eq. (43).

$$a = \begin{cases} 2.3484 S_n + 1 & 0 < S_n \leq 0.13 \\ 1.3128 S_n + 1.1346 & 0.13 < S_n \leq 0.243 \\ 5.3094 S_n + 0.1634 & 0.243 < S_n \leq 0.317 \end{cases} \tag{42}$$

$$b = \begin{cases} 0.9241 & 0 < S_n \leq 0.13 \\ -0.6310 S_n + 1.0061 & 0.13 < S_n \leq 0.243 \\ 8.7581 S_n - 1.2754 & 0.243 < S_n \leq 0.317 \end{cases} \tag{43}$$

4. Discussions on the overall numerical model

So far the description of the numerical model for flow through fishing nets is completed, and below discussions will be given on several topics related to our numerical model. This includes the discussion of VARANS equations and its application in the present model, the inertia effect for flow through fishing nets, the turbulent effects and the reason why no turbulence model was applied in the present model.

4.1. Comments on solid-fluid interaction effects in VARANS equations

In the present model, VARANS equations derived from Jensen et al. (2014) were employed as the governing equations. Meanwhile we notice that in previous works, e.g. Patursson et al. (2010), a different mathematical formulation of porous media flow was used:

$$\frac{\partial u_i}{\partial x_i} = 0 \tag{44}$$

$$\frac{\partial \rho u_i}{\partial t} + \frac{\partial \rho u_i u_j}{\partial x_j} = -\frac{\partial P}{\partial x_i} + \frac{\partial}{\partial x_j}\mu\left(\frac{\partial u_i}{\partial x_j} + \frac{\partial u_j}{\partial x_i}\right) + S_i \tag{45}$$

The main discrepancies between Eq. (44 - 45) and Eq. (5 - 6) lie in the inertia term, and the porosity was not included in Eq. (45). The added mass coefficient will be discussed in Section 4.2, and here it is focused on the influences of including porosity in the governing equations. Actually Eq. (45) implicitly indicated that the porosity of the fishing nets was equal to one. Therefore it was assumed that the volume of the net was neglected, and water was filled in the domain everywhere. The only effect of the net was the resistance force. Essentially instead of volume averaging Eq. (1 - 2), only one extra resistance term was added. This could be considered as a reasonable simplification for clean net, which has a very high porosity value, normally between 0.7 and 0.9. However for nets with biofouling, as shown in Lader et al. (2015), the porosity could be reduced to a very low value. Then this simplification is questionable. However, in the present model, the effect of porosity i.e. net-fluid interaction was neither fully considered, as shown in the derivation of the resistance term S. In Section 3.1, it was seen that the fundamental assumption behind Morison type load model is that due to relatively high porosity, the interaction effects in-between the twines are neglected. This indicated that the load on each twine was calculated individually first, assuming in the infinite fluid domain without the presence of its neighboring twines. Then this was compensated by introducing the interaction coefficients a and b, which are determined based on the experimental data.

4.2. Inertia force for flow through fishing nets

The inertia effect due to presence of the porous skeleton was not accounted for in Eq. (45). But in Eq. (6), this was considered in a generic way, i.e. only as a function of porosity and irrespective the details of the porous skeleton. Previous works show that this term has minor effects in most of the cases, e.g. in del Jesus (2011) and Jacobsen et al. (2015). Actually the inertia force on a fishing net panel should be a small part of the total force, since the ratio between magnitude of inertia force and drag force for a twine of unit length in periodic unsteady flow was expressed as (see Eq. (4.31) in Sumer and Fredsøe (2006)):

$$\frac{F_{I,twine}}{F_{d,twine}} = \frac{C_{I,twine}\pi d^2 \omega U_m}{2C_{d,twine} d U_m^2} = \frac{\pi^2}{KC}\frac{C_{I,twine}}{C_{d,twine}} \tag{46}$$

For net twines whose diameter is normally a few millimeters, KC number is in the order of hundred while $C_I/C_D \approx 2$. So the ratio was expected to be small. Although in Balash et al. (2009) and Lader et al. (2007a), it was reported that inertia force may be important for nets with high solidity ratios, in the present work we focus on the drag force, and the inertia term was just inherited from Jensen et al. (2014) without further investigations.

4.3. Turbulence effects for flow through fishing nets

As shown in Section 2.2, for flow through net structures, it is most probably in the fully turbulent regime. Therefore turbulence is generated in the wake, which is also shown in Bouhoubeiny et al. (2011), Pichot et al. (2009), Kim (2012) and Lader et al. (2007b). However in the numerical model, the geometry of the net was not resolved, so the boundary layers of the twines and knots were not able to be modeled. Instead, the turbulence level in the porous media was represented by $-\rho\langle\overline{u_i'u_j'}\rangle$ in Eq. (6). Ideally this term should be taken into account by a turbulence model. By applying Boussinesq assumption, this term can be approximated as:

$$-\rho\langle\overline{u_i'u_j'}\rangle = \langle\mu_t\rangle\left(\frac{\partial\langle\bar{u}_i\rangle}{\partial x_j}+\frac{\partial\langle\bar{u}_j\rangle}{\partial x_i}\right)-\frac{2}{3}\rho\langle k\rangle\delta_{ij} \tag{47}$$

where δ_{ij} yields Einstein summation and $\delta_{ii}=\delta_{11}+\delta_{22}+\delta_{33}=3$.

This requires that the equations involved in the applied turbulence model should also be volumed averaged. Nakayama and Kuwahara (1999) presented how the transport equations for turbulence kinetic energy and dissipation rate were volume averaged for a $k-\epsilon$ turbulence model. However by following the averaging procedure, some extra unknown terms were introduced representing generation and dissipation of the turbulence kinetic energy. They were determined by numerical experiments to close the system.

For flow through fishing nets, due to its relatively high porosity, in general most of the turbulence can be freely convected through the nets. Only large scale turbulence whose length scale is larger than the mesh bar length will be damped, while small vortex will be generated in the wake of the twines.

However, it was decided not to apply any turbulence model in the present work, i.e. $\langle\mu_t\rangle=0$ and $\langle k\rangle=0$. This concerns that the actual level of turbulence kinetic energy was of minor interests. Meanwhile the flow resistance term S, which was described by Darcy-Forchheimer equation, was introduced to the Navier-Stokes equations as a closure model for handling the porous drag force which cannot be resolved directly in the model. This also corresponds to the concept of a closure model for turbulence modeling. In Section 3 it was shown that the quadratic drag resistance coefficients were written as a function of physical parameters of the fishing nets, and also the so-called interaction coefficient a and b. They were actually calibrated based on the measurements, which already included all the dissipative effects including turbulence. Application of a turbulence model may introduce dual turbulence dissipation. This is considered to be a valid approximation in many engineering applications and it was also applied in Jensen et al. (2014) and Jacobsen et al. (2015). However one should notice that by doing so, the flow in the wake was not described in a correct way by the numerical model, where the turbulence generated behind the fishing nets was not resolved. When studying the circular fish cages, this may affect the analysis in the rear part of the cage.

5. Preliminary tests on convergence analysis

Series of preliminary tests have been run for convergence analysis. The purpose is to find an appropriate mesh resolution for CFD simulations. In addition, for net cages in steady current, analysis was also performed to examine the convergence property in time domain. Some of the conclusions made in Patursson et al. (2010) were also applied in the present model.

Hexahedral mesh was adopted in the simulation where the mesh was refined in the near-net region. The overall aspect ratio was kept between one to two, and the mesh grading was smoothened from far field to the near field. Convergence property of the mesh was studied for cases in Patursson et al. (2010) with $\theta=90^\circ$ and different incoming velocities U_∞. The detailed setup of the numerical model will be given in Section 6.1, and the results for the convergence study are shown in Fig. 3. Here the resolution of the mesh was represented by the number of the layers N used in the porous zone. The exact numerical solution was not known, and the absolute error vector was expressed as the difference between the solutions from the current mesh resolution and the finest mesh resolution for different incoming velocities. The relative error was computed as the second norm of the ratio between absolute error and solutions from the finest mesh resolution, and it is also shown in Fig. 3. It was concluded that the mesh resolution is important for the numerical solution, and the numerical solution is monotonic against mesh resolution, indicating that it is converging towards an exact numerical solution. However, the difference between the numerical results from

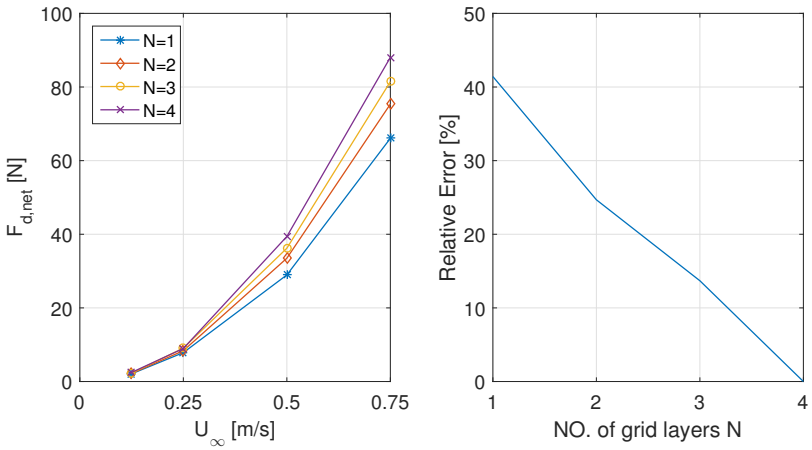

Figure 3: Convergence study for cases in Patursson (2007) with $\theta = 90°$ and different incoming velocities U_∞. The left shows the absolute drag force as a function of incoming velocities for different solidity ratios. The right gives the relative error as a function of mesh resolution.

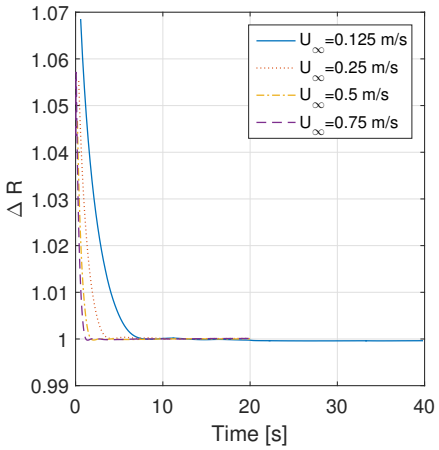

Figure 4: An example of convergence rate for numerical simulation of cases with $\theta = 90°$ in Patursson et al. (2010).

two finest mesh resolutions is around 12%. Therefore we could not conclude that the numerical solution was converged. Compromises were made between the computational cost and accuracy of the numerical solution, and it was decided to use a mesh resolution of $N = 3$ for all the validation cases.

The convergence property in time domain was investigated for fishing nets in steady current. It was found that in general the forces got converged in a rapid speed. An example of convergence in time domain is presented in Fig. 4, where numerical simulations were also carried out for cases in Patursson et al. (2010). In Fig. 4, the ratio ΔR between the instantaneous drag forces and the converged drag forces is plotted as a function of time for the flow with $\theta = 90°$ and four different incoming velocities. For all the four cases, the forces converged at $t = 10$ s, and the convergence rate is proportional to the inverse of the incoming velocities. In Section 6, care was taken to make sure that the probed data were fully converged for the validation cases for nets in steady current.

In Patursson et al. (2010) some conclusions have been drawn on general setup of the numerical model, and the most important conclusion is that, as long as guidelines based on the physical consideration were adhered to, the model was remarkably insensitive to many of the specific choices. The thickness of the porous media representing the net was 50 mm in Patursson et al. (2010), and it was found that this parameter does not affect the simulation significantly. Therefore the same thickness was used throughout the paper. Effects

Table 2: The selected drag force coefficients for the net twines and the calculated quadratic drag resistance coefficients for the net panel used in Patursson et al. (2010) under different incoming velocities

U [m/s]	0.125	0.25	0.5	0.75
Re	350	700	1400	2100
$C_{d,twine}$	1.35	1.15	1.00	1.00
C_1	7.18	6.12	5.32	5.32
C_2	2.32	1.98	1.72	1.72
C_3	2.32	1.98	1.72	1.72

of near wall treatment was also investigated in Patursson (2008). It was concluded that no significant difference was found by using different near wall treatment. In the present work, both slip and no-slip boundary condition were applied in different validation cases.

6. Validation of the numerical model

In this section, the overall numerical model is validated thoroughly against laboratory tests. The validation cases include both plane net panels and also circular net cages. The cases were carried out with the focus on current and wave loads on fishing nets under a variaty of conditions. The selected net panels cover a wide range of solidity ratios in order to demonstrate the universal applicability of the numerical model.

6.1. Current interaction with plane net panel: validation case 1

The first validation case is based on the experimental data presented in Patursson (2007) for a plane net panel in current flow under various attack angles and incoming velocities. The experiments were conducted in the towing tank in University of New Hampshire (UNH) in United States. The towing tank is 37 m long, 3.66 m wide and 2.44 m deep. The net panel was positioned in the center of the cross section and well below the water surface. A rigid frame was used to hold the net so the deformation was negligible. The drag and lift forces on the net panel, and the velocity at 2.5 m behind the net panel were measured. The velocity reduction factor U_r was calculated as

$$U_r = \frac{U_\infty - U_{2.5}}{U_\infty} \tag{48}$$

where $U_{2.5}$ is the velocity at 2.5 m behind the net panel.

The net used in the experiments was a 1 m by 1 m knotless nylon net with $d = 2.8$ mm and $\lambda = 29$ mm. This gave a solidity ratio of 0.184. The measurements were performed at the attack angle of 0°, 15°, 30°, 45°, 60° and 90° and under the towing speed of 12.5, 25, 50, 75 cm/s.

A three dimensional numerical model was set up based on the experiments. The sketch of domain and the measurement point are presented in Fig. 5. According to the mesh bar length and diameter of the twines of the net panel, the porous resistance coefficients were calculated based on Eq. (30 - 32), with the parameters a and b obtained from Eq. (42 - 43). The calculated coefficients are listed in Table 2 with the drag coefficients of the twines chosen from Schlichting and Gersten (2003).

The velocity contours at a variety of attack angles from the CFD simulations are plotted in Fig. 6 for $U_\infty = 0.5$ m/s. In general it has the same characteristics with the flow field shown in Patursson et al. (2010). In cross flow direction, the width of the wake is approximately the same with the net panel. Meanwhile along the flow direction, the reduction of the flow speed starts a short distance in front of the plane net panel, and finally reaches the steady state behind the net panel. But we also notice some differences on the near flow field behind the net panel. In Patursson et al. (2010) a continuous process of reduction was observed, and the distance from the net panel to the start point of the steady flow speed level is approximately one to two times the width of the net panel. But in the present simulations, a very rapid process of the reduction was seen. It might be due to the difference in model setups. In Patursson et al. (2010), the frame was also modeled as small diameter cylinders. But in the present model, it was neglected.

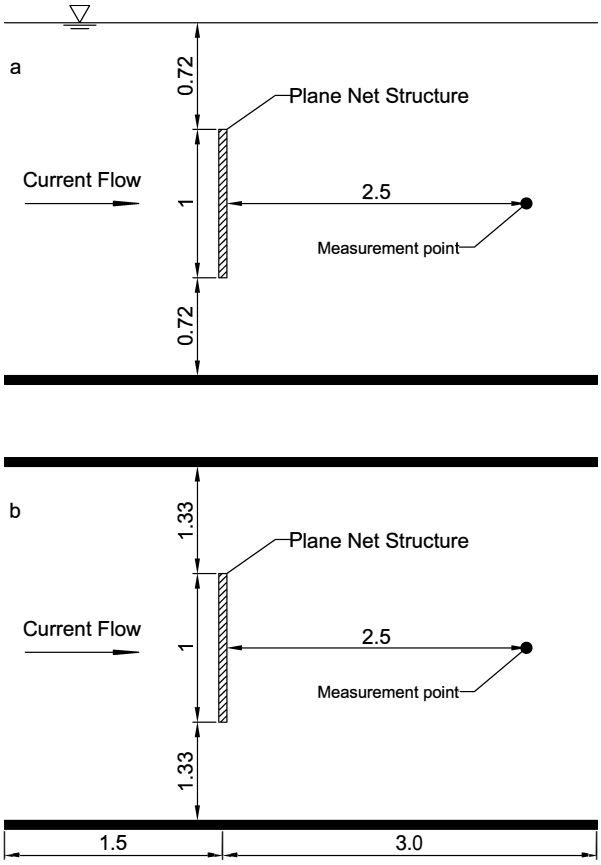

Figure 5: Sketch of the domain for reproduction of the experiments in Patursson (2007). (a) side view. (b) top view. (unit: m)

The drag and lift force coefficients, and the velocity reduction factor calculated from the experimental data in Patursson (2007) and the present numerical model in OpenFOAM are shown in Fig. 7. In addition, the results from Patursson et al. (2010) based on the fitting procedure with different error functions, namely the least square absolute normalized error function (LANE), least square absolute error function (LAE), and least square normalized error function (LSNE) are also presented in Fig. 7. The associated relative error is presented in Fig. 8.

Regarding the drag force coefficients, the present model gave similar predictions with fitting methods. For cases with $U_\infty = 0.25$ m/s, $U_\infty = 0.5$ m/s and $U_\infty = 0.75$ m/s, the drag force coefficients at $\theta = 90°$ were slightly underestimated by 10% by all the methods. The relatively large errors at $\theta = 0$ were induced by the small absolute values of the drag force coefficients. However, there appears discrepancy between the present model and fitting methods for prediction of lift force coefficients at $U_\infty = 0.125$ m/s. Better predictions were given by fitting methods in general, where the present model overestimated the lift force coefficients by $20\% - 30\%$, except at $\theta = 60°$. For cases with the remaining incoming velocities, they have similar performance. The nonzero lift force at $\theta = 90°$ from experiments may be due to the anti-symmetries in the net panel as explained in Patursson et al. (2010), and this results in significant relative errors as shown in Fig. 8. Regarding wake velocity, significant discrepancies were observed between CFD simulations by all the methods and experimental data at small attack angles. In Patursson et al. (2010) the reasons were explained: In the experiment the high velocity in the wake was due to the effect from the frame, while in CFD model the effect from the frame was small (in the numerical model of Patursson et al. (2010)) or nonexistent (in the present model). However, it appears that the present model gave much more reasonable

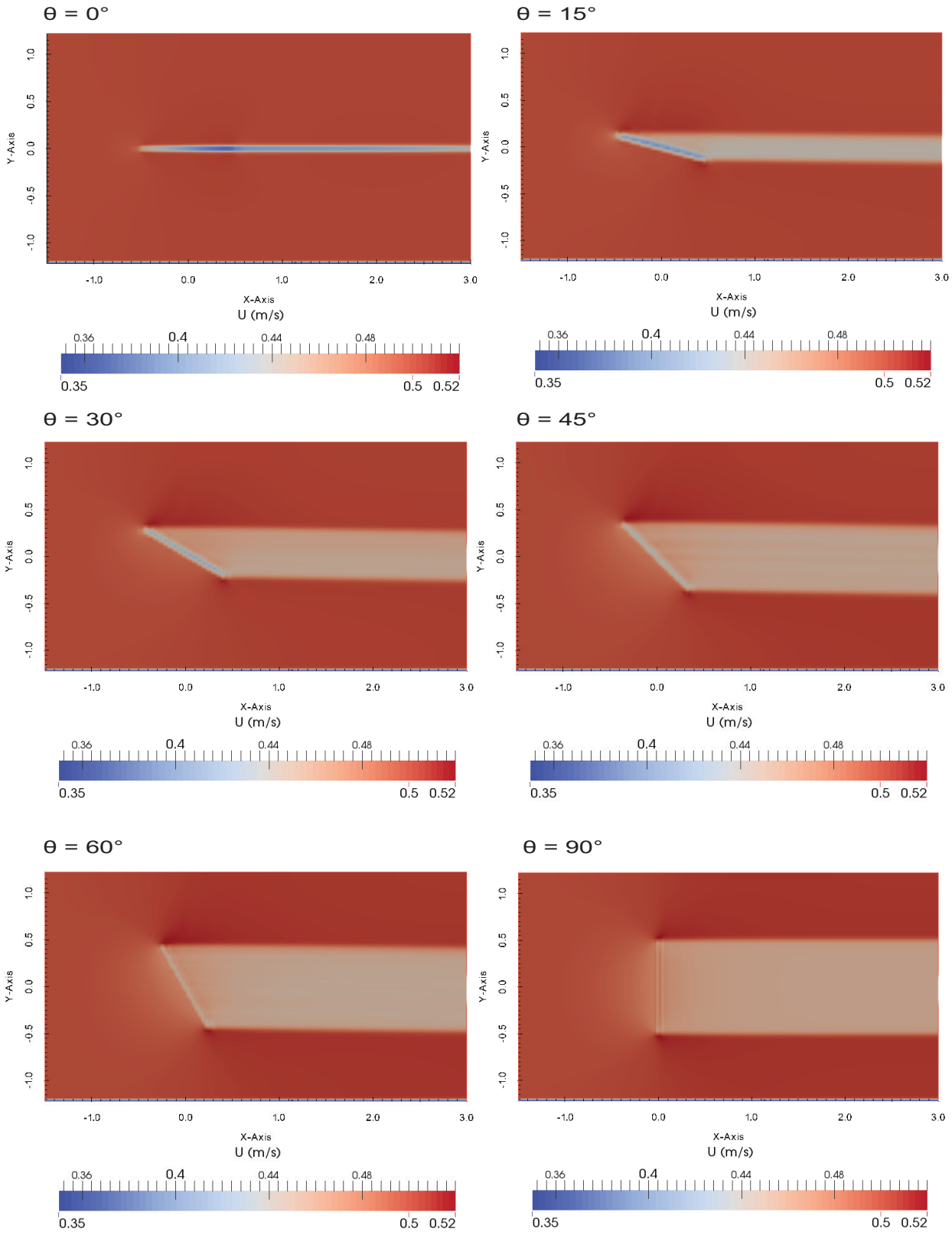

Figure 6: The velocity contours from the present numerical model on a vertical plane cut through the center of the net panel at different angles of attack for incoming velocity of 0.5 m/s.

Table 3: The physical parameters of the net panels in Zhan et al. (2006), and calculation of the corresponding porous resistance coefficients

Net case		1	2	3
λ(m)		0.0125	0.0065	0.0130
d(m)		0.0008	0.0007	0.0015
S_n		0.128	0.215	0.223
S_1(m^3)		0.0588	0.0988	0.1028
S_2(m^3)		0.0593	0.0992	0.1037
V(m^3)		0.0455	0.0455	0.0455
a		1.30	1.42	1.43
b		0.93	0.87	0.87
$U_\infty = 0.25$ m/s	Re	200	175	362
	$C_{d,twine}$	1.55	1.60	1.35
	C_1	5.23	9.86	8.74
	C_2	1.87	3.04	2.66
	C_3	1.85	3.02	2.64
$U_\infty = 0.5$ m/s	Re	400	350	725
	$C_{d,twine}$	1.30	1.35	1.10
	C_1	4.39	8.32	7.13
	C_2	1.57	2.56	2.17
	C_3	1.55	2.55	2.15
$U_\infty = 0.75$ m/s	Re	600	525	1080
	$C_{d,twine}$	1.18	1.20	1.00
	C_1	3.98	7.40	6.48
	C_2	1.42	2.28	1.97
	C_3	1.41	2.27	1.96
$U_\infty = 1$ m/s	Re	800	700	1450
	$C_{d,twine}$	1.10	1.15	1.00
	C_1	3.71	7.09	6.48
	C_2	1.32	2.18	1.97
	C_3	1.31	2.17	1.96

results for the wake velocity at $U_\infty = 0.125$ m/s and $U_\infty = 0.25$ m/s at $\theta = 0°$.

6.2. Current interaction with plane net panel: validation case 2

Further validation cases were carried out for plane net panel in steady current. In order to cover wider range of different net panels, we selected the experiments performed in Zhan et al. (2006) to validate our numerical model. The experiments were conducted in the towing tank at the Department of Applied Mechanics, Zhongshan University in China. The towing tank has a dimension of 204 m $\times$ 6 m $\times$ 3 m. The net panel was 1.3 m long and 0.7 m high, and tightly fixed in the frame where the deformation was negligible. The drag force for the net panel was measured under attack angles of $30°, 60°$ and $90°$. Four towing speeds were applied in the experiments, namely 0.25 m/s, 0.5 m/s, 0.75 m/s and 1 m/s.

Totally three kinds of net panels with different solidity ratios were studied in the experiments. The mesh for all the three nets were square diamond pattern. The physical parameters of the net panels are listed in Table 3, with the associated parameters for calculation of the quadratic drag resistance coefficients.

The sketch of the domain for numerical model is presented in Fig. 9. The depth of the domain was reduced in the numerical model. Moreover, slip condition was applied for the bottom wall. The main reason behind this setup is that the bottom should have negligible effects on flow through the net panels. This is beneficial in the perspective of computational time.

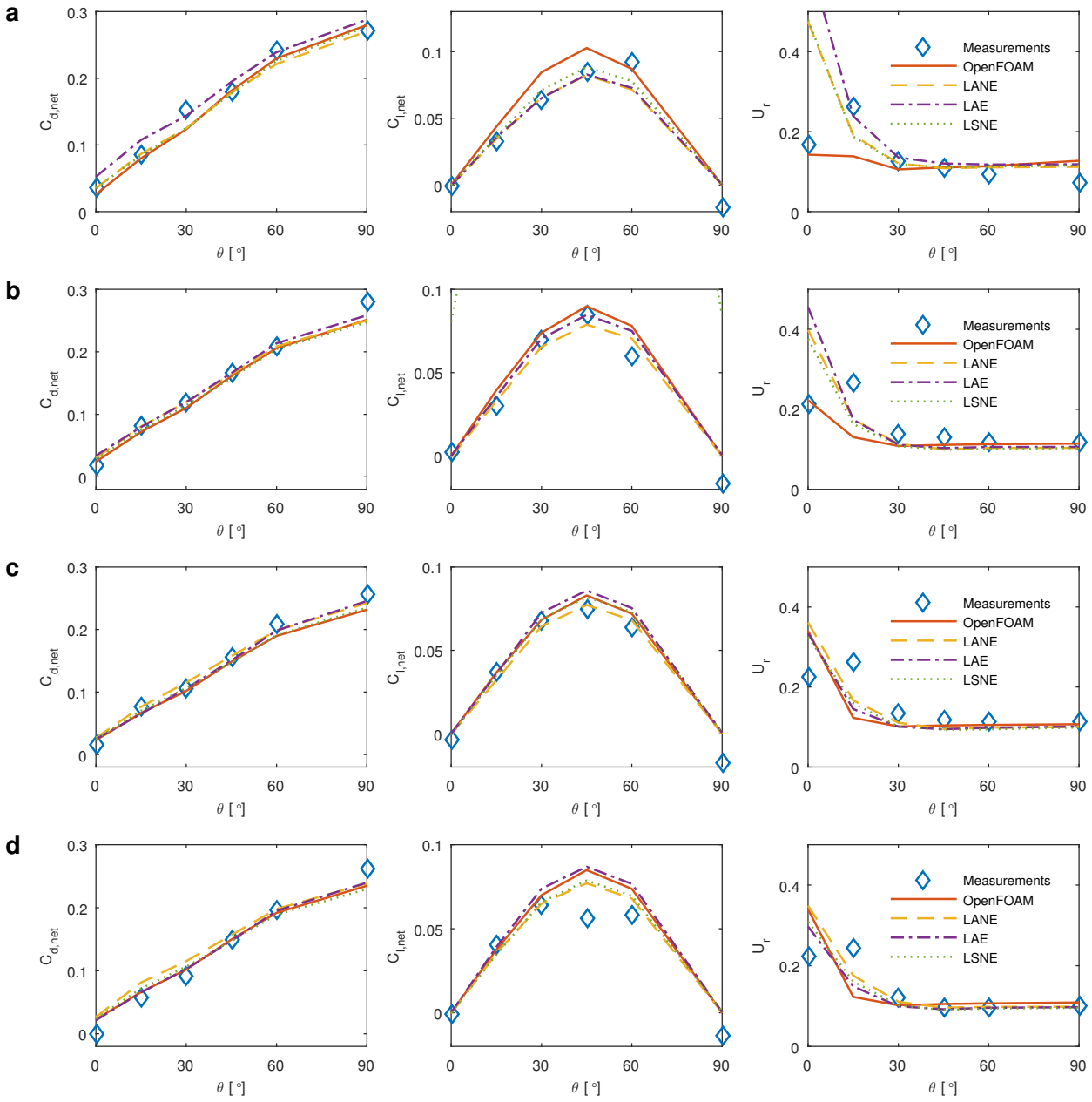

Figure 7: Comparison of the drag force coefficients $C_{d,net}$, lift force coefficients $C_{l,net}$ and velocity reduction factors U_r from experimental data in Patursson (2007) , the present numerical simulations in OpenFOAM, the fitted data based on a least square absolute normalized error (LANE), least square absolute error function(LAE), and least square normalized error function (LSNE) as shown in Patursson et al. (2010) for different incoming velocities: (a) u=0.125 m/s. (b) u=0.25 m/s, (c) u=0.5 m/s, (d) u=0.75 m/s.

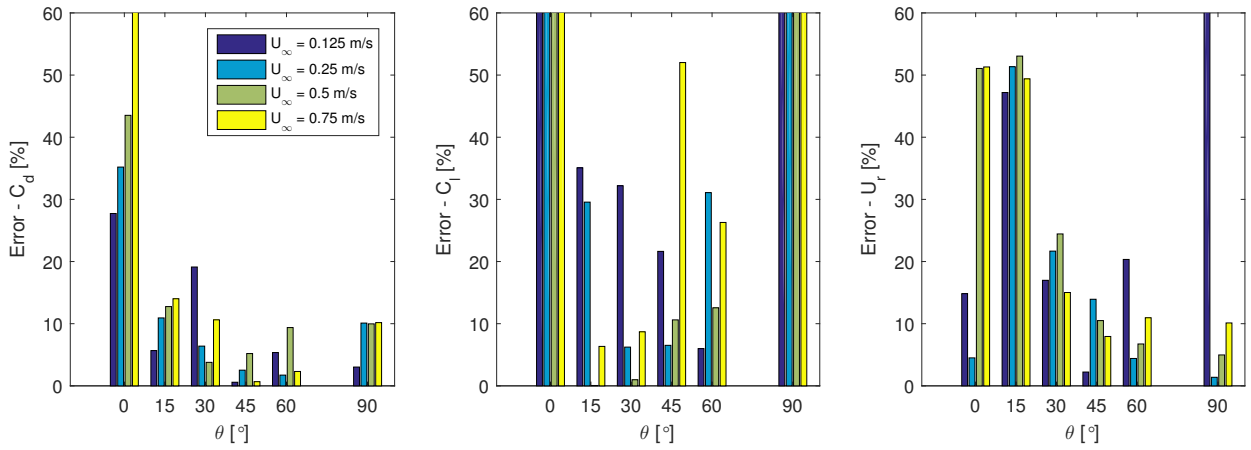

Figure 8: The relative error between numerical simulation and experimental data in Patursson et al. (2010).

The comparison between the numerical simulations and laboratory tests is presented in Fig. 10, and the relative error is given in Fig. 11. For net case 1, the relative errors are varying significantly with different attack angles and incoming velocities. The largest discrepancy between the numerical prediction and experimental data was for case with $\theta = 30°$ and $U_\infty = 0.5$ m/s, where the drag force was overpredicted about 40% by the numerical model. However, the relative errors for most of the remaining cases are well below 20%. The drag force for net case 2 was well predicted by the numerical model, where the errors for most of the cases are about or below 10%. The largest average error was associated with net case 3. The drag force at all incoming velocities and attack angles were underestimated. This somehow indicated an underestimation of a and b for this net panel. For most cases the errors are between $10\% - 20\%$. However, for cases with $U_\infty = 0.75$ m/s and $U_\infty = 1$ m/s at $\theta = 30°$, the relative errors reach 30%.

6.3. Current interaction with fixed circular fish cages

Zhan et al. (2006) also conducted experiments on circular fish cage in steady current, and the numerical model was also validated against this set of experiments. The purpose is to examine the performance of the numerical model for more complex flows. The general setup of the experiments was the same with the experiments described in Section 6.2. The net used in the experiments are also exactly the same, and they were fixed tightly in a circular rigid frame well below the water surface.

The numerical model was set up in the same manner as described in Section 6.2. The sketch of the computational domain is given in Fig. 12. A local cylindrical coordinate was set up for the circular cage, where the origin of the coordinate was aligned with the center line of the circular fish cages. The porous resistance coefficients for the fish cages were exactly the same as shown in Table 3 in this local cylindrical coordinate system, and they were transormed to global coordinate system for each grid cell.

An example of flow visualization is presented in Fig. 13, where the velocity contours is plotted on the horizontal plane through the center of the circular fish cage with $S_n = 0.128$. The incoming velocity is $U_\infty = 0.5$ m/s. In front of the fish cage, there exists a small area where the velocity was reduced. The main velocity reduction area is inside and behind the cage. The wake approximately has the same width with the diameter of the fish cage in the cross flow direction, which is the same with the flow characteristics described in Section 6.2 for plane net panel in current. The velocity inside the circular cage was reduced to approximately $0.96U_\infty$. This is a reasonable value considering the relatively small solidity ratio of the net used in the simulation. Similar results were also reported in Bi et al. (2013b) and Løland (1993). Further reduction was also observed in the wake behind the cage due to the rear part of the cage.

Comparison of the drag force of the circular cages between numerical simulations and experimental data is presented in Fig. 14, and the associated relative errors are plotted in Fig. 15. The overall characteristics of the comparison are the same with the plane net panel in Section 6.2. For net case 1 the significant variation

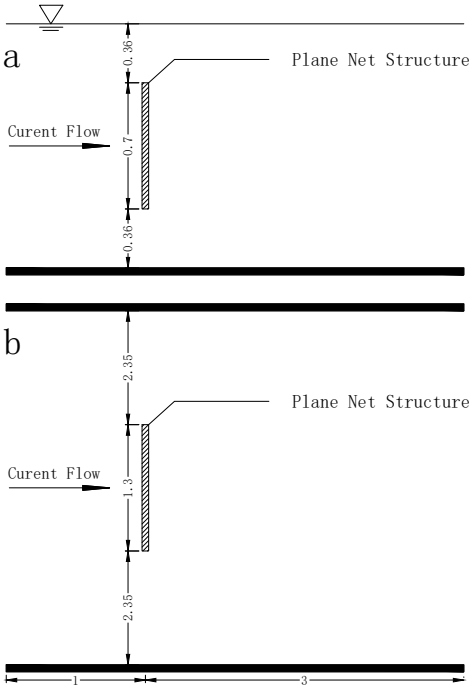

Figure 9: Sketch of the domain for reproduction of the experiments for current interaction with plane net panels in Zhan et al. (2006). (a) side view. (b) top view. (unit: m)

Table 4: The parameters of the regular waves from Lader et al. (2007a) and Lader et al. (2007b)

Wave case no.	1	2	3	4	5
Wave frequency, f (Hz)	1.42	1.42	1.42	1.25	1.00
Wave length, L (m)	0.77	0.77	0.77	1.00	1.54
Wave period, T (s)	0.70	0.70	0.70	0.80	1.00
Wave height, H (m)	0.044	0.064	0.084	0.104	0.165

occurs again for cases with different incoming velocities. But the maximum error was reduced to less than 30% for case with $U_\infty = 0.25$ m/s. The numerical model for net case 2 gave the best prediction, where for all the case the relative error was well below 10%. Meanwhile the underprediction of drag force for net case 3 was also reflected here in the simulation, where for all three incoming velocities, the drag force for the circular cylindrical cage was underestimated by 20% approximately.

6.4. Wave interaction with net panels

In Lader et al. (2007a) and Lader et al. (2007b), series of experiments were performed for analysis of wave interaction with net panels in the hydrodynamic laboratory at the Department of Mathematics, University of Oslo. Net panels with 0.5 m wide and 1.0 m high were positioned in the 8.3 m downstream of the wave maker, and attached at the top and bottom by custom made net forks to hold the net in place. The flume was 25m long, 0.5 m wide and 1.0 m high, and the still water depth was set to 0.62 m. In the experiments three kinds of net panels were used, and they were exposed to five different regular wave conditions. The relevant wave parameters are given in Table 4. A piston type wave maker with a vertical flap was used to generate waves. Two wave gauges were installed in the upstream and downstream with a distance of 1.4 m from the net to measure the surface elevation. Readers are referred to Lader et al. (2007a) and Lader et al. (2007b) for detailed information on setup of the experiments.

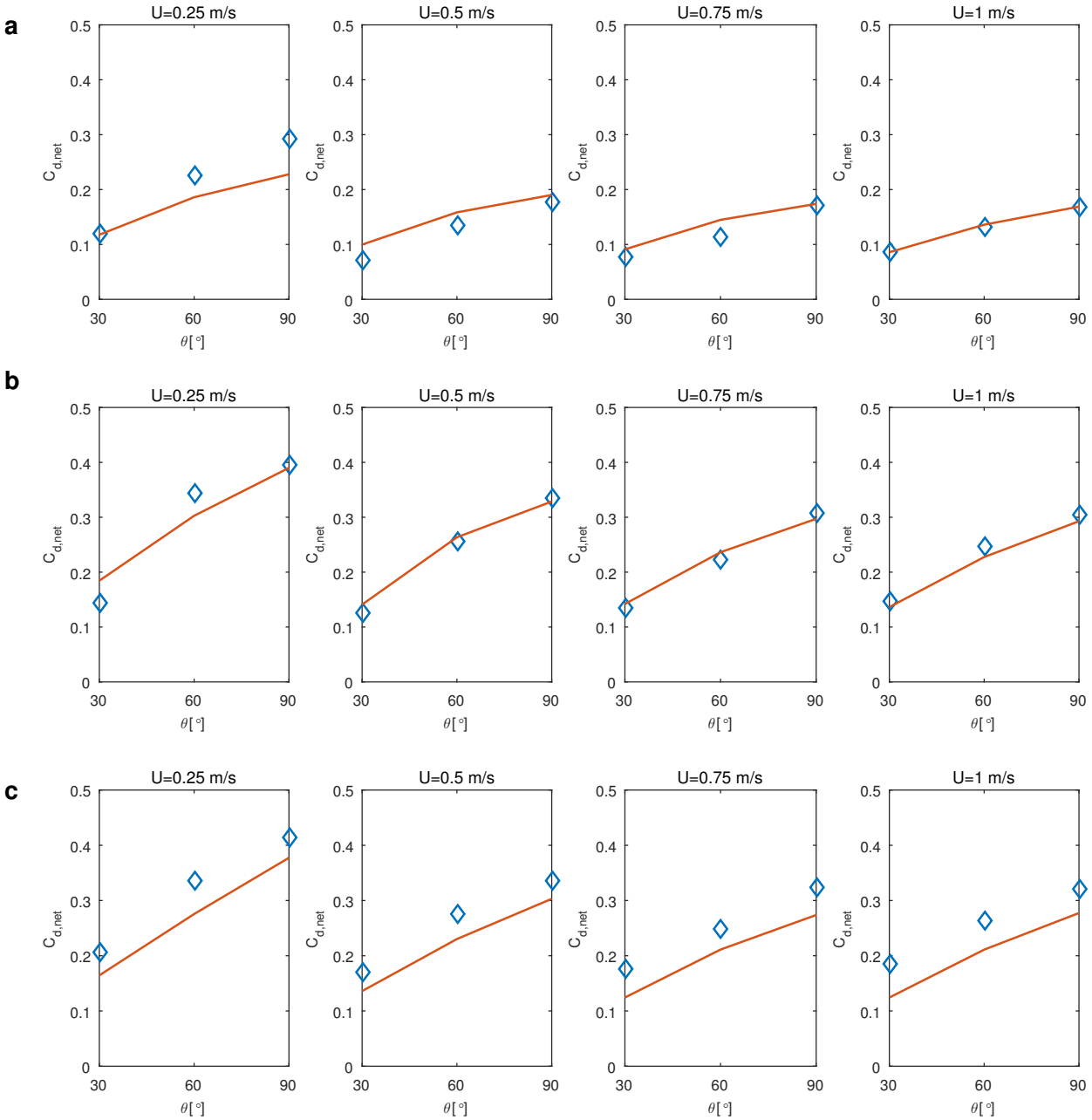

Figure 10: Comparison of the drag force coefficients $C_{d,net}$ between the present numerical simulations in OpenFOAM (solid line) and the data from laboratory tests in Zhan et al. (2006) (diamond) for three net panels: (a) net case 1 (b) net case 2 (c) net case 3.

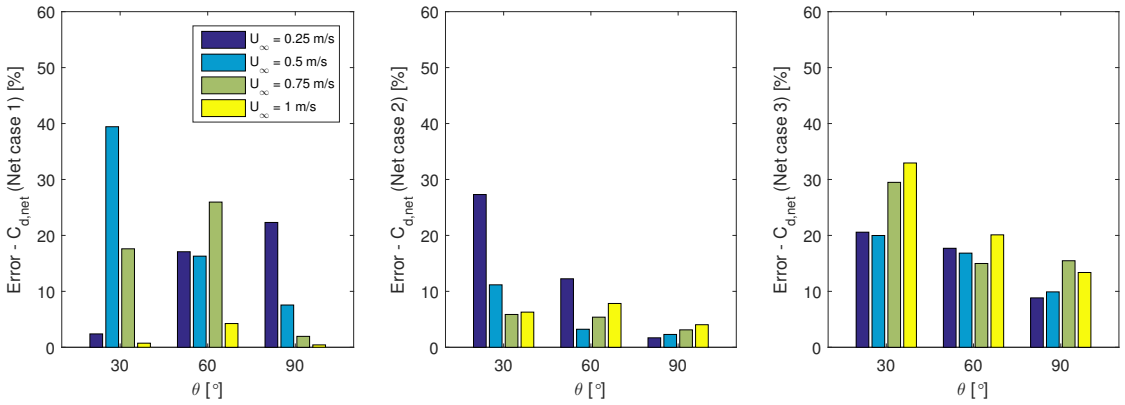

Figure 11: The relative error between numerical simulation and experimental data in Zhan et al. (2006) for plane net panels in steady current.

A two dimensional numerical wave tank was set up based on the physical experiments, since the width of the flume in the experiments was the same with the width of the net panels, and three dimensional effects could be neglected. The utility developed in Jacobsen et al. (2012) was applied for wave generation and absorption. Fig. 16 depicts the domain of the numerical wave tank where two relaxation zones were set up at the inlet and outlet of the numerical tank. In the center of wave tank the net panel was represented by a sheet of porous media with thickness of 50 mm and height of 1 m, and the waves were generated according to the stream function wave theory in Fenton (1988). The calculated quadratic drag resistance coefficients of the three net panels are presented in Table 5, where the drag coefficients were estimated from Sumer and Fredsøe (2006).

Fig. 17 - Fig. 21 depicts comparison of the time series of surface elevation, drag and lift forces between numerical simulations in OpenFOAM and experimental results from Lader et al. (2007a). Fig. 17(a) - Fig. 21(a) presents the surface elevation at the position of net when the wave was propagating without net. It was seen that the higher harmonic components in the wave motion were captured accurately by the numerical simulation and the surface elevation of the generated waves in the numerical model agreed well with the experimental results.

When analyzing the experimental results of wave forces on the net panels, higher harmonic components and multiple extreme points were observed within each zero crossing interval, e.g. in the crest of force cycles in Fig. 19(g). In Lader et al. (2007a) the introduction/increase of the high harmonic components was explained as a result of the nonlinearity in the wave to force process: since the wave force is dependent on not only particle velocity but also exposed surface area, therefore the time series of the wave force should contain higher order components than wave motion itself. Due to the higher harmonics in the force waveforms, multiple extreme points also exists in each zero crossing interval. However, although in the numerical model, the forces were integrated at the instantaneous wet volume of the porous media, the multiple extreme points were not able to be captured, and only single extreme point occurs within each zero crossing interval. It was believed that the occurrence of the multiple extreme points was not only due to the higher harmonic components, but also due to the complex flow interaction between twines and knots, and the vortex shedding behind the twines. The lack of vortex shedding can also partially explain the smoother curves from the numerical simulation compared to the experiments. With such high KC number, the shedding frequency may increase which results in high frequency oscillations. Furthermore, in model scale experiments, the mesh bar length is comparable with the wave height. Therefore the significant variation of instantaneous wet volume might be another reason of this oscillation.

The phase shift is another feature worth mentioning. In general from the experiments it was observed that the horizontal force is approximately in phase with the wave elevation. However for some of the cases a slight shift relative to the wave phase was observed, e.g. the crest of the force signal in Fig. 18(f). This phenomenon was not captured by the numerical model, and the horizontal forces from the numerical

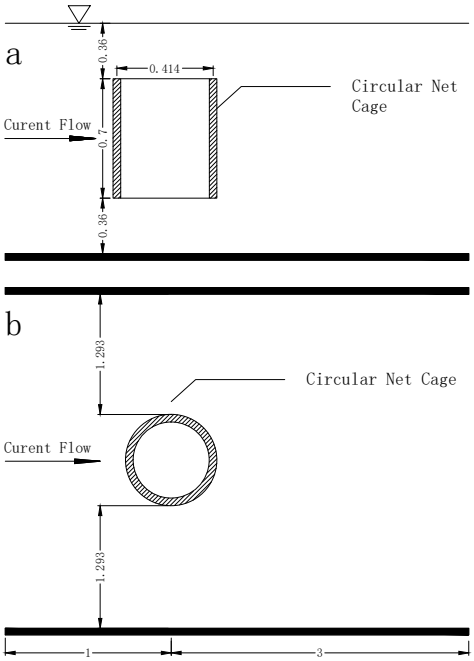

Figure 12: Sketch of the domain for reproduction of the experiments for current interaction with circular fish cages in Zhan et al. (2006). (a) side view. (b) top view. (unit: m)

simulations are in phase with the surface elevation.

Fig. 22 depicts the relative error between the prediected and measured wave height for different cases. The relative error was defined as the average of the ratio between the absolute error of the wave height and the wave height from experimental data. The absolute error includes error from both wave peak and wave trough. By this definition the shift up or down from the numerical results (e.g. the numerical results in Fig. 17(b)) was also accounted for in the error definition. It was found in Fig. 22 that for the first three wave conditions, the relative errors are in-between $20\% - 40\%$ for most of the cases. However, for wave condition 4 and 5, most of the relative errors are reduced to about 20%, except the drag force of net case 2 which suffers from a significant overprediction. We notice that in the experiments, the drag force of net case 2 under wave condition 4 and 5 has almost the same amplitude with drag force of net case 1. This is difficult to explain, since under the same wave condition, the net with higher solidity ratio was expected to be subjected to larger wave load. This has been reflected in the first three wave conditions. Therefore there might be an underestimation to some degree from the experimental data. Meanwhile, the significant overprediction of the wave force from the numerical model may be partially due to the error in estimation of $C_{d,twine}$. This is the motivation of the sensitivity analysis that will be presented in Section 7. In addition, there are some known issues in wave-making by CFD methods (especially OpenFOAM), this has been given in e.g. Wroniszewski et al. (2014). The near-surface kinematics were not able to be reproduced correctly by the solver, which might serve as an error source. Overprediction of the velocity close to the free surface will lead to the overprediction of wave forces. However this seems to be case sensitive, since for the first three wave conditions they are within the reasonable error bound.

7. Sensitivity analysis on porous resistance coefficients

The sensitivity analysis was carried out to examine if the results were still located in a reasonable bound when taking uncertainties of the numerical model into account. The overall procedure of the analysis is the same as shown in Kristiansen and Faltinsen (2012), where one of the selected parameters was varied while the

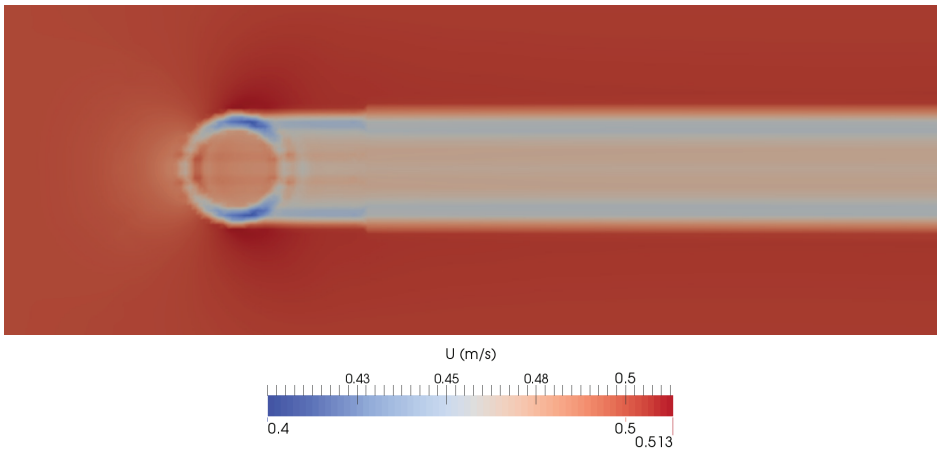

Figure 13: The velocity contours from CFD simulation on a horizontal plane cut through the center of the circular fish cage. The solidity ratio $S_n = 0.128$ (net case 1). The incoming velocity is 0.5 m/s.

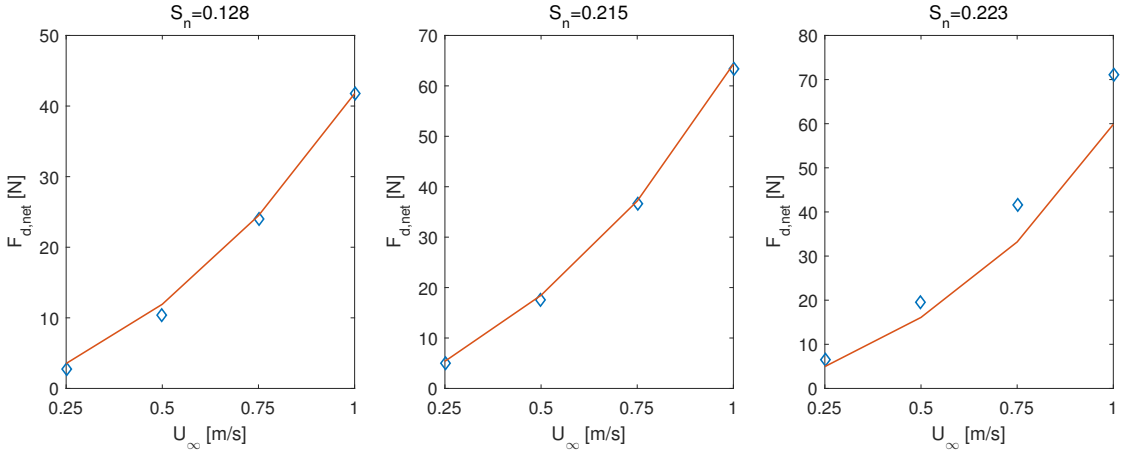

Figure 14: Comparison of the drag force $F_{d,net}$ between the present numerical simulations in OpenFOAM (solid line) and the data from laboratory tests in Zhan et al. (2006) (diamond) for three circular fish cages.

others were kept the same as nominal values. However, in the present work we focused on the uncertainties in calculation of porous resistance coefficients, other uncertainties were not involved in the analysis. The uncertainties of the porous resistance coefficients come from the followings: The drag force coefficient of the twines for a fishing net was assigned with a 10% uncertainty due to i.e. misreading of the figure for drag force coefficients, difference between the shape of the real twine and a cylinder etc.; The projected area S_1 and S_2 for the in-plane and out-of-plane twines were varied with 5%, since they were usually calculated based on the mesh distance λ and the overall dimension of the fishing nets, therefore there exists round-off errors. The other parameters in Eq. (30 - 32) were usually given, therefore uncertainties were not assigned on these values.

The total error bound ΔF of the uncertainties was estimated as:

$$\Delta F = \left(\sum_i (\Delta F_i)^2 \right)^{1/2} \tag{49}$$

where ΔF_i is the error bound due to variation of each parameter. Eq. (49) indicates that the error sources

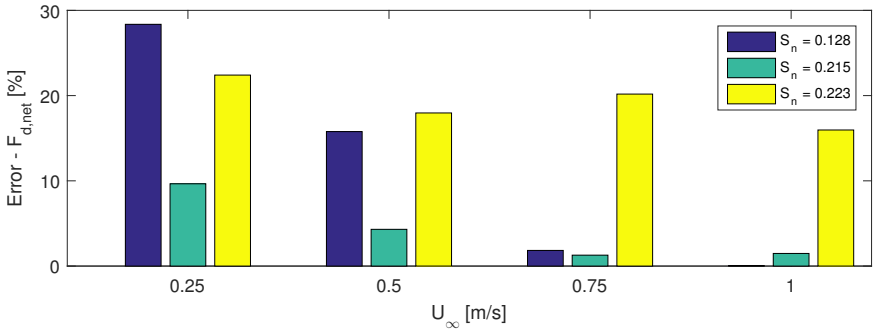

Figure 15: The relative error between numerical simulation and experimental data in Zhan et al. (2006) for three circular fish cages in steady current.

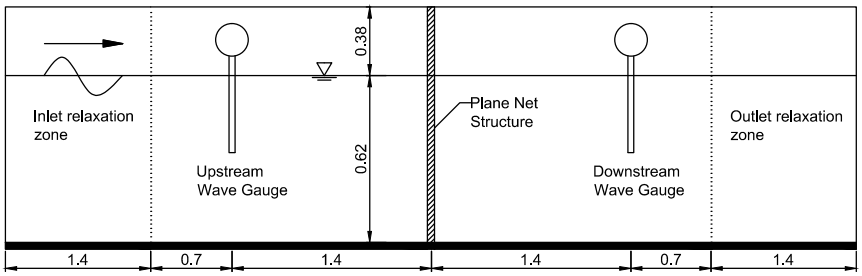

Figure 16: Sketch of the computational domain for simulation of wave interaction with plane net panel. (unit: m)

were assumed to be stochastically independent of each other. ΔF_i was calculated as:

$$\Delta F_i = \frac{1}{2}\sum_{j=1}^{2} |F_j - F_0| \tag{50}$$

where F_0 is the nominal force and F_j is the force from a run with variation.

The results is shown in Fig. 23 for current flow through circular fish cages in Zhan et al. (2006). The case setup has been illustrated in detail in in Section 6.3. The following conclusion were drawn from the presented results: (1) In general solidity ratio has minor effect on the relative error of drag force due to uncertainties of the parameters, i.e. the circular cages with different solidity ratios have the same order of magnitude of error when one specific parameter was varied. (2) The incoming velocity has minor effect on the relative error of drag force, i.e. for a given fish cage, the relative errors of drag force due to variation of one specific parameter with different incoming velocities are in the same order of magnitude. (3) The relative error induced by uncertainties of S_1 and S_2 is insignificant, usually below 5%. (4) The dominant error source is the uncertainty due to $C_{d,twine}$. However, it was found that by 10% variation of drag force coefficient, the relative error of drag force in general is around or less than 10%. We believe that this is an reasonable error bound. This is important or fishing nets in waves, where $C_{d,twine}$ is difficult to find due to relatively small Re number but large KC number. A rough estimation of $C_{d,twine}$ in this case might still produce acceptable results.

8. Conclusions

The present paper investigates the porous media model with application to flow through fishing net structures, where the main effort was paid to derive new expressions for the porous resistance coefficients of the fishing net. The volume averaged Reynolds averaged Navier-Stokes equations were employed as the governing equations, and the differences of the mathematical formulations used in the present work and

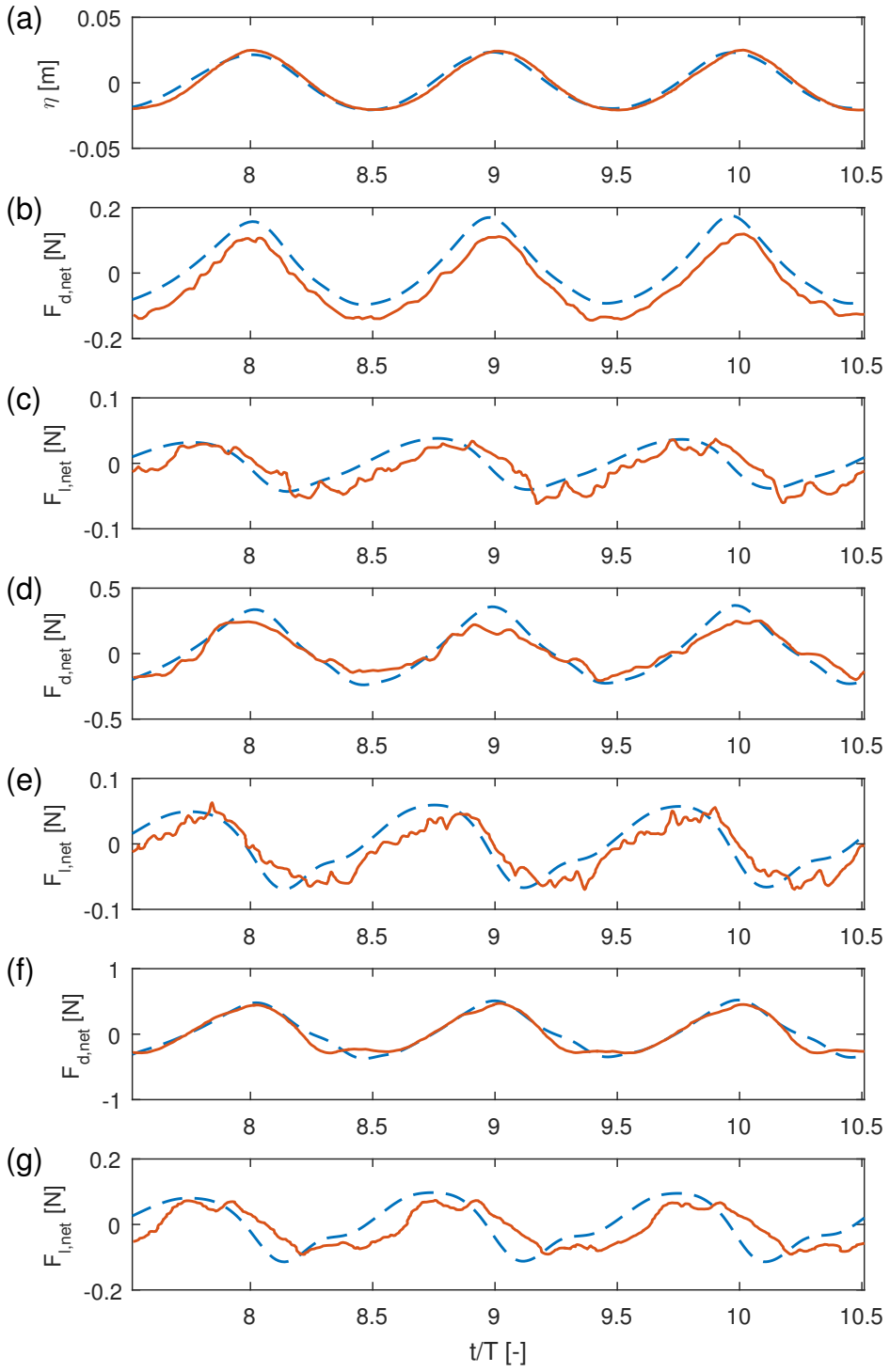

Figure 17: Comparison of time series of surface elevation, drag and lift forces between numerical simulation in OpenFOAM (dashed line) and experiments from Lader et al. (2007a) (solid line) for wave case 1 (wave frequency $f = 1.42$Hz, wave height $H = 0.044$cm). (a) surface elevation at the position of the net when wave propagating without net. (b) drag force for net case 1. (c) lift force for net case 1. (d) drag force for net case 2. (e) lift force for net case 2. (f) drag force for net case 3. (g) lift force for net case 3.

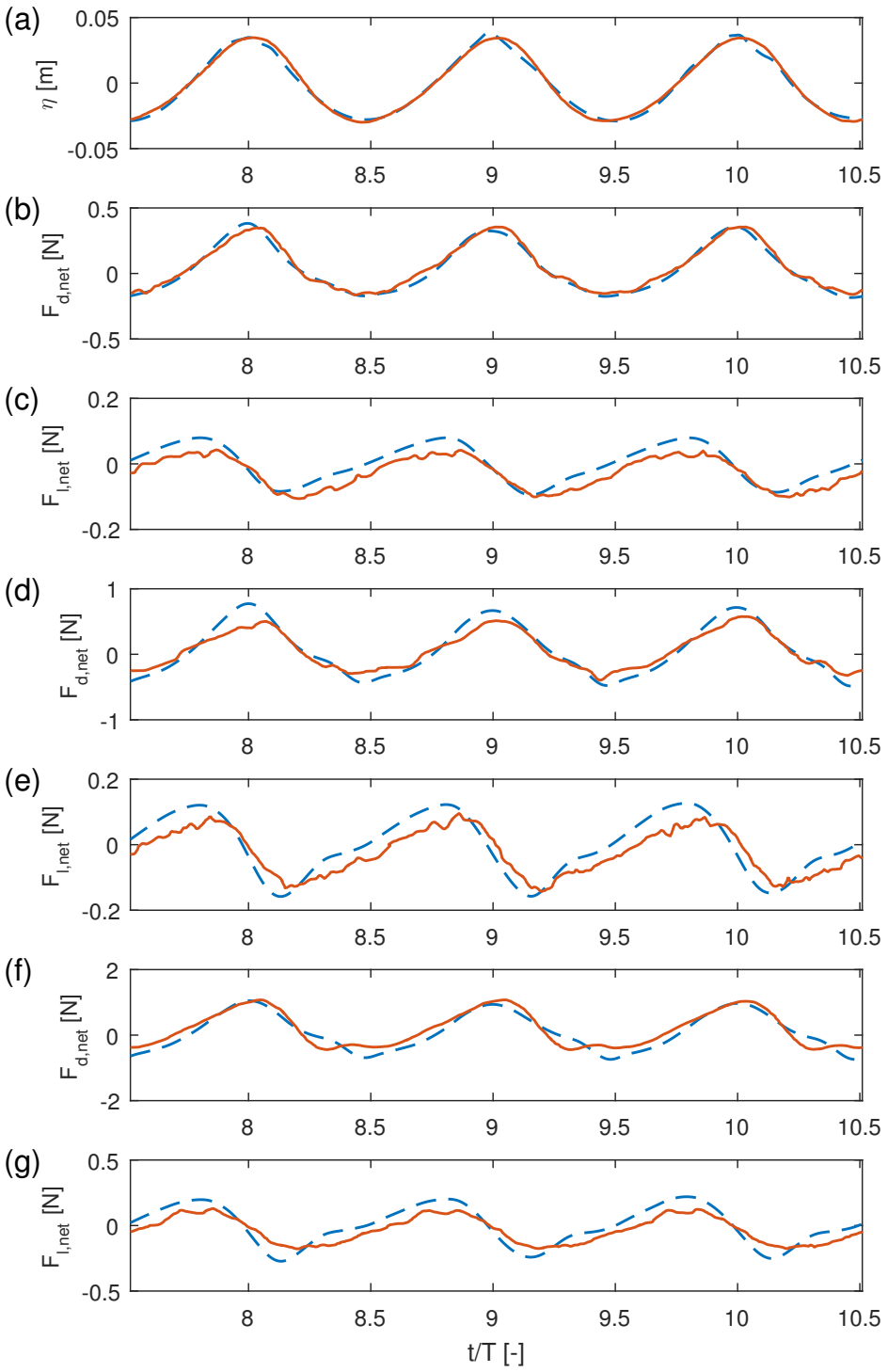

Figure 18: Comparison of time series of surface elevation, drag and lift forces between numerical simulation in OpenFOAM (dashed line) and experiments from Lader et al. (2007a) (solid line) for wave case 2 (wave frequency $f = 1.42$Hz, wave height $H = 0.064$cm). Legend as the same with Fig. 17

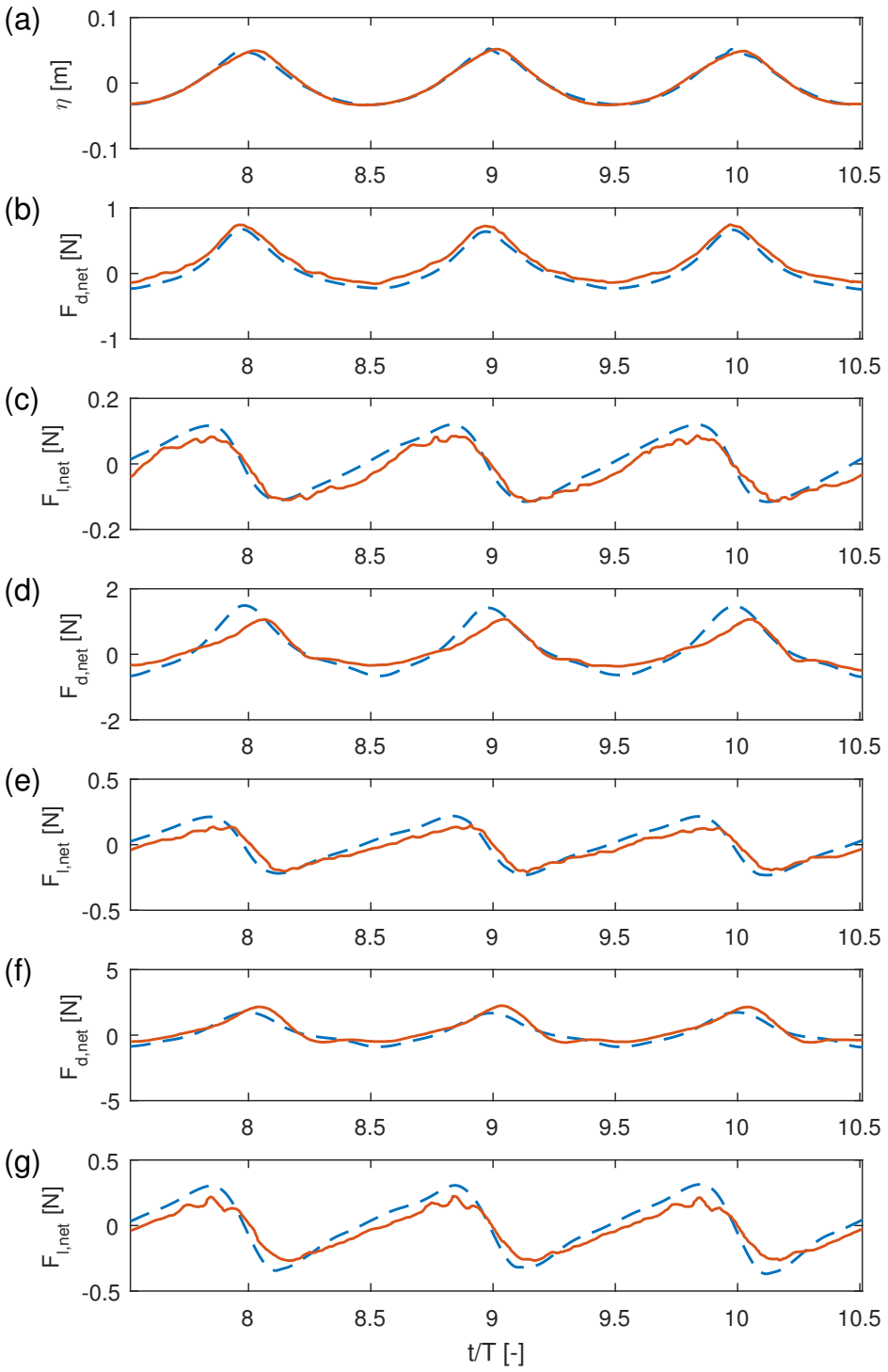

Figure 19: Comparison of time series of surface elevation, drag and lift forces between numerical simulation in OpenFOAM (dashed line) and experiments from Lader et al. (2007a) (solid line) for wave case 3 (wave frequency $f = 1.42$Hz, wave height $H = 0.084$cm). Legend as the same with Fig. 17

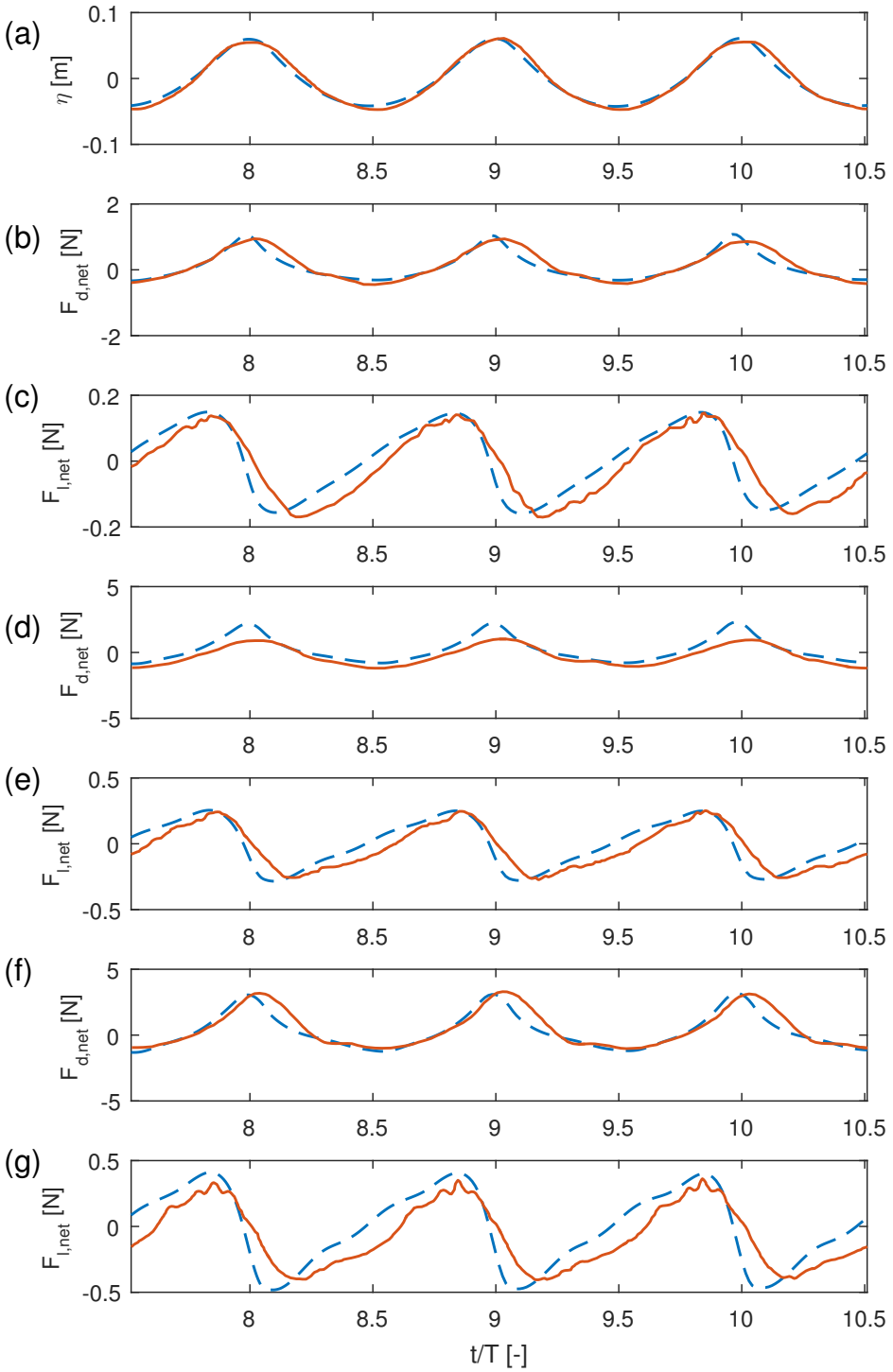

Figure 20: Comparison of time series of surface elevation, drag and lift forces between numerical simulation in OpenFOAM (dashed line) and experiments from Lader et al. (2007a) (solid line) for wave case 4 (wave frequency $f = 1.25$Hz, wave height $H = 0.104$cm). Legend as the same with Fig. 17

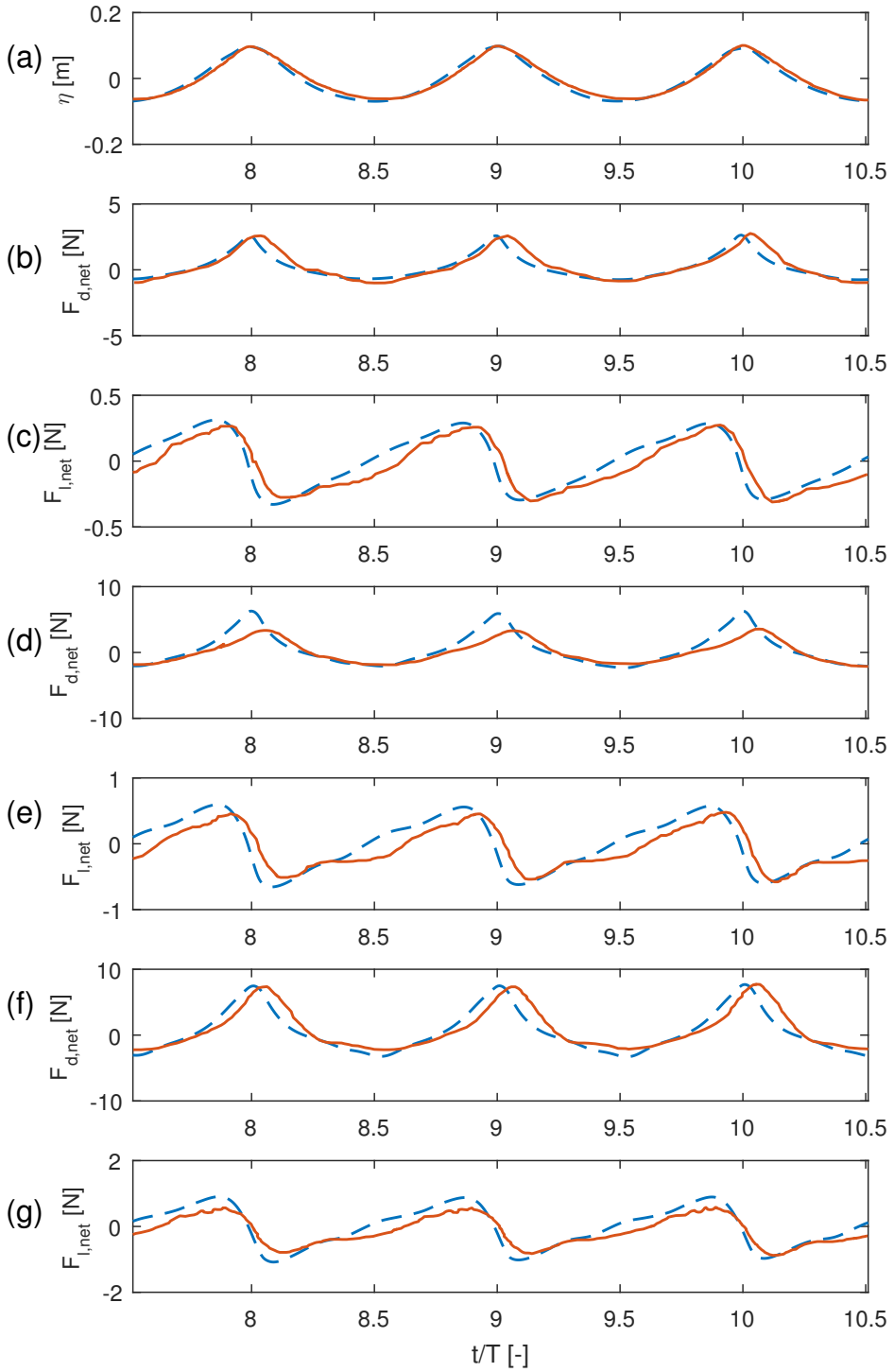

Figure 21: Comparison of time series of surface elevation, drag and lift forces between numerical simulation in OpenFOAM (dashed line) and experiments from Lader et al. (2007a) (solid line) for wave case 5 (wave frequency $f = 1.00$Hz, wave height $H = 0.165$cm). Legend as the same with Fig. 17

Table 5: The physical parameters of the three nets used in Lader et al. (2007a) and Lader et al. (2007b), with calculation of the porous resistance coefficients in five wave conditions. The detailed wave conditions are given in Table 4.

Net case no.		1	2	3
S_n		0.095	0.220	0.288
λ(m)		0.021	0.016	0.025
d(m)		0.0010	0.0018	0.0036
S_1(m^2)		0.0247	0.0571	0.0738
S_2(m^2)		0.0252	0.0581	0.0756
V(m^3)		0.0250	0.0250	0.0250
a		1.22	1.42	1.69
b		0.92	0.87	1.25
Wave case 1	Re	197	355	710
	KC	139	77	38
	$C_{d,twine}$	1.80	1.60	1.60
	C_1	4.63	11.15	15.17
	C_2	1.73	3.37	5.52
Wave case 2	Re	287	516	1033
	KC	202	112	56
	$C_{d,twine}$	1.70	1.50	1.50
	C_1	4.39	10.49	13.15
	C_2	1.64	3.17	4.78
Wave case 3	Re	377	678	1356
	KC	265	147	73
	$C_{d,twine}$	1.50	1.40	1.30
	C_1	4.15	9.84	13.15
	C_2	1.55	2.97	4.78
Wave case 4	Re	410	736	1472
	KC	305	169	85
	$C_{d,twine}$	1.40	1.30	1.30
	C_1	3.91	9.18	13.15
	C_2	1.46	2.77	4.78
Wave case 5	Re	500	898	1796
	KC	499	277	139
	$C_{d,twine}$	1.20	1.30	1.20
	C_1	3.17	7.87	12.14
	C_2	1.19	2.38	4.41

previous works have been discussed. The force acting on the net was obtained by integrating the porous resistance force over the instantaneous wet volume of the porous media.

The linear drag force was neglected in the present work, and only quadratic drag force was accounted for for the porous media resistance. The explanations have been given in terms of porous media model and physical background for flow through fishing nets. A new formula was proposed to address the lack of method on calculation of the quadratic drag force coefficient. The formula was derived based on the transformation of Morison type load model, and it follows the principle that the force acting on the porous media zone should be equal to the force obtained from the Morison type load model. The angle dependence was dropped in the derivation of the formula, in order to get a constant coefficient in time and space domain. This is based on the previous works which gain some good results under this assumption. The interaction effects between twines were accounted for by two new parameters, and they were calibrated by minimizing the error between forces from experimental results and the derived formula. Three reference values of the parameters were obtained based on the available experimental data, and a linear interpolation was used to

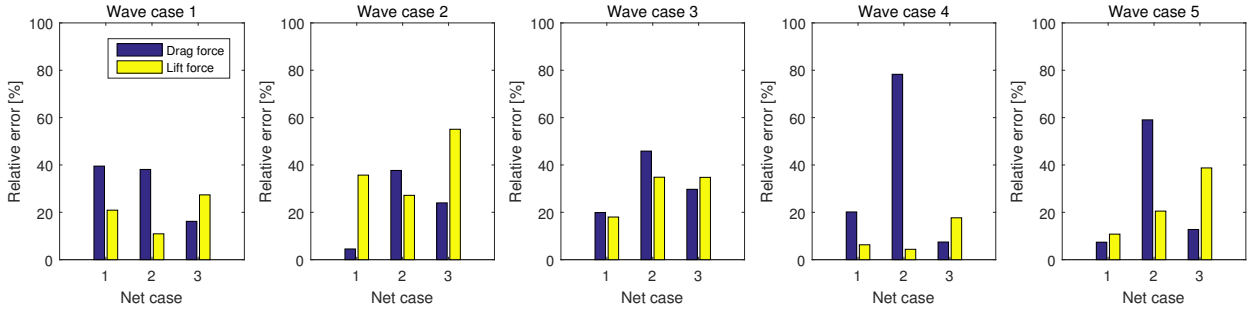

Figure 22: Relative error between results from the present numerical model and experimental data for the mean wave height in Lader et al. (2007a)

obtain the parameters for other nets with different solidity ratios.

The overall numerical model was extensively validated against available experimental data in the current literature. The validation includes both plane net panels and circular fish cages in both steady and unsteady flows. The comparison between numerical and experimental data was given for each validation case, and the relative error was also presented in percentage. It was found that for most of the cases the numerical model could reproduce the experiments adequately. The cases with large relative errors have been investigated and the reason has been explained.

Based on the overall performance, it was concluded that porous media model is a feasible approach for modeling flow through fishing net structures. The derived formula could give porous resistance coefficients of fishing nets within a reasonable error bound, indicating that a and b could account for the interaction effects to a large degree. However, regarding the assumption that angle dependence has minor effects on the numerical results, and application of time and space independent porous resistance coefficients is sufficient for modeling fish cage, more validations are necessary in more complex 3D flow scenarios, i.e. circular fish cages in wave or combined wave and current conditions.

Acknowledgments

We would like to acknowledge the reviewers for their comments and suggestions, which help us understand the problem in depth and improve the quality of the paper. Furthermore, Dr. Bjarne Jensen is acknowledged for his work on development of VARANS equations and porous media model in OpenFOAM, and the enlightening discussions on inertia effects of the porous media. The research was partially supported by FP7-OCEAN-2011 project "Innovative Multi-purpose offshore platforms: planning, design and operation", MERMAID, 288710, under the call "Ocean of Tomorrow".

Appendix A. Comparison of the two coordinate transformation approaches

When modeling flow through fishing nets by porous media model, the anisotropy property must be taken into account since the porous resistance is influenced by the orientation of the porous media. They must be transformed from local to global coordinate system before calculating the resistance forces.

In Patursson et al. (2010) and Zhao et al. (2013b), the porous resistance force was modeled by Darcy-Forchheimer equation as shown in Eq. (9). But two different approaches were applied in the transformation of the porous resistance coefficients. In this section analysis will be given on the differences and limitations of the approaches.

For the most universal cases where neither the flow direction nor the local coordinate of the porous media is aligned with the global coordinate, a strict 3D coordinate transformation matrix R must be employed. Therefore D and C in global coordinate system were formulated as:

$$D_{ij} = R_{ip}R_{jq}D^*_{pq} \quad C_{ij} = R_{ip}R_{jq}C^*_{pq} \tag{A.1}$$

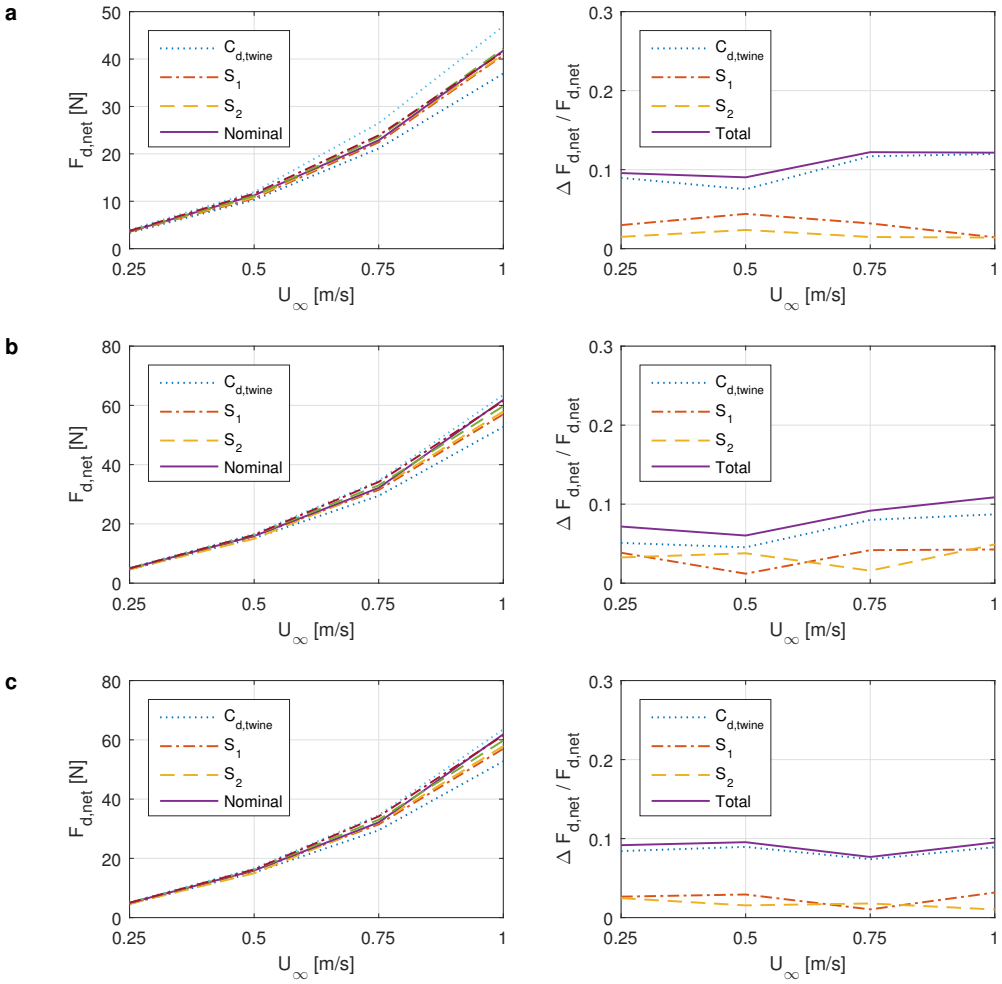

Figure 23: Sensitivity analysis for flow through circular fish cages with different solidity ratios: (a) $S_n = 0.128$. (b) $S_n = 0.215$. (c) $S_n = 0.223$. The left figures shows the error bounds of the drag force of the cages due to numerical model uncertainties: $C_{d,twine}$, S_1 and S_2. The right figures depict the relative error due to these uncertainties.

where

$$R = \begin{bmatrix} \cos(x, x^*) & \cos(x, y^*) & \cos(x, z^*) \\ \cos(y, x^*) & \cos(y, y^*) & \cos(y, z^*) \\ \cos(z, x^*) & \cos(z, y^*) & \cos(z, z^*) \end{bmatrix} \tag{A.2}$$

where $\cos(x_i, x_i^*)$ is the cosines of the angle between x_i axis and x_i^* axis where $i = (x, y, z)$. In 2D cases where z^* and z are aligned, we introduce ζ as the rotation angle from local to global coordinate (the positive direction is based on the right-hand rule). Hereby the transformation matrix was simplified as:

$$R_{ij} = \begin{bmatrix} \cos\zeta & \sin\zeta \\ -\sin\zeta & \cos\zeta \end{bmatrix} \tag{A.3}$$

This matrix is equivalent to the transformation matrix adopted in Patursson et al. (2010). Substituting Eq. (A.3) into Eq. (A.1) gave the final expressions of D and C:

$$D_{ij} = \begin{bmatrix} D_1^* \cos^2(\zeta) + D_2^* \sin^2(\zeta) & -D_1^* \sin(\zeta)\cos(\zeta) + D_2^* \cos(\zeta)\sin(\zeta) \\ -D_1^* \sin(\zeta)\cos(\zeta) + D_2^* \cos(\zeta)\sin(\zeta) & D_1^* \sin^2(\zeta) + D_2^* \cos^2(\zeta) \end{bmatrix} \tag{A.4}$$

$$C_{ij} = \begin{bmatrix} C_1^* \cos^2(\zeta) + C_2^* \sin^2(\zeta) & -C_1^* \sin(\zeta)\cos(\zeta) + C_2^* \cos(\zeta)\sin(\zeta) \\ -C_1^* \sin(\zeta)\cos(\zeta) + C_2^* \cos(\zeta)\sin(\zeta) & C_1^* \sin^2(\zeta) + C_2^* \cos^2(\zeta) \end{bmatrix} \tag{A.5}$$

Instead to use matrix multiplication, Zhao et al. (2013b) employed a simplified method as:

$$D_1 = \frac{D_1^* + D_2^*}{2} + \frac{D_1^* - D_2^*}{2}\cos(2\zeta) = D_1^* \cos^2\zeta + D_2^* \sin^2\zeta \tag{A.6}$$

$$C_1 = \frac{C_1^* + C_2^*}{2} + \frac{C_1^* - C_2^*}{2}\cos(2\zeta) = C_1^* \cos^2\zeta + C_2^* \sin^2\zeta \tag{A.7}$$

$$D_2 = \frac{D_1^* - D_2^*}{2}\sin(-2\zeta) = -D_1^* \sin\zeta\cos\zeta + D_2^* \sin\zeta\cos\zeta \tag{A.8}$$

$$C_2 = \frac{C_1^* - C_2^*}{2}\sin(-2\zeta) = -C_1^* \sin\zeta\cos\zeta + C_2^* \sin\zeta\cos\zeta \tag{A.9}$$

By comparing Eq. (A.4 - A.5) with Eq. (A.6 - A.9), it was found that in the transformed D matrix, $D_{11} = D_1$ but $D_{12} = D_{21} = D_2$, and D_{22} was not calculated in Zhao et al. (2013b). It was the same with C. The formulation of porous resistance in Zhao et al. (2013b) should be expressed as:

$$S = \begin{bmatrix} D_1\mu|u| + \frac{1}{2}C_1\rho u^2 \\ D_2\mu|u| + \frac{1}{2}C_2\rho u^2 \end{bmatrix} \tag{A.10}$$

Therefore the simplification in Zhao et al. (2013b) limits its application, and it is valid only when the flow is unidirectional and the flow direction is aligned with x axis. For wave interaction with fishing nets, Eq. (A.6 - A.9) are not valid anymore, and Eq. (A.4 - A.5) should be used due to the orbital motion of water particles.

Appendix B. The force on porous media based on linear momentum conservation of control volumes

The forces acting on porous media could be obtained by linear momentum conservation on control volume, as shown in Patursson (2008). Below a detailed derivation is presented for this method.

Assume that the porous media is enclosed by the control volume CV. Therefore the integral form of the momentum conservation in the control volume was expressed as:

$$\frac{\mathrm{d}}{\mathrm{d}t}\left(\int_{CV} \rho u_i \,\mathrm{d}V\right) = -\int_{CS} p\mathrm{n}_i \,\mathrm{d}S + \int_{CS} \tau_{ij}\mathrm{n}_j \,\mathrm{d}S + \int_{CV} \rho g_i \,\mathrm{d}V - Q_i \tag{B.1}$$

Here the term in the left hand side in Eq. (B.1) is the material derivative of the momentum on the control volume. The terms on the right-hand side are pressure, viscous stress, body force and finally the force on porous media due to fluid. Note that the force on porous media from the fluid and the force on the fluid from porous media are a pair of force according to Newton's third law.

Furthermore, assume that the control volume is not varying with time, e.g. the porous media is always enclosed by a fixed control volume. Then the volume integral is not a function of time. Then the material derivative of the momentum was given as:

$$\frac{\mathrm{d}}{\mathrm{d}t}\left(\int_{CV} \rho u_i \,\mathrm{d}V\right) = \frac{\partial}{\partial t}\left(\int_{CV} \rho u_i \,\mathrm{d}V\right) + \int_{CV} \frac{\partial}{\partial x_j}(\rho u_i u_j) \,\mathrm{d}V \tag{B.2}$$

By applying Gauss theorem, the second term on the right-hand side of Eq. (B.2) was converted to surface integral, then Eq. (B.2) was rewritten as:

$$\frac{\mathrm{d}}{\mathrm{d}t}\left(\int_{CV} \rho u_i \,\mathrm{d}V\right) = \frac{\partial}{\partial t}\left(\int_{CV} \rho u_i \,\mathrm{d}V\right) + \int_{CS} \rho u_i u_j \mathrm{n}_j \,\mathrm{d}S \tag{B.3}$$

Substituting Eq. (B.3) into Eq. (B.1) yields the final expression of Q_i:

$$Q_i = -\frac{\partial}{\partial t}\left(\int_{CV} \rho u_i \, \mathrm{d}V\right) - \int_{CS} \rho u_i u_j \mathrm{n}_j \, \mathrm{d}S - \int_{CS} p \mathrm{n}_i \, \mathrm{d}S + \int_{CS} \tau_{ij} \mathrm{n}_j \, \mathrm{d}S + \int_{CV} \rho g_i \, \mathrm{d}V \tag{B.4}$$

References

Balash, C., Colbourne, B., Bose, N., Raman-Nair, W., 2009. Aquaculture net drag force and added mass. Aquacultural Engineering 41, 14–21. URL: http://linkinghub.elsevier.com/retrieve/pii/S0144860909000338, doi:10.1016/j.aquaeng.2009.04.003.

Berberović, E., van Hinsberg, N., Jakirlić, S., Roisman, I., Tropea, C., 2009. Drop impact onto a liquid layer of finite thickness: Dynamics of the cavity evolution. Physical Review E 79, 036306. URL: http://link.aps.org/doi/10.1103/PhysRevE.79.036306, doi:10.1103/PhysRevE.79.036306.

Bi, C., Zhao, Y., Dong, G., Zheng, Y., Gui, F., 2014a. A numerical analysis on the hydrodynamic characteristics of net cages using coupled fluid-structure interaction model. Aquacultural Engineering 59, 1–12. URL: http://linkinghub.elsevier.com/retrieve/pii/S014486091400003Xhttp://www.sciencedirect.com/science/article/pii/S014486091400003X, doi:10.1016/j.aquaeng.2014.01.002.

Bi, C.W., Zhao, Y.P., Dong, G.H., Cui, Y., Gui, F.K., 2015. Experimental and numerical investigation on the damping effect of net cages in waves. Journal of Fluids and Structures 55, 122–138. URL: http://linkinghub.elsevier.com/retrieve/pii/S0889974615000523, doi:10.1016/j.jfluidstructs.2015.02.010.

Bi, C.W., Zhao, Y.P., Dong, G.H., Xu, T.J., Gui, F.K., 2013a. Experimental investigation of the reduction in flow velocity downstream from a fishing net. Aquacultural Engineering 57, 71–81. URL: http://linkinghub.elsevier.com/retrieve/pii/S0144860913000691, doi:10.1016/j.aquaeng.2013.08.002.

Bi, C.W., Zhao, Y.P., Dong, G.H., Xu, T.J., Gui, F.K., 2013b. Experimental investigation of the reduction in flow velocity downstream from a fishing net. Aquacultural Engineering 57, 71–81. URL: http://linkinghub.elsevier.com/retrieve/pii/S0144860913000691, doi:10.1016/j.aquaeng.2013.08.002.

Bi, C.W., Zhao, Y.P., Dong, G.H., Xu, T.J., Gui, F.K., 2014b. Numerical simulation of the interaction between flow and flexible nets. Journal of Fluids and Structures 45, 180–201. URL: http://linkinghub.elsevier.com/retrieve/pii/S0889974613002594, doi:10.1016/j.jfluidstructs.2013.11.015.

Bouhoubeiny, E., Germain, G., Druault, P., 2011. Time-Resolved PIV investigations of the flow field around cod-end net structures. Fisheries Research 108, 344–355. URL: http://dx.doi.org/10.1016/j.fishres.2011.01.010, doi:10.1016/j.fishres.2011.01.010.

Burcharth, H., Andersen, O., 1995. On the one dimensional steady and unsteady porous flow equations. Coastal Engineering , 233–257.

Darcy, H., 1856. Les fontaines publiques de la ville de Dijon. Dalmont.

Devilliers, M., Vincent, B., Mnassri, I., 2016. A new adaptive mesh refinement to model water flow around fishing nets. Ocean Engineering 113, 34–43. URL: http://www.sciencedirect.com/science/article/pii/S0029801815006630, doi:10.1016/j.oceaneng.2015.12.009.

Fenton, J., 1988. The numerical solution of steady water wave problems. Computers & Geosciences 14, 357–368. doi:10.1016/0098-3004(88)90066-0.

Forchheimer, H., 1901. Wasserbewegung durch Boden. 45 ed., Zeitschrift des Vereines Deutscher Ingenieure.

van Gent, M.R., 1995. Wave interaction with permeable coastal structures. Ph.d. thesis. Delft University of Technology.

Gopala, V.R., van Wachem, B.G., 2008. Volume of fluid methods for immiscible-fluid and free-surface flows. Chemical Engineering Journal 141, 204–221. URL: http://linkinghub.elsevier.com/retrieve/pii/S1385894708000028, doi:10.1016/j.cej.2007.12.035.

Higuera, P., Lara, J.L., Losada, I.J., 2014a. Three-dimensional interaction of waves and porous coastal structures using OpenFOAM. Part I: Formulation and validation. Coastal Engineering 83, 243–258. URL: http://linkinghub.elsevier.com/retrieve/pii/S0378383913001452, doi:10.1016/j.coastaleng.2013.08.010.

Higuera, P., Lara, J.L., Losada, I.J., 2014b. Three-dimensional interaction of waves and porous coastal structures using OpenFOAM. Part II: Application. Coastal Engineering 83, 259–270. URL: http://linkinghub.elsevier.com/retrieve/pii/S0378383913001464, doi:10.1016/j.coastaleng.2013.09.002.

Hirt, C., Nichols, B., 1981. Volume of fluid (VOF) method for the dynamics of free boundaries. Journal of Computational Physics 39, 201–225. URL: http://www.sciencedirect.com/science/article/pii/0021999181901455, doi:10.1016/0021-9991(81)90145-5.

Hoerner, S., 1965. Fluid-dynamic drag: practical information on aerodynamic drag and hydrodynamic resistance. Hoerner Fluid Dynamics.

Hsu, T.J., Sakakiyama, T., Liu, P.L.F., 2002. A numerical model for wave motions and turbulence flows in front of a composite breakwater. Coastal Engineering 46, 25–50. URL: http://linkinghub.elsevier.com/retrieve/pii/S0378383902000455, doi:10.1016/S0378-3839(02)00045-5.

Huang, C.C., Tang, H.J., Liu, J.Y., 2006. Dynamical analysis of net cage structures for marine aquaculture: Numerical simulation and model testing. Aquacultural Engineering 35, 258–270. URL: http://linkinghub.elsevier.com/retrieve/pii/S014486090600029X, doi:10.1016/j.aquaeng.2006.03.003.

Jacobsen, N.G., Fuhrman, D.R., Fredsoe, J., 2012. A wave generation toolbox for the open-source CFD library: OpenFoam (R). INTERNATIONAL JOURNAL FOR NUMERICAL METHODS IN FLUIDS 70, 1073–1088. doi:10.1002/fld.2726.

Jacobsen, N.G., van Gent, M.R., Wolters, G., 2015. Numerical analysis of the interaction of irregular waves with two dimensional permeable coastal structures. Coastal Engineering 102, 13–29. URL: http://linkinghub.elsevier.com/retrieve/pii/S0378383915000836, doi:10.1016/j.coastaleng.2015.05.004.

Jensen, B., Jacobsen, N.G.l., Christensen, E.D., 2014. Investigations on the porous media equations and resistance coefficients for coastal structures. Coastal Engineering 84, 56–72. URL: http://linkinghub.elsevier.com/retrieve/pii/S0378383913001816, doi:10.1016/j.coastaleng.2013.11.004.

del Jesus, M., 2011. Three-dimensional Interaction of Water Waves with Maritime Structures. Ph.d. thesis. University of Cantabria.

del Jesus, M., Lara, J.L., Losada, I.J., 2012. Three-dimensional interaction of waves and porous coastal structures. Coastal Engineering 64, 57–72. URL: http://linkinghub.elsevier.com/retrieve/pii/S0378383912000245, doi:10.1016/j.coastaleng.2012.01.008.

Kim, Y.H., 2012. Analysis of turbulence and tilt by in-situ measurements inside the codend of a shrimp beam trawl. Ocean Engineering 53, 6–15. URL: http://dx.doi.org/10.1016/j.oceaneng.2012.06.014, doi:10.1016/j.oceaneng.2012.06.014.

Kristiansen, T., Faltinsen, O.M., 2012. Modelling of current loads on aquaculture net cages. Journal of Fluids and Structures 34, 218–235. URL: http://linkinghub.elsevier.com/retrieve/pii/S0889974612000783, doi:10.1016/j.jfluidstructs.2012.04.001.

Kristiansen, T., Faltinsen, O.M., 2015. Experimental and numerical study of an aquaculture net cage with floater in waves and current. Journal of Fluids and Structures 54, 1–26. URL: http://linkinghub.elsevier.com/retrieve/pii/S0889974614002114, doi:10.1016/j.jfluidstructs.2014.08.015.

Lader, P.l., Fredriksson, D.W., Guenther, J., Volent, Z., Blocher, N., Kristiansen, D., Gansel, L., Decew, J., 2015. Drag on hydroid-fouled nets An experimental approach. China Ocean Engineering 29, 369–389. URL: http://link.springer.com/10.1007/s13344-015-0026-y, doi:10.1007/s13344-015-0026-y.

Lader, P.l., Jensen, A., Sveen, J.K., Fredheim, A., Enerhaug, B., Fredriksson, D., 2007a. Experimental investigation of wave forces on net structures. Applied Ocean Research 29, 112–127. URL: http://linkinghub.elsevier.com/retrieve/pii/S0141118707000697, doi:10.1016/j.apor.2007.10.003.

Lader, P.l.F., Olsen, A., Jensen, A., Sveen, J.K., Fredheim, A., Enerhaug, B., 2007b. Experimental investigation of the interaction between waves and net structures-damping mechanism. Aquacultural Engineering 37, 100–114. URL: http://linkinghub.elsevier.com/retrieve/pii/S0144860907000362, doi:10.1016/j.aquaeng.2007.03.001.

Liu, P.L.F., Lin, P., Chang, K.A., Sakakiyama, T., 1999. Numerical modeling of wave interaction with porous structures. Journal of Waterway, Port, Coastal, and Ocean Engineering 125, 322–330. doi:10.1061/(ASCE)0733-950X(2001)127:2(123).

Løland, G., 1993. Current forces on, and water flow through and around, floating fish farms. Aquaculture International 1, 72–89. doi:10.1007/BF00692665.

Losada, I.J., Lara, J.L., Guanche, R., Gonzalez-Ondina, J.M., 2008. Numerical analysis of wave overtopping of rubble mound breakwaters. Coastal Engineering 55, 47–62. doi:10.1016/j.coastaleng.2007.06.003.

Márquez Damián, S., 2013. An Extended Mixture Model for the Simultaneous Treatment of Short and Long Scale Interfaces. Ph.d. thesis. Universidad Nacional del Litoral.

Moe, H., Fredheim, a., Hopperstad, O.S., 2010. Structural analysis of aquaculture net cages in current. Journal of Fluids and Structures 26, 503–516. URL: http://linkinghub.elsevier.com/retrieve/pii/S0889974610000289, doi:10.1016/j.jfluidstructs.2010.01.007.

Nakayama, A., Kuwahara, F., 1999. A Macroscopic Turbulence Model for Flow in a Porous Medium. Journal of Fluids Engineering 121, 427–433.

Patursson, O., 2007. Measurements of drag and lift forces on a net panel and the current reduction in the wake of the panel. Technical Report NVDRit2007:10. University of the Faroe Island. Torshavn, Faro Islands.

Patursson, O., 2008. Flow through and around fish farming nets. Ph.d. thesis. University of New Hampshire.

Patursson, O., Swift, M.R., Tsukrov, I., Simonsen, K., Baldwin, K., Fredriksson, D.W., Celikkol, B., 2010. Development of a porous media model with application to flow through and around a net panel. Ocean Engineering 37, 314–324. URL: http://linkinghub.elsevier.com/retrieve/pii/S0029801809002406, doi:10.1016/j.oceaneng.2009.10.001.

Pichot, G., Germain, G., Priour, D., 2009. On the experimental study of the flow around a fishing net. European Journal of Mechanics, B/Fluids 28, 103–116. URL: http://dx.doi.org/10.1016/j.euromechflu.2008.02.002, doi:10.1016/j.euromechflu.2008.02.002.

Rudi, H., Lø land, G., Furunes, I., 1988. Experiments with nets; forces on and flow through net panels and cage systems. Technical Report MT51 F88-0215. MARINTEK. Trondheim, Norway.

Schlichting, H., Gersten, K., 2003. Boundary-Layer Theory. Springer Berlin Heidelberg.

Sumer, B., Fredsøe, J., 2006. Hydrodynamics Around Cylindrical Strucures. Advanced series on ocean engineering, World Scientific Publishing. URL: https://books.google.dk/books?id=-lbnuyzAXOkC.

Wroniszewski, P.a., Verschaeve, J.C., Pedersen, G.K., 2014. Benchmarking of NavierStokes codes for free surface simulations by means of a solitary wave. Coastal Engineering 91, 1–17. URL: http://linkinghub.elsevier.com/retrieve/pii/S0378383914000842, doi:10.1016/j.coastaleng.2014.04.012.

Xu, T.J., Zhao, Y.P., Dong, G.H., Gui, F.K., 2013a. Analysis of hydrodynamic behavior of a submersible net cage and mooring system in waves and current. Applied Ocean Research 42, 155–167. URL: http://dx.doi.org/10.1016/j.apor.2013.05.007, doi:10.1016/j.apor.2013.05.007.

Xu, T.J., Zhao, Y.P., Dong, G.H., Li, Y.C., Gui, F.K., 2013b. Analysis of hydrodynamic behaviors of multiple net cages in combined wavecurrent flow. Journal of Fluids and Structures 39, 222–236. URL: http://linkinghub.elsevier.com/retrieve/pii/S088997461300042X, doi:10.1016/j.jfluidstructs.2013.02.011.

Zhan, J., Jia, X., Li, Y., Sun, M., Guo, G., Hu, Y., 2006. Analytical and experimental investigation of drag on nets of fish

cages. Aquacultural Engineering 35, 91–101. URL: http://linkinghub.elsevier.com/retrieve/pii/S0144860905001275, doi:10.1016/j.aquaeng.2005.08.013.

Zhao, Y.P., Bi, C.W., Dong, G.H., Gui, F.K., Cui, Y., Guan, C.T., Xu, T.J., 2013a. Numerical simulation of the flow around fishing plane nets using the porous media model. Ocean Engineering 62, 25–37. URL: http://linkinghub.elsevier.com/retrieve/pii/S0029801813000243, doi:10.1016/j.oceaneng.2013.01.009.

Zhao, Y.P., Bi, C.W., Dong, G.H., Gui, F.K., Cui, Y., Xu, T.J., 2013b. Numerical simulation of the flow field inside and around gravity cages. Aquacultural Engineering 52, 1–13. URL: http://linkinghub.elsevier.com/retrieve/pii/S0144860912000593, doi:10.1016/j.aquaeng.2012.06.001.

Zhao, Y.p., Bi, C.w., Liu, Y.x., Dong, G.h., Gui, F.k., Science, M., 2014. Numerical simulation of interaction between waves and net panel using porous media model. Engineering Applications of Computational Fluid Mechanics 8, 116–126.

3 Development of a numerical model for fluid-structure interaction analysis of flow through and around aquaculture net cages

---

Submitted for publication as:
Chen, H. & Christensen, E.D., 2017. Development of a numerical model for fluid-structure interaction analysis of flow through and around aquaculture net cages. Ocean Engineering. Under Review.

Development of a numerical model for fluid-structure interaction analysis of flow through and around aquaculture net cages

Hao Chen[a,*], Erik Damgaard Christensen[a]

[a]*Section of Fluid Mechanics, Coastal and Maritime Engineering, Department of Mechanical Engineering, Technical University of Denmark, DK-2800 Kgs. Lyngby, Denmark*

Abstract

In the present work we developed a numerical model for fluid-structure interaction analysis of flow through and around aquaculture net cages. The numerical model is based on the coupling between a porous media model and a lumped mass structural model. A novel interface was implemented to ensure efficient data exchange and element mapping between the fluid and structural solvers via random-access memory. The main idea is to apply a static mesh in the fluid sub-model, in case that large deformation of the net structure reduces the quality of the mesh. Then the geometry of the net cage was approximated by a set of dynamic porous media zones, where the grid cells were updated at every iteration based on the transferred nodal positions from the structural sub-model. A time stepping procedure was introduced, so the solver is applicable in both steady and unsteady conditions. In order to reduce the computational speed, sub-cycling was applied for the structural solver within one time step, based on the quasi-steady state assumption. The numerical model was validated against experiments in both steady and unsteady conditions. In general the agreement is satisfying.

Keywords: porous media model, lumped mass model, fluid-structure interaction analysis, aquaculture fish cages, coupling scheme

1. Introduction

Aquaculture has been one important resource for food production in the world, and globally it is in a phase of steady expansion. As fresh water aquaculture has been increasingly constrained, space and water availability is driving aquaculture growth towards mariculture, from the bays and fjords with sheltered water to more exposed sites with large currents and waves. Therefore the design for future offshore fish cages requires more accurate analysis and calculations.

Different numerical models have been proposed for analysis of flow through and around net structures. One could either model the net by every individual twine and knot, e.g. in Li et al. (2006), Moe et al. (2010), Tsukrov et al. (2002). Morison equation was applied to calculate the forces on each element, and a structural solver was used to obtain the deformation of the net. Meanwhile another kind of hydrodynamic model has been developed based on the concept of "super element", where each element was represented by a screen, or a membrane, and it has the same properties with the twines and knots that are being simulated. In Lader and Fredheim (2006) Løland formulas developed in Løland (1993) were applied to calculate the hydrodynamic load on each screen element, and a lumped mass model was coupled to solve the deformation of the net. In Kristiansen and Faltinsen (2012) the screen model was further extended to include the effect of Reynold number, and it was applicable for solidity ratio up to 0.5. Kristiansen and Faltinsen (2015) demonstrates the application of this model in waves. Elastic floating ring was also taken into account in the numerical model, therefore a complete rational model for floating fish cage was set up.

*Corresponding author, tel.: (45) 50302416; e-mail address: hchen@mek.dtu.dk; fax (45) 45251961.

Recently the computational fluid dynamic (CFD) method combined with a porous media model was applied for simulating flow through such kind of porous structures in e.g. Patursson et al. (2010), Zhao et al. (2013b), Zhao et al. (2013a) etc. The net structure was modeled as a thin layer of porous media. An extra resistance was added in Navier-Stokes equations to represent the effects of the net structure on the fluid. The advantage of this method is that it is not necessary to model the detailed geometry of the net structure, which keeps the computational time on a reasonable level. From the validation in the above mentioned works, the predictions from the numerical model agree well with the experimental data.

However, in reality, net structures are quite deformable under current and waves. The deformed structure will in turn affect the flow field. So this is a typical fluid-structure interaction (FSI) problem. In general the numerical procedure to solve FSI problems could be broadly classified into two approaches: monolithic approach and partitioned approach (Hou et al., 2012). The monolithic method solves the problem in a matrix concept, i.e. treate the fluid and solid domain in the same mathematical formulation. Hereby the fluid and solid solvers are coupled tightly in a matrix level, and the interfacial conditions are implicit in the solution procedure, see e.g. Hübner et al. (2004), Le Tallec and Mouro (2001) and Michler et al. (2004) etc. This approach can potentially achieve better stability and accuracy, but it requires substantially much more resources and expertise to develop and maintain such a specialized code. Therefore instead of developing a monolithic solver from scratch, we decided to utilize the available code in the computational fluid dynamic toolbox OpenFOAM, coupled with a custom structural solver to realize the FSI analysis. This is the so-called partitioned approach, see e.g. Matthies and Steindorf (2003), Longatte et al. (2009) etc.

For a conventional partitioned solver, the solid domain and the fluid domain are connected but not overlapped. The interfacial conditions are explicit where data are exchanged between the fluid and the structural solver. Arbitrary Lagrangian-Eulerian (ALE) formulation (Hughes et al., 1981) is employed in the fluid solver, which enables the fluid mesh to be deformed in response to the structural deformation. The fluid solver and the structural solver could be coupled either loosely or strongly. Usually loosely coupled scheme is preferred for aeroelastic problems, where only one solution of either field per time step is required. When the densities of the fluid and structure are comparable, instability may occur for a loosely coupled algorithm due to artificial added mass effect, as shown in Förster et al. (2007). This instability is irrespective of the time step that is used, the explicit or implicit scheme that is used in the fluid and structural solver, but purely because of the coupling scheme that is applied. Sub-iterations within one time step is needed to resolve the issue.

Comparing with a conventional FSI solver, the partitioned solver for FSI analysis of net structures has its own characteristics. The geometry of the structure is not resolved in the fluid solver, but the effect of the structure is taken into account in a fictitious manner via the resistance term in the Navier-Stokes equations. Therefore motion and deformation of the structure is represented through movement of the resistance, rather than the interface. The coupling stability is not an issue any more, as long as the stability of the fluid and structural solvers is guaranteed. The reason is that this problem is not a surface-coupling problem like the above mentioned conventional FSI problems. The interface between fluid and solid does not exist in the numerical model, and the fluid domain is always continuous during the simulation.

Theoretically movement of the resistance could be realized in two ways. One is through movement of the internal subset of the mesh which represents the porous media zones. This method has been illustrated in Fig. 1. The motion/deformation of the net structure is represented by the movement of the subset of the mesh which represents the net structure, as the dark zone in Fig. 1. This method has advantages that the grid cells in the subset remain the same during the simulation. Hereby it eases the mesh manipulation for the setup of the numerical model. However, using this method may significantly distort the mesh grid and reduce the quality of the mesh, considering the negligible bending and compression stiffness of the netting materials. Therefore we consider the second method, where a static mesh is employed. The movement of the net structure in the fluid sub-model is represented by updating the grid cells in the porous media zones, based on the solution from the structural solver. Conceptually this is similar to the immerse boundary method (Mittal and Iaccarino, 2005). The key point of this method is to find a fast and reliable algorithm for searching the grid cells that belong to the updated porous media zones at each time step.

Previously among those works which were based on CFD methods for evaluating flow though net structures, few considered the effect of net deformation. In Devilliers et al. (2016), a special solver was imple-

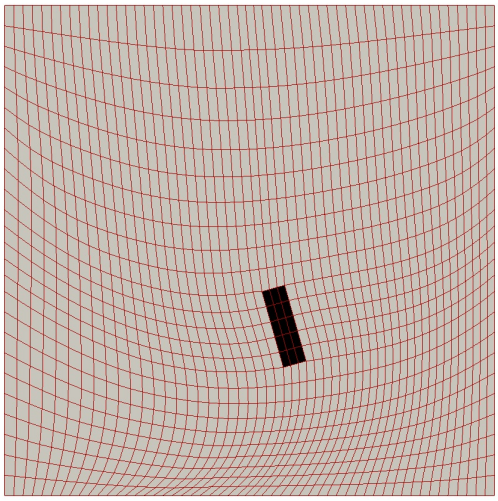

Figure 1: An example on simulation of net structural deformation by moving mesh technique. The dark zone represents the net structures and its movement leads to the deformation of the mesh grid.

mented for FSI analysis of current flow through net structures. The fluid solver solved pseudo-compressible Navier-Stokes equations, and the structure code *DynamiT* was applied to predict the net deformation, which approximated the net as a set of rigid bars. The resistance source term was estimated by Landweber-Ritchmeyer mechanic hypothesis, and the coupling was via output files. Advanced adaptive mesh refinement technique was applied to increase the resolution of the mesh in the net area. In Bi et al. (2014a) and Bi et al. (2014b), attempts have also been made to manually couple the porous media model with a lumped mass structural model. The coupling was based on the concept of "iteration", and under each iteration, steady state condition was assumed. The numerical model reached convergence very fast, usually under 1-3 iterations. In the present paper we will further improve the solver presented in Bi et al. (2014a) and Bi et al. (2014b). The main idea behind it is to achieve the FSI analysis for net structures in both steady state and transient conditions. This includes the following objectives that will be realized:

1. A time stepping procedure will be included, which makes the solver applicable in unsteady conditions.
2. The interaction effects between the current/wave and net cages will be fully considered at every time step. This includes application of the instantaneous relative velocity between flow and net on calculation of porous resistance coefficients, automatic transformation of the local porous resistance coefficients based on the position of the net etc.
3. An interface between two solvers will be implemented which could ensure automatic data exchange and element mapping via random-access memory.
4. Sub-cycling within each time step is applied for the structural solver to accelerate the computation.
5. Thorough validation will be carried out to examine the performance of the solver in both steady and unsteady conditions.

2. Description of the fluid and structural solvers

This is a typical multi-physics problem where different solvers need to be applied in the solid and fluid domains. In the present work, we adopted an existing solver in OpenFOAM as the fluid solver, and implemented a lumped mass solver for the structural deformation of the net. Below in this section, these two solvers are described in detail.

2.1. CFD solver

The net structure in the fluid domain was approximated by a very thin volume of porous media, which requires that the fluid solver has the capability on analysis of flow through porous structures. In Jensen

et al. (2014) the governing equations on flow through porous structures were revised. The relevant library in OpenFOAM was re-implemented based on the new formulation and released as open source together with the *waves2Foam* toolbox developed in Jacobsen et al. (2012). In the present work this library was applied in both transient single phase and two phase flow solver in OpenFOAM, and below a brief description is given on it.

2.1.1. Governing equations

The governing equations for the CFD solver are the volume averaged Reynolds averaged Navier-Stokes (VARANS) equations:

$$\nabla \cdot \langle \bar{\boldsymbol{u}} \rangle = 0 \tag{1}$$

$$(1 + C_m)\frac{1}{n}\frac{\partial \rho \langle \bar{\boldsymbol{u}} \rangle}{\partial t} + \frac{1}{n}\nabla \cdot \frac{\rho}{n}\langle \bar{\boldsymbol{u}} \rangle \langle \bar{\boldsymbol{u}} \rangle^T = -\nabla \langle \bar{p} \rangle^f - \boldsymbol{g} \cdot \boldsymbol{x} \nabla \rho + \frac{1}{n}\nabla \cdot \mu \nabla \langle \bar{\boldsymbol{u}} \rangle + \boldsymbol{S} \tag{2}$$

where $\langle \bar{\boldsymbol{u}} \rangle$ is the volume averaged ensemble averaged velocity in global Cartesian coordinates, ρ is the density of the fluid, μ is the dynamic viscosity, n is the porosity of the net, $\langle \bar{p} \rangle^f$ is the intrinsic volume averaged ensemble averaged excess pressure, $\boldsymbol{S}$ is the resistance force due to the presence of the porous media, ρ is the density field, and C_m is the added mass coefficient, which was calculated as:

$$C_m = \gamma_p \frac{1 - n}{n} \tag{3}$$

where γ_p is an empirical coefficient, and takes the value of 0.34. The resistance force used in Eq. (2) was expressed as:

$$\boldsymbol{S} = -\frac{1}{2}\rho C |\boldsymbol{u} - \boldsymbol{u_n}| (\boldsymbol{u} - \boldsymbol{u_n}) \tag{4}$$

where $\boldsymbol{u}_n$ is the velocity of the net structures. Eq. (4) uses the relative velocity for calculation of the resistance. This is necessary when there exists relative motion between the fluid and net structure. C is the quadratic porous resistance coefficient matrix. In its local coordinate it is given as:

$$C = \begin{bmatrix} C_1 & 0 & 0 \\ 0 & C_2 & 0 \\ 0 & 0 & C_3 \end{bmatrix} \tag{5}$$

If the local coordinate system is not aligned with the global coordinate system, transformation of the coefficient matrix is needed. Due to deformation of the net, the transformation matrix is not constant during the simulation. It will be re-calculated at every time step, based on the nodal positions of the panel elements.

If free surface effect needs to be considered (e.g. waves are modeled in the numerical simulation), an additional equation needs to be solved based on the available Weller-VOF scheme to capture the interface:

$$\frac{\partial \alpha}{\partial t} + \frac{1}{n}\nabla \cdot \boldsymbol{u}\alpha + \frac{1}{n} \cdot \boldsymbol{u}_r \alpha (1 - \alpha) = 0 \tag{6}$$

where $\boldsymbol{u}_r$ is a relative velocity (see Berberović et al. (2009) for details), which aids in retaining a sharp interface. The correction of $1/n$ in Eq. (6) ensures that only the pore volume can be filled with water (see e.g. Jensen et al. (2014) and Jacobsen et al. (2015)).

This set of VARANS equations has already been successfully applied in our previous work in Chen and Christensen (2016) for current and wave interaction with fixed net structures. Readers are referred to that paper for detailed information on application of this model.

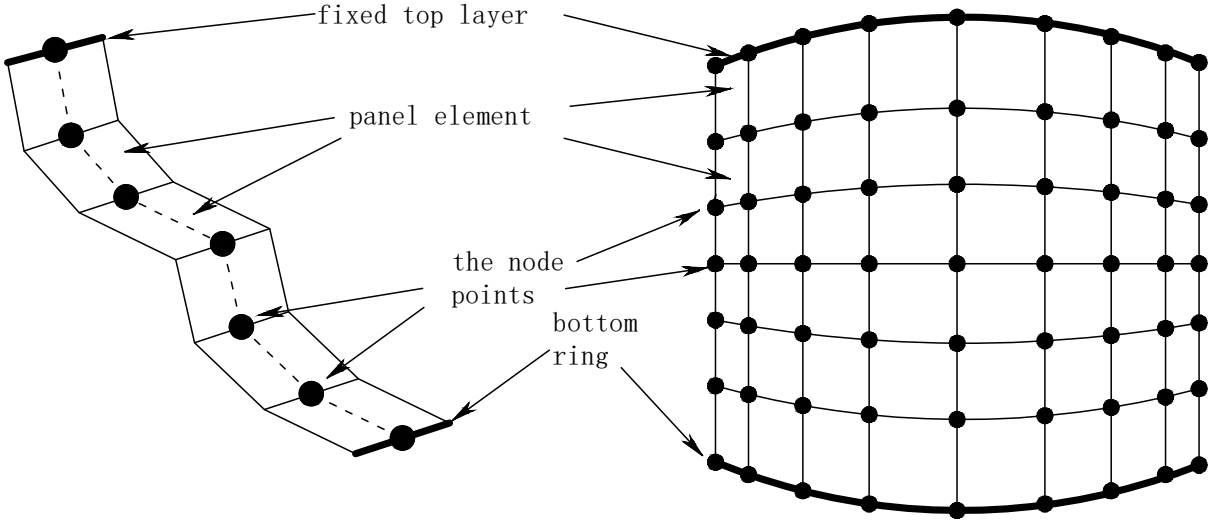

Figure 2: Illustration of the lumped mass model. Left: 2D case. Right: 3D case.

2.1.2. The solution algorithm

The pimple algorithm was employed to solve the velocity-pressure coupling in Navier-Stokes equations. This is a newly created algorithm in OpenFOAM that merges SIMPLE (Semi-Implicit Method for Pressure-Linked Equations, see Patankar and Spalding (1972)) and PISO (Pressure Implicit with Splitting of Operators, see Issa (1986)) algorithms. There exists an outer pimple loop at every time step, inside which the main structure of PISO algorithm was inherited. Meanwhile, after the PISO loop the pressure field was under-relaxed, which was based on the characteristics of SIMPLE algorithm. This algorithm ensures that at every time step the solutions are converged to some certain degree. For simulation of single phase flow, it allows large time step simulations, which relaxes the constraint of Courant number and maintains the stability of the solver. However, for two-phase flow, a special designed solver called multi-dimensionsal limiter for explicit solution (MULES) solver was applied to solve Eq. (6). This solver effectively guarantees the boundness of the α field, but it comes at a cost that MULES solver is explicit. Therefore the time step should be limited by Courant number strictly. An explicit method was applied for discretization of the resistance term, i.e. it was fully treated as a source term at the right-hand side of the discretized equation.

2.2. Lumped mass structure solver

The lumped mass solver presented in Lader and Fredheim (2006) and Lader et al. (2003) was employed as the structural solver. This solver was chosen because of its simple formulation, and it is relatively easy to implement within the framework of OpenFOAM toolbox.

2.2.1. Overview

The net structure was represented by a set of panel elements and nodes in the lumped mass model. For 2D cases, each element was associated with two nodes, while each node was restricted to move within the vertical plane. Furthermore, the panel elements were assumed not to be rotated around the vertical axis. Consequently, the element normal unit vector was restricted to be parallel with the vertical plane. For 3D case, each panel element was associated with four nodes located at the corners of the element, and each node was allowed for full 3D movement. Therefore for the deformed nets, the four nodes associated with the same element were not necessarily in the same plane. Fig. 2 depicts the general configuration of the model for 2D and 3D cases. The mass and the forces acting on the elements were distributed uniformly into its associated nodes, and the equation of motion was evaluated at every node.

2.2.2. Forces on the node

The forces acting on each node include hydrodynamic force F_h, structural force F_s, gravity force F_g and buoyancy force F_w. F_w and F_g were constant and purely determined by the net properties. F_h was calculated based on the solution from the CFD model:

$$\boldsymbol{F}_h = \int_{V_P} \frac{1}{2}\rho C|\boldsymbol{u} - \boldsymbol{u_n}|(\boldsymbol{u} - \boldsymbol{u_n})\,\mathrm{d}V \tag{7}$$

Actually this is simply the integration of the reaction force of the porous resistance over the porous media zones.

Regarding the structural force, F_s on each node was calculated in the structural model. The elastic property of the net structure in the model was represented by a nonlinear spring, and the relationship between force and elongation ϵ was expressed as:

$$F_s = \begin{cases} C_1\epsilon + C_2\epsilon^2 & \epsilon > 0 \\ 0 & \epsilon \leq 0 \end{cases} \tag{8}$$

So the netting material was believed to only have stiffness for tension, and the compression stiffness was neglected. C_1 and C_2 are constants. ϵ is the elongation, defined as $(l - l_0)/l_0$, where l_0 is the undeformed side length and l is the deformed side length of the element. In the present work C_1 and C_2 were taken from Lader and Fredheim (2006) as $C_1 = 1160$ N and $C_2 = 37300$ N.

2.2.3. Equation of motion

The forces acting on the elements were uniformly distributed into all the nodes of the element, then the equation of motion was evaluated at every node:

$$\boldsymbol{F}_s + \boldsymbol{F}_h + \boldsymbol{F}_g + \boldsymbol{F}_w = m_n\boldsymbol{a_n} \tag{9}$$

where m_n is the mass and $\boldsymbol{a_n}$ is the acceleration for each node.

Fig. 3 gives an example of the forces acting on each node in 2D case. Each element was connected by two nodes, therefore the hydrodynamic force acting on the element was distributed into these two nodes. Meanwhile the structural force on each node was calculated based on the positions of the node itself and its neighbors. The motion equation was then evaluated at each node to obtain its acceleration.

2.2.4. Time integration

The displacement and velocity of each node was obtained from explicit time integration of the acceleration for each node:

$$\boldsymbol{u}_n = \int \boldsymbol{a}_n\,\mathrm{d}t \tag{10}$$

$$\boldsymbol{x}_n = \int \boldsymbol{u}_n\,\mathrm{d}t \tag{11}$$

Runge-Kutta method provided in OpenFOAM library was applied for the integration. The problem has quite stiff characteristics and the time step needs to be very small especially at the beginning of the simulation. Therefore quasi steady-state approximation was applied for the coupling of two solvers to accelerate the computation. This will be introduced in detail in Section 3.

3. Coupling between two solvers

The main contribution of this work is the coupling scheme between two solvers. The use of open source software OpenFOAM as the fluid solver and the author-implemented lumped mass structure solver enables both solvers to be combined into a single executable. Both solvers were written in an object-oriented manner therefore coupling between them was straight-forward. Data exchange between the solvers was through random-access memory rather than output files to increase the computational speed. Below details will be given on this coupling scheme.

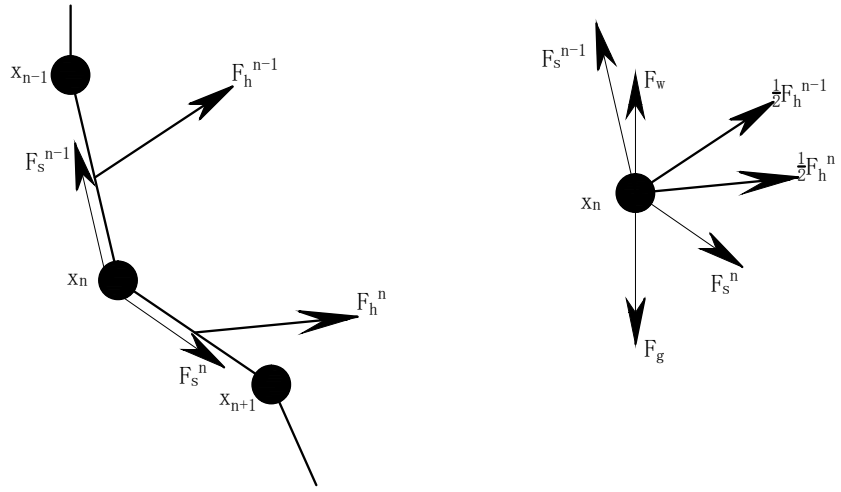

Figure 3: Left: hydrodynamic and structural forces acting on the panel elements and the nodes in 2D case. Right: the forces acting on the node in 2D case.

3.1. Overview

The flow chart of the algorithm for the solver is presented in Fig. 4. At the beginning of the simulation, the physical parameters of the net structure were read by the solver, and the initial configuration of the net structure was calculated. Corresponding to this initial configuration, the fluid solver created the porous media zones, while the structure solver initialized the position vector field for the computation.

When the simulation started, at each pimple iteration, if waves were involved in the simulation, α field was obtained from the MULES solver first. Based on the α field, the density and viscosity field were updated. Then the porous resistance coefficients were transformed into the global coordinate system based on the positions of the updated porous media zones from the last time step. In addition, the porous resistance was calculated and added to the momentum equation. To begin with the PISO algorithm, the momentum predictor produced an intermediate velocity field where the pressure field in the equation was obtained from the last iteration. This velocity field was not divergence free, hereby it was followed by three pressure correctors to correct the velocity field. A divergence free velocity field was produced after the correction, and it was used to calculate the porous forces for the structural solver. Based on the received porous forces, the structural solver evaluated the position of each node, from which the porous media zones were updated. This formed a closed pimple iteration. At every time step three pimple iterations were performed to ensure an intermediate to strong coupling between the fluid and structural solver.

The interaction between the fluid and structure was reflected by the following perspectives in the numerical model:

- The geometry of the net was updated at every iteration of pimple loop according to the solution from the structural solver.
- The coordinate transformation matrix for the porous resistance coefficients was updated at every iteration of pimple loop based on the instantaneous orientation of the porous media zones.
- The porous resistance force was calculated based on the instantaneous relative velocity between the porous media and the net structure, and the instantaneous porous coefficient matrix in the global coordinate system.

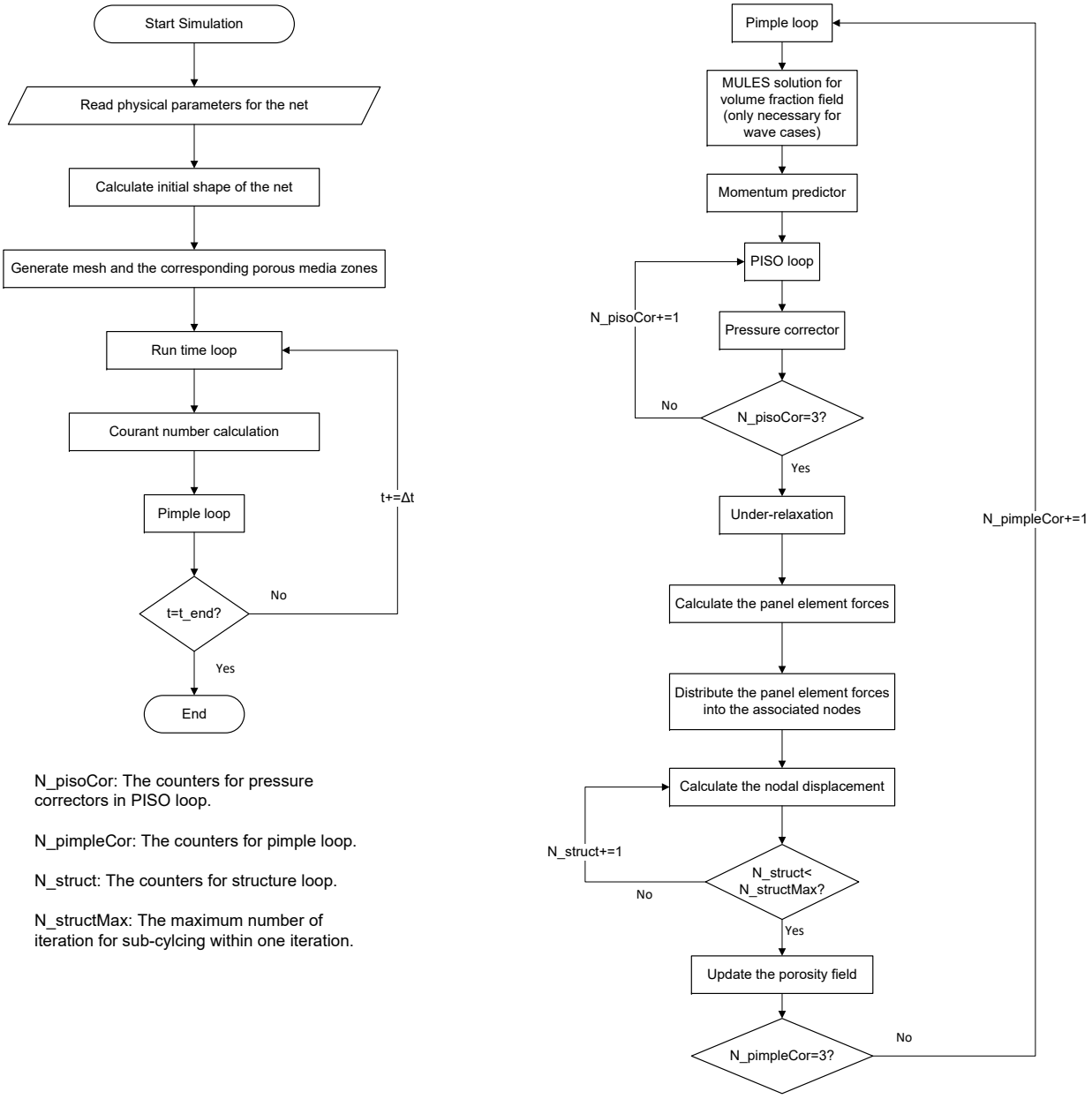

Figure 4: The flow chart for the algorithm of the solver

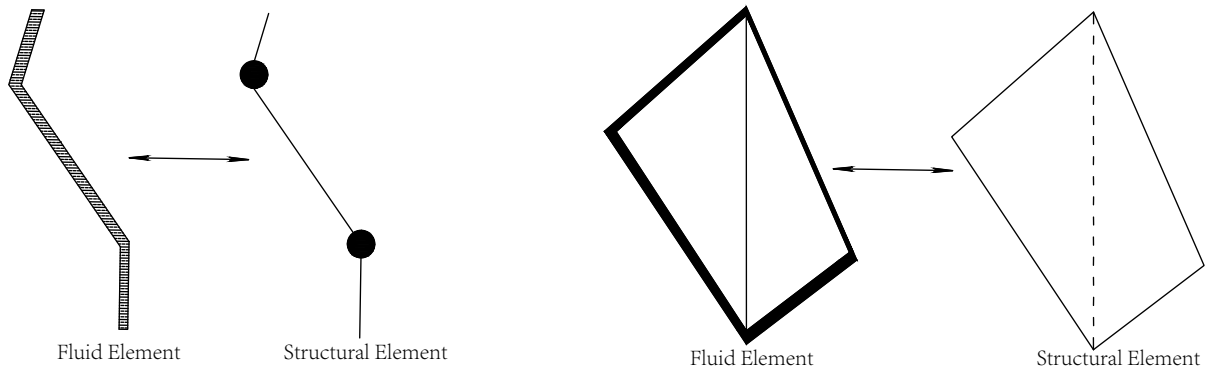

Figure 5: Illustration on mapping of the elements between fluid and structure sub-models. Left: 2D cases. Right: 3D cases.

3.2. Data exchange and mapping of elements

The basic idea for element mapping in the present work is to adopt a one to one mapping method between the elements in the structural and fluid sub-model. Therefore in principle interpolation is not needed. However one could notice that the elements in the structural sub-model are significantly larger than the fluid mesh cells. Hereby we decided to use the structural element as the basic element for date exchange. The corresponding element in the fluid sub-model is the porous media zone, i.e. in the fluid sub-model, the geometry of the net was approximated by a set of porous media zones. Fig. 5 gives an example on the mapping between the fluid and structural elements in 2D and 3D cases. It could be seen that the main difference between two elements is that the element in fluid sub-model has always one higher dimension than in structural sub-model. This is illustrated as follows. In 2D cases, the net structure in the structural sub-model was represented by line elements with two vertexes, while in the fluid sub-model, the element was extended to the porous media zone of plane rectangular with thin thickness. In 3D cases, the structural sub-model was composed of four node elements. Since the four nodes are not necessarily in the same plane under deformation, in the fluid sub-model the four node plane was first split into two triangular planes and then extended to two prisms with very thin thickness.

The data that need to be exchanged at run time are the porous forces and the nodal positions of the elements. Application of one to one mapping method eases the data exchange, and the main issue here in this coupling scheme is to update the grid cells in the porous media zone based on the transferred nodal positions from the structural sub-model at every pimple iteration. This is illustrated in the following part.

3.2.1. Updating the porous media zone

The principle to update the porous media zone based on the known nodal position is to loop through all the cells in the mesh and insert the cells that match the conditions. The conditions were typically a set of mathematical inequalities derived based on the nodal positions and the thickness of the porous media zones. In the 2D case, each element (porous media zone) in the fluid sub-model has two nodes with their coordinates denoted as $\boldsymbol{x_1}$ and $\boldsymbol{x_2}$. Given the coordinate of an arbitrary cell center denoted as $\boldsymbol{x}$, the distance d between this cell center and the line composed of these two vertexes could be obtained. An example of the configuration is shown in Fig. 6. Therefore two criteria needs to be satisfied if one cell belongs to the porous media zone: (1) $d < 1/2t_0$ where t_0 is the thickness of the porous media zone. (2) $\alpha_1 < \pi/2, \alpha_2 < \pi/2$. By looping through all the cells of the fluid mesh grids, the cells which satisfied the criteria were inserted into the cell zone. In 3D case, as mentioned above, the four node element in the structure sub-model was split into two triangular elements first. The corresponding two porous media zones in the fluid sub-model were determined by the nodal positions of these two triangular elements. The general configuration for 3D cases is shown in Fig. 7. If one cell is within the porous cell set, two conditions need to be satisfied: (1) $d < 1/2t_0$. (2) x_0 is within the triangular $x_1x_2x_3$. Again we looped through all the cells of the fluid mesh

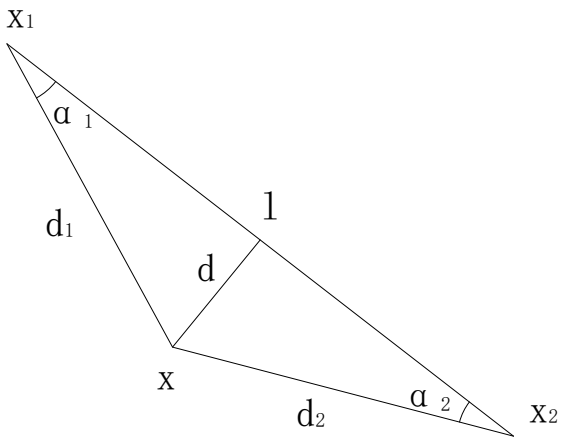

Figure 6: An example of the configuration on calculation of the distance d in 2D cases between an arbitrary cell center and the line composed of two nodes. d_1 is the length of line xx_1 and d_2 is the length of line xx_2. l is the length of line x_1x_2. α_1 and α_2 are the angles between xx_1, xx_2 and x_1x_2, respectively.

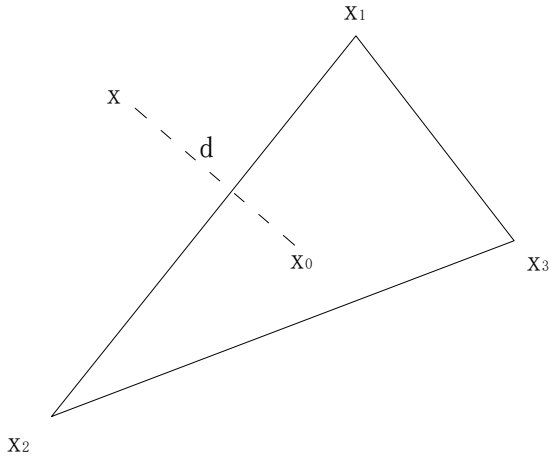

Figure 7: An example of the configuration on calculation of the distance d in 3D cases between an arbitrary cell center and the triangular composed of three nodes. x_0 is the perpendicular foot.

grids, and the cells which satisfied the criteria will be inserted into the cell zone. The details on how these variables were calculated are given in Appendix A.

3.3. Quasi steady-state assumption and sub-cycling

As mentioned above in Section 2.1.2, the pimple algorithm allows large time step simulation for single phase flow. Even for two phase flow, the time step is usually in the order of 10^{-3}. However the structural solver strictly requires a very small time step, typically about $10^{-4} \sim 10^{-5}$ s. This is due to that the structural solver is fundamentally explicit, and the ordinary differential equations that we solved, i.e. Eq. (10) and Eq. (11) have quite stiff characteristics due to the high structural eigen-frequency as shown in Lader et al. (2003).

In order to accelerate the computation, the time step for the whole solver was chosen based on the fluid solver, and quasi steady-state assumption was applied within one iteration of the pimple loop. This means that during this iteration, the forces output from the fluid solver were assumed to be constant, and the position of the net was evolved under this constant hydrodynamic force. A much smaller time step was applied for the evolution of the structural position, approximately $1/100 \sim 1/1000$ of the time step for

the global solver, depending on the simulated case. Therefore sub-cycling was applied within each pimple iteration. Since the computational time for the fluid sub-model was significantly more than the structural sub-model, the computational speed was dramatically improved by application of this assumption.

4. Numerical study and sensitivity analysis

In this section we applied the numerical model described above to perform series of simulations. The purpose is to examine the performance of the numerical model under different net geometries and environmental conditions. First the numerical model was validated against experiments in Bi et al. (2014b) for plane net panel in steady current. Considering that the simulation for this case is not time consuming, we conducted a sensitivity analysis to investigate the influences of the parameters that were introduced in the model. Furthermore, the model was also validated against experiments in Zhao et al. (2008) and Bi et al. (2014a), for plane net panel in waves and steady current interaction with circular net cages. In all the validation cases, the nets were fixed at the top layer, and in the bottom layer a sinker was attached. Under different flow velocities, the nets could deform freely, which in turn affects the flow field. Therefore strong coupling between the flow field and structural deformation occurs, and they could be used to properly validate our numerical model.

4.1. Plane net panel in current flow

The first set of experiments was described in Bi et al. (2014b), which was performed in a wave-current flume at the State Key Laboratory of Coastal and Offshore Engineering, Dalian University of Technology, China. The flume has a dimension of 22 m $\times$ 0.45 m $\times$ 0.6 m, and the depth of the water was set to 0.4 m in the tests. Steady current with the velocity $U = 0.226$ m/s was generated by a pump located at one end of the flume.

The net used in the experiments was a 0.3 m $\times$ 0.3 m knotless polyethylene net. The twine diameter $d_w = 2.6$ mm, and the mesh bar length $\lambda = 20$ mm. This gave a solidity ratio of 0.26. This net was positioned in the center of the flume and well below the free surface. A steel bar with density of 8610 kg/m^3 was mounted in the bottom of the net as a sinker system. It had the same length with the net panel, and the diameter of it was 6 mm. The mass of the sinker was 73 g in air while in water it was 64.5 g by subtracting the buoyancy.

A 2D numerical model was set up based on the experiment. The sketch of the computational domain is shown in Fig. 8. The net was divided into 5 panel elements, therefore each element contains three meshes vertically and 15 meshes horizontally. For the structural sub-model, the mass of the element was uniformly distributed into its two nodes, and the mass of the sinker was added at the bottom lumped mass point. In the fluid sub-model, the thickness of the porous media zone was set to 20 mm, and the porous resistance coefficients were calculated based on the formula proposed in Chen and Christensen (2016), where $C_1 = 27.9$ m^{-1} and $C_2 = C_3 = 9.0$ m^{-1}. The sinker was not modeled in the fluid sub-model, but the forces on it were directly added on the corresponding lumped mass point in the structure sub-model.

4.1.1. Current load on the net panel

We directly output the time series of the drag force from the numerical computation. It was found that an oscillation-free time series requires a small time step for both the fluid solver, i.e. the global time step and the structural solver. Fig. 9 depicts the time series of the drag force under different combination of Courant number, and number of sub-cycling. Although stability of the numerical model was ensured for all the cases, only case (e) was qualified for an oscillation free time series. The amplitude of the oscillation was tightly related to both parameters. However the mean drag force was approximately the same, as shown in Fig. 9 (f). Comparing with the measurement result, the mean drag was slightly underestimated for about 10%.

The oscillation was induced purely due to the numerical error. As shown in Section 3.3, the sub-cycling was under the assumption of constant load within that global time step. However, the load itself was computed based on the relative velocity, i.e. the difference of fluid velocity and the velocity of the net.

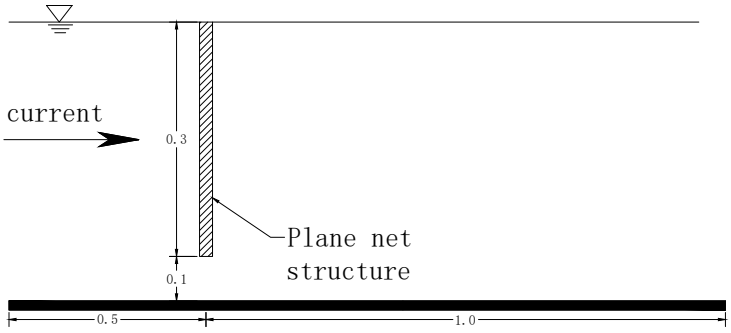

Figure 8: Computational domain for plane net panel in steady current.

A large time step of the fluid solver may introduce a large difference of the fluid velocity between the consecutive two time steps. Meanwhile the time step of the structural solver affects the velocity of the net panel element, and the resistance coefficients in the global coordinate system due to the change of the geometry of the net panels. Therefore they both affect the oscillation amplitude for the output series.

Eliminating/controlling this oscillation is important in some certain cases. For instance, if the net panel is connected with a floater, the motion of the floater should be determined by the instantaneous forces, including the force from the net. The spikes of the force may lead to instability of the motion of the floater. In unsteady cases such as waves, large amplitude oscillation of the drag force may also cause unreasonable net deformation. Otherwise under steady condition, mild amplitude of oscillation as shown in Fig. 9 (c) - (d) is acceptable, since the mean drag converges to the same value. From the results of the measurement, the drag is also not a constant value even if in steady current condition. This is due to e.g. vortex shedding in the wake of the net panel.

4.1.2. Net deformation

The deformation of the net panel is presented in Fig. 10. In general the numerical model could reproduce the deformation of the net accurately. The displacement at the bottom of the net panel was approximately the same. However, one could notice the small gaps between the connecting panels, as shown in Fig. 10. This is due to the imperfection of the algorithm to update the porous media zones, and the application of the static mesh, which is naturally only possible to *approximate* the net panel geometry. The show-up of the gaps will impact the wake in the downstream. We will further touch this issue again in Section 4.1.3.

4.1.3. Flow field and turbulence effects

One important issue left for discussion is the turbulence effects. In our previous work Chen and Christensen (2016) we used a laminar model for flow through net panels. This considers to avoid dual dissipation due to application of a turbulence model. This approximation has been accepted and applied in e.g. Jensen et al. (2014) and Jacobsen et al. (2015). However we notice that the net structure occupies a much smaller region and has a smaller resistance comparing with a breakwater. Therefore this effect might be small. On the other hand, by using a laminar model, the downstream flow was not simulated correctly, which will be presented below. Presently we thoroughly discuss the possibility of using a turbulence model. We tested four turbulence model based on Reynolds-averaged Navier-Stokes (RANS) equations. They are $k-\epsilon$, $k-\omega$, $k-\omega$ SST and realizable $k-\epsilon$ model.

Fig. 11 depicts the time series of the drag force using different turbulence models. No significant differences were observed comparing with laminar model. The time series from $k-\omega$ model seems to be quite irregular, and the oscillating amplitude was amplified slightly in the end, while the rest three were finally stabilized and oscillate with constant amplitude.

However, application of a turbulence model may produce a physically more reasonable downstream velocity field for the numerical model. Fig. 12 presents comparison of the velocity field using laminar and turbulence flow models. In Fig. 12(a) for laminar flow field, rectangular 1 remarks the layer with higher

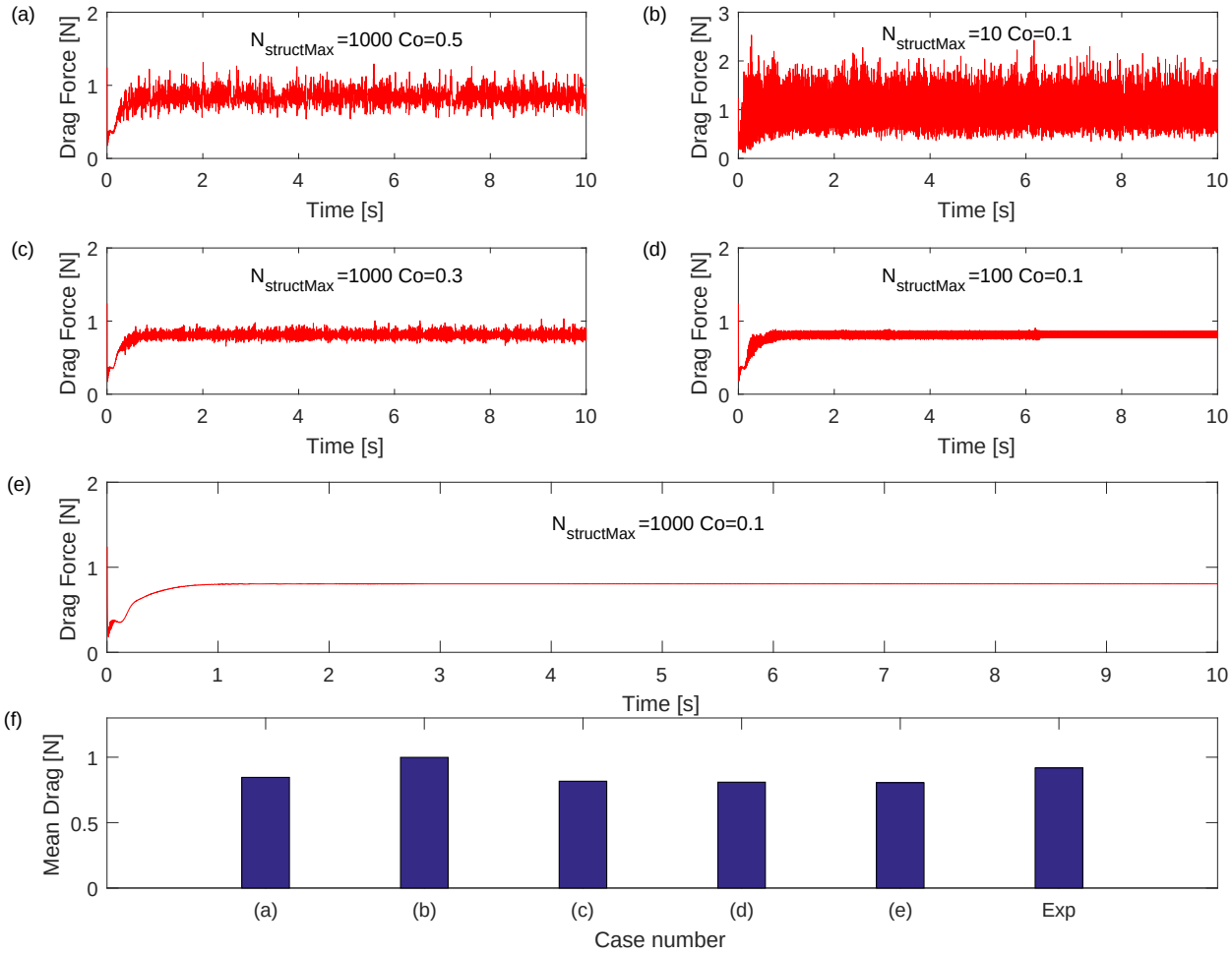

Figure 9: Comparison of time series of the drag force and the mean drag acting on the net panel. Figure (a) - (e) present time series of the drag force for cases with different combinations of Courant number and the number of sub-cycling $N_{structMax}$. Figure (f) presents the mean drag force of (a) - (e) and the drag force measured from experiments in Bi et al. (2014b). The mean drag was determined from the time series of the drag force between 4 s - 10 s.

velocity, which causes the oscillation of the velocity profile. This could be quantitatively demonstrated in Fig. 13, which shows the velocity profiles at horizontal and vertical cut. The spikes in Fig. 13 for laminar model are induced by the gaps between the connecting panels. Regarding Fig. 13(a) for the horizontal cut at 0.15 m beneath the free surface, the spikes were induced by the gap indicated by the lower circle mark in Fig. 10, which is exactly located at $y = -0.15$ m. But for Fig. 13(b), all the gaps contributes to the generation of the spikes. Physically, the gaps between the panels caused a slightly higher downstream velocity behind it, due to the loss of one or several porous cells. With laminar model, due to less diffusion process the velocity at this layer kept higher than its neighboring layers, producing spikes in the velocity profile. This disappears when using a turbulence model, as also shown in Fig. 12 and Fig. 13. The extra turbulent diffusion caused momentum exchanges in-between the layers, which smooth the velocity profiles.

In addition, the transition between the wake and the outer region is very sharp when using laminar flow model, which is not reasonable. Physically the wake region forms behind the net panel as a result of interaction between the wake of the twines and the knots. The loss of velocity in the wake occurs as a result of a loss of momentum owing to the drag force (Løland, 1993). Since the net panel was modeled as a sheet of porous media, therefore the detailed flow status in the wake was not modeled, but only the dissipation effect of the net panel was modeled, i.e. the mean flow velocity in the downstream should

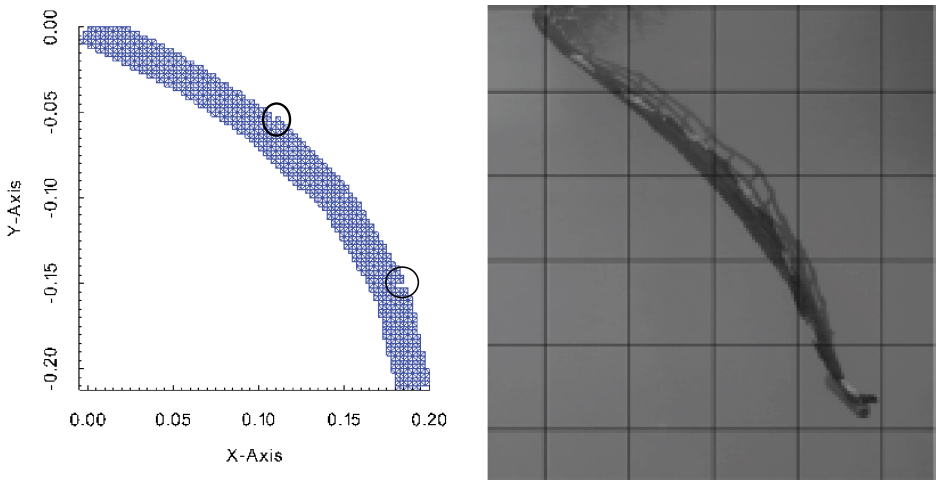

Figure 10: Comparison of the net deformation between numerical simulation (left) and experimental result (right). The right figure was reproduced from Fig. 19 in Bi et al. (2014b). The coordinate system was given in the left figure. In the right figure, each mesh has a length of 50 mm.

be described correctly. Owing to the difference of the velocity between the wake and the outer region, a transition between them took place in a thin mixture zone, which is of turbulent boundary-layer nature. Application of a conventional turbulence model (here "conventional" means the turbulence model without volume averaging) can not correctly account for the turbulence generated due to the presence of the net. Instead it was assumed that the turbulence was freely convected through the net panel, i.e. the turbulence level was the same in the upstream and downstream. But even if under this assumption, it could give a more reasonable velocity profile in the transition region. In Fig. 13(b), the transition region is smoother and thicker by using a turbulence model, due to the extra turbulent viscosity. Therefore we in general recommend to use a turbulence model. In the following work, we applied the $k-\epsilon$ model for the rest validations cases.

4.2. Submerged plane net in waves

In order to demonstrate the applicability of the numerical model in unsteady conditions, we further validated the numerical model against experiments conducted in Zhao et al. (2008) for submerged plane net in waves. This set of experiments were also carried out in Dalian University of Technology, but the dimension of the wave flume was changed to $69 \times 2 \times 1.8$ m. The water depth was set to 1.0 m, while the net was positioned 0.1 m beneath the still free surface. The plane net was made of Polyethylene and was knotted with a square mesh size of 60 mm and twine thickness of 1.8 mm. This gave a solidity ratio of 0.059. The net had a length of 0.78 m and height of 0.6 m. At the bottom a horizontal bar was attached as a sinker system. The sinker was weighted as 82 g, and the diameter was measured to be 4 mm.

We set up a 2D wave tank in order to reproduce the experiment. The general configuration of the domain is shown in Fig. 14. The toolbox developed by Jacobsen et al. (2012) was applied to generate nonlinear stream function waves. The parameters of the selected wave conditions for validation of the numerical model are given in Table 1. At two ends of the numerical wave tank, two relaxation zones were arranged to generate and absorb the waves. The length of each relaxation zone was approximately the same with the generated wave length. The net was placed in the the same position with the experiment, i.e. 0.1 m beneath the free surface, and the thickness of the porous media zone that represented the net was set to 20 mm.

A snapshot of the free surface wave and the response of the net is given in Fig. 15 for wave case 1. Furthermore, the time series of the drag force on the net panel, the surface elevation at the net position, the displacement of the net panel at bottom and middle point are depicted in Fig. 16. During the simulation, the time step was restricted with $Co = 0.1$ and $N_{structMax} = 6000$. This ensures a relatively smooth force

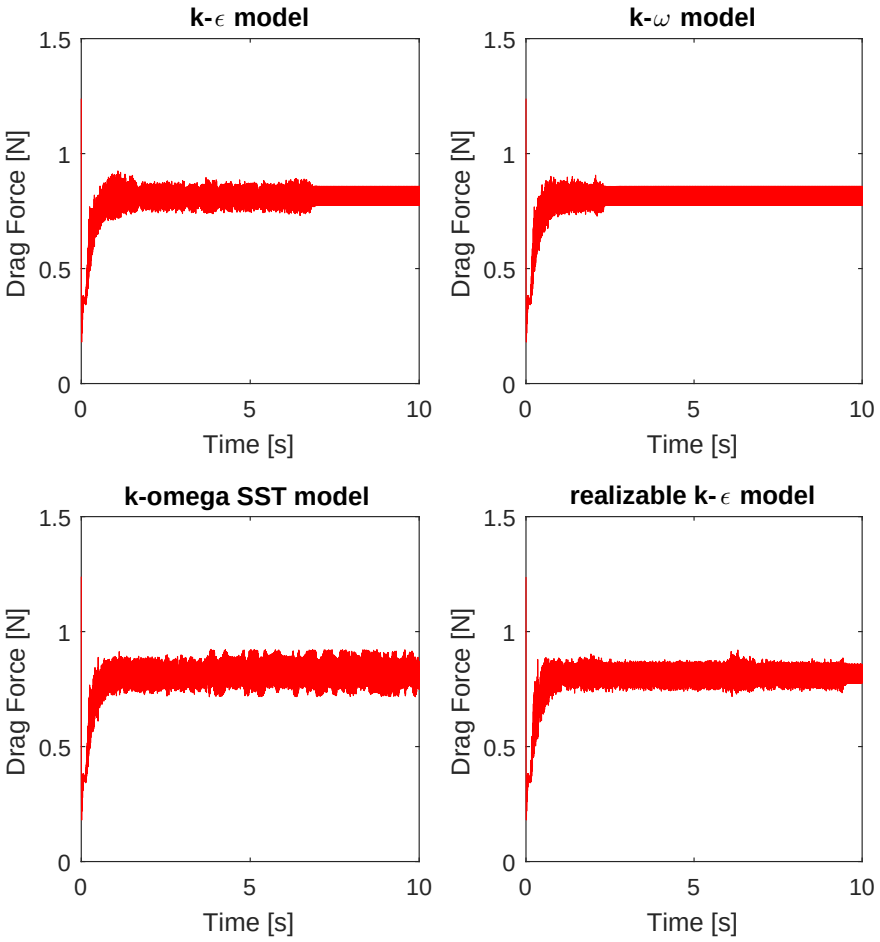

Figure 11: Time series of the drag force using different turbulence models with $Co = 0.1$, $N_{structMax} = 100$.

series. This is important since an oscillating force series may pollute the numerical result, where nonphysical deformation of the net panel may be obtained.

From Fig. 16 we observe that the surface elevation is leading before the force series, while the displacement of the net panel at middle and bottom point is lagging behind them. In principle, the crest of surface elevation creates maximum velocity. If the drag force is the dominant force on the net panel, it should be in phase with the surface elevation. However this is usually the case for forces on fixed net panels. For such kind of flexible structures, the deformation of the panel is also an important factor that affects the total force. The inertia force was believed to have minor effect on the panel, especially for such kind of low solidity ratio nets.

The amplitude of the displacement is shown in Fig. 17, where the experimental data from Zhao et al. (2008) is also given for comparison. In general we observe a better agreement for displacement at the middle point of the net panel, and the displacement at the bottom point was overestimated. One important error source from the numerical simulation is the 3D flow effect. In the numerical model the flow was 2D to save

Table 1: The parameters of the selected wave conditions for validation of the numerical model

Wave case no.	1	2	3
Wave period, T [s]	1.40	1.40	1.40
Wave height, H [m]	0.10	0.12	0.15

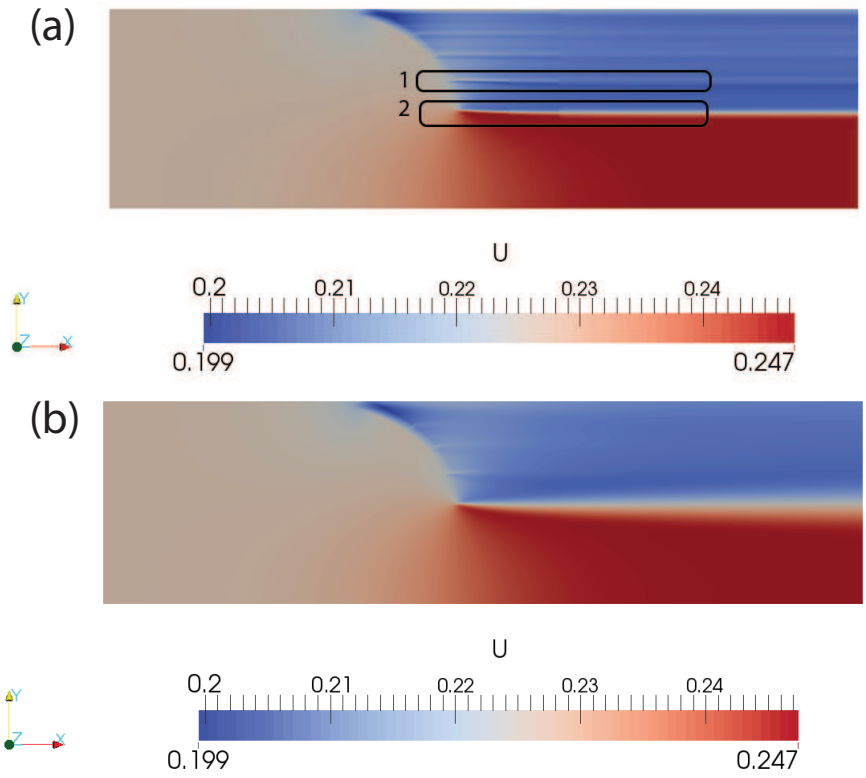

Figure 12: Snapshot of the flow field for steady flow through plane net panel. (a) using laminar model. The rounded rectangles mark the oscillation and sharp transition of the velocity field. (b) using $k - \epsilon$ model.

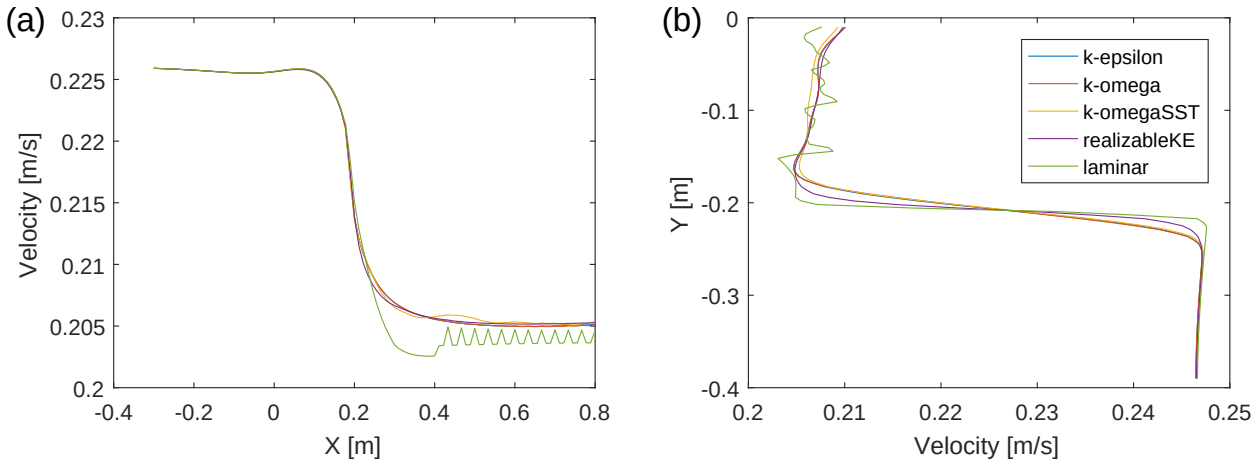

Figure 13: Sample of velocity profiles by using laminar and different turbulence models. (a) velocity profile at the horizontal line at 0.15 m below the free surface. (b) velocity profile at the vertical line at 0.5 m downstream behind the net panel.

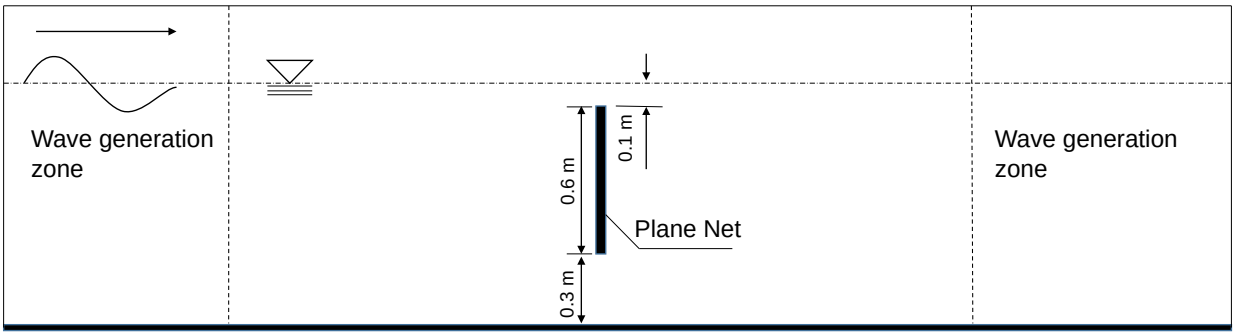

Figure 14: Sketch of the computational domain for submerged plane net in waves

the computational time. However in the experiments, the net panel is narrower than the width of the flume, therefore 3D flow effects including and tank wall effects may play a role.

4.3. Circular cages in current flow

The third validation case was carried out for 3D flow through and around circular net cages. The experiments have been described in Bi et al. (2014a), which were conducted in the same flume with the experiment described in Section 4.1. A net made from polyamides was used in the experiments, with the mesh distance $\lambda = 20$ mm and $d_w = 1.2$ mm. This gave a solidity ratio of 0.12. The net cage has a diameter of 0.254 m and depth of 0.15 m. In the circumferential direction of the cage there were 40 meshes, while in vertical direction there were 8 meshes. It was put in the steady current with velocities of 0.122, 0.178 and 0.242 m/s. The weight of the sinker for all the cases was 8 g.

The 3D numerical model was set up corresponding to the experimental setup. The sketch of the computational domain was presented in Fig. 18, where the net cage was divided into 16 panels in the circumferential direction and 5 panels in the vertical direction. The solver generated the initial configuration of the net cage based on the input parameters of the net cage, which is shown in Fig. 19. It should be mentioned that in reality, the net cage in still water is not completely vertical due to the sag in the net cage, see (Kristiansen and Faltinsen, 2015). The diameter at the lower end is approximately 10% smaller than at the top. But this effect was neglected in the present study, and the initial shape of the net cage was set vertical completely. Furthermore, Fig. 19 also presents the computational mesh, where the mesh in the net cage area was refined. This is to ensure that the porous media zones could be updated accurately. The thickness of the porous media zones was chosen to be 20 mm, and the corresponding porous resistance coefficients $C_1 = 9.16$ m^{-1}, $C_2 = C_3 = 5.67$ m^{-1}.

4.3.1. Cage deformation

The deformation of the cage is shown in Fig. 20 where comparison is given with figures from the experiments in Bi et al. (2014a). In addition, the bird view of the cage deformation is given in Fig. 21. In general the agreement is fair. However, we observe that the curvature at the front part of the cage was not modeled in a correct way, especially close to the bottom. This is due to the effect of the bottom sinker. In the experiment, it was a ring with circular cross section. But in the numerical model, the ring was not resolved by the computational mesh. Instead the forces acting on it were distributed into each lumped mass point. Therefore this modeling error induced the discrepancy of the curvature between the numerical model and the experiments. Refining the mesh can not resolve this issue.

4.3.2. Drag force and downstream velocity

Comparison of the drag force on the net cage is given in Fig. 22 for different incoming velocities. Similar to the 2D case as shown in Section 4.1.3, we found a slight but consistent 10% - 15% underestimation of the drag force, the reason is unknown yet. In addition, the downstream velocity at the measurement point

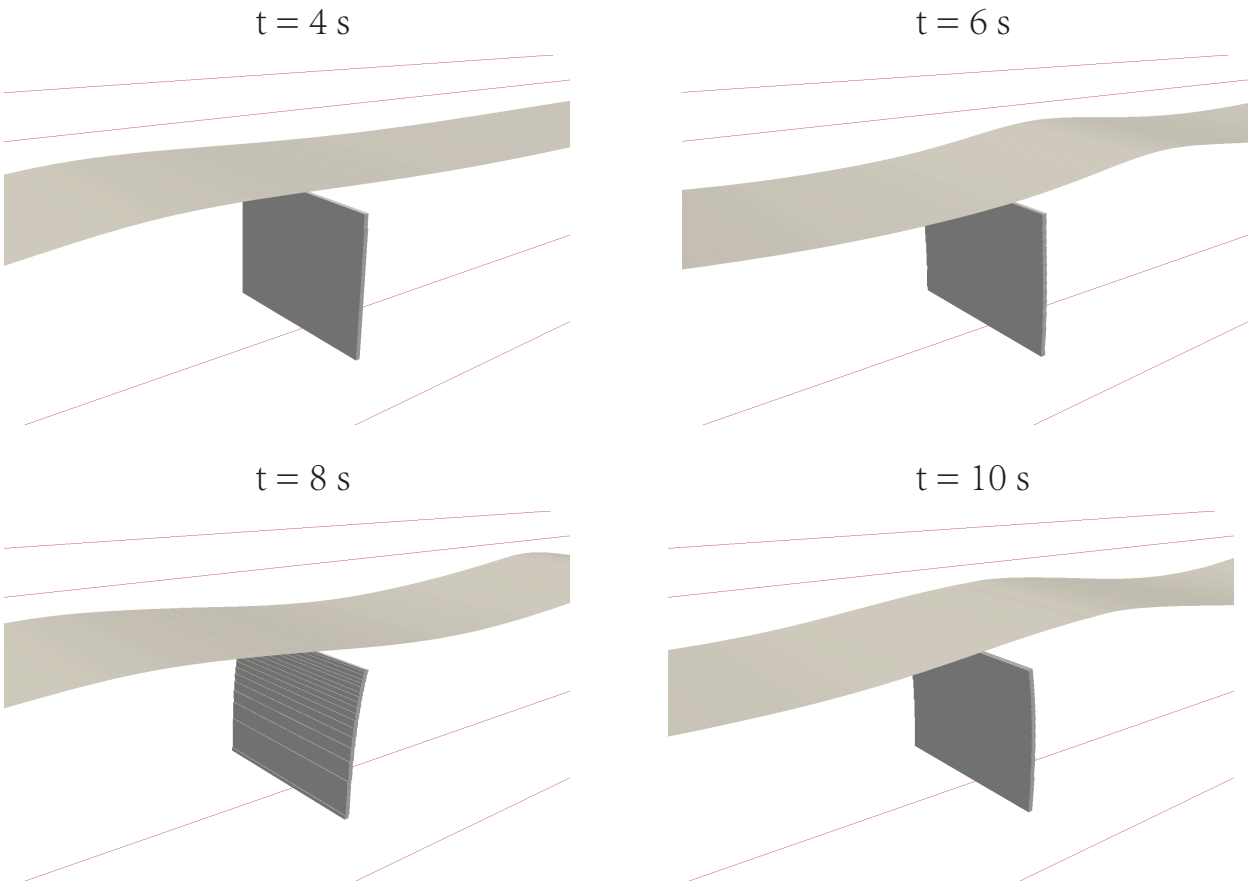

Figure 15: Snapshot of the free surface wave and the deformation of the plane net at different time for wave case 1.

(the location is given in Fig. 18) is also presented in Fig. 23. It was found that the numerical model could in general gave a better prediction on the downstream velocity. The maximum error occurs for case with $U = 0.242$ m/s, where the downstream velocity was overestimated by 9.5%.

5. Summary and conclusion

In the present work we developed a numerical model for analysis of flow through and around aquaculture net cages. The motivation to develop such a model is to consider the deformation of the net in the originally proposed porous media model. The foundation of the work is the model previously developed in Bi et al. (2014a) and Bi et al. (2014b), where the porous media model was coupled with a lumped mass structural model based on the concept of "iteration". We further improved this model by implementing an interface between these two solvers. The interaction effects between the net and the flow was fully considered, and the time stepping procedure was introduced. This enables the solver to be applied in both steady and unsteady conditions.

During the development of this model, several characteristics were noticed. The fluid solver allows a rather large time step, while the structure solver restricts it to be very small. However, the main computational burden is on the fluid sub-model. The structure sub-model takes much less time per time step. Therefore in order to reduce the computational time, the global time step was set equal to the time step for the fluid solver. Quasi steady-state condition was assumed within one time step, and sub-cycling was applied for the structural solver. However, one should be careful on the selection of the global and structural

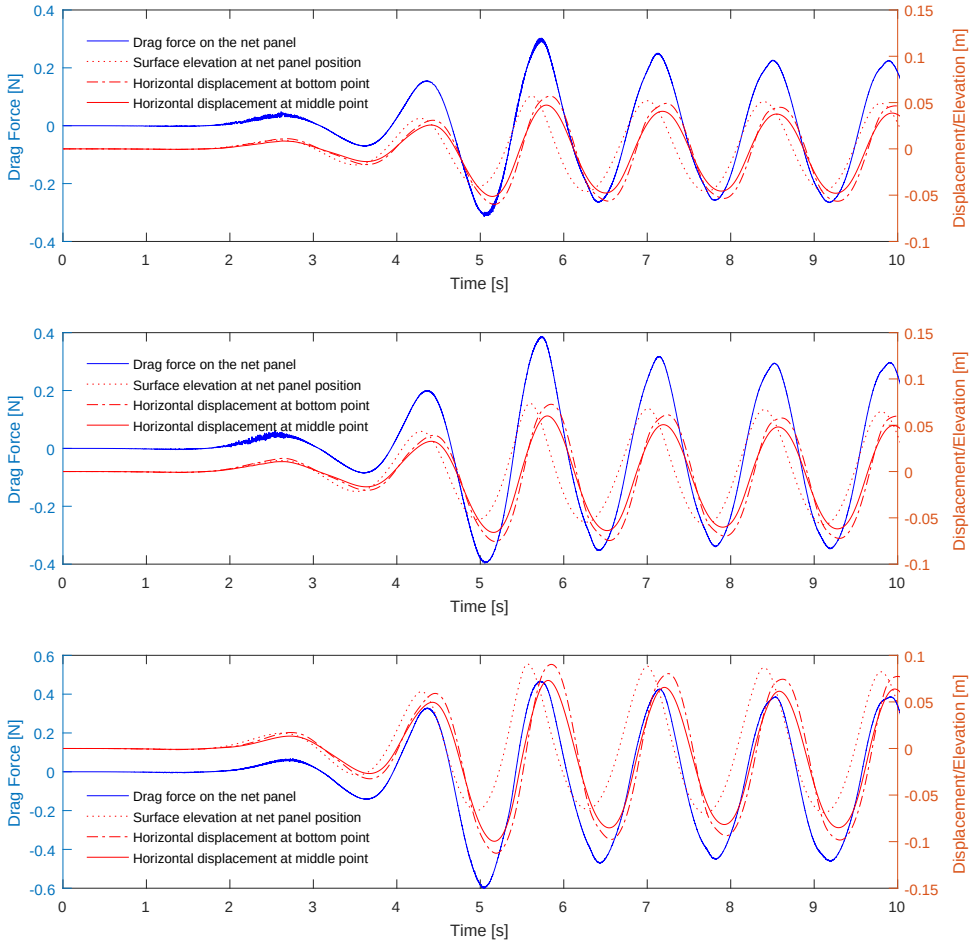

Figure 16: Examples of the time series of the drag force on the net panel, surface elevation at the net panel position, horizontal displacement of the net panel at bottom and middle point. Top: wave case 1. Middle: wave case 2. Bottom: wave case 3.

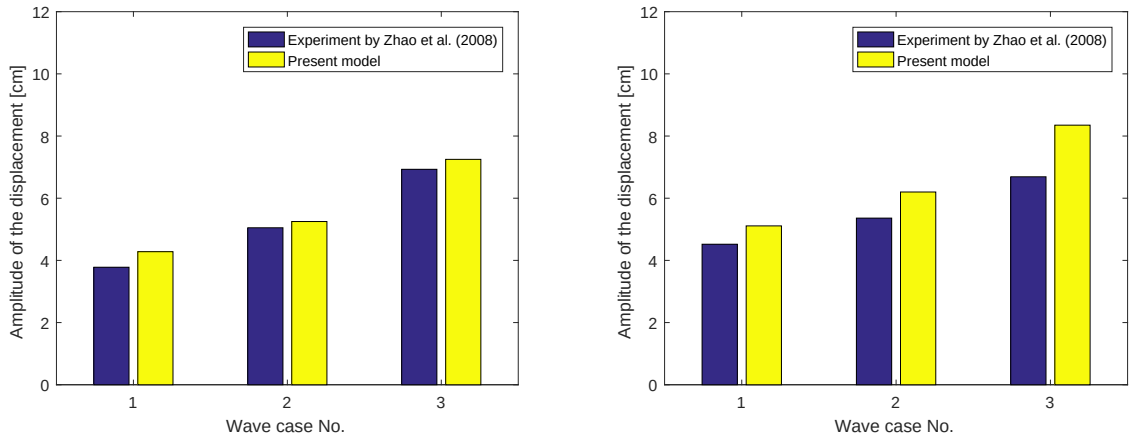

Figure 17: Comparison of the amplitude of the displacement of the net between results from the present model and experimental data from Zhao et al. (2008). Left: displacement at the middle of the net panel. Right: displacement at the bottom of the net panel.

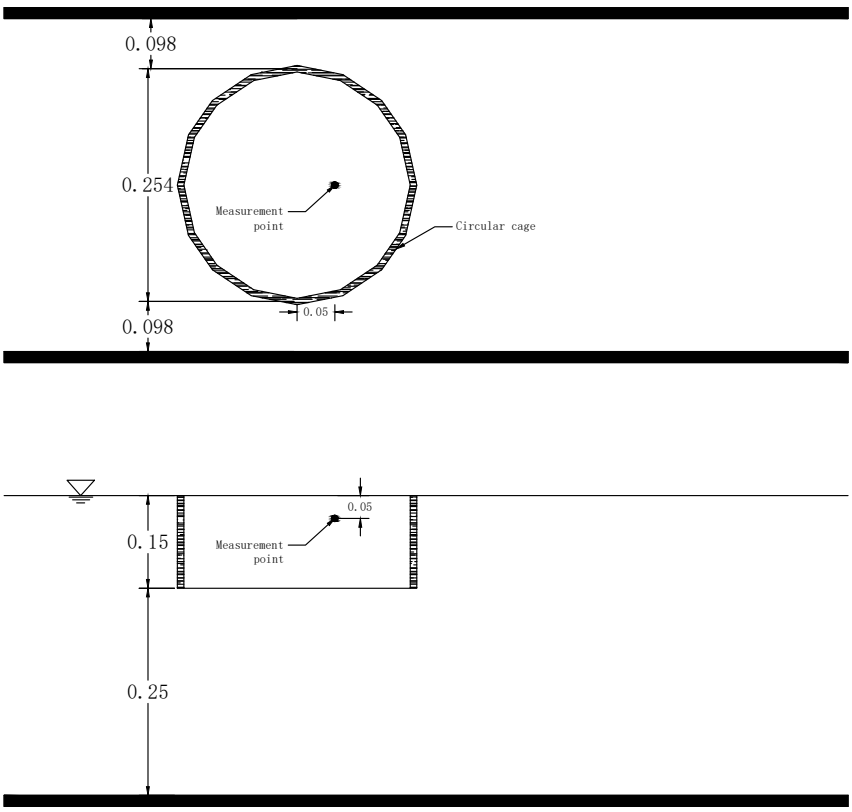

Figure 18: Sketch of the computational domain of the numerical model for flow through circular cages.

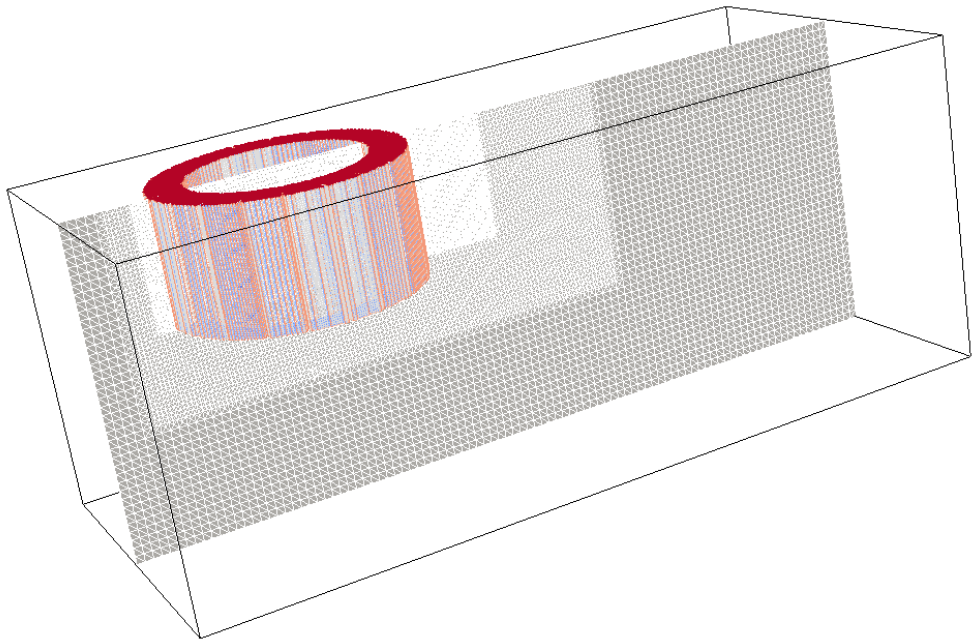

Figure 19: The initial shape of the circular fish cage and the computational mesh in the numerical model.

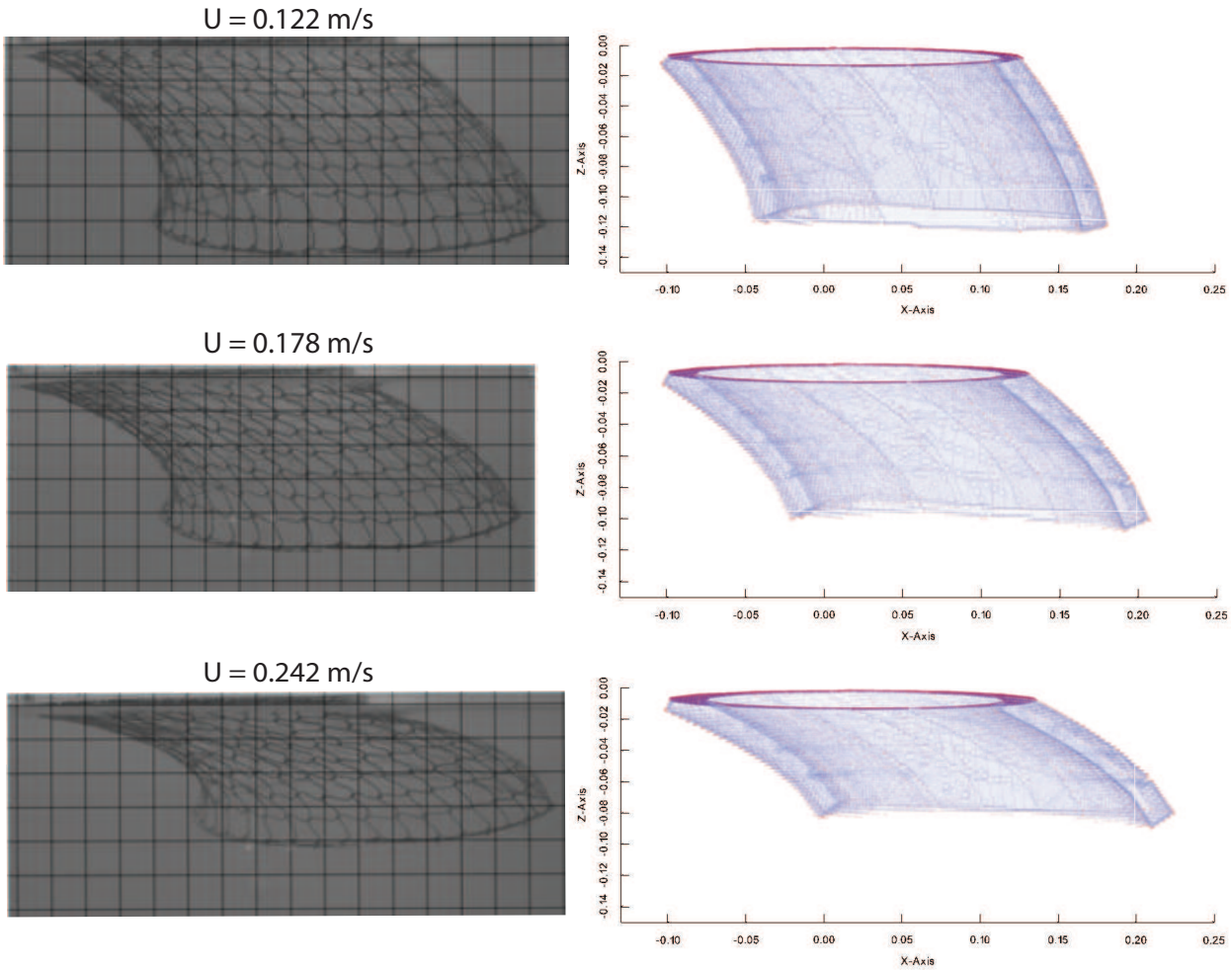

Figure 20: Comparison of the net cage deformation between the present model (right) and the experimental results (left) in Bi et al. (2014a). The experimental figures in the right were reproduced from Fig. 10 in Bi et al. (2014a), where the side length of the mesh is 25 mm.

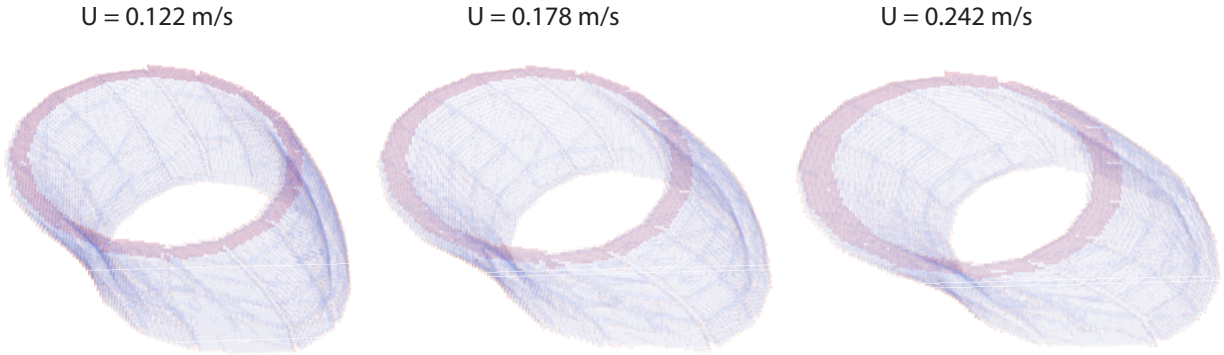

Figure 21: Bird view of the net deformation under three current velocities.

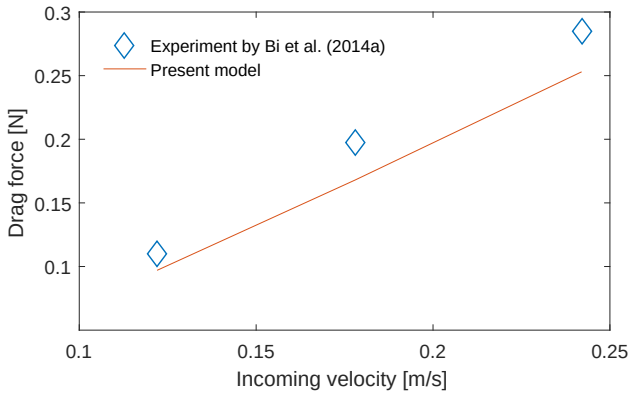

Figure 22: Comparison of the drag force between the present model and the experimental data in Bi et al. (2014a).

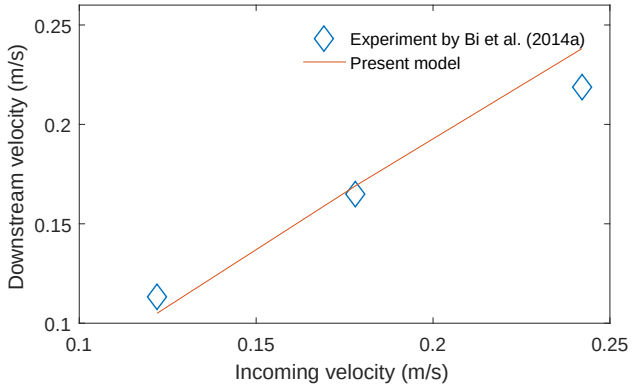

Figure 23: Comparison of the downstream velocities between the present model and the experimental data in Bi et al. (2014a).

time step. They both affect the oscillation of the time series of the load on the net structures. By properly reducing the time steps, the amplitude of the oscillation could be reduced or even eliminated.

The numerical model was validated against three sets of experiments, for plane net panel in steady current and regular waves, and for circular cages in steady current. In all the experiments, the net was top fixed and bottom weighted. The deformation of the net, the velocity at downstream and the drag forces were compared with the experimental data for plane net and circular cage in steady current. In general the agreement was fair, but we found a consistent underestimation of the drag force. For regular wave interaction with plane net panel, we compare the amplitude of the displacement at the bottom and middle of the net panel. A better prediction was given for the middle point, while at the bottom point the displacement was overestimated. We believe that 3D effect is an important reason for that.

Future work will be focused on floater-net interaction effects. The floating rings will be incorporated in the numerical model, and its rigid body motion will be solved by a six degree of freedom motion solver. Therefore the top layer of the net cages will not be fixed, but follow the motion of the ring.

Acknowledgement

The authors would like to thank Dr. Chunwei Bi from Dalian University of Technology for kindly providing the experimental data and the relative figures. Furthermore, Prof. Trygve Kristiansen from NTNU is acknowledged for the discussions on turbulent effects and for hosting the first author during the preparation of this paper. The research was partially supported by FP7-OCEAN-2011 project Innovative multi-purpose offshore platforms: planning, design and operation, MERMAID, 288710, under the call Ocean of Tomorrow.

Appendix A. Calculation of the variables used in updating the porous media zones

Calculation of variables used in 2D cases

The following part will introduce the method to calculate the distance d, α_1 and α_2. Given the coordinate the of the vertexes $\boldsymbol{x_1}$ and $\boldsymbol{x_2}$, and also the coordinate of the cell center $\boldsymbol{x}$, the length d_1, d_2 and l could be easily calculated as:

$$\begin{aligned} d_1 &= mag(\boldsymbol{x} - \boldsymbol{x_1}) \\ d_2 &= mag(\boldsymbol{x} - \boldsymbol{x_2}) \\ l &= mag(\boldsymbol{x_1} - \boldsymbol{x_2}) \end{aligned} \tag{A.1}$$

where *mag* defines the magnitude of the vector. Recalling the Pythagorean theorem, the following relation was deduced:

$$l = \sqrt{d_1^2 - d^2} + \sqrt{d_2^2 - d^2} \tag{A.2}$$

By some mathematical manipulation, the distance d was expressed as:

$$d = \sqrt{d_1^2 - \frac{1}{4l^2}\left(d_1^2 - d_2^2 + l^2\right)^2} \tag{A.3}$$

The values of $\cos\alpha_1$ and $\cos\alpha_2$ were calculated as:

$$\cos\alpha_1 = (\boldsymbol{x} - \boldsymbol{x_1}) \cdot (\boldsymbol{x_2} - \boldsymbol{x_1}) / (mag(\boldsymbol{x} - \boldsymbol{x_1}) mag(\boldsymbol{x_2} - \boldsymbol{x_1})) \tag{A.4}$$

$$\cos\alpha_2 = (\boldsymbol{x} - \boldsymbol{x_2}) \cdot (\boldsymbol{x_1} - \boldsymbol{x_2}) / (mag(\boldsymbol{x} - \boldsymbol{x_2}) mag(\boldsymbol{x_1} - \boldsymbol{x_2})) \tag{A.5}$$

With the calculated d, α_1 and α_2, one could determine if one cell was with the updated porous media zone or not.

Calculation of variables used in 3D cases

The distance d was calculated based on the normal vector of the plane $\boldsymbol{n}$, which was based on the cross product of the arbitrary two in-plane vectors, e.g. $\boldsymbol{x_1} - \boldsymbol{x_2}$ and $\boldsymbol{x_2} - \boldsymbol{x_3}$. But this normal vector has to be in the same half space with the point $\boldsymbol{x}$. Then d was calculated as

$$d = (\boldsymbol{x} - \boldsymbol{x_2}) \cdot \boldsymbol{n} \tag{A.6}$$

Therefore the perpendicular foot $\boldsymbol{x_0}$ was obtained as:

$$\boldsymbol{x_0} = \boldsymbol{x} - d\boldsymbol{n} \tag{A.7}$$

If $\boldsymbol{x_0}$ is within the triangular $x_1x_2x_3$, the total area of the triangular $x_0x_1x_2$, $x_0x_1x_3$ and $x_0x_2x_3$ should be equal to the area of the triangular $x_1x_2x_3$, where an error of machine precision was allowed. If both d and $\boldsymbol{x}_0$ satisfied the conditions, the cell was inserted into the cell zone.

References

Berberović, E., van Hinsberg, N., Jakirlić, S., Roisman, I., Tropea, C., 2009. Drop impact onto a liquid layer of finite thickness: Dynamics of the cavity evolution. Physical Review E 79, 036306. URL: http://link.aps.org/doi/10.1103/PhysRevE.79.036306, doi:10.1103/PhysRevE.79.036306.

Bi, C., Zhao, Y., Dong, G., Zheng, Y., Gui, F., 2014a. A numerical analysis on the hydrodynamic characteristics of net cages using coupled fluid-structure interaction model. Aquacultural Engineering 59, 1–12. URL: http://linkinghub.elsevier.com/retrieve/pii/S014486091400003Xhttp://www.sciencedirect.com/science/article/pii/S014486091400003X, doi:10.1016/j.aquaeng.2014.01.002.

Bi, C.W., Zhao, Y.P., Dong, G.H., Xu, T.J., Gui, F.K., 2014b. Numerical simulation of the interaction between flow and flexible nets. Journal of Fluids and Structures 45, 180–201. URL: http://linkinghub.elsevier.com/retrieve/pii/S0889974613002594, doi:10.1016/j.jfluidstructs.2013.11.015.

Chen, H., Christensen, E.D., 2016. Investigations on the porous resistance coefficients for fishing net structures. Journal of Fluids and Structures 65, 76–107. URL: http://www.sciencedirect.com/science/article/pii/S0889974615301687, doi:10.1016/j.jfluidstructs.2016.05.005.

Devilliers, M., Vincent, B., Mnassri, I., 2016. A new adaptive mesh refinement to model water flow around fishing nets. Ocean Engineering 113, 34–43. URL: http://www.sciencedirect.com/science/article/pii/S0029801815006630, doi:10.1016/j.oceaneng.2015.12.009.

Förster, C., Wall, W.a., Ramm, E., 2007. Artificial added mass instabilities in sequential staggered coupling of nonlinear structures and incompressible viscous flows. Computer Methods in Applied Mechanics and Engineering 196, 1278–1293. URL: http://linkinghub.elsevier.com/retrieve/pii/S0045782506002544, doi:10.1016/j.cma.2006.09.002.

Hou, G., Wang, J., Layton, A., 2012. Numerical Methods for Fluid-Structure Interaction - A Review. Communications in Computational Physics 12, 337–377. URL: http://www.global-sci.com/issue/abstract/readabs.php?vol=12{&}page=337{&}issue=2{&}ppage=377{&}year=2012, doi:10.4208/cicp.291210.290411s.

Hübner, B., Walhorn, E., Dinkler, D., 2004. A monolithic approach to fluid-structure interaction using space-time finite elements. Comput. Methods Appl. Mech. Engrg. 193, 2087–2104. doi:10.1016/j.cma.2004.01.024.

Hughes, J.R., Liu, W.K., Zimmermann, K., 1981. LAGRANGIAN-EULERIAN FINITE ELEMENT FORMULATION FOR INCOMPRESSIBLE VISCOUS FLOWS. Computer Methods in Applied Mechanics and Engineering 29, 249–329.

Issa, R.I., 1986. Solution of the implicitly discretised fluid flow equations by operator-splitting. J. Comput. Phys. 62, 40–65. URL: http://dx.doi.org/10.1016/0021-9991(86)90099-9, doi:10.1016/0021-9991(86)90099-9.

Jacobsen, N.G., Fuhrman, D.R., Fredsoe, J., 2012. A wave generation toolbox for the open-source CFD library: OpenFoam (R). INTERNATIONAL JOURNAL FOR NUMERICAL METHODS IN FLUIDS 70, 1073–1088. doi:10.1002/fld.2726.

Jacobsen, N.G., van Gent, M.R., Wolters, G., 2015. Numerical analysis of the interaction of irregular waves with two dimensional permeable coastal structures. Coastal Engineering 102, 13–29. URL: http://linkinghub.elsevier.com/retrieve/pii/S0378383915000836, doi:10.1016/j.coastaleng.2015.05.004.

Jensen, B., Jacobsen, N.G., Christensen, E.D., 2014. Investigations on the porous media equations and resistance coefficients for coastal structures. Coastal Engineering 84, 56–72. URL: http://linkinghub.elsevier.com/retrieve/pii/S0378383913001816, doi:10.1016/j.coastaleng.2013.11.004.

Kristiansen, T., Faltinsen, O.M., 2012. Modelling of current loads on aquaculture net cages. Journal of Fluids and Structures 34, 218–235. URL: http://linkinghub.elsevier.com/retrieve/pii/S0889974612000783, doi:10.1016/j.jfluidstructs.2012.04.001.

Kristiansen, T., Faltinsen, O.M., 2015. Experimental and numerical study of an aquaculture net cage with floater in waves and current. Journal of Fluids and Structures 54, 1–26. URL: http://linkinghub.elsevier.com/retrieve/pii/S0889974614002114, doi:10.1016/j.jfluidstructs.2014.08.015.

Lader, P., Enerhaug, B., 2005. Experimental Investigation of Forces and Geometry of a Net Cage in Uniform Flow. IEEE Journal of Oceanic Engineering 30, 79–84. URL: http://ieeexplore.ieee.org/lpdocs/epic03/wrapper.htm?arnumber=1435578, doi:10.1109/JOE.2004.841390.

Lader, P.F., Enerhaug, B., Fredheim, A., Krokstad, J., 2003. Modelling of 3D net structures exposed to waves and current, in: Proceedings of International Conference on hydroelasticity in marine technology, pp. 19–26.

Lader, P.F., Fredheim, A., 2006. Dynamic properties of a flexible net sheet in waves and current-A numerical approach. Aquacultural Engineering 35, 228–238. URL: http://linkinghub.elsevier.com/retrieve/pii/S0144860906000161, doi:10.1016/j.aquaeng.2006.02.002.

Le Tallec, P., Mouro, J., 2001. Fluid structure interaction with large structural displacements. Computer Methods in Applied Mechanics and Engineering 190, 3039–3067. URL: http://linkinghub.elsevier.com/retrieve/pii/S0045782500003819, doi:10.1016/S0045-7825(00)00381-9.

Li, Y.C., Zhao, Y.P., Gui, F.K., Teng, B., 2006. Numerical simulation of the hydrodynamic behaviour of submerged plane nets in current. Ocean Engineering 33, 2352–2368. URL: http://linkinghub.elsevier.com/retrieve/pii/S0029801806000370, doi:10.1016/j.oceaneng.2005.11.013.

Løland, G., 1993. Current forces on, and water flow through and around, floating fish farms. Aquaculture International 1, 72–89. doi:10.1007/BF00692665.

Longatte, E., Verreman, V., Souli, M., 2009. Time marching for simulation of fluidstructure interaction problems. Journal of Fluids and Structures 25, 95–111. URL: http://linkinghub.elsevier.com/retrieve/pii/S0889974608000339, doi:10.1016/j.jfluidstructs.2008.03.009.

Matthies, H.G., Steindorf, J., 2003. Partitioned strong coupling algorithms for fluidstructure interaction. Computers & Structures 81, 805–812. URL: http://linkinghub.elsevier.com/retrieve/pii/S0045794902004091, doi:10.1016/S0045-7949(02)00409-1.

Michler, C., Hulshoff, S.J., van Brummelen, E.H., de Borst, R., 2004. A monolithic approach to fluid-structure interaction. Computers and Fluids 33, 839–848. doi:10.1016/j.compfluid.2003.06.006.

Mittal, R., Iaccarino, G., 2005. Immersed Boundary Methods. Annual Review of Fluid Mechanics 37, 239–261. doi:10.1146/annurev.fluid.37.061903.175743.

Moe, H., Fredheim, a., Hopperstad, O.S., 2010. Structural analysis of aquaculture net cages in current. Journal of Fluids and Structures 26, 503–516. URL: http://linkinghub.elsevier.com/retrieve/pii/S0889974610000289, doi:10.1016/j.jfluidstructs.2010.01.007.

Patankar, S., Spalding, D., 1972. A calculation procedure for heat, mass and momentum transfer in three-dimensional parabolic

flows. International Journal of Heat and Mass Transfer 15, 1787 – 1806. URL: http://www.sciencedirect.com/science/article/pii/0017931072900543, doi:http://dx.doi.org/10.1016/0017-9310(72)90054-3.

Patursson, Ø., Swift, M.R., Tsukrov, I., Simonsen, K., Baldwin, K., Fredriksson, D.W., Celikkol, B., 2010. Development of a porous media model with application to flow through and around a net panel. Ocean Engineering 37, 314–324. URL: http://linkinghub.elsevier.com/retrieve/pii/S0029801809002406, doi:10.1016/j.oceaneng.2009.10.001.

Tsukrov, I., Eroshkin, O., Fredriksson, D., Swift, M.R., Celikkol, B., 2002. Finite element modeling of net panels using a consistent net element. Ocean Engineering 30, 251–270.

Zhao, Y.P., Bi, C.W., Dong, G.H., Gui, F.K., Cui, Y., Guan, C.T., Xu, T.J., 2013a. Numerical simulation of the flow around fishing plane nets using the porous media model. Ocean Engineering 62, 25–37. URL: http://linkinghub.elsevier.com/retrieve/pii/S0029801813000243, doi:10.1016/j.oceaneng.2013.01.009.

Zhao, Y.P., Bi, C.W., Dong, G.H., Gui, F.K., Cui, Y., Xu, T.J., 2013b. Numerical simulation of the flow field inside and around gravity cages. Aquacultural Engineering 52, 1–13. URL: http://linkinghub.elsevier.com/retrieve/pii/S0144860912000593, doi:10.1016/j.aquaeng.2012.06.001.

Zhao, Y.P., Li, Y.C., Dong, G.H., Gui, F.K., Wu, H., 2008. An experimental and numerical study of hydrodynamic characteristics of submerged flexible plane nets in waves. AQUACULTURAL ENGINEERING 38, 16–25. doi:10.1016/j.aquaeng.2007.10.004.

4 On the wave generation and interaction with fixed fish cage floaters in OpenFOAM

In preparation as:
Chen, H. & Christensen, E.D., 2017. On the wave generation and interaction with fixed fish cage floaters in OpenFOAM. To be submitted.

On the wave generation and interaction with fixed fish cage floaters in OpenFOAM

Hao Chen[a,*], Erik Damgaard Christensen[a]

[a]*Section of Fluid Mechanics, Coastal and Maritime Engineering, Department of Mechanical Engineering, Technical University of Denmark, DK-2800 Kgs. Lyngby, Denmark*

Abstract

This paper presents numerical investigations of wave generation and interaction with fixed fish cage floaters in OpenFOAM. Previously it has been reported several times that the two phase flow solver in OpenFOAM suffers from spurious current at the interface due to large density ratio between two phases. This may introduce an overestimation of wave force on horizontal cylinders at the free surface, which typically serve as fish cage floaters. In the present work, we thoroughly investigated the mathematical model, the algorithm of the solver, and different schemes provided in OpenFOAM. Series of preliminary tests were performed to examine the sensitivity of the quality of the generated waves on different applied schemes and parameters. It was found that by application of a higher order discretization scheme for the time derivative term of the transport equation for the volume fraction, the spurious current could be effectively reduced or eliminated. The transport equation itself was solved by the semi-implicit variant of multi-dimensional limiter for explicit solution (MULES) solver, where an implicit predictor was first executed followed by several explicit correctors. In order to ensure both stability and accuracy of the numerical solution, we adopted a blending scheme between Crank-Nicolson and Euler for discretization of the time derivative term. The influences of Courant number, compression coefficient and mesh resolution were also investigated in the preliminary tests, and the optimal combination of them was found. This combination of parameter settings were used in two validation cases for wave forces on partially submerged fish cage floaters. The results in general agree well with the experimental data.

Keywords: fish cage floater, OpenFOAM, nonlinear wave-structure interaction, spurious current

1. Introduction

The global aquaculture industry was expanding fast during last few decades, and since mid 1990s it has been the engine driving growth in total fish production as global capture has leveled off. However, this fast expanding faces challenges, primarily the space limitations of the sheltered areas, where nearshore aquaculture competes with other usages, e.g. recreational activities. This is driving the need to move aquaculture to more exposed sites, and the significant wave height is up to 3 m according to Kristiansen and Faltinsen (2008). Under such sea state, the structural collapse of fish cage floaters becomes more severe, and overtopping of waves may result in escape of fish. Thus a precise prediction of wave induced effects on floaters is of vital importance.

Wave interaction with cylindrical structures has been a traditional research topic in marine hydrodynamic field, and there exits considerable publications, especially for vertical surface piercing cylinders, *e.g.* Liu et al. (2001), Molin (1979), Chau and Eatock Taylor (1992), Eatock Taylor and Hung (1987) Bai and Eatock Taylor (2007) and Park et al. (2003). Particular interests are on the topics of wave induced linear and nonlinear hydrodynamic forces, and the disturbances produced by the cylinder on the wave field. However,

*Corresponding author, tel.: (45) 50302416; e-mail address: hchen@mek.dtu.dk

Nomenclature

α	volume fraction field
$\boldsymbol{\tau}$	the deviatoric stress tensor field
$\boldsymbol{F}$	wave induced force on the floater
$\boldsymbol{g}$	gravitation acceleration
$\boldsymbol{n}$	unit normal vector of the interface
$\boldsymbol{n}_f$	unit normal vector of the cell face
$\boldsymbol{S}_f$	cell face vector, with its magnitude equal to the area of the face and direction equal to the normal direction of the face
$\boldsymbol{T}$	the total stress tensor field
$\boldsymbol{u}$	center of mass velocity field
$\boldsymbol{u}_r$	the compression velocity field
$\boldsymbol{v}$	center of volume velocity field
$\boldsymbol{x}$	the Cartesian coordinate system where $\boldsymbol{x} = (x, y, z)$, where x is along the direction of wave propagation, y is in the upward direction.
Δt	time step size
η	surface elevation
κ_α	averaged curvature of the interface
λ	the limiter in MULES solver
$\mathbb{R}$	the explicit reconstruction of cell center value from cell face value
$\mathcal{A}$	the linear algebraic equation resulted from discretization of the momentum equation with only the time derivative term, the convection and diffusion terms
$\mathcal{A}_A$	the coefficient matrix part of $\mathcal{A}$
$\mathcal{A}_D$	the diagonal part of $\mathcal{A}_A$
$\mathcal{A}_H$	the H operator defined as $\mathcal{A}_H = \mathcal{A}_S - \mathcal{A}_N\boldsymbol{u} = \mathcal{A}_D\boldsymbol{u}$
$\mathcal{A}_N$	the off-diagonal part of $\mathcal{A}_A$
$\mathcal{A}_S$	the source part of $\mathcal{A}$
μ	dynamic viscosity field
ω	wave frequency
Φ	the mass flux defined as $\Phi = \rho\boldsymbol{u}_f \cdot \boldsymbol{S}_f$
ϕ	the volumetric flux defined as $\phi = \boldsymbol{u}_f \cdot \boldsymbol{S}_f$
ϕ_r	the volumetric flux for the compression term in α equation, defined as $\phi_r = \boldsymbol{u}_{r,f} \cdot \boldsymbol{S}_f$
ρ	density field
ρ_w	density of water
σ_T	surface tension constant
θ	off-centered coefficient
C_α	the compression coefficient
Co	Courant number
D	diameter of the floater
d_w	still water depth of the numerical wave tank
E_k	total kinetic energy of wave
E_p	total potential energy of wave
f	Fourier amplitude of the wave force
f_n	the face unit flux
F_{AD}	the anti-diffusive total flux for the convection term in α transport equation, defined as $F_{AD} = F_{HO} - F_{BD}$
F_{BD}	the first order bounded total flux for the convection term in α transport equation, defined as $F_{BD} = (\phi\alpha_f)$ where α_f was descritized by first order upwind scheme
F_{HO}	the high order total flux for the convection term in α transport equation, defined as $F_{HO} = (\phi + \phi_r)\alpha_f$ where α_f was descritized by some high order scheme
H	wave height
k	wave number
l	length of the floater
p	excess pressure field
Q_+	the absolute value of the allowed incoming flux for a cell to reach the local maximum
Q_-	the allowed outgoing flux for a cell to reach the local minimum
T	wave period
V^{cell}	volume of the grid cell
V_{water}	total amount of water volume

the information on horizontal cylinders is relatively sparse, especially for the case of partially submerged cylinders. It is well known that wave forces on fully submerged slender structures can be calculated by Morison equation proposed in Morison et al. (1950), based on the assumption that the diameter of the structure is small and does not disturb the incident wave field. Dixon et al. (1979) modified it by adding a time-varying displacement term, to make it capable of predicting forces on partially submerged cylinders. It agreed well with the experimental results for small amplitude waves, but was starting to deviate for steep waves. Easson et al. (1985) expanded this method with application to random sea conditions.

For large bodies, whose presence alters the incident wave system significantly, Morison equation can not produce a satisfying result any more. It is generally accepted that the diffraction effect becomes important when the ratio between diameter of the structure and wave length is larger than 0.2 (Sumer and Fredsøe (1997)). Under this condition potential flow theory is used, since the Keulegan-Carpenter (KC) number is usually smaller than two and flow around the body is not separated. There exists a few analytical solutions based on diffraction theory for wave forces on either submerged or partially submerged horizontal cylinders. Dean (1948), Ursell (1950a) and Ursell (1950b) are the earliest works on submerged horizontal cylinders, where the linear diffraction problem was formulated and solved by the multipoles method. A remarkable fact was found that there was no reflection from the cylinder. The transmitted wave had the same amplitude as the incident wave, but with a phase shift in passing the cylinder. Mehlum (1980) applied some certain recursive relations on the problem and the same conclusion was drawn. In Ogilvie (1963) the second order wave forces on a submerged horizontal cylinder was obtained by applying the same method with Ursell (1950a). Wu and Taylor (1990) generalised the analysis of Ogilvie (1963) to finite water depth. For partially submerged cylinders, Martin and Dixon (1983) solved the linear diffraction problem and compared the analytical solution with experimental results. Discrepancies were observed for forces induced by steep waves due to the nonlinear effects.

Fish cage floaters are characterized as partially submerged slender cylinders in the free surface zone. The typical diameter of a floater could be in the order of 0.5 m to 2 m, which is usually much smaller than the wave length. However, from Martin and Dixon (1983), even for a cylinder with diameter of 0.1 m, the experiments show that the reflection coefficient could reach 0.3 for a incoming wave train with $H = 0.01$ m, $T = 1$ s, which gave a wave length of $L = 1.5$ m. Therefore we believe that diffraction may play an important role under many conditions when the wave length is not sufficiently large. Meanwhile, when the incoming wave train becomes steep, the resulted wave system due to presence of the cylinder at free surface could be highly nonlinear, where violent motion of free surface may occur, e.g. local breaking or overtopping. This indicated that viscous effect may also be important. Hereby in the present paper in order to handle such cases, it was decided to use a Computational Fluid Dynamic (CFD) solver with a free surface model, instead of a single value free surface solver.

Previously different methods have been proposed to track the interface of free surface flow. This includes e.g. height function method and line segment method, which are the simplest techniques to represent and configure a free surface. However they have difficulties when two surfaces intersect or when a surface folds over on itself. These difficulties were overcome by the marker and cell (MAC) method proposed in Harlow and Welch (1965), where the interface was tracked by massless particles in a Lagrangian manner. It has been used in e.g. Christensen and Deigaard (2001) for simulating breaking waves. Alternatively the level set method or volume of fluid method could be used to implicitly capture the surface in an Eulerian way. The level set (LS) method was introduced in Osher (1988) where the interface was defined as the one on which a level-set function is equal to zero. This level set function is continuous across the interface, therefore is not significantly influenced by the numerical diffusion. However the original proposed level set method suffered from mass conservation problems. This issue has been resolved in e.g. Olsson and Kreiss (2005) and Olsson et al. (2007), and it was also used in Filip (2013) for high-resolution simulation of turbulent interfacial marine flows.

The volume of fluid (VOF) method proposed by Hirt and Nichols (1981) uses local volume fraction of the phases to evolve the interface. Only one scalar convective equation needs to be solved to propagate the volume fraction. But one of the critical issues for VOF method is to discretize this equation with a proper convection scheme. First order upwind scheme can maintain the boundness of the scalar but smears the interface due to numerical diffusion. Meanwhile, high order schemes may lead to overshooting and

undershooting of the scalar field. Attempts have been made to alleviate this issue by e.g. donor-acceptor scheme in Hirt and Nichols (1981), CICSAM in Ubbink and Issa (1999), or FCT in Boris and Book (1973) and Zalesak (1979). Christensen (2006) adopted the concept of VOF method in his CFD solver for large simulation of spilling and plunging breakers. In his model CICSAM scheme was employed to solve the volume fraction transport equation. This automatically satisfied the kinematic boundary condition for the free surface. From the volume fraction of each cell the free surface was reconstructed and the dynamic boundary condition was assigned to the free surface boundary.

The Open source CFD toolbox OpenFOAM is gaining popularity recently and it includes a variety of solvers with application to chemistry reactions, combustion engines etc. The VOF based solver in OpenFOAM, called *interFoam*, has been successfully applied in many multiphase flow modelling cases. This is underpinned by the development of the multi-dimensional limiter for explicit solution (MULES) solver as a very effective method of guaranteeing boundedness of volume fraction. Recently it was introduced in the coastal and ocean engineering field, where the utilities for generation and absorption of free surface waves have been developed and released in e.g. Jacobsen et al. (2012) and Higuera et al. (2013). Under this modeling framework, significant success has been achieved on regular and irregular wave interaction with a vertical bottom mounted cylinder from intermediate to deep water, as shown in Chen et al. (2014) and Paulsen et al. (2014).

However, although both employed VOF free surface model, *interfoam* solver and the solver in Christensen (2006) are fundamentally different. In Christensen (2006) by assigning the dynamic boundary condition on the free surface, the air phase was neglected and the numerical model was transformed to a single phase system. But in *interFoam* solver, both phases were retained and solved by one set of governing equations. This gives the possibility to simulate the cases where air-entrainment is important, but arises the problem that spurious current in the transition region between two phases may be generated when the density ratio is large, as reported in Wroniszewski et al. (2014). This is not a unique phenomenon that only occurs in gravity wave simulations. It was also observed by several authors in surface tension simulations, e.g. Francois et al. (2006), Hoang et al. (2013) and Scardovelli and Zaleski (1999). Generation of this spurious current at the interface is not due to external forces but solely numerical issues. For surface tension dominant flow, this is induced by the error in calculation of interface curvature. For inertia dominant flow such as gravity waves, the error in evaluation of density gradient term plays an important role. When simulating wave interaction with fish cage floaters in the free surface zone, this effect will be amplified since a large part of the immersed area is in the vicinity of the free surface.

The objective of the present work is to find a set of parameters and schemes in OpenFOAM to reduce this spurious current to an acceptable level, and validate the numerical model with the experimental data for wave load on partially submerged fish cage floaters. The modeling framework is OpenFOAM-2.4.0. The remaining of the paper is organized as follows. In Section 2, the governing equations for the VOF formulation of the two-phase flow systems is derived formally from the local instant formulation. Section 3 gives a detailed description the solver. This includes the implementation of both PISO algorithm and MULES solver. In Section 4 series of preliminary tests are conducted to investigate the sensitivity of spurious current velocity on different applied schemes and parameters. The best combination of these schemes and parameters are used to validate the numerical model in Section 5, for wave load on fixed fish cage floaters from non-steep to steep but non-breaking regular waves. Finally the conclusions are drawn in Section 6.

2. Description of the numerical model

2.1. Governing equations

For a typical two phase flow system, the most fundamental and standard formulation is the local instant formulation, where the mass and momentum conservation equations are the governing equations for each single phase with a proper jump condition across the moving interface. Any macroscopic formulations of the two phase flow system including VOF formulation should be derived based on this. In the present paper, the detailed derivation process is given in Appendix A, and below only the final governing equations are given:

$$\nabla \cdot \boldsymbol{u} = 0 \tag{1}$$

$$\frac{\partial \rho \boldsymbol{u}}{\partial t} + \nabla \cdot (\rho \boldsymbol{u})\boldsymbol{u} - \nabla \cdot [\mu(\nabla \boldsymbol{u})] = -\nabla p - (\boldsymbol{g} \cdot \boldsymbol{x})\nabla \rho + \sigma_T \kappa_\alpha \nabla \alpha \tag{2}$$

From the derivation in Appendix A, the variables in Eq. (1) and Eq. (2) were clearly linked to the variables in the local instant formulations, which clarifies their physical meanings. In addition, several important characteristics were noticed in the derivation, and they were summarized here: (1) In the context of VOF formulation, the two phase system was treated as a mixture, where only one set of governing equations were applied on this mixture fluid system. Therefore it is sometimes called one-fluid method. (2) The density and viscosity etc., which were usually constant in single phase flow, are non-constant scalar fields for the mixture fluid. But from a Lagrangian point of view, their substantial derivatives are zero. (3) The interface between two phases is sharp and long-scale, which could be resolved by the computational mesh. Therefore the velocity profile is continuous across the interface, indicating that the slip velocity between two phases is null. This condition eliminates some terms e.g. complex momentum transfer between two phases, and results in Eq. (1) and Eq. (2) as the governing equations for the system. (4) The velocity field for the mixture fluid still satisfies divergence free condition. This has already been demonstrated in Appendix A. Since *interFoam* solver is a segregated pressure-based solver, this is an important condition for the solver to formulate pressure equation.

It should be mentioned that in the present work, turbulence effects were neglected and a laminar model was used. This is due to the reason that the main contributions to the nonlinear wave forces on the floater come from the inertia and free surface effect. Turbulence effect plays a minor role since it is still in the inertia dominant regime, see Sumer and Fredsøe (1997).

2.2. Free surface model

In VOF method, the evolution of the phase fraction was governed by the advection equation under the velocity field $\boldsymbol{u}$:

$$\frac{\partial \alpha}{\partial t} + \nabla \cdot \boldsymbol{u}\alpha = 0 \tag{3}$$

As mentioned in Section 1, the main difficulty for solving Eq. (3) lies on the discretization schemes. Application of improper schemes may result in unbounded solution or numerical diffusion. The solution algorithm of Eq. (3) in OpenFOAM will be illustrated in detail in Section 3.2.

2.3. Wave generation and absorption

In order to generate and absorb waves at the inlet and outlet of the numerical wave tank, the utility waves2Foam developed by Jacobsen et al. (2012) was adopted in the numerical model. This is a generic wave generation and absorption toolbox where a variety of wave theories are available. Explicit relaxation zones have been implemented to avoid reflection of waves from outlet boundaries and further to avoid waves reflected internally in the computational domain to interfere with the wave-maker boundary:

$$\psi = \alpha_R \psi_{computed} + (1 - \alpha_R)\psi_{target} \tag{4}$$

where ψ is either $\boldsymbol{u}$ or α. ψ_{target} is the quantities given by wave theories while $\psi_{computed}$ is the computed velocity. In the present work throughout all the computations, the generated waves were based on the stream function wave theory given by Fenton (1988). α_R is the relaxation function defined as:

$$\alpha_R(\chi_R) = 1 - \frac{\exp(\chi_R^{3.5} - 1)}{\exp(1) - 1} \tag{5}$$

where χ_R is the local coordinate and it is always between 0 and 1.

2.4. Post-processing and data manipulation

2.4.1. Extraction of surface elevation

In the numerical model the surface elevation was captured implicitly, hereby the position of free surface was not known. A native utility included in waves2Foam extracts the surface elevation η in the following manner:

$$\eta = \int_{y_{\alpha=1}}^{y_{\alpha=0}} \alpha \, \mathrm{d}y - y_{\alpha=1} \tag{6}$$

where the integration of volume fraction was performed in a vertical line, and the free surface must be located in between the integration limits, i.e. $y_{\alpha=0}$ and $y_{\alpha=1}$. Eq. (6) expressed the position of free surface as height of the water column above the level $y_{\alpha=1}$.

2.4.2. Computation of wave force

Wave induced force on the floater $\boldsymbol{F}$ was resulted from the pressure p and viscous stress $\boldsymbol{\tau}$. In the numerical model the force was directly integrated from the pressure and viscous stress over the instantaneous wet surface S_b as:

$$\boldsymbol{F} = -\int_{S_b} p\boldsymbol{n}_b \, \mathrm{d}S - \int_{S_b} \boldsymbol{\tau} \cdot \boldsymbol{n}_b \, \mathrm{d}S \tag{7}$$

where $\mathbf{n}_b$ is the unit normal vector of the floater, pointing to the fluid domain. The Fourier amplitudes at the fundamental and higher order were obtained by transforming the integrated forces from time domain to frequency domain:

$$f^{(j)} = \left| \frac{2}{T'} \int_t^{t+T'} \boldsymbol{F}(\tau) e^{\mathrm{i}j\omega\tau} \mathrm{d}\tau \right| \tag{8}$$

where $f^{(j)}$ is the amplitude of jth harmonic, T' is the time interval over which the harmonic force is determined. In this paper T' is the time interval of at least five wave periods after the computation reaches steady state.

2.4.3. Extraction of total water volume, potential and kinetic energies for the propagating waves

In Section 4, three quantities were used to examine the mass and energy conservation property of the generated waves, namely the total water volume, total potential and kinetic energy. The total amount of water volume V_{water} in the computational domain was calculated based on the volume fraction α at each cell i:

$$V_{water} = \sum_{i=1}^{K} \alpha_i V_i^{cell} \tag{9}$$

where K is the number of cells in the computational grid. The total kinetic energy of the propagating waves E_k was calculated as:

$$E_k = \frac{1}{2} \sum_{i=1}^{K} \rho_i \alpha_i \boldsymbol{u}_i^2 V_i^{cell} \tag{10}$$

The total potential energy E_p was determined based on the position of free surface waves:

$$E_p = \frac{1}{8} \rho_w g \sum_{i=1}^{M-1} (\eta_i + \eta_{i+1})^2 (x_{i+1} - x_i) \tag{11}$$

where the free surface position was defined by M points (x_i, η_i).

3. The algorithm of the solver

In OpenFOAM the cell centered finite volume method was used to discretize the Navier-Stokes equations on unstructured mesh. In order to avoid checkerboard oscillation, the discretization follows the spirit of Rhie and Chow interpolation (Rhie and Chow, 1983). The overall algorithm includes two parts, namely MULES algorithm for solution of Eq. (3) and the pressure implicit with splitting of operator (PISO) algorithm (Issa, 1986) for velocity-pressure coupling. The are presented in Section 3.1 and 3.2, respectively. The overall algorithm could be summarized as:

1. Solve the transport equation for the volume fraction field α.
2. Correct the fluid and interface properties.
3. Solve the momentum equation using the pressure from the previous time step (Momentum Prediction).
4. Formulate the pressure equation and loop through the velocity correctors (Pressure Solution and Velocity Correction).

3.1. Pressure-velocity coupling

The main issues that need to be resolved in solving the N-S equations are the nonlinear convection term in Eq. (2) and the velocity-pressure coupling. A fundamental assumption on PISO algorithm is that under the condition of low Courant number (small time step), the pressure-velocity coupling is much stronger than the nonlinear coupling. Therefore the nonlinear term was linearized, i.e. $\nabla \cdot \boldsymbol{u}\boldsymbol{u} = \nabla \cdot \boldsymbol{u}_o \boldsymbol{u}_n$, where n denotes the current time step and o denotes the old time step. Then the discretization of momentum equation was safely frozen through a series of explicit correctors. This indicated that the velocity field was corrected in an explicit way, i.e. assume that the velocity error comes only from the pressure term, and the corrections due to transported influence of the neighbouring velocities were neglected. This will be illustrated in details in the following. Actually a general description on the implementation of PISO algorithm has been documented in Jasak (1996). However one should note that in the present work, in Eq. (2) there exists body forces such as surface tension and gravity forces. Attention should be paid on evaluation of these forces.

In the following work we adopted the notation in Weller (2002), which is designed for finite volume method. This notation avoids the possible ambiguity in the discretisation practice. Here we just briefly summaries the key points of the notation: (1) In an arbitrary equation, each term could be discretized explicitly or implicitly. (2) The discretised term arising from an implicit operator $\mathcal{L}$ is denoted as $[\![\mathcal{L}[\phi]]\!]$. (3) Explicit terms are not put into the bracket.

Denote the system of linear algebraic equations from discretization of the momentum equations with only the time derivative term, the convection and diffusion terms as:

$$\mathcal{A} := \left[\!\!\left[\frac{\partial \rho[\boldsymbol{u}]}{\partial t} \right]\!\!\right] + [\![\nabla \cdot (\Phi[\boldsymbol{u}]_f)]\!] - [\![\nabla \cdot (\mu \nabla[\boldsymbol{u}])]\!] \tag{12}$$

where the subscript f denotes the value at cell face. Note that for the convective term, we directly introduce the mass flux Φ in the notation, where $[\![\nabla \cdot (\Phi[\boldsymbol{u}]_f)]\!] = \sum_f \Phi \boldsymbol{u}_f$. $\mathcal{A}$ contains full linear system equations including the matrix $\mathcal{A}_A$ and the source term $\mathcal{A}_S$. Several useful operators based on $\mathcal{A}$ should be clarified here to conveniently extract the matrix coefficients : (1) The D operator $\mathcal{A}_D$ is the diagonal part of the matrix $\mathcal{A}_A$. (2) The N operator $\mathcal{A}_N$ is the off-diagonal part of $\mathcal{A}_A$. (3) The H operator defined as $\mathcal{A}_H = \mathcal{A}_S - \mathcal{A}_N \boldsymbol{u} = \mathcal{A}_D \boldsymbol{u}$. By analysis of matrix structure, it could be seen that this H operator includes contributions from the neighboring cells and also the source part.

3.1.1. Derivation of pressure equation

An important characteristic for incompressible fluid flow is that the density is constant and decoupled with the pressure. Therefore the equation for mass conservation becomes a scalar constraint on the velocity field, i.e. Eq. (1). Meanwhile, in N-S equations, the equation for the pressure field does not explicitly exist. Hence the first step here is to recast the continuity equation into an explicit equation for pressure.

The starting point for the derivation here is the semi-discretized form of Eq. (2). At this stage the pressure was not discretized, and application of this semi-discretized form can keep the discretization of the

derived pressure equation consistent with the momentum equation. With the operators defined above, the semi-discretized form of Eq. (2) was reformulated as:

$$\mathcal{A}_D \boldsymbol{u} = \mathcal{A}_H - \nabla p - (\boldsymbol{g} \cdot \boldsymbol{x}) \nabla \rho + \sigma_T \kappa_\alpha \nabla \alpha \tag{13}$$

From Eq. (13) the cell centered velocity was expressed as:

$$\boldsymbol{u} = \frac{\mathcal{A}_H}{\mathcal{A}_D} + \frac{1}{\mathcal{A}_D}(-\nabla p - (\boldsymbol{g} \cdot \boldsymbol{x}) \nabla \rho + \sigma_T \kappa_\alpha \nabla \alpha) \tag{14}$$

Invoking Eq. (14) into Eq. (1), the pressure equation was obtained:

$$\nabla \cdot \left(\frac{1}{\mathcal{A}_D} \left(\nabla p + (\boldsymbol{g} \cdot \boldsymbol{x}) \nabla \rho - \sigma_T \kappa_\alpha \nabla \alpha \right) \right) = \nabla \cdot \left(\frac{\mathcal{A}_H}{\mathcal{A}_D} \right) \tag{15}$$

3.1.2. Momentum Prediction

We start from the momentum prediction step. At this step, the momentum equation was discretized and solved with the pressure field and conservative flux from the last time step. The discretized momentum equation was written as:

$$\mathcal{A} = \mathbb{R}\llbracket |\boldsymbol{S}_f| \left((\sigma_T \kappa_\alpha)_f \nabla_f^\perp \alpha - (\boldsymbol{g} \cdot \boldsymbol{x})_f \nabla_f^\perp \rho - \nabla_f^\perp p \right) \rrbracket \tag{16}$$

where $\nabla_f^\perp$ is the surface normal gradient evaluated at cell face. $\mathbb{R}\llbracket \cdot \rrbracket$ is explicit reconstruction of the cell center value from the cell face value. Note that the transport equation was solved before the momentum equation, therefore the density field and the volume fraction field at the current time step were known values. However the pressure field was unknown and taken from the last time step.

From Eq. (16) it was observed that the pressure gradient and the body forces were not directly evaluated as source terms using Gauss theorem, which may cause unphysical spikes in the velocity field when the density ratio is large in multiphase flow systems (see Mencinger and Žun (2007) and Zhang et al. (2014)). By first interpolating these terms onto cell faces, and then reconstructing to the cell centers, the body force field was smoothed and the defects was effectively eliminated. The detail of this reconstruction procedure is illustrated in Appendix B, where it has been demonstrated that it is second order accurate.

Solution of Eq. (16) is an intermediate velocity field $\boldsymbol{u}^*$, which does not satisfy divergence free condition. Then the volumetric flux ϕ^*, defined as $\boldsymbol{u}_f^* \cdot \boldsymbol{S}_f$, was calculated based on Eq. (14):

$$\phi^* = \left(\frac{\mathcal{A}_H}{\mathcal{A}_D} \right)_f \cdot \boldsymbol{S}_f + \left(\frac{1}{\mathcal{A}_D} \right)_f |\boldsymbol{S}_f| \left((\sigma_T \kappa_\alpha)_f \nabla_f^\perp \alpha - (\boldsymbol{g} \cdot \boldsymbol{x})_f \nabla_f^\perp \rho \right) + \phi_e \tag{17}$$

Here several comments are given on the flux calculation: (1) In OpenFOAM, the flux is the primary variable in OpenFOAM representing the velocity field, which should be conservative. The cell-centered velocity field is merely regarded as a secondary variable, used in the construction of the momentum equation (Rusche, 2002). This actually also mimics the staggered grid arrangement since the flux is always defined at cell faces and has a tight pressure gradient stencil similar from a staggered grid formulation. (2) In Eq. (17), the flux ϕ^* does not contain any contribution from pressure. Indeed the contribution from pressure was added after the pressure solution was obtained. This could also be regarded as an implicit representation of Rhie and Chow interpolation (Karrholm, 2008). (3) It contains an extra contribution ϕ_e, which is undocumented. ϕ_e was expressed as:

$$\phi_e = \frac{\gamma \rho}{\mathcal{A}_D \Delta t} \left(\phi_o - \boldsymbol{S}_f \cdot \boldsymbol{u}_{f,o} \right) \tag{18}$$

where γ is the coupling coefficient:

$$\gamma = 1 - \min \left(\frac{|\phi_o - \boldsymbol{u}_{f,o} \cdot \boldsymbol{S}_f|}{|\phi_o| + \epsilon}, 1 \right) \tag{19}$$

where ϵ is a very small number to avoid division by zero. This term accounts for the difference of the interpolated velocity and the flux at the previous time step, and it was also discussed in Vuorinen et al. (2014), where it shows that this term increases numerical dissipation in some specific cases. It should be noted that due to the version difference, the expression for the extra term is slight different in Vuorinen et al. (2014). In the present paper, this term was retained without any modification.

3.1.3. Pressure solution and velocity correction

Given the derived pressure equation, namely Eq. (15), one could now discretize it as follows:

$$\left[\!\left[\nabla \cdot \left(\frac{\nabla[p]}{\mathcal{A}_D}\right)\right]\!\right] = \nabla \cdot \left(\frac{\mathcal{A}_H}{\mathcal{A}_D} - (\boldsymbol{g} \cdot \boldsymbol{x})\nabla\rho + \sigma_T \kappa_\alpha \nabla\alpha\right) \tag{20}$$

As shown in Eq. (20), the terms in right-hand side were treated explicitly, since the purpose of solving this equation was to find the pressure field. This updated pressure field was used to correct the flux field as follows:

$$\phi = \phi^* + \phi^{**} \tag{21}$$

where ϕ^{**} is the adjustment of the flux due to effect of pressure gradient and was expressed as:

$$\phi^{**} = -|\boldsymbol{S}_f| \cdot \left(\left(\frac{1}{\mathcal{A}_D}\right)_f \nabla_f^{\perp} p\right) \tag{22}$$

Here a few comments are given on the final flux ϕ: (1) The final flux ϕ takes into account all the effects, including pressure, gravity and surface tension. (2) As mentioned in Section 3.1.2, The primary variable in OpenFOAM representing the velocity field is ϕ, which should be conservative. The final corrected flux ϕ here is guaranteed to be conservative. (3) The flux field could be updated for several times in this velocity correction loop. However, discretization of the momentum equation with the associated operator were frozen and updated until next time step. This is under the small Courant number assumption, as stated in the beginning of Section 3.1. (4) In order to consider the influence of pressure field on the flux in a consistent way, ϕ^{**} was directly obtained and stored from Eq. (20) by evaluating the off-diagonal matrix coefficients, instead of performing any interpolation. By this way, OpenFOAM enforces the continuity condition, and ensures the flux to be conservative.

3.2. VOF scheme

As mentioned in Section 1, achieving bounded and non-diffusive solution of Eq. (3) is not easy. Given that ϕ is conservative, (as obtained from the PISO algorithm in the last time step), the discretized matrix of Eq. (3) is diagonally dominant only if first order upwind scheme is used. Any other differencing scheme is likely to create negative coefficients, violate the diagonal equality and potentially create an unbounded solution (Rusche (2002)). However application of upwind scheme may lead to significant numerical diffusion, which smears the interface. In OpenFOAM, the VOF solver introduced two noticeable improvements to resolve the above issues: (1) A surface compression term was introduced in the transport equation for volume fraction, in order to sharpen the interface. (2) MULES solver was applied to solve the equation, in order to obtain a bounded solution. Actually MULES solver was first introduced in OpenFOAM-1.4, and it was further updated and improved in the following versions with better boundedness and consistency. Later on in OpenFOAM-2.3.0, the semi-implicit variant of MULES was introduced to combine operator splitting with application of the MULES limiter to an explicit correction rather than to the complete flux (Greenshields (2014)).

Below in this section, focus will be given on the above mentioned issues of the VOF scheme that is used in OpenFOAM. In Section 3.2.1, the modified phase transport equation is derived. Particularly, the analysis is given on the compression term. Then Section 3.2.2 and Section 3.2.3 illustrates the principles and its implementation of the explicit and semi-implicit MULES solver respectively.

3.2.1. The phase transport equation using an extra compression term

The modified formulation of the phase transport equation used in OpenFOAM was actually originated from Eq. (A.13) in Appendix A. This concept is based on the two-fluid method, where Eq. (A.13) is the transport equation for phase 1. Due to the assumption that both fluids in the mixture are incompressible, the density is constant. Therefore, it gave the following expression:

$$\frac{\partial \alpha}{\partial t} + \nabla \cdot (\alpha \hat{\boldsymbol{u}}_1) = 0 \tag{23}$$

where α is the volume fraction field for phase 1, and $\hat{\boldsymbol{u}}_1$ is the mass weighted average of the velocity for phase 1. Recall that in VOF, we do not explicitly distinguish between the mass of center velocity and volume of center velocity, as shown in Appendix A. Based on the concept of volume of center velocity, as defined in Eq. (A.20), then the following relation could be derived:

$$\alpha \hat{\boldsymbol{u}}_1 = \alpha \boldsymbol{u} + \alpha(1-\alpha)\boldsymbol{u}_r \tag{24}$$

where $\boldsymbol{u}_r = \hat{\boldsymbol{u}}_1 - \hat{\boldsymbol{u}}_2$. Substituting Eq. (24) into Eq. (23) gave the following equation:

$$\frac{\partial \alpha}{\partial t} + \nabla \cdot \boldsymbol{u}\alpha + \nabla \cdot (\boldsymbol{u}_r \alpha(1-\alpha)) = 0 \tag{25}$$

Comparing with Eq. (3), Eq. (25) has an extra term. Several comments are given here on this term: (1) The origin of Eq. (25) is Eq. (23). Actually when the interface is sharp enough, i.e. the volume fraction field is a delta function, Eq. (25) and Eq. (23) are the same. Since VOF method is a kind of DNS method where the interface length scale is directly resolved by the mesh grid, the difference between Eq. (23) and Eq. (3) was usually neglected. (2) Due to no-slip interface condition, this extra term should vanish in VOF formulation. But it was deliberately included here for compression of the interface. So the velocity field $\boldsymbol{u}_r$ should be interpreted as a velocity field that is suitable to compress the interface. (3) This compression term only acts on the interface due to the term $\alpha(1-\alpha)$. (4) Due to the non-zero value of $\boldsymbol{u}_r$, introducing the compression term may lead to numerical errors on convection of the free surface. Seng (2012) derived the non-conservative formulation of Eq. (25) as:

$$\frac{\partial \alpha}{\partial t} + (\boldsymbol{u} + \boldsymbol{u}_r(1-2\alpha)) \cdot \nabla\alpha + \alpha(1-\alpha)\nabla \cdot \boldsymbol{u}_r = 0 \tag{26}$$

If Eq. (26) is equivalent to Eq. (3), two conditions needs to be satisfied: (1) The compression velocity field is divergence free. (2) At the interface region $(1-2\alpha)$ is null. If the interface was located as the contour with $\alpha = 0.5$, the second condition was automatically satisfied. However, the position of the interface was unknown, and may be not located exactly at $\alpha = 0.5$. which serves as an error source. In addition, another requirement is that $\boldsymbol{u}_r$ should be divergence free. The implemented model in OpenFOAM fulfills this requirement, as shown below in Eq. (28).

Discretization of Eq. (25) leads to the following equation:

$$\left[\!\left[\frac{\partial [\alpha]}{\partial t} \right]\!\right] + [\![\nabla \cdot (\phi[\alpha])]\!] + [\![\nabla \cdot (\phi_r[\alpha])]\!] = 0 \tag{27}$$

The magnitude of the compression flux ϕ_r has been changing during the recent versions, since there are many possibilities on modeling this term. It was selected based on the practical experience rather than a formal derivation. But the applications of the model demonstrates that it works well in most of the cases. The direction of the flux should be always perpendicular to the interface, hereby to compress the interface effectively. In this version, the compression flux ϕ_r was given as:

$$\phi_r = f_n(1-\alpha_f)C_\alpha \left(\frac{|\phi|}{|\boldsymbol{S}_f|} \right) \tag{28}$$

where C_α is the compression coefficient. f_n is the face unit normal flux and it was evaluated based on the gradient of the volume fraction at the cell face:

$$f_n = \frac{(\nabla\alpha)_f \cdot \boldsymbol{S}_f}{|(\nabla\alpha)_f + \delta|} \tag{29}$$

where δ is just a stabilization factor to avoid division by zero:

$$\delta = \epsilon \left(\frac{\sum_{i=1}^{K} V_i^{cell}}{K} \right) \tag{30}$$

where K is the number of mesh cells in total and V_i is the volume of each mesh cell. The second multiplier within the bracket gives the average volume of each mesh cell.

3.2.2. Fully explicit MULES solver

The α field should be strictly bounded between 0 and 1, in order to have physical meanings. Any overshooting or undershooting will result in unphysical solution, which should be avoided. In OpenFOAM this is achieved via the MULES solver, either explicitly or in a semi-implicit manner. Until now, to the author's knowledge, Márquez Damián (2013) is the only reference where the algorithm for fully explicit MULES solver has been documented. In this section we briefly summarize the principle of the algorithm for explicit MULES solver, therefore to ease the illustration for the semi-implicit variant of MULES solver in Section 3.2.3.

Recall that Eq. (27) is essentially a pure convection equation without any diffusion term, where α field is advected under the flux $\phi + \phi_r$. In addition, α has a steep gradient close to the interface. Under such condition, convectional schemes may not correctly handle the advection of α as mentioned in the beginning of Section 3.2. This is the motivation to introduce MULES solver.

In explicit MULES solver, Eq. (27) was discretized with an explicit time scheme. This leads to the following discretized equation if evaluated at one single cell (explicit Euler scheme here was applied for simplicity of illustration):

$$\frac{\alpha_n - \alpha_o}{\Delta t} V^{cell} + \sum_f F_{cor,o} = 0 \tag{31}$$

where F_{cor} is the so-called *corrected* flux. This is explained as follows. Recall that only first order upwind scheme gives a bounded solution, while high order scheme reduces the numerical diffusion. Therefore, the essential idea of explicit MULES solver is to use a corrected flux from both higher order scheme F_{HO}, where $F_{HO} = (\phi + \phi_r)\alpha_f$, and first order upwind scheme F_{BD}, i.e. $F_{cor} = F_{BD} + \lambda F_{AD}$, where $F_{AD} = F_{HO} - F_{BD}$ is the anti-diffusive flux. So indeed the principal idea behind MULES solver is the same with flux corrected transport (FCT) method (Zalesak, 1979), namely to use a bounded flux plus a limited portion of anti-diffusive flux. Here the flux limiter λ, is the key of the MULES solver. Due to λ this corrective flux is nonlinear, depending on the value of α from cell to cell. $\lambda = 1$ indicates that the flux is fully second order accurate. $\lambda = 0$ gives a fully first order upwind flux.

Considering the transport properties of Eq. (25), the function of the limiter is to control the anti-diffusive flux, so no new maxima or minima should be generated, i.e. the solution should not accentuate already existing extrema. Therefore in MULES solver λ was determined based on two kinds of fluxes. The first one was the extreme anti-diffusive flux that was allowed to flow in and out, in order to maintain the boundness of the solution. Another one was the actual anti-diffusive flux.

In order to obtain the extreme anti-diffusive flux, the first step was to determine the local extrema for each cell. Since the volume fraction is always between zero and one, they were set to be the global extrema. The local extrema for each cell was first determined by the values at its cell center and cell neighbours, then this value was compared with the global extrema to obtain the final local extrema for this cell, denoted as α^{max} and α^{min}.

Considering that F_{BD} always produces a bounded solution, therefore the unbounded solution is only possible to be created by the anti-diffusive flux. So the anti-diffusive fluxes needed to reach the local extrema values were calculated based on Eq. (31):

$$Q_n^- = \frac{V^{cell}}{\Delta t}(\alpha_n^{max} - \alpha_o) + \sum_f F_{BD,o} \tag{32}$$

$$Q_n^+ = -\frac{V^{cell}}{\Delta t}(\alpha_n^{min} - \alpha_o) - \sum_f F_{BD,o} \tag{33}$$

where the superscript $^-$ indicates the incoming flux and $^+$ indicates the outgoing flux, so Q^- and Q^+ are the *absolute value* of the negative incoming anti-diffusive flux to reach the maximum value, and the positive outgoing anti-diffusive flux to reach the minimum value, respectively.

Once Q^+ and Q^- were determined, the limiter could be obtained. It was calculated in OpenFOAM in an iterative manner, where the number of the loop was hard-coded to be three. Inside the loop the limiter for each cell was calculated as:

$$\lambda_n^{\mp,k+1} = \max\left[\min\left(\frac{\pm\sum_f \lambda_f^k F_{AD,o}^{\pm} + Q_o^{\mp}}{\mp\sum_f F_{AD,o}^{\mp}}, 1\right), 0\right] \tag{34}$$

where λ_f was calculated by Eq. (36) as shown below. However, the original FCT method proposed in Zalesak (1979) gave an explicit expression of the limiter λ as shown below:

$$\lambda_n^{\mp} = \max\left[\min\left(\frac{Q_o^{\mp}}{\mp\sum_f F_{AD,o}^{\mp}}, 1\right), 0\right] \tag{35}$$

Eq. (35) actually assumes that α^{max} is only created by F_{AD}^-, namely the incoming anti-diffusive flux, and the contribution of outgoing anti-diffusive flux is neglected. This is relatively conservative. Comparing with Eq. (34) and Eq. (35), it was found that Eq. (34) also considers the contribution of outgoing flow for calculation of α^{max}. Meanwhile for α^{min}, the contribution from incoming flux is also considered. In Márquez Damián (2013) it was concluded that in case of small inflows and outflows, the λ values calculated from Eq. (34) rapidly converges to Eq. (35).

Somehow the limiter should act on the flux, which are for cell faces. So we consider to interpolate the limiter on the cell face. Due to principle of mass conservation, the anti-diffusive flux flowing out from one cell must enter into its neighbouring cell. Therefore, each cell face should have only one limiter. However, concerning the boundness of the solution, the smaller one should be adopted:

$$\lambda_{f,n} = \begin{cases} \min(\lambda_{O,n}^+, \lambda_{N,n}^-), & \text{if } F_{AD} > 0 \\ \min(\lambda_{O,n}^-, \lambda_{N,n}^+), & \text{if } F_{AD} \leq 0 \end{cases} \tag{36}$$

where λ_O is the λ value at the owner of the the cell face, and λ_N is the λ value at the neighbor cell.

From above it is illustrated how this method can maintain the boundness property of the solution. Meanwhile, it could be seen that it is fundamentally an explicit method, as shown in Eq. (31) that it was discretized and solved in an explicit time stepping method, and the limiter was acting on the fully explicit flux. Hereby this method has a strict requirement on Courant number. From many practical application as reported in Gopala and van Wachem (2008), Márquez Damián (2013) and also the author's opinion, the Courant number should be restricted below 0.2 or even lower. This may be a heavy burden even for high performance computing (HPC) clusters in some large scale simulations.

3.2.3. Semi-implicit MULES solver

In order to reduce the limitation on Courant number, the semi-implicit variant of MULES solver was introduced from OpenFOAM-2.3. This is based on a predictor-corrector approach where it first executes

an implicit predictor step, based on purely bounded numerical operators before constructing an explicit correction on which the MULES limiter is applied. It is further explained below.

Again starting from Eq. (3), discretization of this equation by bounded scheme e.g. Euler implicit scheme plus upwind convection scheme gave the following equation at the predictor step:

$$\frac{\alpha_n^{pre} - \alpha_o}{\Delta t} V + \sum_f F_{BD,n}^{pre} = 0 \tag{37}$$

where α_n^{pre} and $F_{BD,n}^{pre}$ are the predicted volume fraction and total bounded flux at new time step.

Solution of Eq. (37) gave a bounded but diffusive α field, since both the schemes and the volumetric flux are bounded. The predicted α field was further corrected by several explicit MULES correctors. The principle of the correction is the same with the fully explicit MULES solver as explained in Section 3.2.2, where a limited portion of the anti-diffusive flux was taken into account. The anti-diffusive flux was written as:

$$F_{AD,n}^{cor} = F_{HO,n}^{cor} - F_{BD,n}^{pre} \tag{38}$$

The limiter λ was also determined from the allowed extreme flux and the actual anti-diffusive flux. The difference between the extreme fluxes that was allowed and the fluxes that was induced by α_n^{pre} were calculated as:

$$P_n^{-,cor} = \frac{V^{cell}}{\Delta t}(\alpha_n^{max} - \alpha_n^{pre}) \tag{39}$$

$$P_n^{+,cor} = -\frac{V^{cell}}{\Delta t}(\alpha_n^{min} - \alpha_n^{pre}) \tag{40}$$

Then λ was calculated by Eq. (34) and Eq. (36), where Q was substituted by P in these equations. But the number of iteration for corrections was not hard-coded but user-selected, since in general it requires more frequent corrections for implicit solutions. The corrected α field was calculated as:

$$\alpha_n^{cor} = \alpha_n^{pre} - \frac{\Delta t}{V^{cell}} \sum_f \lambda_{f,n} F_{AD,n}^{cor} \tag{41}$$

In principle, this approach can maintain boundedness and stability at an arbitrarily large Courant number. Hereby it was used in the sensitivity analysis in Section 4, where the Courant number effect was investigated by carrying out simulations with different time step. For each predicted solution, the number of correctors was fixed to five.

4. Optimization of the discretization schemes and parameter settings on wave generation

As mentioned in Section 2, the VOF model is a macroscopic model in which the microscopic formulation has been averaged. Therefore the two phase system actually were treated as a continuum, and Eq. (1) and Eq. (2) are the governing equations for the whole continuum including both phases. However naturally there exists discontinuities between water and air phases. But in VOF these discontinuities were smeared out and represented by continuous functions. Due to large density ratios between air and water, sharp changes occur at the interface where density gradient can not be evaluated accurately. This induces unbalanced forces which further causes spurious current generated at the interface. In order to improve the near surface kinematics and reduce the magnitude of the spurious current velocity at the interface, series of preliminary tests are conducted to generate gravity waves with different schemes and parameters. The generated wave will propagate on a flat bed with the water depth of $d_w = 0.6$ m, and the designated wave height $H = 0.07$ m and wave period $T = 1$ s. The main focus in this section will be the influences of the schemes and parameters on the velocity profile and surface elevation. In the end of this section a brief summary is given on the best combination of the schemes and parameters, and they will be used in Section 5 for validation of the numerical model.

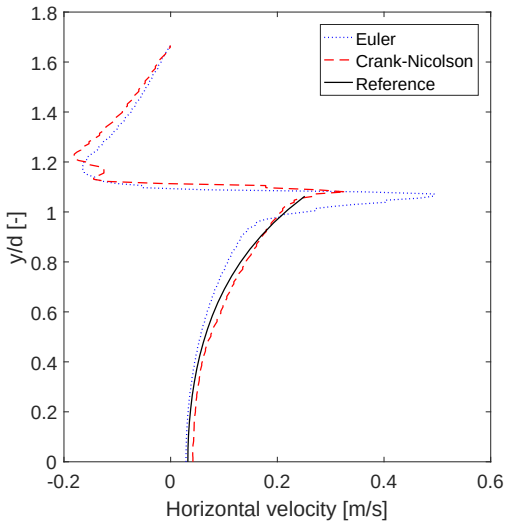

Figure 1: Comparison of horizontal velocity profiles using Euler scheme and Crank-Nicolson scheme with Courant number $Co = 0.3$. The reference solution extends to the top of the wave.

4.1. Discretization scheme

Among various discretization schemes applied in the simulation, it was found that the scheme for time derivative term, which was used in the discretization of transport equation for the volume fraction field, i.e. Eq. (25), is the key to suppress the spurious current velocity. With first order Euler scheme, large spurious current velocity was generated close to the interface. Therefore we consider the possible alternative scheme, namely the Crank-Nicolson scheme. This scheme only uses values at new and old time step, the additional terms relating to the fluxes and sources are evaluated at the mid point of the time step. This provides the opportunity for MULES solver to limit the fluxes and ensure boundedness while maintaining greater accuracy compared to the Euler scheme. Other second order scheme e.g. backward differencing scheme is not bounded due to its extrapolative behavior in time.

However, fully second order Crank-Nicolson scheme was found to be extremely unstable, and may easily blow up the simulation. Hereby an off-centered coefficient θ was applied to stabilize the simulation, which indeed represents a blending between Euler and Crank-Nicolson scheme. Define the off-centered coefficient θ where $\theta = 1$ is equivalent to pure Crank-Nicolson scheme and $\theta = 0$ is equivalent to Euler scheme. It was suggested to use $\theta = 0.9$ in OpenFOAM, which is suitable for a range of cases and could provide higher order accuracy than Euler scheme. Therefore below, the terminology "Crank-Nicolson" represents the blending scheme between Crank-Nicolson and Euler scheme with $\theta = 0.9$, instead of the fully centered Crank-Nicolson scheme, except specially mentioned.

By series of numerical experiments, it was found that by application of Crank-Nicolson scheme, the spurious current velocity could be effectively reduced. An example on comparison of the averaged horizontal velocity profiles over five periods is given in Fig. 1 between Euler scheme and Crank-Nicolson scheme. A clear difference is shown near the free surface area. By using Crank-Nicolson scheme, the spurious current velocity was reduced significantly and the velocity profile agrees much better with the analytical solution.

However it was observed that Crank-Nicolson scheme may trigger oscillation of the surface elevation. A detailed analysis of the generated waves using Euler scheme and Crank-Nicolson scheme is given in Fig. 2, where the surface elevation η, the relative volume of water V_{water} normalized by the initial water volume $V_{water,0}$, the total potential energy E_k and the total kinetic energy E_p are depicted. It is clearly shown that for the waves generated using Crank-Nicolson scheme, with the propagation of the wave, the surface elevation was not steady and started to oscillate at $t = 12$ s. The total water volume remained the same with Euler scheme, but both kinetic and potential energy were growing to an higher level and stayed in that level. Although the final energy could be controlled in a constant value, this high steady level of energy

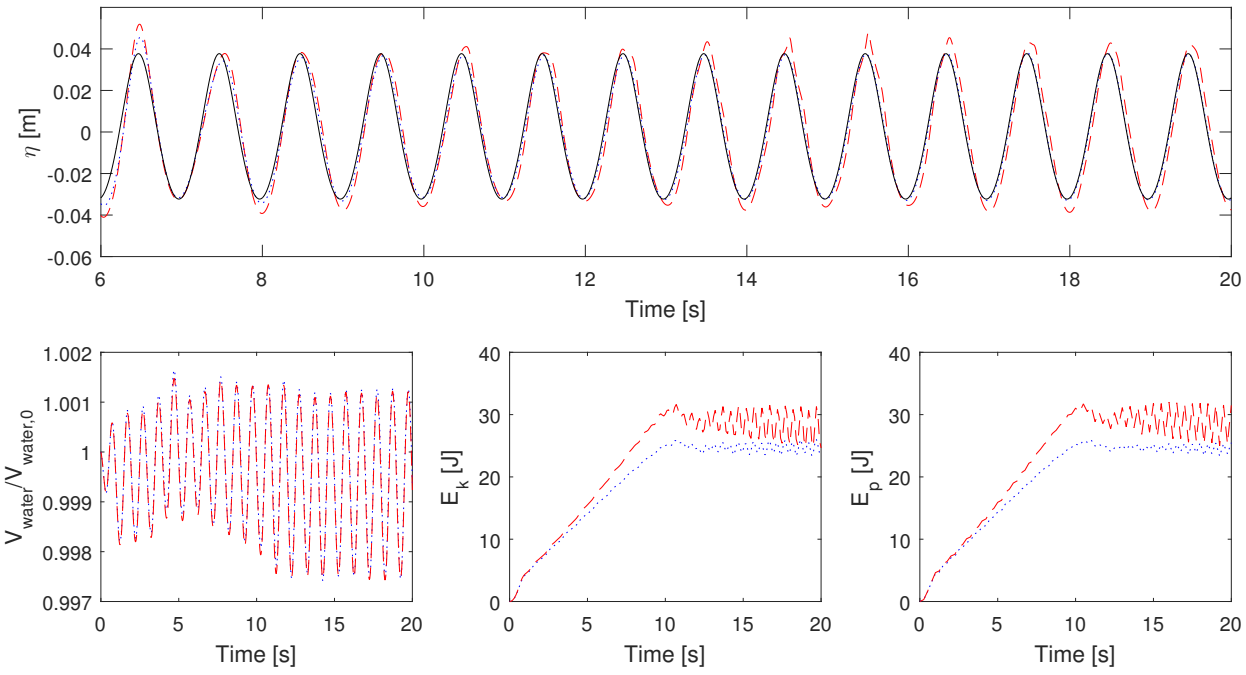

Figure 2: Comparison of the surface elevation, relative amount of water, potential and kinetic energy using Euler scheme (blue dotted line) and Crank-Nicolson scheme (red dashed line). The reference solution for surface elevation is given in solid line.

may result in overestimation of wave load on floaters. Therefore we consider to reduce the value of θ, in order to reduce the oscillation of surface elevation and improve the accuracy of the wave velocity profile simultaneously. Numerical experiment shows that a blending of Euler and Crank-Nicolson scheme with $\theta = 0.4$, coupled with a high resolution scheme with QUICK limiter for the convection term of Eq. (2) makes the best compromise between surface elevation and velocity profile. A brief summary on the applied discretization schemes are given in Table 1.

4.2. Parameter settings

Except applied schemes, the parameter settings will also influence the stability and accuracy of the generated waves. The main parameters concerned in wave generation are the compression coefficient C_α, the mesh resolution and the Courant number. It is important that by setting these parameters properly, both the velocity profiles and surface elevation should agree well with the analytical solution.

The overall impact of these three parameters on the quality of the generated waves are depicted in Fig. 3. The compression coefficient determines the level of sharpness of the interface. $C_\alpha = 1$ gave a moderate compression and this is used in most of the VOF multiphase flow cases. With $1 < C_\alpha \leq 4$ the compression effect can be enhanced and $C_\alpha = 0$ indicates no compression. The influence of C_α on velocity profile and surface elevation is given in Fig. 3(a). It was found that enhanced compression may have side effects on both velocity profile and surface elevation, since for case with $C_\alpha = 2$, the magnitude of spurious current velocity increased significantly, and strange surface elevation profile was generated with double peak and/or high wave amplitude. In addition, for case with $C_\alpha = 0$, although an accurate wave elevation profile was produced but the trade-off is lose of the interface sharpness. Smearing of the interface was not reflected by the surface elevation profile since it was calculated by Eq. (6). However from the velocity profile for $C_\alpha = 0$, it was seen that the velocity profile for the water phase from the numerical simulation extends further than wave top of the analytical solution, demonstrating the smearing of the interface.

By using the semi-implicit MULES solver, the Courant number restriction was relaxed and the stability was enhanced for high Courant number simulations. However on the other hand, one should take care of the accuracy of the numerical solution when using high Courant number. From Fig. 3 (b) it was concluded

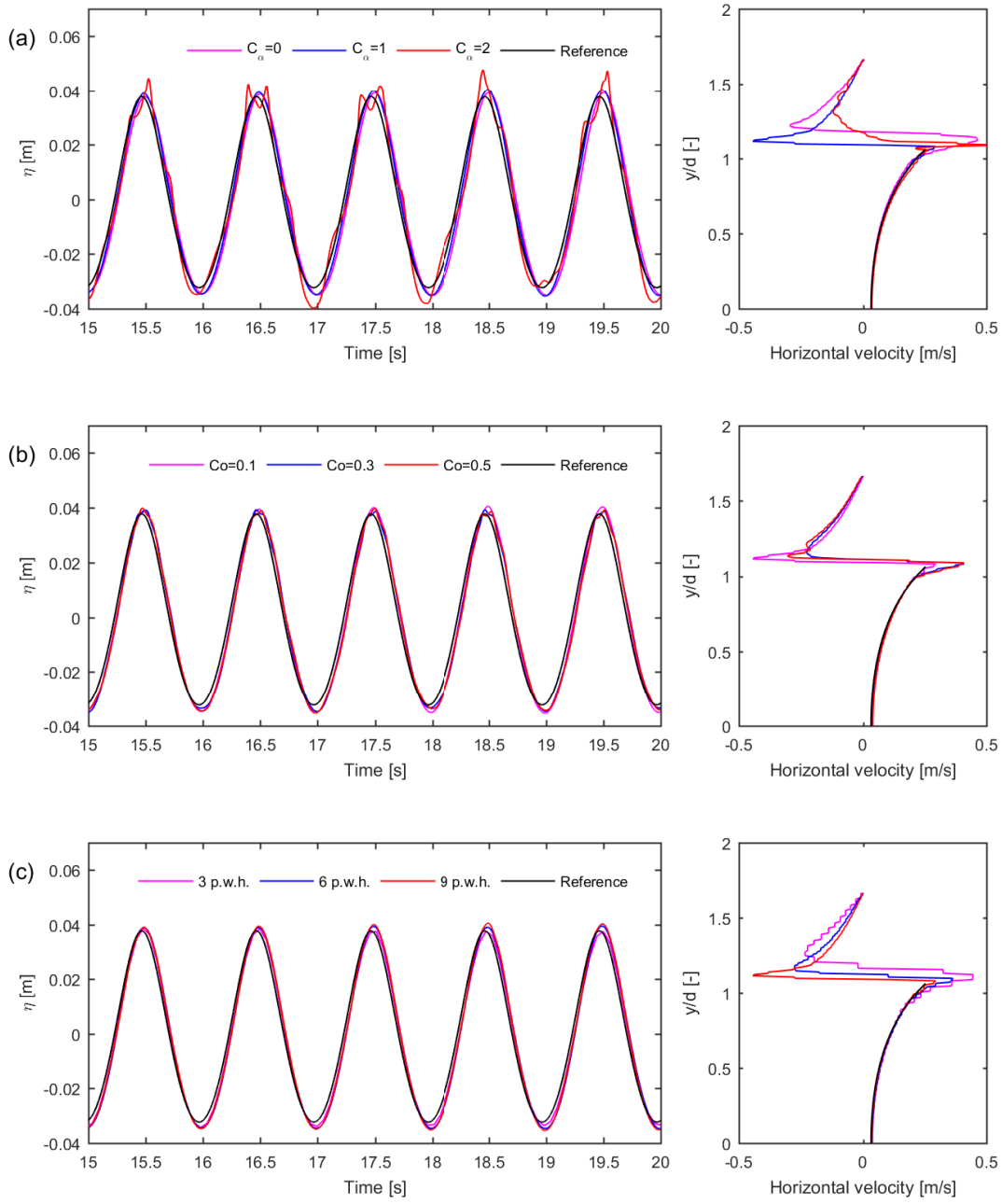

Figure 3: Sensitivity analysis of velocity profile and surface elevation on different combinations of parameter settings. (a) with different compression coefficients C_α. (b) with different Courant number Co. (c) with different mesh resolutions. The base combination for the comparison is $C_\alpha = 1$, $C_o = 0.1$, and 9 cells p.w.h.

Table 1: Applied discretization scheme for each term in the numerical model

Term	Applied schemes in OpenFOAM	Brief explanation
$\frac{\partial \alpha}{\partial t}$	CrankNicolson 0.4	Crank-Nicolson scheme with $\theta = 0.4$
$\nabla \cdot (\alpha \boldsymbol{u})$	vanLeer01	TVD scheme with Vanleer limiter bounded between 0 and 1
$\nabla \cdot (\boldsymbol{u}_r \alpha(1-\alpha))$	interfaceCompression	a special designed high resolution scheme for interface compression term
$\frac{\partial \rho \boldsymbol{u}}{\partial t}$	CrankNicolson 0.4	Crank-Nicolson scheme with $\theta = 0.4$
$\nabla \cdot (\rho \boldsymbol{u}) \boldsymbol{u}$	QUICKV	TVD scheme with QUICK limiter
$\nabla \cdot (\mu \nabla \boldsymbol{u})$	linear corrected	μ and $\nabla \boldsymbol{u}$ from centtre differenccing scheme, with explicit non-orthogonal corrections for $\nabla \boldsymbol{u}$
$\nabla_f^{\perp} \chi^*$	corrected	centre differencing scheme from neighboring cells, with explicit non-orthogonal corrections
$(\chi^*)_f$	linear	linear interpolation of values from cell center to cell face

χ^* stands for an arbitrary quantity.

that Courant number has a minor impact on the surface elevation profile. But the main issue on using a relatively high Courant number is that the spurious current velocity may increase. Therefore the maximum Courant number used in the present simulations are still limited to 0.1.

The mesh resolution was measured by the number of cells per wave height, since the mesh in the free surface zone should resolve the generated waves properly. Again it was found that for the selected three mesh resolutions, the main influence is on the wave velocity profile. By properly refining the mesh, the spurious current could be suppressed effectively. On the other hand, even for the coarsest mesh (i.e. 3 cells per wave height), a very accurate wave elevation profile was obtained. Since one of the important goal in this work is to suppress the spurious current, at least 9 cells per wave height was adopted in the following simulations.

4.3. Brief summary

From the sensitivity analysis above, the best combination of the applied discretization schemes and parameters was found. The semi-implicit variant of MULES solver was used with a blending of Crank-Nicolson scheme and Euler scheme to discretize the time derivative term in Eq. (25). This is the key point to suppress the spurious current velocity. Adjustable time step was used with $Co_{max} = 0.1$, and the compression coefficient $C_\alpha = 1$. A relatively fine mesh was demonstrated to be good for reducing the spurious current. Therefore a resolution of at least 9 cells per wave height should be guaranteed. Under this combination, the wave surface elevation and velocity profile is given in Fig. 4 where both surface elevation and velocity profile agree well with analytical solution. This combination of applied schemes and parameter settings will be used in Section 5 for validation of the numerical model.

5. Validation of the numerical model

In this section two case studies are presented to validate the numerical model on wave forces on partially submerged fish cage floaters. The first validation case compares the time series of the wave forces and its Fourier amplitudes at the fundamental wave frequency and higher order frequencies under two selected wave conditions. The second validation case compares the average amplitudes of the wave forces from non-steep to steep but non-breaking waves.

5.1. Validation case 1

The numerical model was first validated against the laboratory test in Kristiansen (2010). The model test was performed in a narrow flume at the Division of Marine Civil Engineering in Norwegian University of Science and Technology in 2006. The dimension of the flume was 26.5 m $\times$ 0.6 m $\times$ 0.543 m. A piston

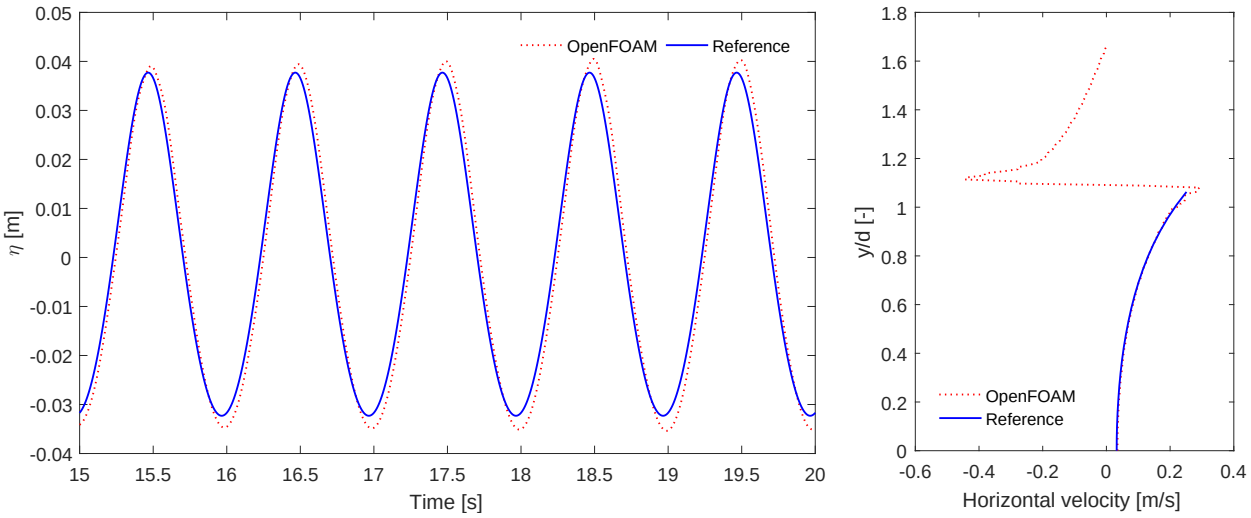

Figure 4: Comparison of the surface elevation and velocity profile between the numerical simulation in OpenFOAM and analytical solution. The reference solution extends to the top of the wave.

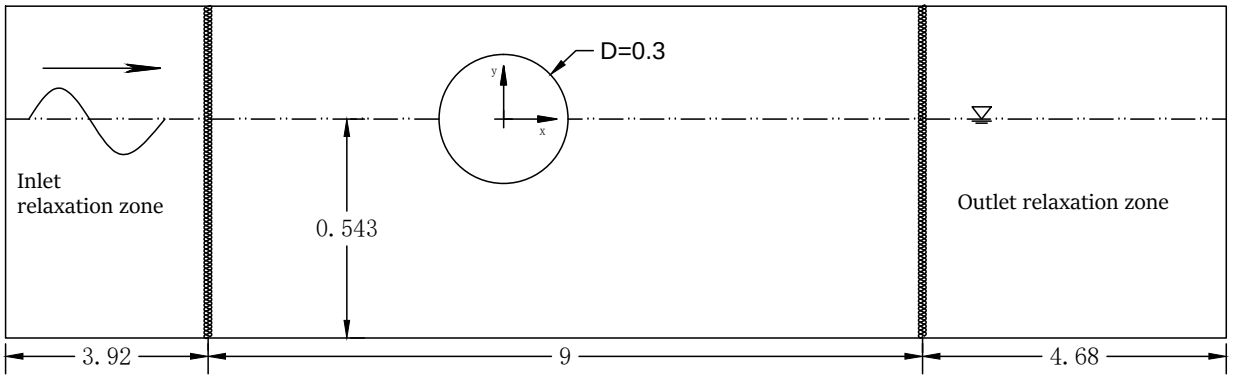

Figure 5: The computational domain for reproduction of the experiment conducted in Kristiansen (2010) (unit: m).

type wavemaker was used to generate waves. The wavemaker software in the laboratory test applied a linear theory to estimate the necessary stroke of the wave board for generating waves with a given wave height. The diameter of the floater $D = 0.3$ m and the length of the floater $l = 0.59$ m. Two test cases were selected to validate the numerical model, where for the first case $H = 0.087$ m and $T = 1.084$ s, for the second case, $H = 0.130$ m and $T = 1.348$ s. In both cases, the floater was half immersed.

A 2D numerical model was set up corresponding to the physical tests, as shown in Fig. 5. The length of the numerical wave tank is shortened to save computational time. Two relaxation zones were applied at the inlet and out let to avoid wave reflections. The wave was generated from the inlet boundary and propagated towards the outlet.

The time series and the Fourier amplitudes of the inline and lift forces are presented in Fig. 6 and Fig. 7 for the two test cases. In general the numerical results agree well with the experimental data, although the inline forces were somewhat overpredicted slightly in both cases. It was observed that the overprediction mainly comes from the linear harmonic. The differences are around 10 % and 15%, respectively. Higher order harmonics were predicted accurately by the numerical model. For the lift force the numerical model gave a very good prediction, and the differences were less than 5% for the amplitudes of all the harmonics in both cases. However, unlike inline force, third order harmonic is also presented in the lift force signals.

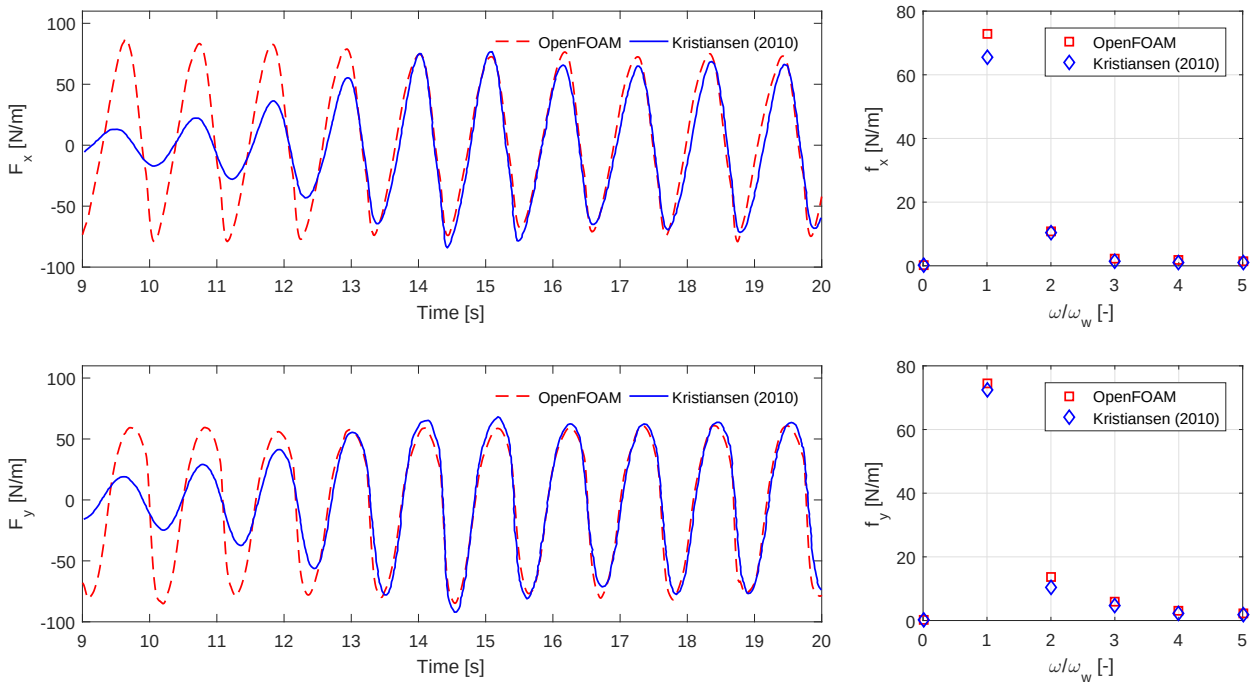

Figure 6: Comparison of the time series and the corresponding Fourier amplitudes of the inline and lift forces between the numerical results from OpenFOAM and the experimental results from Kristiansen (2010) for half immersed floater under wave condition of $H = 0.087$ m, $T = 1.084$ s. ω_w is the fundamental wave frequency.

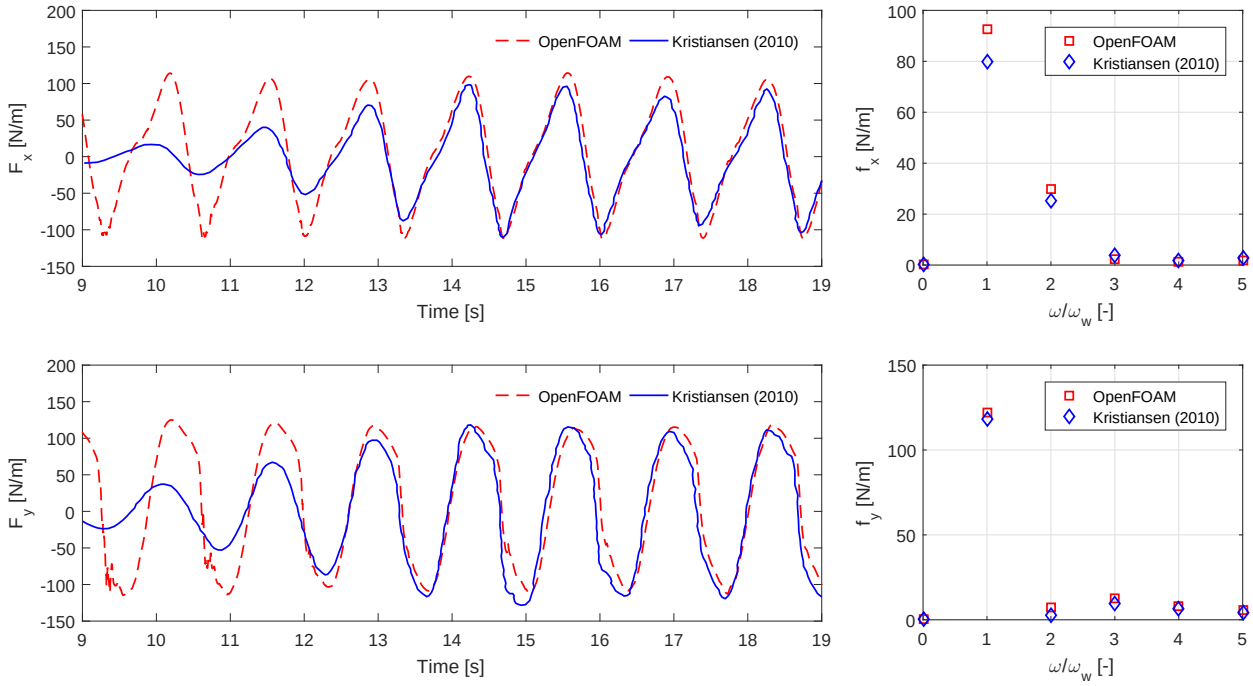

Figure 7: Comparison of the time series and the corresponding Fourier amplitudes of the inline and lift forces between the numerical results from OpenFOAM and the experimental results from Kristiansen (2010) for half immersed floater under wave condition of $H = 0.130$ m, $T = 1.348$ s. ω_w is the fundamental wave frequency.

Table 2: The selected cases for validation against the experiments in Martin and Dixon (1983)

Case ID	T(s)	kh	H(m)	kH	KC	Re
a	1	2.45	0.02	0.082	0.628	6.37×10^3
b	1	2.45	0.03	0.122	0.943	9.57×10^3
c	1	2.45	0.04	0.161	1.26	12.7×10^3
d	1	2.43	0.05	0.203	1.57	15.8×10^3
e	1	2.43	0.06	0.243	1.89	19.0×10^3
f	1	2.42	0.07	0.283	2.20	22.1×10^3
g	1	2.41	0.08	0.322	2.5	25.1×10^3
h	1	2.39	0.10	0.400	3.14	31.1×10^3

5.2. Validation case 2

Furthermore the numerical model was validated against the experiments conducted in Martin and Dixon (1983). In Martin and Dixon (1983) a narrow wave tank with a dimension of $10 \times 0.3 \times 0.6$ m was used for the experiments at the University of Edinburgh. A half immersed horizontal cylinder with $D = 0.1$ m was located in the center of the wave flume. At one end of the tank a hinged-plate wave maker was applied. Incoming waves with a variety of wave periods and amplitudes were generated in the flume. At the other end of the tank, there was a beach to absorb the propagating waves. The general configuration of the numerical model used for validation of this set of cases is the same with the model used in Section 5.1. But the dimensions of the cylinder and the wave tank were chosen based on this experiment. Totally eight cases were selected in this section, and a complete list of them is presented in Table 2.

Following the data manipulation method in Martin and Dixon (1983), the time series of the force signal was nondimensionalized as:

$$\boldsymbol{F}_{non}(t) = \frac{4\boldsymbol{F}(t)}{\rho_w g D H l} \tag{42}$$

The nondimensional force signal for case (h), i.e. with the highest wave is presented in Fig. 8 together with the Fourier amplitudes. In this case the incoming wave amplitude is the same with the radius of the floater. Therefore, overtopping may occur within one wave period. This creates a quite asymmetric signal for both the inline and the lift forces. Strong nonlinearity was observed from the transformed Fourier amplitudes, especially for the inline force.

In Dixon et al. (1979) the lift force signal over one wave period was given for this set of experiments, and it was used here for the validation purpose. However, one should note that Dixon et al. (1979) adopted a different way to nondimensionalize the force signal. Here we persist to use Eq. (42) for the reason of consistency. The nondimensional lift force signal versus time is presented in Fig. 9 for case (h), case(c) and case(a). For the lift forces generated by non-steep incoming waves, i.e. case (c) and case (a), the lift force was precisely reproduced by the numerical model. For case (h), the overall trend of the force distribution was also captured well by the numerical model. But the amplitude of the force was slightly overpredicted.

The average amplitude of the force was computed based on the root mean square force $\boldsymbol{F}^{rms}$ given by:

$$\boldsymbol{F}_{amp} = \sqrt{2}\boldsymbol{F}_{rms} = \frac{\sqrt{2}}{T}\int_0^T \boldsymbol{F}_{non}^2(t)\,\mathrm{d}t \tag{43}$$

Comparison of the amplitudes of the inline and lift forces against H/D is given in Fig. 10 between the numerical and experimental results. Meanwhile the analytical solution in Martin and Dixon (1983) based on linear diffraction theory is also included. It should be mentioned that the analytic solution is independent of H/D, due to its nature of linearity.

Regarding the inline forces, the numerical model again slightly overpredicted the force amplitudes, where the error was at most 10% for case (e). A better result was obtained for the lift forces, and the errors were below or around 5% for all the cases. It was believed that the spurious current may still be the main reason for overprediction of the inline force. Physically the inline force was mainly determined by the inertia

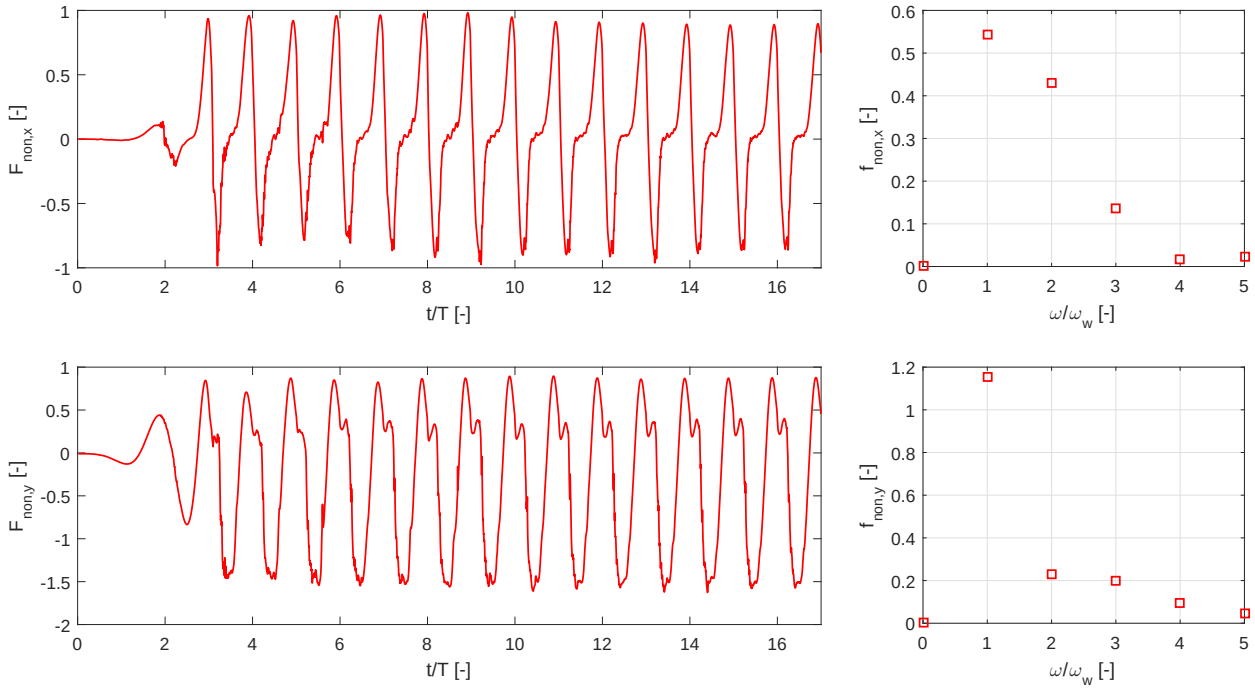

Figure 8: The time series and the Fourier amplitudes of the inline and lift forces for case (h) from the present model.

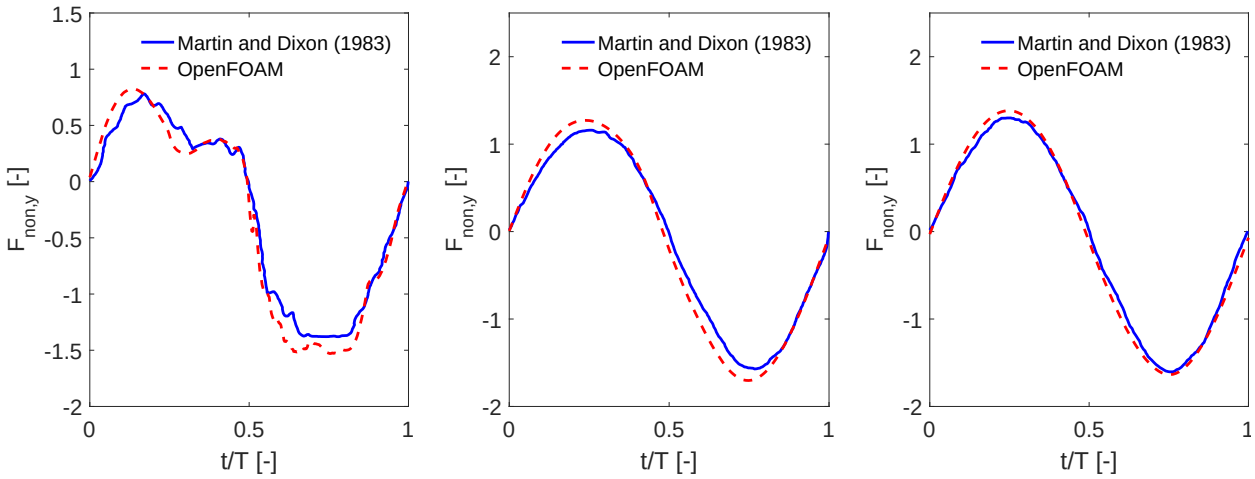

Figure 9: Comparison of the time series of the lift force within wave period. Left: case (h). Middle: case (c). Right: case (a).

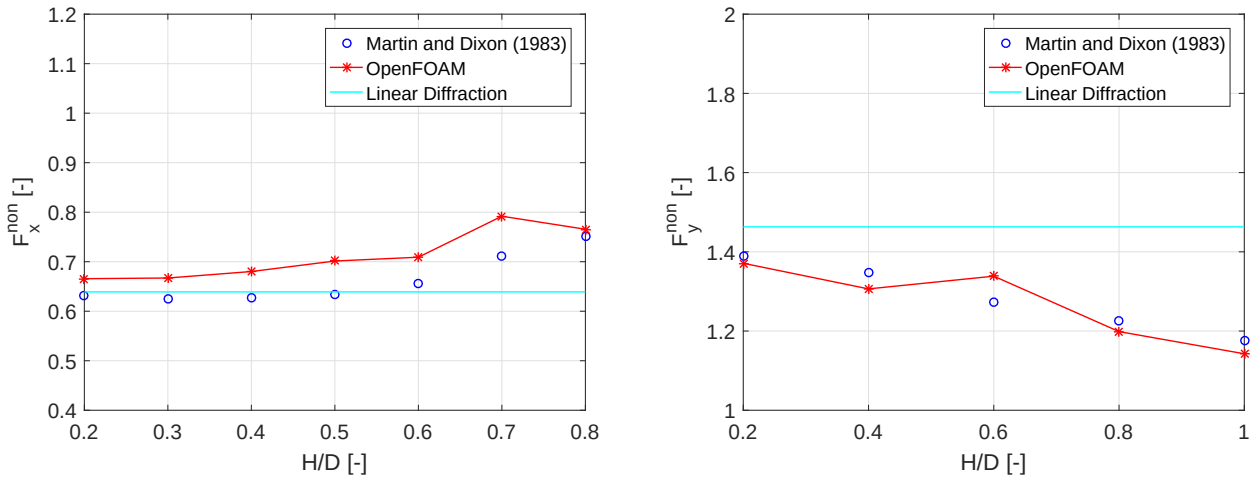

Figure 10: Comparison of the inline and lift force amplitudes between the numerical results from OpenFOAM and the analytical and experimental results in Martin and Dixon (1983).

force. Therefore, overshooting of the horizontal velocity directly affects the inertia force, which results in the overprediction of inline force. Meanwhile the lift force fundamentally is an interplay between buoyancy and inertia force, since drag force has been neglected. For the half immersed cylinder, variation of buoyancy plays an important role on the total force (Chen et al., 2015). Recalling that buoyancy is only related to surface elevation, which is not affected by the spurious current velocity, it could be predicted precisely by the numerical model. Therefore, the impact of spurious current on the lift forces was less pronounced than on the inline forces.

6. Conclusion

The present paper investigates wave generation and interaction with fixed half submerged horizontal fish cage floaters in the two-phase flow solver in OpenFOAM. Considering that a large area of floater is in the vicinity of the free surface, the key issue is to suppress the spurious current velocity generated by this solver. In order to achieve that, we thoroughly investigated the mathematical model and numerical algorithm on the solver. A detailed introduction on them was given in the present work. The governing equations in VOF formulation was derived from the local instant formulation, where the quantities used in VOF formulation were linked to the original physical quantities in local instant formulation. The principal idea behind MULES solver was documented thoroughly, and the semi-implicit MULES solver was adopted in the present work.

A sensitivity analysis was performed to examine the influences of different schemes and parameters on the magnitude of spurious current velocity. It was found that the key point to suppress it is to use higher order scheme for the time derivative term in discretization of transport equation for the volume fraction. In order to maintain the boundness of the solution, the bounded Crank-Nicolson scheme was chosen. However it was also observed that Crank-Nicolson scheme has poor stability behavior, and may trigger numerical oscillations. Therefore an off-centered coefficient of 0.4 was used to blend the Euler scheme and Crank-Nicolson scheme. Application of this scheme ensures that one can achieve stability and accuracy simultaneously. Meanwhile the Courant number was restricted to 0.1, and the mesh at free surface was also refined to be 9 cells per wave height. The results from numerical simulations shows good agreement with analytical solution on both velocity profile and surface elevation.

By applying this set of schemes and parameters, the numerical model was validated against two laboratory experiments on the wave induced forces on fish cage floaters. In the first validation case a direct comparison of force signals in time domain was presented. The force signal was also transformed into frequency domain to obtain the amplitudes at wave frequency and higher frequencies. For the second validation case, a wide

range of wave conditions from non-steep to steep but non-breaking waves was covered. The averaged square root amplitude of the wave forces were compared with the experimental data. For both cases, the numerical model has a very good performance. Therefore it was concluded that by using this set of schemes and parameters the spurious current was reduced to an acceptable level, and the numerical model is able to predict the wave forces on horizontal half immersed cylinders precisely.

Acknowledgments

Dr David Kristiansen is acknowledged for kindly providing the experimental data. The research was partially supported by FP7-OCEAN-2011 project "Innovative Multi-purpose offshore platforms: planning, design and operation", MERMAID, 288710, under the call "Ocean of Tomorrow".

Appendix A. Derivation of VOF formulation in OpenFOAM for two immersible and incompressible fluids without phase change

The mathematical formulation of the VOF method used in the present numerical model will be formally derived in this section. VOF is a kind of macroscopic description on two phase flow systems, in which the system is treated as a continuum. Only one set of equations is used to describe both phases and the motion of the interface. This actually requires to properly average the local instant formulation of the system, which filters the unnecessary fluctuations and retain the averaged properties. We shall start from the local instant formulation, where the flow field was subdivided into single phase regions with an interface separating them. The governing equations for each phase was given as:

$$\frac{\partial \rho_k}{\partial t} + \nabla \cdot (\rho_k \boldsymbol{u}_k) = 0 \tag{A.1}$$

$$\frac{\partial \rho_k \boldsymbol{u}_k}{\partial t} + \nabla \cdot (\rho_k \boldsymbol{u}_k)\boldsymbol{u_k} = \nabla \cdot \boldsymbol{T}_k + \rho_k \boldsymbol{g} \tag{A.2}$$

where the subscript k denotes the phases, i.e. water or air. ρ_k is the density for the k^{th} phase, $\boldsymbol{u}_k$ is the velocity field for the k^{th} phase, and $\boldsymbol{T}_k$ is the stress tensor for the k^{th} phase. Across the interface, the jump condition was developed to specify the mass and momentum exchange (Drew (1983) and Delhaye (1974)):

$$\|\rho \boldsymbol{n} \cdot (\boldsymbol{u} - \boldsymbol{u}_i)\| = 0 \tag{A.3}$$

$$\|\rho \boldsymbol{n} \cdot (\boldsymbol{u} - \boldsymbol{u}_i)\boldsymbol{u} - \boldsymbol{n} \cdot \boldsymbol{T}_k\| = \sigma_T \kappa'_\alpha \boldsymbol{n} \tag{A.4}$$

where $\|$ denotes the jump across the interface. The jump of a property f between water and air was defined as $\|f\| = f_w - f_a$, where f_w and f_a are the limiting value of f from the water side and air side. $\boldsymbol{u}_i$ is the velocity of the interface. κ'_α here is the exact curvature of the interface. For a sharp interface, the relative velocity between water and air vanishes (Bohorquez (2008)), i.e. no slip condition on the interface was applied. Therefore the jump condition was simplified as:

$$\|\boldsymbol{n} \cdot \boldsymbol{T}_k\| = \sigma_T \kappa'_\alpha \boldsymbol{n} \tag{A.5}$$

The above set of equations for each phase plus a interface jump condition gave a complete description for the two phase flow system. However this formulation results in a multi-boundary problem with unknown position of the interface. The coupling between the field equations of each phase and the interfacial conditions, the existence of the fluctuations of variables due to turbulence and interface motions, the local jump of the variables at the interface makes the formulation mathematically difficult to solve, as shown in Ishii and Hibiki (2010). Certain averaging process needs to be done to simplify the mathematical model and filter the unnecessary flow details. There have been considerable works on different averaging processes, e.g. in Ishii and Hibiki (2010) and Vernier and Delhaye (1968). However here we follow the statistical averaging

method in Drew (1983). The detailed averaging process was neglected and only the averaged equations are given:

$$\frac{\partial \langle X_k \rho_k \rangle}{\partial t} + \nabla \cdot \langle X_k \rho_k \boldsymbol{u}_k \rangle = 0 \tag{A.6}$$

$$\frac{\partial \langle X_k \rho_k \boldsymbol{u}_k \rangle}{\partial t} + \nabla \cdot \langle X_k \rho_k \boldsymbol{u}_k \boldsymbol{u}_k \rangle = \nabla \cdot \langle X_k \boldsymbol{T}_k \rangle + \langle X_k \rho_k \boldsymbol{g} \rangle + \langle [-\boldsymbol{T}]^k \cdot \nabla X_k \rangle \tag{A.7}$$

where $\langle\rangle$ denotes the averaging process. X_k was introduced to account for the probability of occurrence for phase k, and it was defined as:

$$X_k = \begin{cases} 1 & \text{if } x \text{ is in phase } k \text{ at time } t \\ 0 & \text{otherwise} \end{cases} \tag{A.8}$$

$[f]^k$ means to evaluate f from phase k side, since the derivative of X_k causes discontinuities. The last term in the right-hand side of Eq. (A.7), i.e. $\langle [-\boldsymbol{T}]^k \cdot \nabla X_k \rangle$, represents the interfacial momentum transfer $\boldsymbol{M}_k$. The averaged jump condition was expressed as

$$\sum_{k=1}^{2} \boldsymbol{M}_k = \sigma_T \langle \kappa'_\alpha \nabla X_1 \rangle = \boldsymbol{M}_m \tag{A.9}$$

where $\boldsymbol{M}_m$ represents the surface tension effect.

In order to evaluate each term in Eq. (A.6) and Eq. (A.7), the volume fraction of phase k, known as α_k, was introduced here:

$$\alpha_k = \langle X_k \rangle \tag{A.10}$$

Meanwhile, the phasic weighted average and mass weighted average of the variable ϕ, denoted as $\tilde{\phi}$ and $\hat{\phi}$, were also introduced:

$$\tilde{\phi}_k = \langle X_k \phi \rangle / \alpha_k \tag{A.11}$$

$$\hat{\phi}_k = \langle X_k \rho \phi \rangle / \alpha_k \tilde{\rho}_k \tag{A.12}$$

With Eq. (A.10 - A.12), the averaged mass and momentum equations became:

$$\frac{\partial \alpha_k \tilde{\rho}_k}{\partial t} + \nabla \cdot (\alpha_k \tilde{\rho}_k \hat{\boldsymbol{u}}_k) = 0 \tag{A.13}$$

$$\frac{\partial \alpha_k \tilde{\rho}_k \hat{\boldsymbol{u}}_k}{\partial t} + \nabla \cdot (\alpha_k \tilde{\rho}_k \hat{\boldsymbol{u}}_k \hat{\boldsymbol{u}}_k) = \nabla \cdot (\alpha_k \tilde{\boldsymbol{T}}_k) + \alpha_k \tilde{\rho}_k \boldsymbol{g} + \boldsymbol{M}_k \tag{A.14}$$

Eq. (A.13 - A.14) gave the governing equations for statistically averaged two-phase flows. They are the foundation of VOF based formulation. Define the density for the two phase flow systems:

$$\rho = \sum_{k=1}^{2} \alpha_k \tilde{\rho}_k \tag{A.15}$$

and the center of mass velocity:

$$\boldsymbol{u} = \frac{1}{\rho} \sum_{k=1}^{2} \alpha_k \tilde{\rho}_k \hat{\boldsymbol{u}}_k \tag{A.16}$$

By substituting Eq. (A.15) and Eq. (A.16) into Eq. (A.13), and summing up for both phases, the continuity equation was rewritten as:

$$\frac{\partial \rho}{\partial t} + \nabla \cdot (\rho \boldsymbol{u}) = 0 \tag{A.17}$$

Then we will demonstrate that the velocity field in the two phase flow system is also divergence free, as the same with single phase incompressible flow. By simple mathematical manipulation on Eq. (A.17), the divergence of the velocity field was expressed as:

$$\nabla \cdot \boldsymbol{u} = -\frac{1}{\rho}(\frac{\partial \rho}{\partial t} + \boldsymbol{u}\nabla\rho) = -\frac{1}{\rho}\frac{\mathrm{D}\rho}{\mathrm{D}t} \tag{A.18}$$

where $\mathrm{D}/\mathrm{D}t$ is the substantial derivative. In this case when the two phase flow system was composed of two incompressible and immersible fluids without phase change, the substantial derivative of the density field is equal to zero. This concludes that the velocity field is still divergence free. Therefore we have:

$$\nabla \cdot \boldsymbol{u} = 0 \tag{A.19}$$

This relation was used to formulate the pressure equation in the solver.

Note that similar relation could be obtained for center of volume velocity field $\boldsymbol{v}$, defined as:

$$\boldsymbol{v} = \sum_{k=1}^{2} \alpha_k \hat{\boldsymbol{u}}_k \tag{A.20}$$

If we divide Eq. (A.13) by $\tilde{\rho}_k$, assuming that for each phase $\tilde{\rho}_k$ is a constant. Then sum up the equations for the two phases, we obtain the following relation:

$$\nabla \cdot \boldsymbol{v} = 0 \tag{A.21}$$

This indicated that $\boldsymbol{u} = \boldsymbol{v}$. Actually this is due to the no-slip interface condition. Therefore in VOF method we do not explicitly distinguish the difference between the center of mass velocity and center of volume velocity.

The same methodology was adopted to evaluate each term in Eq. (A.14). Start from the first term in the left-hand side of Eq. (A.14):

$$\sum_{k=1}^{2} \frac{\partial \alpha_k \tilde{\rho}_k \hat{\boldsymbol{u}}_k}{\partial t} = \frac{\partial \rho \boldsymbol{u}}{\partial t} \tag{A.22}$$

Substituting of Eq. (A.16) into the convective term gave the following expression (Eq. (16) in Manninen and Taivassalo (1996))

$$\sum_{k=1}^{2} \nabla \cdot (\alpha_k \tilde{\rho}_k \hat{\boldsymbol{u}}_k \hat{\boldsymbol{u}}_k) = \nabla \cdot (\rho \boldsymbol{u})\boldsymbol{u} + \nabla \cdot \sum_{k=1}^{2} \alpha_k \rho_k \boldsymbol{u}_{Mk} \boldsymbol{u}_{Mk} \tag{A.23}$$

where $\boldsymbol{u}_{Mk}$ is the diffusion velocity. In VOF formulation this velocity vanishes due to no slip boundary condition on the interface.

The averaged stress tensor was rewritten in terms of pressure and extra stresses:

$$\tilde{\boldsymbol{T}}_k = -\tilde{P}_k \boldsymbol{I} + \tilde{\boldsymbol{\tau}}_k \tag{A.24}$$

Define the averaged pressure and stress as:

$$P = \sum_{k=1}^{2} \alpha_k \tilde{P}_k \tag{A.25}$$

$$\boldsymbol{\tau} = \sum_{k=1}^{2} \alpha_k \tilde{\boldsymbol{\tau}}_k \tag{A.26}$$

Therefore the summation of molecular diffusion term for both phases yields:

$$\sum_{k=1}^{2} \nabla \cdot (\alpha_k \tilde{\boldsymbol{T}}_k) = -\nabla P + \nabla \cdot \boldsymbol{\tau} \tag{A.27}$$

Substituting Eq. (A.22), Eq. (A.23) and Eq. (A.27) into Eq. (A.14) yields the averaged momentum equation:

$$\frac{\partial \rho \boldsymbol{u}}{\partial t} + \nabla \cdot (\rho \boldsymbol{u})\boldsymbol{u} = -\nabla P + \nabla \cdot \boldsymbol{\tau} + \rho \boldsymbol{g} + \boldsymbol{M}_m \tag{A.28}$$

Here the deviatoric stress tensor $\boldsymbol{\tau}$ should usually contain contributions from molecular stress, turbulence stress and extra stress due to diffusion. However the last two contributions were neglected due to neglect of turbulence effect (See Section 2.1 for reasons), and no slip interface condition. Only bulk molecular stress was retained. Recall the constitutive relation for Newtonian fluid:

$$\boldsymbol{\tau} = \mu \left[\nabla \boldsymbol{u} + (\nabla \boldsymbol{u})^T - \frac{2}{3}(\nabla \cdot \boldsymbol{u})\mathbf{I} \right] \tag{A.29}$$

where

$$\mu = \sum_{k=1}^{2} \alpha_k \tilde{\mu}_k \tag{A.30}$$

Inserting Eq. (A.29) into Eq. (A.28) reads:

$$\frac{\partial \rho \boldsymbol{u}}{\partial t} + \nabla \cdot (\rho \boldsymbol{u})\boldsymbol{u} = -\nabla P + \nabla \cdot \left\{ \mu \left[\nabla \boldsymbol{u} + (\nabla \boldsymbol{u})^T - \frac{2}{3}(\nabla \cdot \boldsymbol{u})\mathbf{I} \right] \right\} + \rho \boldsymbol{g} + \boldsymbol{M}_m \tag{A.31}$$

The surface tension effect, i.e. $\boldsymbol{M}_m$, was evaluated as

$$\boldsymbol{M}_m = \sigma_T \langle \kappa'_\alpha \nabla X_1 \rangle = \sigma_T \kappa_\alpha \nabla \alpha \tag{A.32}$$

where κ_α is the averaged curvature of the interface. So indeed the surface tension force here was converted to a volume force applied in the interface transition region, based on the continuum surface force (CSF) model proposed in Brackbill et al. (1992).

In the implementation of the solver, instead of using total pressure, the excess pressure p^* was used:

$$p = P - \rho \boldsymbol{g} \cdot \boldsymbol{x} \tag{A.33}$$

where $\boldsymbol{x}$ is the coordinate vector. Substituting Eq. (A.33) and Eq. (A.32) into Eq. (A.31) reads:

$$\frac{\partial \rho \boldsymbol{u}}{\partial t} + \nabla \cdot (\rho \boldsymbol{u})\boldsymbol{u} = -\nabla p - (\boldsymbol{g} \cdot \boldsymbol{x})\nabla \rho + \nabla \cdot \left\{ \mu \left[\nabla \boldsymbol{u} + (\nabla \boldsymbol{u})^T - \frac{2}{3}(\nabla \cdot \boldsymbol{u})\mathbf{I} \right] \right\} + \sigma_T \kappa_\alpha \nabla \alpha \tag{A.34}$$

It could be seen that due to Eq. (A.19), $(\nabla \cdot \boldsymbol{u})\mathbf{I} = 0$. However in the implementation of OpenFOAM, this term was not removed but slightly changed. Having in mind that:

$$\nabla \cdot \boldsymbol{u} = \mathrm{Tr}((\nabla \boldsymbol{u})^T) = 0 \tag{A.35}$$

By substituting of Eq. (A.35) into Eq. (A.29) yields the constitutive relation used in OpenFOAM:

$$\boldsymbol{\tau} = \mu \left[\nabla \boldsymbol{u} + (\nabla \boldsymbol{u})^T - \frac{2}{3}(\nabla \cdot \boldsymbol{u})\mathbf{I} \right] = \nabla \cdot [\mu(\nabla \boldsymbol{u})] + \nabla \cdot \left\{ \mu \left[(\nabla \boldsymbol{u})^T - \frac{2}{3}\,\mathrm{Tr}((\nabla \boldsymbol{u})^T)\mathbf{I} \right] \right\} \tag{A.36}$$

This gives the momentum conservation equation actually coded in *interFoam* solver:

$$\frac{\partial \rho \boldsymbol{u}}{\partial t} + \nabla \cdot (\rho \boldsymbol{u})\boldsymbol{u} - \nabla \cdot [\mu(\nabla \boldsymbol{u})] - \nabla \cdot \left\{ \mu \left[(\nabla \boldsymbol{u})^T - \frac{2}{3}\,\mathrm{Tr}((\nabla \boldsymbol{u})^T)\mathbf{I} \right] \right\} = -\nabla p - (\boldsymbol{g} \cdot \boldsymbol{x})\nabla \rho + \sigma_T \kappa_\alpha \nabla \alpha \tag{A.37}$$

The reason why $2/3\,\mathrm{Tr}((\nabla \boldsymbol{u})^T)\boldsymbol{I}$ was retained was not clear to the author, but most probably it was used to numerically stabilize the solution, since divergence free velocity field can not be always guaranteed when applying Eq. (A.37). However in the present work, the fourth term on the left-hand side of Eq. (A.37) was not further investigated. This gave the final governing equation for two phase system in the context of VOF formulation:

$$\nabla \cdot \boldsymbol{u} = 0 \tag{A.38}$$

$$\frac{\partial \rho \boldsymbol{u}}{\partial t} + \nabla \cdot (\rho \boldsymbol{u})\boldsymbol{u} - \nabla \cdot [\mu(\nabla \boldsymbol{u})] = -\nabla p - (\boldsymbol{g} \cdot \boldsymbol{x})\nabla \rho + \sigma_T \kappa_\alpha \nabla \alpha \tag{A.39}$$

Appendix B. The reconstruction of cell center value from cell face value in OpenFOAM

In OpenFOAM the reconstruction of cell center value from cell face value is via the function fvc::reconstruct. Assume two vector fields $\boldsymbol{a}$ and $\boldsymbol{a}_f$, where $\boldsymbol{a}_f$ is the known vector field at the cell faces and $\boldsymbol{a}$ is the cell center vector field that will be reconstructed from $\boldsymbol{a}_f$. The following relation is the basic assumption for the reconstruction:

$$\sum_f \boldsymbol{n}_f(\boldsymbol{S}_f \cdot \boldsymbol{a}) = \sum_f \boldsymbol{n}_f(\boldsymbol{S}_f \cdot \boldsymbol{a}_f) \tag{B.1}$$

With the relation that

$$\boldsymbol{n}_f(\boldsymbol{S}_f \cdot \boldsymbol{a}) = (\boldsymbol{n}_f \otimes \boldsymbol{S}_f) \cdot \boldsymbol{a} \tag{B.2}$$

the following equation was obtained:

$$\sum_f (\boldsymbol{n}_f \otimes \boldsymbol{S}_f) \cdot \boldsymbol{a} = \sum_f \boldsymbol{n}_f(\boldsymbol{S}_f \cdot \boldsymbol{a}_f) \tag{B.3}$$

Recall the distributive property of the inner product, the summation could be performed before inner production in the left-hand side of Eq. (B.3):

$$\sum_f ((\boldsymbol{n}_f \otimes \boldsymbol{S}_f) \cdot \boldsymbol{a}) = \left(\sum_f (\boldsymbol{n}_f \otimes \boldsymbol{S}_f) \right) \cdot \boldsymbol{a} \tag{B.4}$$

Combine Eq. (B.4) and Eq. (B.3), the vector field $\boldsymbol{a}$ was obtained as:

$$\boldsymbol{a} = \left(\sum_f \boldsymbol{n}_f \otimes \boldsymbol{S}_f \right)^{-1} \cdot \left(\sum_f \boldsymbol{n}_f(\boldsymbol{S}_f \cdot \boldsymbol{a}_f)) \right) \tag{B.5}$$

This reconstruction procedure indeed recovers the cell values by integrating the contributions of the face values. Below it is demonstrated that Eq. (B.1) is second order accurate on one dimensional equidistant mesh with Δx as the grid space between two nodes. The general arrangement of the grid is shown in Fig. B.1, where $\boldsymbol{a}_w$ and $\boldsymbol{a}_e$ are the known values at west and east faces of the grid cell. In one dimensional finite volume formulation, all the vectors were reduced to scalars with positive or negative sign indicating the directions. Meanwhile the face normal vectors were the same as face unit vectors, since each grid cell has a unit face area. Assume the direction of $\boldsymbol{a}$ is positive, then Eq. (B.1) was simplified as:

$$a - a_e + a - a_w = 0 \tag{B.6}$$

Expand the velocity field from cell center to cell face by Taylor series, the following expression was obtained:

$$a_w = a - \frac{1}{2}\Delta x \frac{\partial a}{\partial x} + \frac{1}{8}\Delta x^2 \frac{\partial^2 a}{\partial x^2} + \dots \tag{B.7}$$

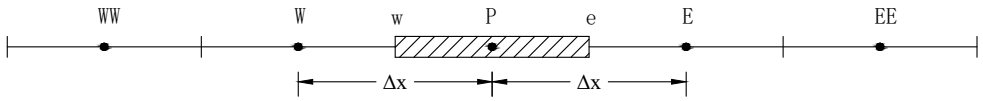

Figure B.1: The equidistant mesh grid in 1D for demonstration of order of accuracy of Eq. (B.1).

$$a_e = a + \frac{1}{2}\Delta x \frac{\partial a}{\partial x} + \frac{1}{8}\Delta x^2 \frac{\partial^2 a}{\partial x^2} + \dots \tag{B.8}$$

By inserting Eq. (B.7) and Eq. (B.8) into Eq. (B.6), it was found that the leading truncation error is

$$-\frac{1}{4}\Delta x^2 \frac{\partial^2 a}{\partial x^2} \tag{B.9}$$

Therefore Eq. (B.1) (or the reconstruction procedure) is second order accurate, and this conclusion could be easily extended to three dimensional finite volume mesh.

References

Bai, W., Eatock Taylor, R., 2007. Numerical simulation of fully nonlinear regular and focused wave diffraction around a vertical cylinder using domain decomposition. Applied Ocean Research 29, 55–71. doi:10.1016/j.apor.2007.05.005.

Bohorquez, P., 2008. Study and numerical simulation of sediment transport in free surface flow. Phd thesis. University of Malaga.

Boris, J.P., Book, D.L., 1973. Flux-corrected transport. I. SHASTA, a fluid transport algorithm that works. Journal of Computational Physics 11, 38–69. URL: http://dx.doi.org/10.1016/0021-9991(73)90147-2, doi:10.1016/0021-9991(73)90147-2.

Brackbill, J., Kothe, D., Zemach, C., 1992. A continuum method for modeling surface tension. Journal of Computational Physics 100, 335–354. URL: http://www.sciencedirect.com/science/article/pii/002199919290240Y, doi:10.1016/0021-9991(92)90240-Y.

Chau, F.P., Eatock Taylor, R., 1992. Second-order wave diffraction by a vertical cylinder. Journal of Fluid Mechanics 240, 571. doi:10.1017/S0022112092000211.

Chen, B., Lu, L., Greated, C.a., Kang, H., 2015. Investigation of wave forces on partially submerged horizontal cylinders by numerical simulation. Ocean Engineering 107, 23–31. URL: http://linkinghub.elsevier.com/retrieve/pii/S002980181500339X, doi:10.1016/j.oceaneng.2015.07.026.

Chen, L., Zang, J., a.J. Hillis, Morgan, G., a.R. Plummer, 2014. Numerical investigation of wavestructure interaction using OpenFOAM. Ocean Eng. 88, 91–109. URL: http://linkinghub.elsevier.com/retrieve/pii/S0029801814002169, doi:10.1016/j.oceaneng.2014.06.003.

Christensen, E.D., 2006. Large eddy simulation of spilling and plunging breakers. Coastal Engineering 53, 463–485. URL: http://linkinghub.elsevier.com/retrieve/pii/S0378383905001705, doi:10.1016/j.coastaleng.2005.11.001.

Christensen, E.D., Deigaard, R., 2001. Large eddy simulation of breaking waves. Coastal Engineering 42, 53–86. doi:10.1016/S0378-3839(00)00049-1.

Darwish, M.S., Moukalled, F., 2003. TVD schemes for unstructured grids. International Journal of Heat and Mass Transfer 46, 599–611. doi:10.1016/S0017-9310(02)00330-7.

Dean, W.R., 1948. On the reflexion of surface waves by a submerged circular cylinder. Mathematical Proceedings of the Cambridge Philosophical Society 44, 483–491. doi:10.1017/S0305004100024506.

Delhaye, J.M., 1974. Jump conditions and entropy sources in two phase systems. Local instant formulation. International journal of multiphase flow 1, 395–409.

Dixon, A.G., Greated, C.A., Salter, S.H., 1979. Wave forces on partially submerged cylinders. J. Waterw. Port Coastal Ocean Eng. URL: http://cedb.asce.org/cgi/WWWdisplay.cgi?5014996.

Drew, D.a., 1983. Mathematical Modeling of Two-Phase Flow. volume 15. doi:10.1146/annurev.fl.15.010183.001401.

Easson, W.J., Greated, C.A., Duranni, T.S., 1985. Force Spectra from Partially Submerged Circular Cylinders in Random Seas. J. Waterw. Port Coastal Ocean Eng. 111, 856–879. doi:10.1061/(ASCE)0733-950X(1985)111:5(856).

Eatock Taylor, R., Hung, S.M., 1987. Seond order diffraction forces on a vertical cylinder in regular waves. Applied Ocean Research 9, 19–30. doi:10.1016/S0141-1187(88)80017-8.

Fenton, J., 1988. The numerical solution of steady water wave problems. Computers & Geosciences 14, 357–368. doi:10.1016/0098-3004(88)90066-0.

Filip, G.P., 2013. High-Resolution Numerical Simulation of Turbulent Interfacial Marine Flows. Ph.d. thesis. University of Michigan.

Francois, M.M., Cummins, S.J., Dendy, E.D., Kothe, D.B., Sicilian, J.M., Williams, M.W., 2006. A balanced-force algorithm for continuous and sharp interfacial surface tension models within a volume tracking framework. Journal of Computational Physics 213, 141–173. doi:10.1016/j.jcp.2005.08.004.

Godunov, S.K., 1959. A difference method for numerical calculation of discontinuous solutions of the equations of hydrodynamics. Matematicheskii Sbornik 89, 271–306.
Gopala, V.R., van Wachem, B.G., 2008. Volume of fluid methods for immiscible fluid and free surface flows. Chemical Engineering Journal 141, 204–221. URL: http://linkinghub.elsevier.com/retrieve/pii/S1385894708000028, doi:10.1016/j.cej.2007.12.035.
Greenshields, C., 2014. OpenFOAM 2.3.0: Multiphase Modelling. http://openfoam.org/release/2-3-0/multiphase. Accessed: 2016-07-13.
Harlow, F.H., Welch, J.E., 1965. Numerical calculation of time-dependent viscous incompressible flow of fluid with free surface. Physics of fluids 8, 2182–2185. doi:10.1063/1.1761178.
Harten, A., 1983. High resolution schemes for hyperbolic conservation laws. Journal of computational physics 49, 357–393.
Higuera, P., Lara, J.L., Losada, I.J., 2013. Realistic wave generation and active wave absorption for Navier-Stokes models. Application to OpenFOAM. Coastal Engineering 71, 102–118. doi:10.1016/j.coastaleng.2012.07.002.
Hirt, C., Nichols, B., 1981. Volume of fluid (VOF) method for the dynamics of free boundaries. J. Comput. Phys. 39, 201–225. URL: http://linkinghub.elsevier.com/retrieve/pii/0021999181901455, doi:10.1016/0021-9991(81)90145-5.
Hoang, D.a., van Steijn, V., Portela, L.M., Kreutzer, M.T., Kleijn, C.R., 2013. Benchmark numerical simulations of segmented two-phase flows in microchannels using the Volume of Fluid method. Computers & Fluids 86, 28–36. URL: http://linkinghub.elsevier.com/retrieve/pii/S0045793013002612, doi:10.1016/j.compfluid.2013.06.024.
Isaacson, M., Cheung, K.f., 1990. Time Domain Solution for Second Order Wave Diffraction. J. Waterw. Port Coastal Ocean Eng. 116, 191–210. doi:10.1061/(ASCE)0733-950X(1990)116:2(191).
Ishii, M., Hibiki, T., 2010. Thermo-Fluid Dynamics of Two-Phase Flow. SpringerLink : Bücher, Springer New York. URL: https://books.google.dk/books?id=K9LP5omwjQcC.
Issa, R.I., 1986. Solution of the implicitly discretised fluid flow equations by operator-splitting. Journal of Computational Physics 62, 40–65. URL: http://www.sciencedirect.com/science/article/pii/0021999186900999, doi:10.1016/0021-9991(86)90099-9.
Jacobsen, N.G., Fuhrman, D.R., Fredsøe, J., 2012. A wave generation toolbox for the open-source CFD library: OpenFoam. Int. J. Numer. Methods Fluids 70, 1073–1088. doi:10.1002/fld.2726.
Jasak, H., 1996. Error Analysis and Estimation for the Finite Volume Method with Applications to Fluid Flows. Phd thesis. Imperial College, University of London.
Karrholm, F.P., 2008. Numerical Modelling of Diesel Spray Injection , Turbulence Interaction and Combustion. Ph.d. thesis. Chalmers University of Technology.
Kristiansen, D., 2010. Wave Induced Effects on Floaters of Aquaculture plants. Ph.d. thesis. Norwegian University of Science and Technology.
Kristiansen, D., Faltinsen, O.M., 2008. A study of wave loads on fixed horizontal cylinders in the free surface, in: Proceedings of 8th International Conference on Hydrodynamics.
Liu, Y., Xue, M., Yue, D.K.P., 2001. Computations of fully nonlinear three-dimensional wavewave and wavebody interactions. Part 2. Nonlinear waves and forces on a body. Journal of Fluid Mechanics 438, 41–66. doi:10.1017/S0022112001004384.
Longuet-Higgins, M.S., Cokelet, E.D., 1976. The Deformation of Steep Surface Waves on Water. I. A Numerical Method of Computation. Proceedings of the Royal Society A: Mathematical, Physical and Engineering Sciences 350, 1–26. doi:10.1098/rspa.1976.0092.
Manninen, M., Taivassalo, V., 1996. On the mixture model for multiphase flow. Technical Report. Technical Research Center of Finland.
Márquez Damián, S., 2013. An Extended Mixture Model for the Simultaneous Treatment of Short and Long Scale Interfaces. Ph.D. thesis. UNIVERSIDAD NACIONAL DEL LITORAL.
Martin, P., Dixon, A., 1983. The scattering of regular surface waves by a fixed, half-immersed, circular cylinder. Appl. Ocean Res. 5, 13–23. doi:10.1016/0141-1187(83)90053-6.
Mehlum, E., 1980. A circular cylinder in water waves. Applied Ocean Research 2, 171–177. URL: http://linkinghub.elsevier.com/retrieve/pii/0141118780900152, doi:10.1016/0141-1187(80)90015-2.
Mencinger, J., Žun, I., 2007. On the finite volume discretization of discontinuous body force field on collocated grid: Application to VOF method. Journal of Computational Physics 221, 524–538. doi:10.1016/j.jcp.2006.06.021.
Molin, B., 1979. Second-order diffraction loads upon three-dimensional bodies. Applied Ocean Research 1, 197–202. doi:10.1016/0141-1187(79)90027-0.
Morison, J., Johnson, J., Schaaf, S., 1950. The Force Exerted by Surface Waves on Piles. J. Petroleum Technology 2, 149–154. doi:http://dx.doi.org/10.2118/950149-G.
Ogilvie, T.F., 1963. First- and second-order forces on a cylinder submerged under a free surface. J. Fluid Mech. 16, 451–472. doi:10.1017/S0022112063000896.
Olsson, E., Kreiss, G., 2005. A conservative level set method for two phase flow. Journal of Computational Physics 210, 225–246. URL: http://linkinghub.elsevier.com/retrieve/pii/S0021999105002184, doi:10.1016/j.jcp.2005.04.007.
Olsson, E., Kreiss, G., Zahedi, S., 2007. A conservative level set method for two phase flow II. Journal of Computational Physics 225, 785–807. doi:10.1016/j.jcp.2006.12.027.
Osher, S., 1988. Fronts propagating with curvature- dependent speed: algorithms based on Hamilton-Jacobi formulations. Journal of Computational Physics 79, 12–49.
Park, J.C., Kim, M.H., Miyata, H., Chun, H.H., 2003. Fully nonlinear numerical wave tank (NWT) simulations and wave run-up prediction around 3-D structures. Ocean Engineering 30, 1969–1996. doi:10.1016/S0029-8018(03)00041-6.
Paulsen, B.T., Bredmose, H., Bingham, H.B., Jacobsen, N.G., 2014. Forcing of a bottom-mounted circular cylinder by steep regular water waves at finite depth. J. of Fluid Mech. 755, 1–34. URL: http://www.journals.cambridge.org/abstract_

S0022112014003863, doi:10.1017/jfm.2014.386.
Rhie, C.M., Chow, W.L., 1983. Numerical study of the turbulent flow past an airfoil with trailing edge separation. AIAA Journal 21, 1525–1532. URL: http://dx.doi.org/10.2514/3.8284, doi:10.2514/3.8284.
Rusche, H., 2002. Computational Fluid Dynamics of Dispersed Two-Phase Flows at High Phase Fractions. Phd thesis. The university of London. doi:10.1145/1806799.1806850.
Scardovelli, R., Zaleski, S., 1999. Direct Numerical Simulation of Free-Surface and Interfacial Flow. Annual Review of Fluid Mechanics 31, 567–603. URL: http://www.annualreviews.org/doi/abs/10.1146/annurev.fluid.31.1.567, doi:10.1146/annurev.fluid.31.1.567.
Seng, S., 2012. Slamming And Whipping Analysis Of Ships. Phd thesis. Technical University of Denmark.
Skotner, C., Jonsson, I., Skourup, J., 1994. Wave forces on a large, horizontal submerged cylinder. Ocean Eng. 8018, 711–731. URL: http://www.sciencedirect.com/science/article/pii/0029801894900485.
Skourup, J., Jonsson, I., 1992. Computations of forces on, and particle orbits around, horizontal cylinders under steep waves. doi:10.1016/0029-8018(92)90022-V.
Sumer, B., Fredsøe, J., 1997. Hydrodynamics Around Cylindrical Structures. Advanced series on ocean engineering, World Scientific. URL: http://books.google.dk/books?id=CZJSngEACAAJ.
Ubbink, O., Issa, R., 1999. A Method for Capturing Sharp Fluid Interfaces on Arbitrary Meshes. Journal of Computational Physics 153, 26–50. URL: http://www.sciencedirect.com/science/article/pii/S0021999199962769, doi:10.1006/jcph.1999.6276.
Ursell, F., 1950a. Surface waves on deep water in the presence of a submerged circular cylinder. I. Mathematical Proceedings of the Cambridge Philosophical Society 46, 141–152.
Ursell, F., 1950b. Surface waves on deep water in the presence of a submerged circular cylinder. II. Mathematical Proceedings of the Cambridge Philosophical Society 46, 153–158.
Vada, T., 1987. A numerical solution of the second-order wave-diffraction problem for a submerged cylinder of arbitrary shape. J. Fluid Mech. 174, 23. doi:10.1017/S0022112087000028.
Van Leer, B., 1977. Towards the ultimate conservative difference scheme III. Upstream-centered finite-difference schemes for ideal compressible flow. Journal of Computational Physics 23, 263–275. URL: http://www.sciencedirect.com/science/article/pii/0021999177900948, doi:http://dx.doi.org/10.1016/0021-9991(77)90094-8.
Vernier, P., Delhaye, J., 1968. General two-phase flow equations applied to the thermohydrodynamics of boiling nuclear reactor. Energie primaire 4, 3–43.
Vuorinen, V., Keskinen, J.P., Duwig, C., Boersma, B., 2014. On the implementation of low-dissipative RungeKutta projection methods for time dependent flows using OpenFOAM. Computers & Fluids 93, 153–163. URL: http://linkinghub.elsevier.com/retrieve/pii/S0045793014000334, doi:10.1016/j.compfluid.2014.01.026.
Weller, H., 2002. A code independent notation for finite volume algorithmns. Technical Report. Nabla Ltd.
Wroniszewski, P.a., Verschaeve, J.C., Pedersen, G.K., 2014. Benchmarking of NavierStokes codes for free surface simulations by means of a solitary wave. Coastal Engineering 91, 1–17. URL: http://linkinghub.elsevier.com/retrieve/pii/S0378383914000842, doi:10.1016/j.coastaleng.2014.04.012.
Wu, G., Taylor, R.E., 1990. The second order diffraction force on a horizontal cylinder in finite water depth. Applied Ocean Research 12, 106–111. doi:10.1016/S0141-1187(05)80001-X.
Zalesak, S.T., 1979. Fully multidimensional flux-corrected transport algorithms for fluids. Journal of Computational Physics 31, 335–362. URL: http://www.sciencedirect.com/science/article/pii/0021999179900512, doi:10.1016/0021-9991(79)90051-2.
Zhang, S., Zhao, X., Bayyuk, S., 2014. Generalized formulations for the rhie-chow interpolation. Journal of Computational Physics 258, 880–914. URL: http://dx.doi.org/10.1016/j.jcp.2013.11.006, doi:10.1016/j.jcp.2013.11.006.

5 Simulating the responses of floating fish cages in current and waves

---

In preparation as:
Chen, H. & Christensen, E.D., 2017. Simulating the responses of floating fish cages in current and waves. To be Submitted.

Simulating the responses of floating fish cages in current and waves

Hao Chen[a,*], Erik Damgaard Christensen[a]

[a]*Section of Fluid Mechanics, Coastal and Maritime Engineering, Department of Mechanical Engineering, Technical University of Denmark, DK-2800 Kgs. Lyngby, Denmark*

Abstract

We present a novel numerical model for simulating current and wave interaction with aquaculture fish cages. The numerical model is based on the computational fluid dynamic approach, and the modelling framework is OpenFOAM-3.0.x. The floater, the net and its interaction effects were considered in the model. The sinker and the mooring lines were not directly resolved, but their effects were partially considered. The model couples a hydrodynamic solver, a rigid body motion solver, a mesh motion solver and a structural solver in a segregated manner. In the numerical model, the net cage was modelled as a set of dynamic porous media zones, and a lumped mass model was coupled with it to realize fluid-structure interaction analysis for the net cage. The floater was treated as a rigid body, and it was resolved by the body-fitted computational mesh in the fluid domain. The motion equation for the floater was set up based on the principle of linear and angular momentum balance, and different motion integration schemes were implemented and tested in the numerical model. The numerical model was successfully validated against three sets of available experimental data in the open literature. The first set of validation cases treat the floater motion in regular waves. The purpose is to validate the six degree of freedom motion solver for the floater. The second set of validation cases focus on the fluid-structure interaction analysis of the net cage. The final one was related to the whole floater-net system in regular waves, and combined current and wave condition.

Keywords: fish cage, floating body, fluid-structure interaction, OpenFOAM

1. Introduction

Hydrodynamic analysis on the floating fish farms for offshore aquaculture has been presented during the past few years. This comes with the fast development of aquaculture industry in the world. With the growing demand of food due to increasing population over the world, aquaculture is expected to continue making important contributions on world food security and nutrition supplement.

The fish cage itself is a compliant and flexible system, whose components interact with each other. It usually contains four important components, namely the net cage, the floater, the mooring system and the sinker system. Each of them plays an important role and has its unique functionality. It is in general not straightforward to perform global analysis on the floating fish cage system. Some simplifications and assumptions are needed, in order to set up a realistic numerical model. For instance, there exist a large number of twines and knots for a net cage, which are usually grouped together into fewer meshes in the numerical model. The geometry of the floater sometimes is complex, and contains several torus. But it is usually simplified into a circular cross section in the numerical model. However, on the other side one still needs to properly take the effects of all the components into account, although sometimes it may be not necessary to model all of them.

There exist several publications on investigations of fish cages in current and waves in 2D scenario, both numerically and experimentally. Fu et al. (2014) conducted series of experiments to investigate the roles of the net and the floater in steady and oscillatory flow. In their experiments the wave condition was

*Corresponding author, tel.: (45) 50302416; e-mail address: hchen@mek.dtu.dk; fax (45) 45251961.

Nomenclature

α	volume fraction field
β	parameter for Newmark integration scheme
$\boldsymbol{\tau}_f$	torque on the floater
$\boldsymbol{a}_f$	linear acceleration of the floater
$\boldsymbol{F}_f^{buoy}$	buoyancy force on the floater
$\boldsymbol{F}_f^{grav}$	gravitation force on the floater
$\boldsymbol{F}_f^{moor}$	mooring line force on the floater
$\boldsymbol{F}_f^{net}$	force on the floater due to the connecting net cage
$\boldsymbol{F}_f^{wave}$	wave force on the floater
$\boldsymbol{F}_n^{buoy}$	buoyancy force on the node in the lumped mass model
$\boldsymbol{F}_n^{grav}$	gravitation force on the node in the lumped mass model
$\boldsymbol{F}_n^{struct}$	structural force on the node in the lumped mass model
$\boldsymbol{F}_n^{wave}$	wave force on each panel element in the lumped mass model
$\boldsymbol{g}$	gravitation acceleration
$\boldsymbol{L}_f$	angular momentum
$\boldsymbol{Q}_f$	altitude of the floater
$\boldsymbol{q}_f$	rotation quaternion for the floater
$\boldsymbol{q}_m$	rotation quaternion for the mesh cells
$\boldsymbol{r}$	The difference between the acceleration of the floater at current and previous time step
$\boldsymbol{r}$	the difference between the acceleration of the floater at current and previous time step
$\boldsymbol{S}$	porous resistance due to net
$\boldsymbol{u}$	fluid velocity field
$\boldsymbol{u}_c$	The convective velocity field in arbitrary Lagrangian-Eulerian formulation, defined as $\boldsymbol{u}_c = \boldsymbol{u} - \boldsymbol{u}_m$
$\boldsymbol{u}_f$	linear velocity of the floater
$\boldsymbol{u}_m$	The mesh velocity field
$\boldsymbol{u}_n$	velocity field for the net cage
$\boldsymbol{u}_r$	compression velocity field
$\boldsymbol{x}$	Cartesian coordinate system
$\boldsymbol{x}_f$	center of mass of the floater
$\boldsymbol{x}_m$	mesh cell position
Δt	time step
γ	parameter for Newmark integration scheme
γ_p	empirical coefficient for the added mass coefficient C_m
$\langle \boldsymbol{u} \rangle$	volume averaged velocity field
$\langle p_d \rangle^f$	intrinsic volume averaged pore pressure field
μ	dynamic viscosity
ω	relaxation factor for the acceleration of the floater
ω_a	parameter for Crank-Nicolson integration scheme
ω_u	parameter for Crank-Nicolson integration scheme
ρ	density field
a_m	A scalar field for motion scale of each grid cell
C	quadratic porous resistance coefficients
C_m	added mass coefficient due to presence of the net
d	The distance from the cell center to the boundary patch of the floater
k	the counter for sub-iteration within one time step
k_{max}	the maximum number of sub-iteration within one time step
m_f	mass of the floater
$m_{f,a}$	added mass of the floater
n	porosity of the net
p	total pressure field
p_d	excess pressure field
S_n	solidity ratio of the net cage
U	magnitude of steady current velocity
W_S	weight of the sinker

realized by forced oscillation of the system, therefore the effects of the vertical motion of water particles were neglected. The magnitude of the forces on the floater-net system under these conditions were measured and analysed. Based on the experimental data, a hybrid empirical-numerical method was proposed in Ma et al. (2016). In Bardestani and Faltinsen (2013), real waves were generated in a narrow wave tank to investigate the interaction between the net, floater and sinker system. Meanwhile, the numerical model was also developed in their work. The force model they applied was based on the screen type force model developed in Kristiansen and Faltinsen (2012). A time domain potential code was used for computation of the floater motion, where a convolution integral term appeared in the equation which accounts for the memory effects. In their experiments, it was found that due to the relative motion between the sinker and the floater, very high snap load was observed under regular wave condition with some certain wave period and height. This kind of load occurred in very short time, but the magnitude is several times larger than the load in steady state condition. Their numerical model could also reproduce this phenomenon with satisfying agreement. In addition, the mooring line forces in combined current and wave conditions were also measured in experiments and predicted by the numerical model.

3D computation on the model scale fish cage has also been presented in the previous works, but with different level of simplifications. Zhao et al. (2007) presented a numerical study where the floater, net and bottom sinker were all included. The floater was treated as a rigid body, and six degree of freedom motion was considered, where the hydrodynamic force on the floater was calculated based on Morison type force model. The net panel was represented by a lumped mass model, and the forces on the panel were also calculated based on Morison equation. Similar model was also applied in e.g. Xu et al. (2013) and Xu et al. (2014). Further improvement was introduced in Zhao et al. (2015), where a curved beam model was used for structural response of the floater. Modal superposition method was introduced to express the deformation of the floater as a weighted sum of eigenmodes. Kristiansen and Faltinsen (2015) extended his previous developed screen type force model to include the other important components of the fish cage. A truss model was applied for modeling of net cage deformation, where a linear system of equations for the truss tensions were solved at each time step. The hydrodynamic force on the floater not only includes viscous force and Froude-Kriloff force, but also diffraction and radiation force. This considers disturb of the floater motion on the incoming wave field. A variety of experiments were also conducted in Kristiansen and Faltinsen (2015), to provide benchmark data for the numerical model.

With the increasing computer resources which enhance the ability to handle nonlinear equations, the computational fluid dynamic (CFD) approach is progressively gaining attention in coastal and offshore hydrodynamic community over the past decades. From the recent publications, CFD method has also been applied to model flow through fishing nets as shown in Patursson et al. (2010) and Zhao et al. (2013), where the net was modeled as a sheet of porous media, and the geometry of the net at pore scale was not resolved. This indicates that the CFD approach combined with a porous media model is a feasible way to model the flow through and around net cages.

However, there still exist some limitations on this approach. The net cage itself is quite flexible under current and wave conditions, but currently the CFD approach is mainly applied to model net cages fixed in a framework. Attempts have also been made to couple the lumped mass model with the porous media model to achieve fluid-structure interaction (FSI) analysis in Yao et al. (2016), Bi et al. (2014b) and Bi et al. (2014a), but only under steady current condition. In general, in steady current the floater can be neglected in the numerical model. The net cage is the main component to stand the current load. The only influence of the floater is that, a boundary layer is formulated when the current flows around the floater. But this only affects the forces at the top layer of the net. However, under wave condition, simulating the motion of the floater is important, since it is the main contributor to the forces on the net (Lader and Fredheim, 2006). As mentioned above, due to relative motion between the floater and the sinker, the net may get slack and very high snap load may occur.

Therefore, in the present work we aim to develop a CFD model for integrated analysis of the flexible floating fish cage system in current and wave conditions, where motion of the floater will also be considered. Hereby the model will fully consider the fluid-structure interaction effects of the net cage, and the interaction between the flow field and the rigid body motion of the floater. The mooring lines and sinkers are not modelled, but their effects are partially considered. The modelling framework is the open source toolbox

OpenFOAM, and the version 3.0.x is utilized. Here .x means bug fixed version. This version introduces some new features on the rigid body motion solver, therefore is preferred and used.

The remainder of the paper is organized as follows. In Section 2 a detailed description of the numerical model is given, which includes an overview of the numerical model in Section 2.1, a description of the hydrodynamic model for the floater and the net cage in Section 2.2, a description of the rigid body motion model for the floater in Section 2.3, a description of the mesh motion model in Section 2.4 and a description of the structural model for the net cage and its coupling with the floater motion model and the hydrodynamic model in Section 2.5. Then the numerical model is carefully validated against three sets of existing experimental data in the open literature in Section 3. The first set of validation cases concern with the motion of the floater in regular wave conditions, which validate the six degree of freedom motion solver. The second set of validation cases are focused on the plane net panel in steady current, which demonstrates the applicability of the FSI solver for the net cage. Then the final validation cases move on to the global analysis of the floating fish cages, where the snap load on the net cage and the mooring line forces are compared with the experimental data. Finally conclusions are given in Section 4.

2. Description of the numerical model

2.1. Overview of the numerical model

In the present numerical model, we mainly consider to model the floater-net system for a fish cage. More specifically, a body-fitted mesh was applied in the numerical model, where the floater was resolved by the mesh, i.e. the floater was treated as a boundary patch in the fluid domain. A six degree of freedom motion solver was applied to obtain the motion status of the floater at each time step. The net cage was modelled as a sheet of porous media, and it was coupled with a lumped mass structural model. The advantage of the applied coupling scheme is that, the hydrodynamic solver for the net did not require the mesh to conform the deformed geometry of the net. This means that the mesh only deformed according to the motion of the floater. Then the porous media zones representing the net were updated based on the nodal position of the deformed net. The relative information was transferred between the floater and the net by the mutual mass points that were attached in both the net and the floater.

2.1.1. Assumptions and simplifications

Presently in our numerical model, the mooring lines were not directly resolved. Instead, the restoring forces from the mooring lines were added into the motion equation for the floater. There exist different choices for the force-elongation relation. However, we mainly use the simple linear relation, i.e. the mooring lines were simplified as linear springs. Therefore, the mooring line dynamics and its coupling with the floater were not considered in the numerical model.

In addition, the sinker of the fish cage was also neglected in the numerical model. But the constant forces on the sinker were added to the bottom mass points of the net cage. Therefore, the whole model was simplified from a multi-body problem to a single body problem. The reason for this simplification is that, the constant force on the sinker completely dominated the fluctuating part, and in principle, the constant force was not difficult to estimate. In steady current, it includes the gravity force, buoyancy force and the mean drag force, which was calculated based on Morison equation. But in wave condition, the mean drag force was also neglected, considering the rather weak orbital motion of water particles at that depth.

The benefit of neglecting the sinker in the model is that it greatly eases the manipulation of the mesh. The mesh quality for a single body problem is usually much better than for a multi-body problem, especially considering the amplitude of motion of the sinker. In large steady current flow, the movement of the sinker may easily distort the mesh. But the price we paid is that the transient load on the sinker and its interaction effects with the net cage were not considered. However, if one wants to include the sinker motion in the model, immerse boundary method should be applied.

2.1.2. Flowchart of the algorithm

The numerical model was extended based on the solver developed in Jacobsen et al. (2012), which is a multiphase solver for two incompressible, isothermal and immiscible fluids with the functionality on generation and absorption of gravity water waves. In the present work, it was coupled with the rigid body motion solver, the mesh motion solver, and the structural solver for the net in a segregated manner. A flow chart of the solver is given in Fig. 1.

For modeling of the floater motion in waves, one should be careful on the so-called artificial added mass effect. This is due to that the densities of the floater and the water are usually in the same order of magnitude. Therefore, part of the fluid may act as an extra mass on the structural degrees of freedom at the coupling interface. In sequentially staggered schemes the fluid forces depend upon the predicted displacement of the floater rather than the corrected ones, which contain a portion of incorrect coupling forces. It is this artificial contribution to the coupling which yields the instability (Förster et al., 2007). Therefore, in order to handle this issue properly, we introduced the concept of sub-iteration within one time step in the numerical model, which converges the computed quantities to some degree.

To begin with a sub-iteration, the forces on the floater were updated first by adding the gravity force, the updated wave force, mooring line force and the force from the net cage. Then the linear acceleration $\boldsymbol{a}_f$ and the torque $\boldsymbol{\tau}_f$ were obtained based on the force and momentum balance equations. Given $\boldsymbol{a}_f$ and $\boldsymbol{\tau}_f$, the linear velocity $\boldsymbol{u}_f$, angular momentum $\boldsymbol{L}_f$, position of center of mass $\boldsymbol{x}_f$ and altitude $\boldsymbol{Q}_f$ were calculated by choosing a proper integration method. Then the boundary patch of the floater was moved, and the mesh was deformed based on the calculated motion status. Following the dynamic mesh motion solver, the flow solver solved Navier-Stokes equations for a mixture of water and air phases. Specifically in the porous media region, the Navier-Stokes equations were volume averaged to consider the effect of the net cage on the fluid. With the updated pressure and velocity field, one could determine the hydrodynamic forces on the net cage. A lumped mass structural model was coupled with the hydrodynamic model to resolve the deformation of the net cage. This forms a closed sub-iteration.

From our practical experience, in many cases with small to medium wave amplitudes, a loosely coupled algorithm is still capable and can produce results with satisfying accuracy. But when the wave height is increasing, which leads to large amplitude of floater motion, sub-iterations are necessary. We usually choose 4 - 8 sub-iterations within one time step. Too many sub-iterations do not necessarily improve the simulation results. Below from Section 2.2 to 2.5, a thorough introduction on each part of the numerical model is given, with illustrations on how it is coupled with other solvers.

2.2. Hydrodynamic model

2.2.1. Hydrodynamic model for the floater

The governing equations in the fluid domain except the net region are the mass and momentum conservation for two incompressible, isothermal and immiscible fluids:

$$\nabla \cdot \boldsymbol{u} = 0 \tag{1}$$

$$\frac{\partial \rho \boldsymbol{u}}{\partial t} + \nabla \cdot \rho \boldsymbol{u}\boldsymbol{u}_c - \nabla \cdot \mu \nabla \boldsymbol{u} = -\nabla p_d - (\boldsymbol{g} \cdot \boldsymbol{x}) \nabla \rho \tag{2}$$

Due to application of the moving mesh technique, the relative velocity $\boldsymbol{u}_c$ was applied as the convective velocity field, which allows the physical quantities to be described in arbitrary Lagrangian-Euler formulation. $\boldsymbol{u}_c$ itself is not necessary to be divergence free, but was constrained to obey the space conservation law, in case any mass conservation error was introduced. In addition, the excess pressure field p_d was applied in Eq. (2), and the total pressure field was reconstructed at every time step as:

$$p = p_d + \rho \boldsymbol{g} \cdot \boldsymbol{x} \tag{3}$$

In order to handle the generation and propagation of free surface waves, a free surface tracking method needs to be applied. Volume of fluid (VOF) method was applied in the present model, and a transport

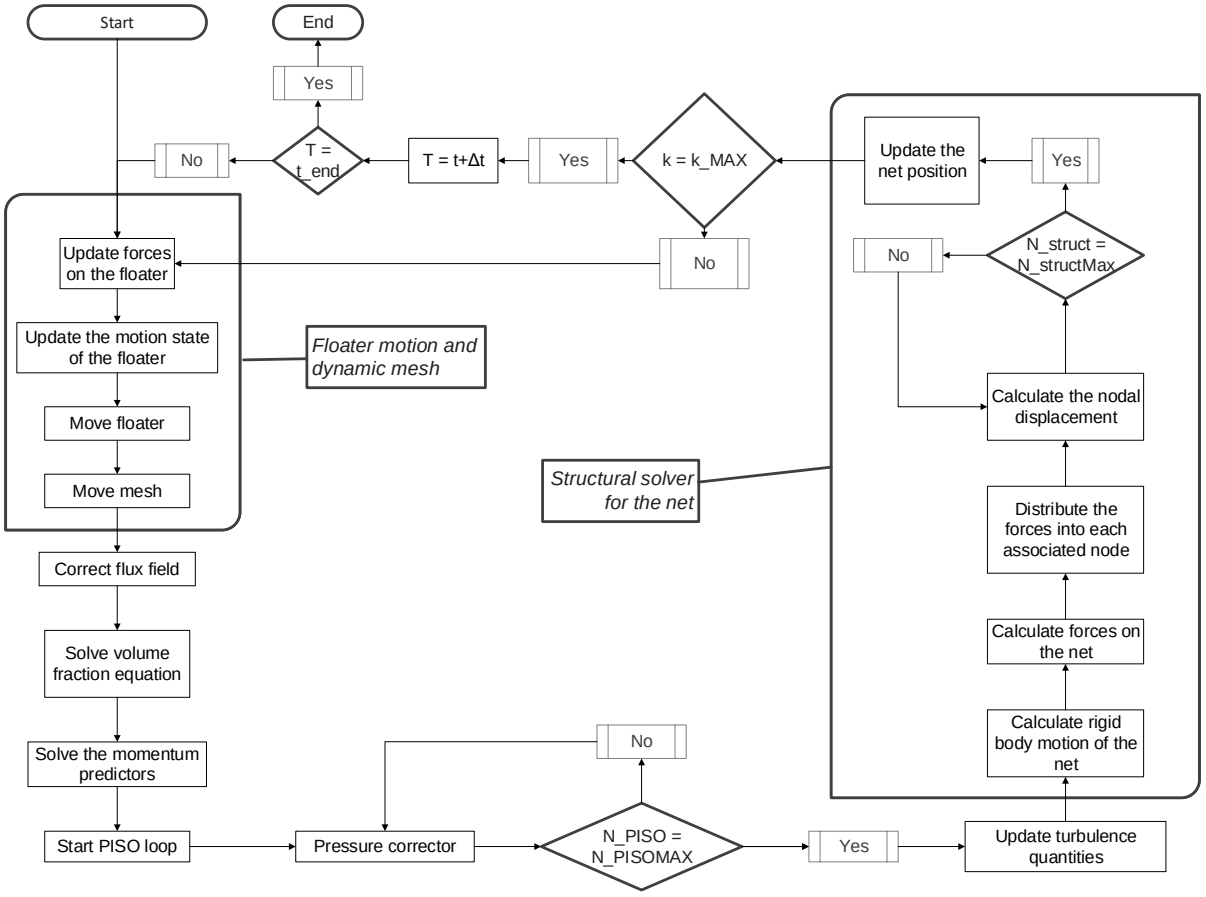

Figure 1: Flow chart of the custom solver.

equation for the volume fraction field was solved:

$$\frac{\partial \alpha}{\partial t} + \nabla \cdot \boldsymbol{u}_c \alpha + \nabla \cdot (\boldsymbol{u}_r \alpha (1-\alpha)) = 0 \tag{4}$$

Eq. (4) is a modified version of the original scalar transport equation, e.g. as shown in Hirt and Nichols (1981). An extra term was introduced to sharpen the free surface. The formulation itself was inherited from the two-fluid model, where $\boldsymbol{u}_r$ was denoted as the relative velocity between two fluids. However in volume of fluid method, the slip velocity does vanish. $\boldsymbol{u}_r$ was retained solely to numerically compress the free surface, and it is only active in the free surface region, due to the multiplication of $\alpha(1-\alpha)$.

2.2.2. Hydrodynamic model for the net

The porous media model was applied to describe the flow through the net cage, where it was represented by a sheet of porous media structures. Jensen et al. (2014) revised the formulation for porous media model, based on the volume averaged Navier-Stokes equations. This set of equations were directly applied in the present model:

$$\nabla \cdot \langle \boldsymbol{u} \rangle = 0 \tag{5}$$

$$(1+C_m)\frac{1}{n}\frac{\partial\rho\langle\boldsymbol{u}\rangle}{\partial t}+\frac{1}{n}\nabla\cdot\frac{\rho}{n}\langle\boldsymbol{u}\rangle\langle\boldsymbol{u}_c\rangle=-\nabla\langle p_d\rangle^f-\boldsymbol{g}\cdot\boldsymbol{x}\nabla\rho+\frac{1}{n}\nabla\cdot\mu\nabla\langle\boldsymbol{u}\rangle+\boldsymbol{S} \tag{6}$$

In Eq. (6), due to the averaging process, several new quantities were introduced. The coefficient C_m represents the added mass effect on the porous skeleton, and was expressed as:

$$C_m=\gamma_p\frac{1-n}{n} \tag{7}$$

where γ_p is an empirical coefficient, and takes the value of 0.34. The resistance force used in Eq. (6) was expressed as:

$$\boldsymbol{S}=-\frac{1}{2}\rho C|\boldsymbol{u}-\boldsymbol{u_n}|(\boldsymbol{u}-\boldsymbol{u_n}) \tag{8}$$

Eq. (8) uses the relative velocity for calculation of the resistance. This is necessary when there exists relative motion between the fluid and net structure. C is the quadratic porous resistance coefficient matrix. In its local coordinate it is given as:

$$C=\begin{bmatrix}C_1 & 0 & 0\\ 0 & C_2 & 0\\ 0 & 0 & C_3\end{bmatrix} \tag{9}$$

The formula proposed in Chen and Christensen (2016) was applied in the present work to relate the magnitude of C_1, C_2 and C_3 with the physical parameters of the net cage. Eq. (4) was also revised to include the porosity effect:

$$\frac{\partial\alpha}{\partial t}+\frac{1}{n}\nabla\cdot\boldsymbol{u}_c\alpha+\frac{1}{n}\nabla\cdot\boldsymbol{u}_r\alpha(1-\alpha)=0 \tag{10}$$

The correction by the factor 1/n ensures that it is only the pore volume that can be filled with water.

2.3. Rigid body motion model for the floater

A rigid body motion solver was applied to obtain the motion status of the floater, which includes the altitude $\boldsymbol{Q}_f$, the linear velocity $\boldsymbol{u}_f$, the linear acceleration $\boldsymbol{a}_f$, the torque $\boldsymbol{\tau}_f$, the angular momentum $\boldsymbol{L}_f$ and the position of center of mass of the floater $\boldsymbol{x}_f$. However, below for simplicity, we only focus on the linear quantities, namely $\boldsymbol{a}_f$, $\boldsymbol{u}_f$ and $\boldsymbol{x}_f$. But the angular quantities in principle are obtained in the same way. Note that the momentum balance was evaluated in the local body reference which was aligned with the principle axis of the inertia and with origin at the center of mass, since the moment of inertia was not changing in that coordinate system. Transformation of the quantities between local and global reference was via the altitude tensor of the body $\boldsymbol{Q}_f$. For instance, the torque was transformed to the local body reference before calculating the angular momentum as:

$$\boldsymbol{\tau}_{f,local}=\boldsymbol{Q}_f^T\cdot\boldsymbol{\tau}_f \tag{11}$$

For the linear motion, the governing equation is the Newton's second law:

$$m_f\boldsymbol{a}_f=\boldsymbol{F}_f^{wave}+\boldsymbol{F}_f^{grav}+\boldsymbol{F}_f^{moor}+\boldsymbol{F}_f^{net} \tag{12}$$

where the wave force on the floater is simply the integration of the total pressure and the viscous forces on the floater boundary patch at the instantaneous wet surface at each time step:

$$\boldsymbol{F}_f^{wave}=-\int_{S_b}p\boldsymbol{n}_b\,\mathrm{d}S-\int_{S_b}\boldsymbol{\tau}\cdot\boldsymbol{n}_b\,\mathrm{d}S \tag{13}$$

where S_b is the boundary surface of the floater, $\boldsymbol{n}_b$ is the normal unit vector of the floater surface pointing to the fluid domain. $\boldsymbol{\tau}$ is the viscous stress of the fluid flow. The gravity force was a constant input from the user. The mooring forces were determined by the instantaneous position of the floater and the anchor.

The force from the net cage was transferred from the lumped mass model. Then the velocity and center of mass of the floater was obtained by integrating the acceleration at each time step:

$$\boldsymbol{u}_f = \int \boldsymbol{a}_f \, \mathrm{d}t \tag{14}$$

$$\boldsymbol{x}_f = \int \boldsymbol{u}_f \, \mathrm{d}t \tag{15}$$

There exists different schemes for numerical integration of Eq. (14) and Eq. (15). In the present work we tested four of them, namely the leapfrog scheme, the Newmark scheme, the implicit-explicit Adams-Bashforth-Moulton scheme and the Crank-Nicolson scheme. below we will give a detailed introduction on each scheme.

2.3.1. Leapfrog scheme

Leapfrog scheme is a scheme that is particularly useful for mechanical dynamic system. It has the strength of time-reversibility. In addition, due to its symplectic nature, it conserves the energy of the system, therefore maintains the stability in long-time simulations. The implementation of this scheme follows the way as shown in Dullweber et al. (1997), which consists of three steps to update the motion state:

1. Update the velocity at half new time step (Eq. (16)), and update the position at new time step based on the half time-step velocity (Eq. (17)).
2. Update the force and acceleration at new time step.
3. Update the velocity at new time step (Eq. (18)).

$$\boldsymbol{u}_{f,n}^{0.5} = \boldsymbol{u}_{f,o} + \frac{1}{2}\boldsymbol{a}_{f,o}\Delta t \tag{16}$$

$$\boldsymbol{x}_{f,n}^{1} = \boldsymbol{x}_{f,o} + \boldsymbol{u}_{f,n}^{0.5}\Delta t \tag{17}$$

$$\boldsymbol{u}_{f,n}^{1} = \boldsymbol{u}_{f,n}^{0.5} + \frac{1}{2}\boldsymbol{a}_{f,n}^{1}\Delta t \tag{18}$$

Here the subscript n denotes the value at new time step, o denotes the value at old time step. The number at the superscript denotes the number of sub-iteration, e.g. $\boldsymbol{u}_{f,n}^{1}$ is the velocity of the floater at the first sub-iteration at new time step, i.e. the predicted velocity of the floater at new time step.

The leapfrog scheme is second order accurate. Furthermore, from the above description, it is shown that the leapfrog scheme is fundamentally an explicit scheme. Therefore, one should note that when coupling it with the flow solver, the leapfrog scheme must be applied *only once* within one time step. This indeed requires that only weakly/loosely coupled algorithm is allowed for this FSI problem, i.e. no implicit iterations within one time step. In addition, leapfrog scheme formally is only stable for fixed time step (see e.g. Devolder et al. (2015a) and Birdsall and Langdon (2004)). Therefore, if the simulation is performed using variable time step, stability issues may arise due to both reasons. In Section 3.1 when we validated the motion solver, we suffered from some stability problems using this integration method for simulation of floater motion in large amplitude waves. Hereby In Section 3.1 no results are presented using this method.

2.3.2. Newmark scheme

Newmark (1959) proposed an integration method that is widely used in numerical evaluation of the dynamic response of structures. It is a one step implicit method that consists of two parameters β and γ (Note that if $\gamma = 0$ and $\beta = 0$, it reduces to an explicit method). The formulation to update the velocity and position of the body is given below:

$$\boldsymbol{u}_{f,n}^{k+1} = \boldsymbol{u}_{f,o} + \Delta t(\gamma \boldsymbol{a}_{f,n}^{k} + (1-\gamma)\boldsymbol{a}_{f,o}) \tag{19}$$

$$\boldsymbol{x}_{f,n}^{k+1} = \boldsymbol{x}_{f,o} + \boldsymbol{u}_{f,o}\Delta t + \beta(\Delta t)^2 \boldsymbol{a}_{f,n}^{k} + (0.5-\beta)(\Delta t)^2 \boldsymbol{a}_{f,o} \tag{20}$$

We adopted a set of commonly used parameters with $\gamma = 0.5$ and $\beta = 0.25$, which yields the so-called constant average acceleration method. This means that within one time step the acceleration is presumed to be constant. It is second order accurate and unconditionally stable.

2.3.3. Adams-Bashforth-Moulton scheme

An alternative integration method was adopted in Seng (2012) and Chow and Ng (2016). It is based on the predictor-corrector method, where at the predictor stage an explicit second order Adams-Bashforth method is applied. The predicted solution was further corrected by several implicit correctors based on Adams-Moulton scheme. Since typically Adams-Bashforth scheme requires known values at the previous two time step, the values at the first time step were calculated based on Newmark scheme.

The detailed description of this explicit-implicit Adams-Bashforth-Moulton scheme for variable time step is given below:

1. At the predictor stage, apply Eq. (21) and Eq. (22) for prediction of velocity and displacement.
2. At the corrector stage:
   - Update the force and acceleration based on the velocity and displacement from the previous iterations.
   - Correct the velocity and displacement based on Eq. (23) and Eq. (24).
   - Set $k = k + 1$ and repeat the correctors until $k = k_{max}$.

$$\boldsymbol{u}_{f,n}^{1} = \boldsymbol{u}_{f,o} + \frac{\Delta t}{2}\left[\left(2 + \frac{\Delta t}{\Delta t_0}\right)\boldsymbol{a}_{f,o} - \frac{\Delta t}{\Delta t_0}\boldsymbol{a}_{f,oo}\right] \tag{21}$$

$$\boldsymbol{x}_{f,n}^{1} = \boldsymbol{x}_{f,o} + \frac{\Delta t_0}{16}\left[\left(1 + \frac{8\Delta t}{\Delta t_0}\right)\boldsymbol{u}_{f,n}^{1} + \left(\frac{7\Delta t}{\Delta t_0} - 1\right)\boldsymbol{u}_{f,o} + \frac{\Delta t}{\Delta t_0}\boldsymbol{u}_{f,oo}\right] \tag{22}$$

$$\boldsymbol{u}_{f,n}^{k+1} = \boldsymbol{u}_{f,o} + \frac{\Delta t_0}{16}\left[\left(1 + \frac{8\Delta t}{\Delta t_0}\right)\boldsymbol{a}_{f,n}^{k} + \left(\frac{7\Delta t}{\Delta t_0} - 1\right)\boldsymbol{a}_{f,o} + \frac{\Delta t}{\Delta t_0}\boldsymbol{a}_{f,oo}\right] \tag{23}$$

$$\boldsymbol{x}_{f,n}^{k+1} = \boldsymbol{x}_{f,o} + \frac{\Delta t_0}{16}\left[\left(1 + \frac{8\Delta t}{\Delta t_0}\right)\boldsymbol{u}_{f,n}^{k+1} + \left(\frac{7\Delta t}{\Delta t_0} - 1\right)\boldsymbol{u}_{f,o} + \frac{\Delta t}{\Delta t_0}\boldsymbol{u}_{f,oo}\right] \tag{24}$$

where the subscript *oo* denotes the value at the previous two time step.

2.3.4. Crank-Nicolson scheme

Crank-Nicolson scheme was introduced as a blending scheme between the explicit and implicit Euler scheme. Two parameters ω_a and ω_v were applied to adjust the blending. The formulation of Crank-Nicolson scheme was given as:

$$\boldsymbol{u}_{f,n} = \boldsymbol{v}_{f,o} + \Delta t(\omega_a \boldsymbol{a}_{f,n} + (1-\omega_a)\boldsymbol{a}_{f,o}) \tag{25}$$

$$\boldsymbol{x}_{f,n} = \boldsymbol{x}_{f,o} + \Delta t(\omega_u \boldsymbol{u}_{f,n} + (1-\omega_u)\boldsymbol{u}_{f,o}) \tag{26}$$

If $\omega_a = 0.5$ and $\omega_u = 0.5$, this method is equivalent to the Newmark integration with $\gamma = 0.5$ and $\beta = 0.25$. We choose another set of parameter where $\omega_a = 0.9$ and $\omega_u = 0.9$, and the results are given in Section 3.1.

2.3.5. Dynamic under-relaxation factor for the acceleration

As mentioned above in Section 2.1.2 within each time step, we introduced several sub-iterations. From the second sub-iteration, i.e. the first corrector step, we adopted an under-relaxation factor for the acceleration. Therefore, the acceleration at kth sub-iteration was relaxed as:

$$\boldsymbol{a}_{f,n}^{k} = \omega_n^k \boldsymbol{a}_{f,n}^{k} + (1-\omega_n^k)\boldsymbol{a}_{f,n}^{k-1} \tag{27}$$

The purpose to apply under-relaxation is to enhance the stability of the motion solver. When we compute the acceleration and integrate the motion based on Eq. (12), one part of the force is in phase with the acceleration, namely the added mass force in $\boldsymbol{F}_f^{wave}$. But for a CFD solver, it is usually impossible to separate this part and move it to the left hand of Eq. (12). Hereby this is a source that leads to the instability for the numerical integration. Application of under-relaxation could effectively stabilize the solver.

Proper selection of the relaxation factor is important for the integration schemes. A too high under-relaxation factor may not work robustly, while too low value may slow down the convergence. We applied a dynamic under-relaxation factor as the same in Dunbar et al. (2015), and it was calculated as:

$$\omega_n^k = -\omega_n^{k-1} \frac{\boldsymbol{r}_n^{k-1} \cdot (\boldsymbol{r}_n^k - \boldsymbol{r}_n^{k-1})}{\left|\boldsymbol{r}_n^k - \boldsymbol{r}_n^{k-1}\right|^2} \tag{28}$$

where $\boldsymbol{r}^k$ was defined as the difference between acceleration of the floater at the current and the previous sub-iteration:

$$\boldsymbol{r}_n^k = \boldsymbol{a}_{f,n}^{k} - \boldsymbol{a}_{f,n}^{k-1} \tag{29}$$

Note that application of Eq. (28) requires the availability of $\boldsymbol{r}^k$ and $\boldsymbol{r}^{k-1}$, hereby it was applied from the third sub-iteration. At the second sub-iteration, we applied a fixed under-relaxation factor. Actually Söding (2001) found that the optimal relaxation factor was tightly related to the added mass of the floating body:

$$\boldsymbol{a}_{f,n}^{k} = \frac{m_f \boldsymbol{a}_{f,n}^{k} + m_{f,a}\boldsymbol{a}_{f,n}^{k-1}}{m_{f,a} + m_f} = \omega_n^k \boldsymbol{a}_{f,n}^{k} + (1-\omega_n^k)\boldsymbol{a}_{f,n}^{k-1} \tag{30}$$

which leads to the following expression:

$$\omega_n^k = \frac{m_f}{m_f + m_{f,a}} \tag{31}$$

Devolder et al. (2015b) shows some different convergence behavior by using different relaxation factors when the ratio between the added mass and mass of the floating body was fixed. If Eq. (31) was applied to calculate the under-relaxation factor, the solution was converged very fast. However, in the present work we did not apply Eq. (31), since the added mass is usually not straightforward to estimate and it is frequency dependent. A fixed value of 0.3 was applied in the second sub-iteration for the acceleration of the floater.

2.4. Mesh motion model

In the present model we applied the deforming mesh technique. This method has the advantages that it could precisely describe the moving boundary, which means that no interpolation method is needed like immerse boundary method. However, care should be taken when there exists large amplitude of motion for the moving boundaries, especially for rotation motion. Mesh quality can often degrade under such motions. Presently we applied the newly developed mesh morphing technique in OpenFOAM to preserve the mesh quality near the floater.

By application of this method, the computational domain was divided into three regions based on the movement of the cells. These three mesh regions were identified by the distance d from the cell center to the moving boundary. Two values d^i and d^o were designated by the user in the input file. For each cell, if $d < d^i$, then it belongs to the inner region. On the contrast, if $d > d^o$, the cell is in the outer region. The rest are in the middle region. The mesh cells in the inner region, which were close to the moving

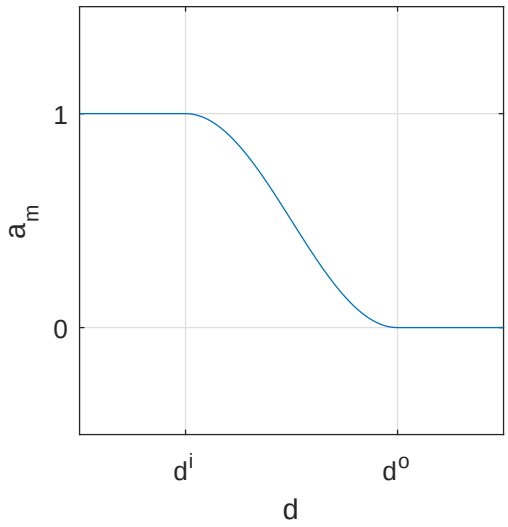

Figure 2: Variation of the motion scale a_m as a function of distance d.

boundary, were moved like a rigid body following the motion of the moving boundary. Hereby the mesh quality near the moving boundary was preserved. In addition, there exists an outer region, where the cells were stationary. Therefore it is not necessary to move all the cells in the computational domain, which may significantly reduce the computational time when the domain is large. In between the outer region and the inner region, the cells were moved based on the interpolated displacement of the floater motion. In practice, Palm et al. (2016) suggests that d^i should be in the order of boundary layer thickness, which is the minimum requirement, since the cells immersed in the boundary layer should be in high quality. Presently we set it equal to the diameter of the floater. d^o should be determined based on the motion amplitude of the floater, but it is limited by the minimum distance to any domain boundary.

The spherical linear interpolation (SLERP) method was applied to interpolate the cell displacement and rotation in the middle region. A non-dimensional scale parameter a_m was defined here for SLERP method:

$$a_m = \frac{1}{2} - \frac{1}{2}\cos\left(\pi \frac{d^o - d}{d^o - d^i}\right) \tag{32}$$

It was seen that a cosine profile was applied in this region, as shown in Fig. 2 which plots the value of a_m as a function of d. This guarantees a smooth transition for the cell displacement and rotation between the outer region and the inner region.

In OpenFOAM, the implementation of SLERP method uses the concept of quanternion to ease the expression for rotation motion. In addition, the translation and rotation were wrapped together as the so-called septernion. Each septernion was composed of a translation vector and a rotation quaternion. The translation vector for a specific cell at the new time step was scaled as:

$$\boldsymbol{x}^k_{m,n} = \boldsymbol{x}_{m,0} + a^k_{m,n}(\boldsymbol{x}^k_{f,n} - \boldsymbol{x}_{f,0}) \tag{33}$$

where the subscript 0 denotes the value of the quantity at the initial state. In addition, the rotation quaternion was scaled based on the rotation quaternion of the floater $\boldsymbol{q}_{f,n}$:

$$\boldsymbol{q}^k_{m,n} = \boldsymbol{q}_I(\boldsymbol{q}_I^{-1}\boldsymbol{q}^k_{f,n})^{a^k_{m,n}} \tag{34}$$

where $\boldsymbol{q}_{f,n}$ was transformed from the altitude matrix of the floater at the current time step and at the initial state, i.e. $\boldsymbol{Q}_{f,n}$ and $\boldsymbol{Q}_{f,0}$. $\boldsymbol{q}_I$ was the unit quanternion defined as $1 + 0\boldsymbol{i} + 0\boldsymbol{j} + 0\boldsymbol{k}$.

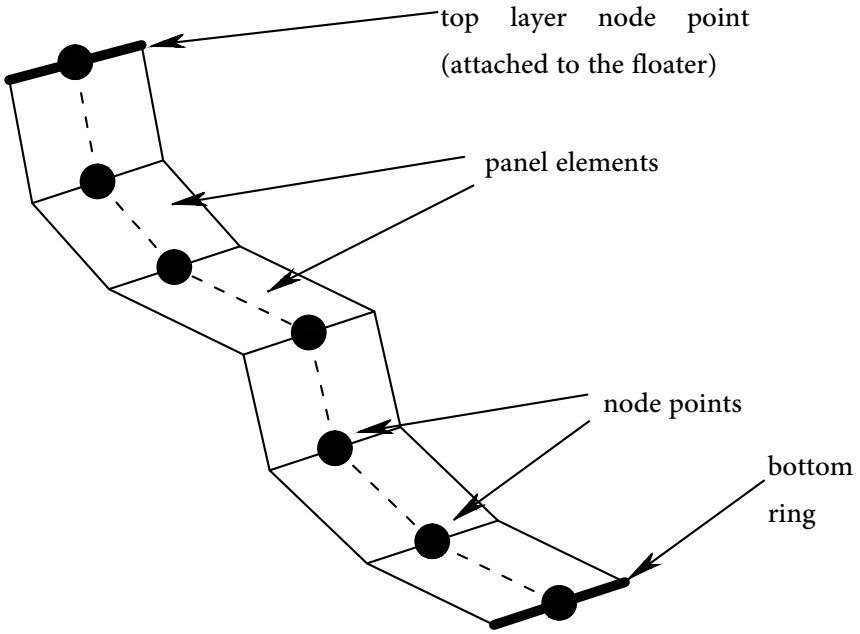

Figure 3: Illustration of the lumped mass structural model in 2D case.

2.5. Structure model for the net

2.5.1. Introduction to the lumped mass model

In order to resolve the deformation of the net at each time step, a lumped mass structural model was implemented and coupled with the hydrodynamic model. The implementation was based on Lader and Fredheim (2006). The idea is to represent the net as a set of nodes and panel elements. In 2D cases the net was vertically divided into panel elements with a node point at the intersection between each element, as shown in Fig. 3. In 3D cases the node points were placed at the element corners.

The forces acting on each node include hydrodynamic force $\boldsymbol{F}_n^{wave}$, structural force $\boldsymbol{F}_n^{struct}$, gravity force $\boldsymbol{F}_n^{grav}$ and buoyancy force $\boldsymbol{F}_n^{buoy}$. $\boldsymbol{F}_n^{grav}$ and $\boldsymbol{F}_n^{buoy}$ were constant and solely determined by the net properties. Wave force on each panel element was output from the hydrodynamic model based on the flow velocity and the net velocity:

$$\boldsymbol{F}_n^{wave} = \int_{V_P} \frac{1}{2}\rho C|\boldsymbol{u} - \boldsymbol{u_n}|(\boldsymbol{u} - \boldsymbol{u_n})\,\mathrm{d}V \tag{35}$$

where V_P is the volume of porous media zone. This force on the panel was distributed evenly into each node.

The connection between two nodes were modeled as a nonlinear spring. The constitutive relationship of the spring was obtained from experiments as shown in Lader and Fredheim (2006). The relation between the structural force and elongation was expressed as:

$$F_n^{struct} = \begin{cases} E_1\epsilon + E_2\epsilon^2 & \epsilon > 0 \\ 0 & \epsilon \leq 0 \end{cases} \tag{36}$$

where ϵ is the elongation of the spring. Hereby in the numerical model, the net only has negligible compression stiffness. The fitted coefficients are $E_1 = 1160$ N and $E_2 = 37300$ N. It should be mentioned that the experiments were conducted for a specific net panel made from Nylon, with a mass density of 1130 kg/m^3. Therefore, there might be variations for these two coefficients for other type of net material. Furthermore, the wet net may have a different constitution relationship from a dry net. And the application of anti-fouling

techniques on the net may also alter the coefficients. However, in the present work we applied this set of coefficients without further investigations, due to very limited data.

Given the forces on each node, Newton's second law was applied to obtain the acceleration. The linear velocity and the displacement were obtained in the same way with the floater motion, as shown in Eq. (14) and Eq. (15). An explicit Runge-Kutta method provided in OpenFOAM library was applied for the integration.

2.5.2. Coupling with the hydrodynamic model

The coupling of the hydrodynamic model with the structural model for the net was based on the concept of *dynamic porous media zone* in the static mesh. This means that in the hydrodynamic model, the net was represented by a set of dynamic porous media zones corresponding to the panel elements in the structural model. The mesh was not deformed again due to the deformation of the net. Instead at each time step, after moving the mesh due to the motion of the floater, the nodal position was transferred from the structural model to the hydrodynamic model. Then the grid cells in the porous media zones were updated based on the transferred nodal positions.

Sub-cycling of the time step for the structural solver was applied, as shown in Fig. 1 where the number of sub-cycling was denoted as N_{struct}. This is due to that the structural solver requires a rather small time step, approximately in the order of 10^{-5} s, while usually in flow solver the time step was around $10^{-3} - 10^{-4}$ s. Therefore the time step in flow solver was set as the global time step. It was assumed that under each global time step, the hydrodynamic load was constant. Under such constant load, the position of the net was evolved.

However, one should note that even with sub-cycling, the time step could not be too large. This is due to two reasons. The first reason is that with very large time step, the oscillations may occur for the hydrodynamic load of the net cages. The oscillation may further pollute the solution from the motion solver for the floater. Meanwhile, the solution for Eq. (4) also requires a rather small time step, in order to generate the incoming waves with very good quality. Hereby presently we set the maximum Courant number to be around 0.15 - 0.25.

2.5.3. Coupling with the floater motion

The interaction effects between the floater and the net cage were achieved by utilizing mutual mass points that were attached to both the floater and the net cage, as shown in Fig. 3 for the top layer node point. At each time step, the structural force from the top layer node point was calculated based on Eq. (36), and transferred from the lumped mass model to the floater motion model. After solving Eq. (14) and Eq. (15), the translation and rotation of the floater at the positions of the mass points were also stored. Hereby the structural force on the net cage and the induced deformation were calculated based on the updated positions of the top layer mass points.

3. Validation of the numerical model

3.1. Validation of the motion solver

The first set of validation cases are dedicated to the motion of floater without occurrence of the net cage. The purpose of the validation is to examine the performance of the motion solver for the floater, especially the different motion integration schemes. The experimental data we used were from Kristiansen (2010), where series of experiments were performed on wave interaction with a moored horizontal cylinder. The experiments were conducted in a narrow wave flume at the Department of Marine Technology, Norwegian University of Science and Technology. The flume has a dimension of $13.67 \times 0.6 \times 1.3$ m, which was equipped with a single-flap wavemaker to generate waves. The water depth was set to be 1 m. A circular horizontal cylinder was positioned at the free surface with diameter $D = 0.1$ m. It has a length of 0.58 m, and at two ends of the cylinder, end-plates made from transparent plexi-glass were applied to reduce the 3D flow effects. This gave a 5 mm gap at each end between the end plate and the walls of the tank to avoid any contact. The cylinder was placed at a distance of 6.5 m from the hinge of the wave paddle and kept its position by

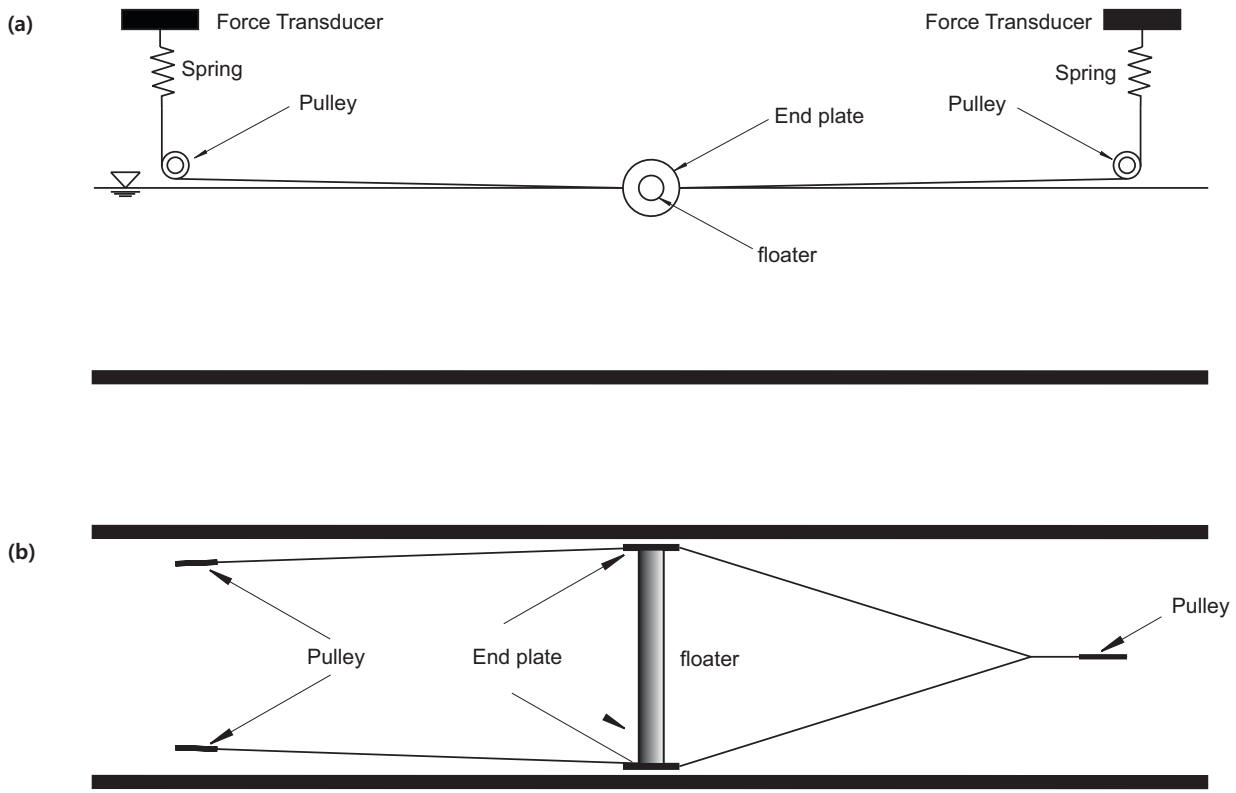

Figure 4: General setup for the experiments in Kristiansen (2010) for wave interaction with moored floaters. (a) side view. (b) top view.

Table 1: The parameters of the selected wave conditions for validation of the motion solver

Wave case no.	1	2	3	4	5
Wave period, T [s]	0.497	0.544	0.601	0.761	0.878
Wave height, H [m]	0.028	0.033	0.040	0.065	0.086

four mooring lines. Each mooring line was pointing nearly horizontally. On the wave maker side, the two mooring lines were applied and connected to two pulleys. Meanwhile on the other side towards the beach, two mooring lines were first joined to form a crowfoot before connecting to the pulley. A general sketch of the setup of the experiments is given in Fig. 4.

A 2D numerical wave tank was set up in order to reproduce the experiments. The simplified computational domain is shown in Fig. 5. The wave generation toolbox developed in Jacobsen et al. (2012) was applied to generate stream function waves. Two relaxation zones were applied at two ends of the tank to generate and absorb the waves. Since the end-plates of the cylinder was not modeled, an equivalent mass of the circular with end-plates $M = 3.940$ kg/m was used in the model. The mooring lines was not resolved but modeled as two linear springs, where the far end were pin-pointed at the coordinates of the contact point between the mooring line and the pulley. The other end of the mooring line was located at the model center, and moving with the body. The equivalent mooring stiffness was set to 88.2 N/m. Five wave conditions were selected for validation purpose as shown in Table 1.

The heave and sway motion of the floater under five wave conditions are given in Fig. 6 - 10. Three different motion integration methods as described in Section 2.3 were tested for all the five wave conditions, and the results are reported in these figures. The results from leapfrog scheme were not reported, since

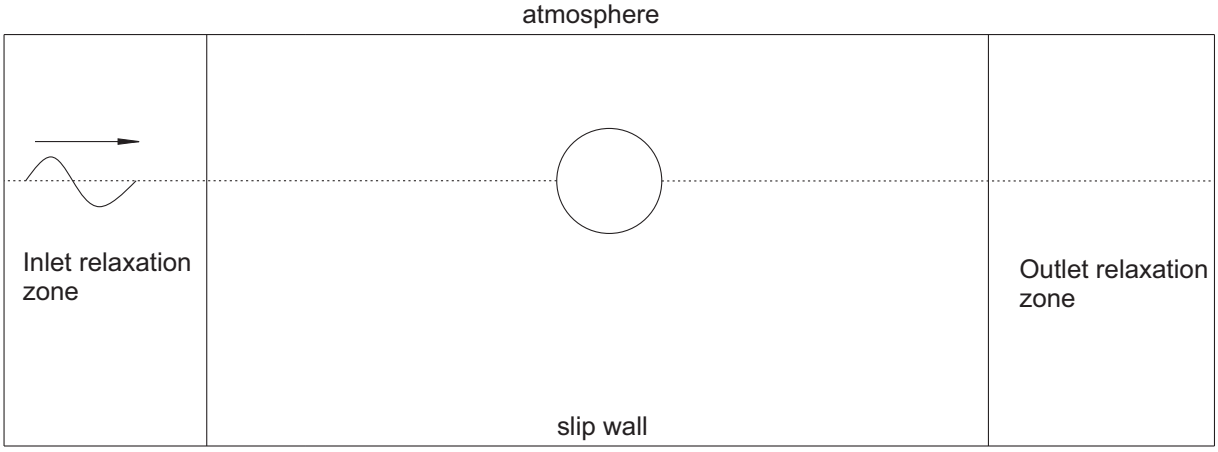

Figure 5: Sketch of the computational domain in the numerical model.

we suffered from some stability issues for cases with steep wave conditions, which has been also mentioned in Section 2.3. From the comparison between the simulated results and the experimental data, it was observed that the numerical model could in general reproduce the motion of the floater adequately within an acceptable error bound. A snapshot of the free surface wave and the floater at different time for wave case 5 is shown in Fig. 11, which clearly shows an overtopping process. This creates strong nonlinearity on free surface motions. In addition, during the overtopping process, the flow was locally separated from the boundary layer, where vorticity was induced. This creates a drag force, indicating that viscous effect plays a role. This has been explained in e.g. Kristiansen (2010) and Ong et al. (2017).

However in terms of the performance of different integration methods, we found that no one preforms consistently better in all the wave conditions than the others. The response amplitude operator (RAO) for heave and sway motion from the present model, the linear solution and the experiments in Kristiansen (2010) are given in Fig. 12, where a simple derivation for the linear solution is given in Appendix A. Note that RAO could only partially reflect the performance of the different methods, since the amplitudes of nonlinear motions were obtained as the mean value of half of difference between the crest and the trough. Therefore, in principle the shift up and down of the numerical results from the experimental data gave the same RAO value.

It was observed that in relatively long waves e.g. in wave case 5, the RAO value in heave motion is approaching one via linear solution. This means that the the floater simply follows the evolution of the free surface waves. This is due to that the ratio between the wave length and floater diameter is rather large, so the wave simply can not see the floater. Therefore diffraction effect is negligible. However, in reality overtopping created a quite irregular crest for the time series of heave motion, where dual peak may occur as shown in Fig. 10. The RAO value also slightly deviates from one in experimental data and numerical results. Meanwhile, we found some scattering on the experimental data in this case. But the numerical results from all the integration methods are within the bound of the data. Regarding the performance of each methods, we found that in such long waves, especially Crank-Nicolson scheme and the Newmark scheme have very similar performance. Adams-Bashforth-Moulton scheme also gave similar results except in wave case 5.

In shorter wave conditions, e.g. in wave case 1 and 2, the numerical results from different integration methods are distinguishable. For wave case 2, as described in Kristiansen (2010) instability was observed in the experiments, where the sway motion was increasing until the motion became significantly large and violent that contact between the model and the side walls occurred. Therefore the RAO value in sway mode in wave condition 2 is not plotted in Fig. 12. But in Fig. 7, by direct comparison of the time series of the sway motion, we notice that the same phenomenon was also observed from the numerical results. However, the amplitude of the sway motion was amplified more significantly than in the experiments. Results from

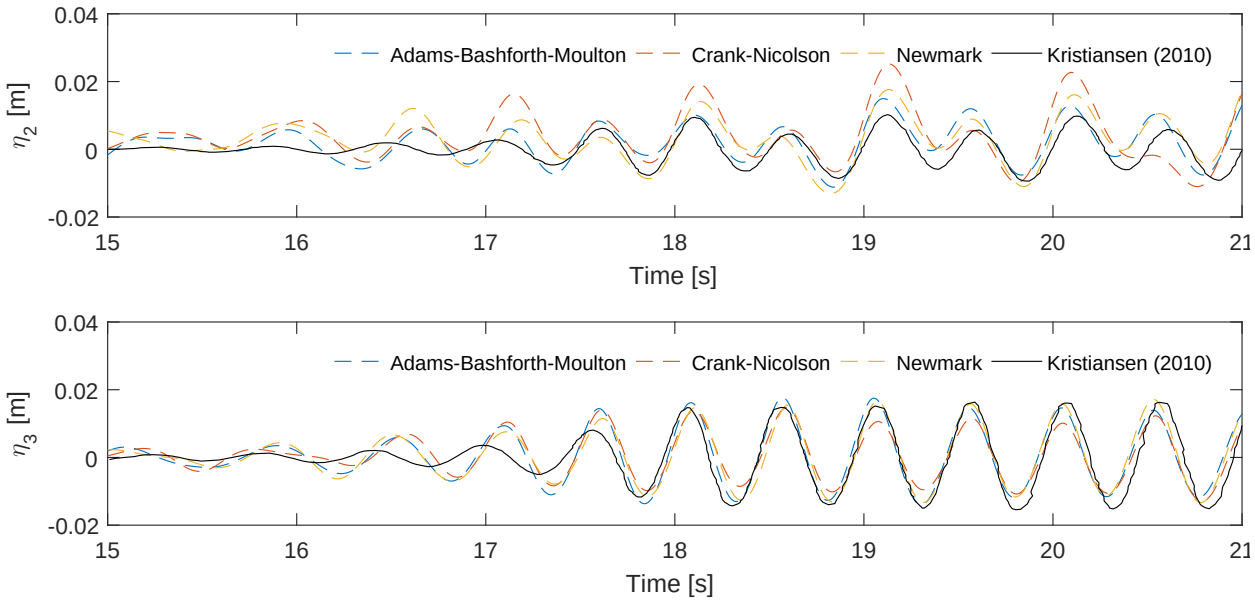

Figure 6: Comparison of sway and heave motion between the results from the present numerical model and the experimental data from Kristiansen (2010) for wave case 1 with H=0.028 m and T=0.497 s.

Newmark integration gave the most reasonable estimation. On the other side for wave case 1, the steady state condition was reached in both experiments and numerical simulations. In this case, Adams-Bashforth-Moulton scheme gave a better prediction. In both cases, Crank-Nicolson scheme gave the worst predictions. In the following part in Section 3.3 for simulating the floater-net system in waves and combined current and waves, we chose the Adams-Bashforth-Moulton scheme as the integration method for floater motion equation.

3.2. Validation of the net solver

The hydrodynamic and structural solver for the net were validated against a set of experiments in Bardestani and Faltinsen (2013) for current interaction with plane flexible net panels. The experiments were performed in the same wave flume as in Kristiansen (2010). Three different net panels were applied with solidity ratio $S_n = 0.16, 0.19, 0.23$. The net was made from Raschel material with square meshes. The twine diameters of the nets were 2.5 mm, 2.5 mm, and 1.8 mm, and the unstretched length and width of the net panels were 0.76 m and 0.51 m, respectively. In the experiments three sinkers with different weights were attached in the bottom of the net, the weight of which were Ws =1.2, 1.4, and 1.6 kg. The diameter and the length of the sinker were reported as 5 cm and 55 cm. No floater was involved in this set of experiments, instead the net was fixed in the top in a bar, and deformed freely under steady current.

According to the experiments, we set up a 2D numerical model. A snapshot of the computational domain and computational mesh is given in Fig. 13. The net was represented by a sheet of moving porous media, where the thickness is 50 mm. The porous resistance coefficients were calculated based on the formula proposed in Chen and Christensen (2016). The bottom wall effect was neglected, and treated as slip wall, since the boundary layer developed at the bottom has minor effect on the net. The water depth in the numerical model was the same as in the experiments, but the length was shortened to save the computational time. The mesh near the net region was refined, in order to better capture the geometry of the net, and the total number of mesh is in the order of three hundred thousand.

It is worth mentioning that in this set of experiments, the diameter of the sinker was significantly larger than the twine diameter. This indicated that the bottom effect might be important. Since the sinker was not modeled, only the forces were added to the structural model. Therefore selection of the drag coefficient for the sinker is important. In reality the net was connected to the sinker, which might alternate the pressure

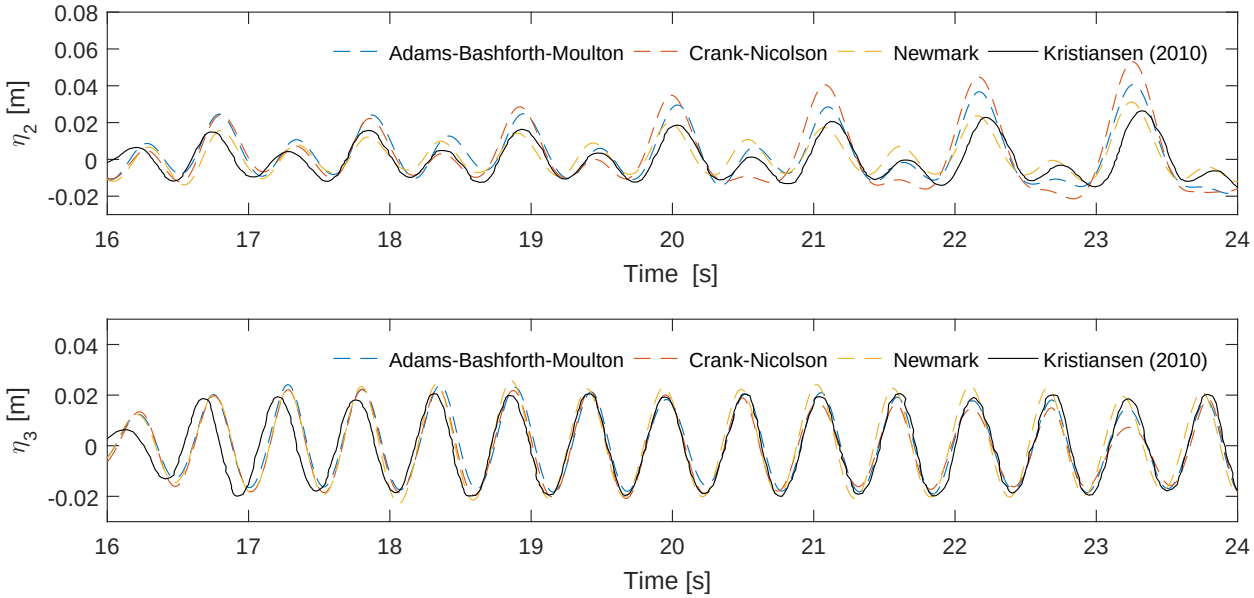

Figure 7: Comparison of sway and heave motion between the results from the present numerical model and the experimental data from Kristiansen (2010) for wave case 2 with H=0.033 m and T=0.544 s.

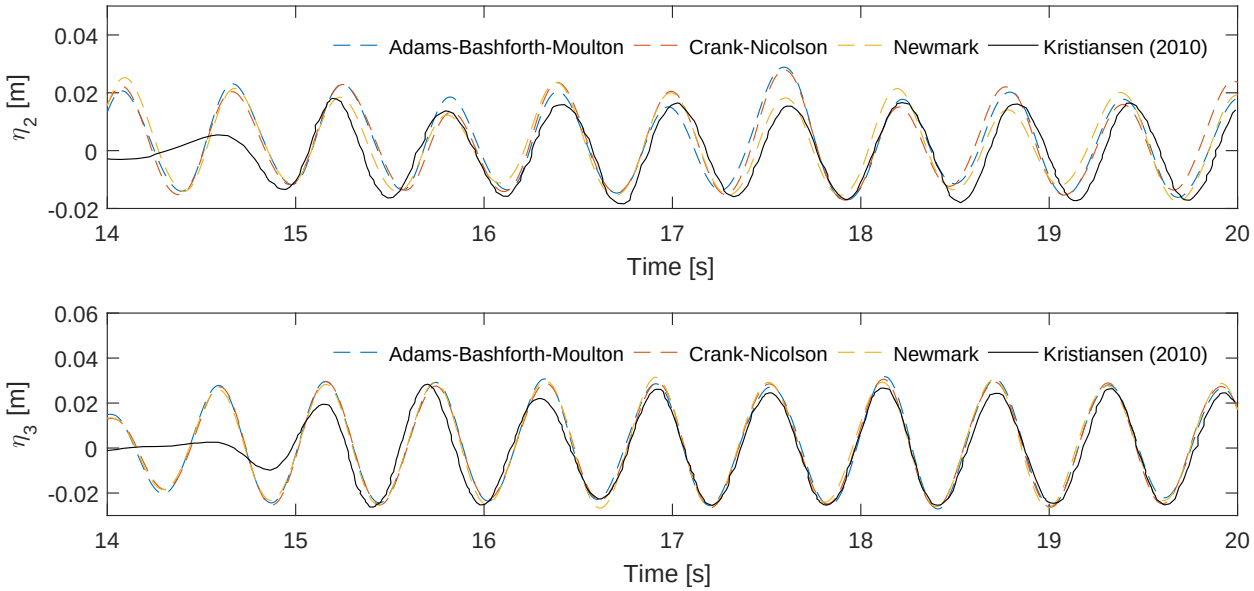

Figure 8: Comparison of sway and heave motion between the results from the present numerical model and the experimental data from Kristiansen (2010) for wave case 3 with H=0.040 m and T=0.601 s.

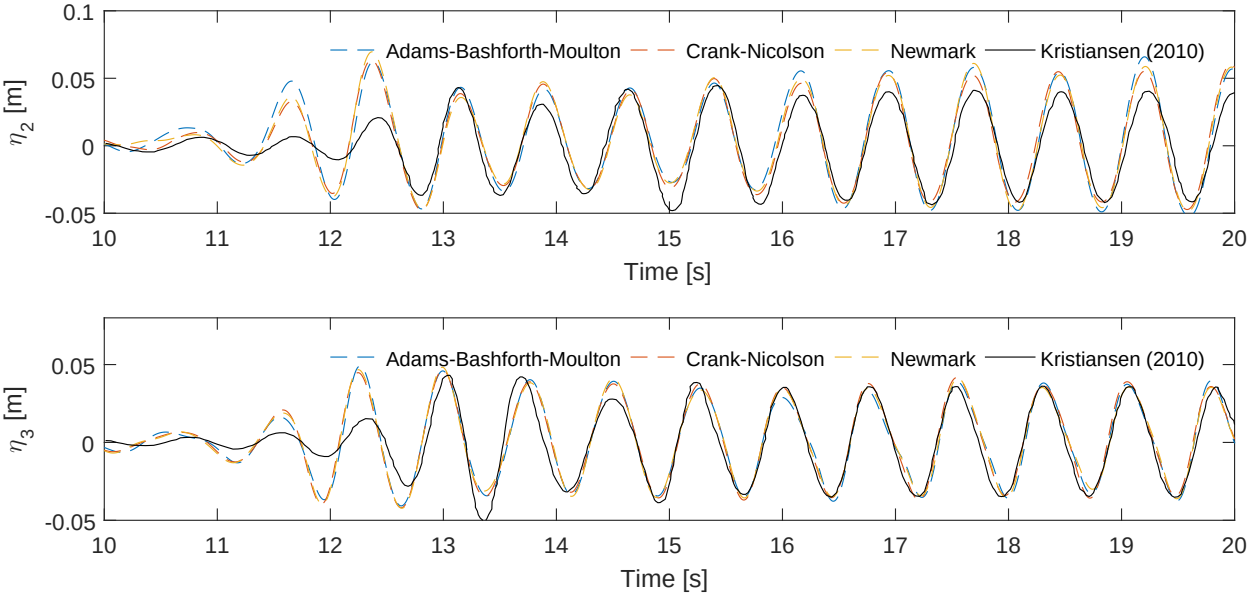

Figure 9: Comparison of sway and heave motion between the results from the present numerical model and the experimental data from Kristiansen (2010) for wave case 4 with H=0.065 m and T=0.761 s.

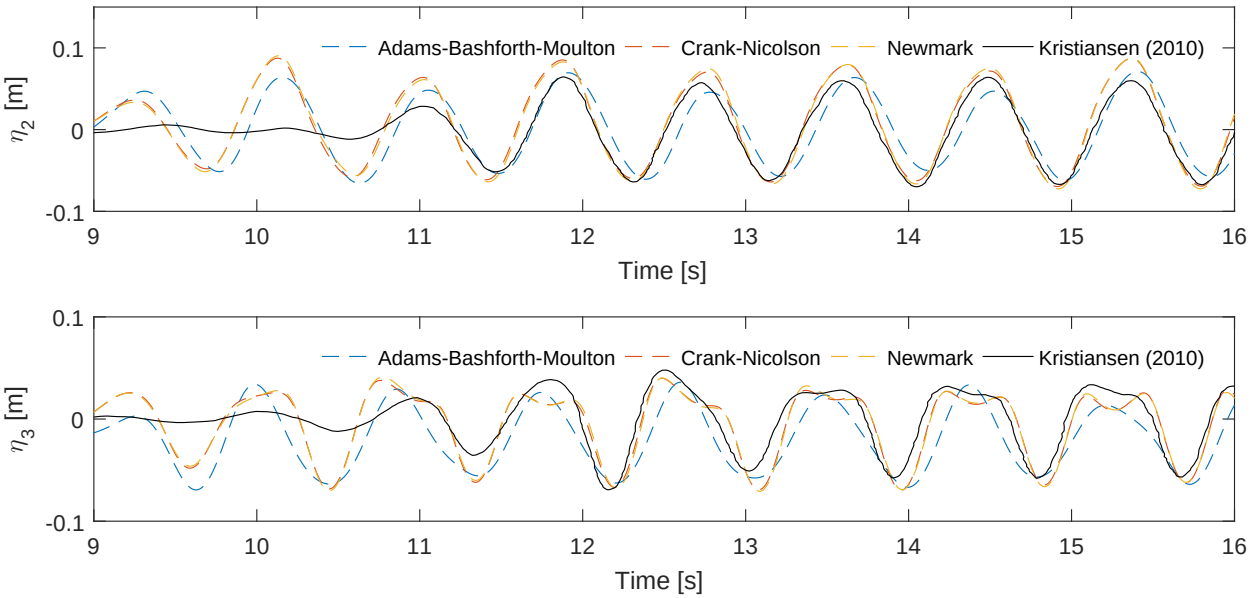

Figure 10: Comparison of sway and heave motion between the results from the present numerical model and the experimental data from Kristiansen (2010) for wave case 5 with H=0.086 m and T=0.878 s.

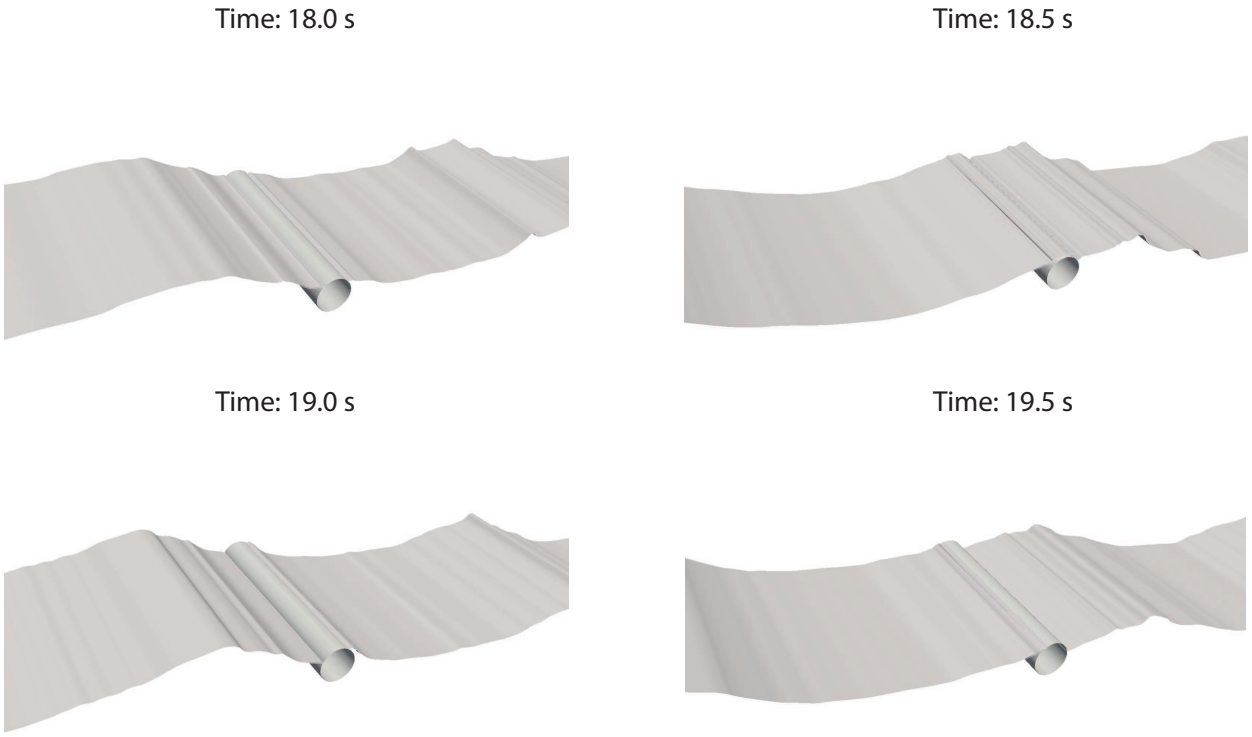

Figure 11: Snapshot of the free surface wave and the floater at different time for wave case 5.

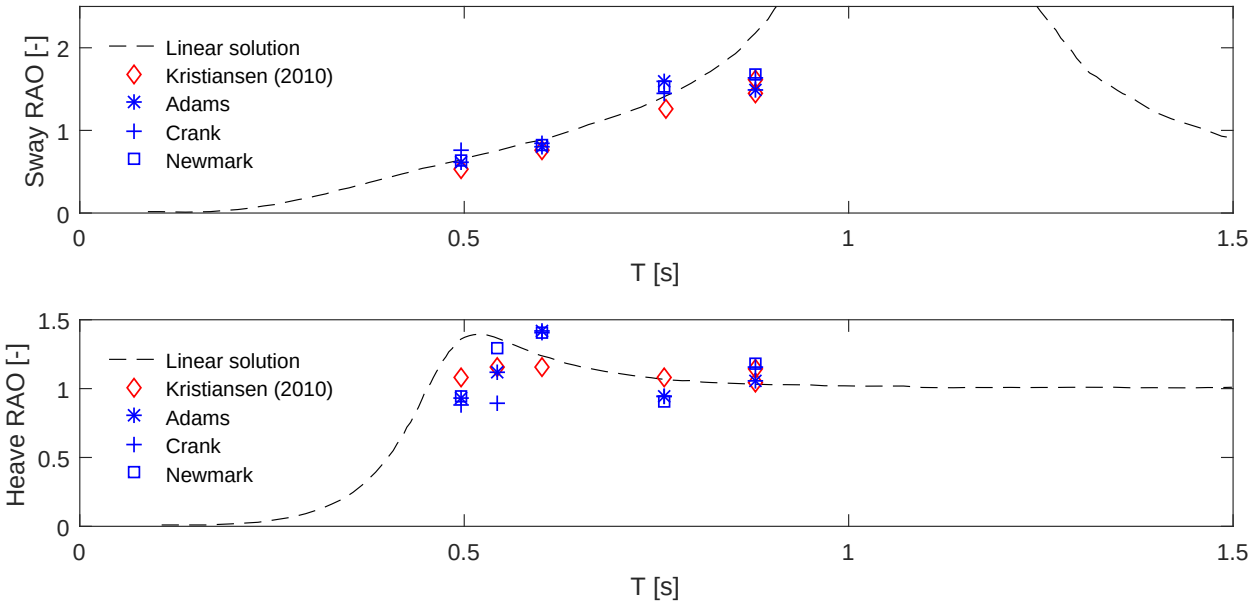

Figure 12: Comparison of the response amplitude operator for heave and sway motion between linear solution, experimental data from Kristiansen (2010) and the present model with different motion integration methods.

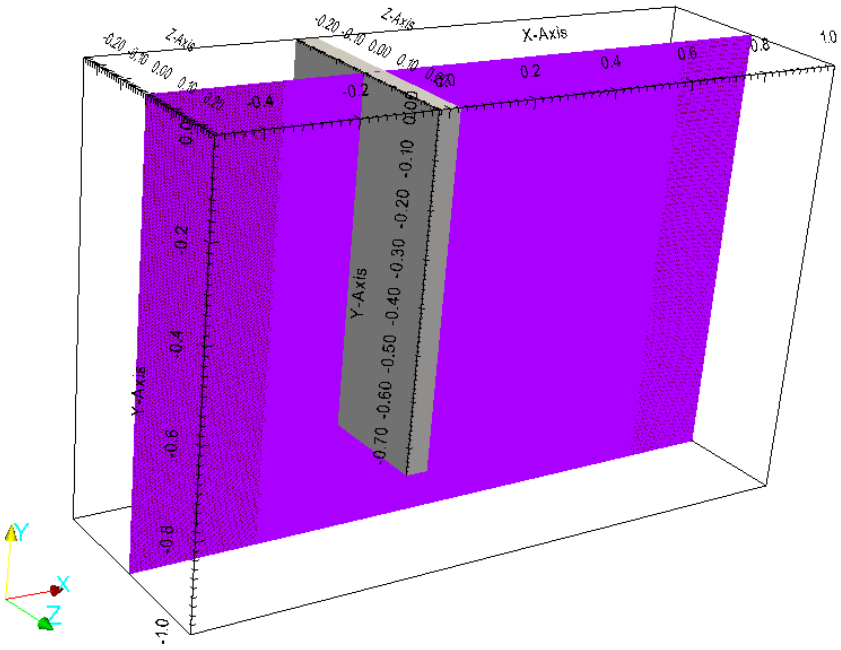

Figure 13: The computational domain and computational mesh for reproduction of experiments in Bardestani and Faltinsen (2013) for net panel in steady current.

distribution and the separation point. Bardestani and Faltinsen (2013) mentioned that in such a condition where the cylinder was connected with a tripping wire, considerable increase of the drag coefficient should be expected. Some relevant results have been reported in James and Truong (1972), according to which we used a drag coefficient of 1.8 here for all the cases.

Examples of the deformation is given in Fig. 14 for the net panel with $S_n = 0.19$. The current velocity $U = 0.2$ m/s, and the sinker weight W_S =1.2, 1.4 and 1.6 kg. In general, by qualitative comparison, the results from our numerical model and the screen type force model agree well with the experiments. In Bardestani and Faltinsen (2013), the figures from the experiments were not given in a coordinate system, therefore the detailed coordinate of each point for the net panel was unknown, and quantitive comparison is not possible. But it was observed that our numerical model consistently predicted a slightly larger deformation than the screen type force model. As mentioned in Bardestani and Faltinsen (2013), due to use of too few elements, the results from the screen type force model slightly underestimated the deformation. So in principle our numerical model should give a slightly better prediction in this case.

Comparison of the tension force is given in Fig. 15 between our numerical model and the experimental data in Bardestani and Faltinsen (2013). In general we found a very good agreement. The largest error occurs for the case with $W_S = 1.2$ kg, $S_n = 0.16$, with the current velocity $U = 0.3$ m/s, which reaches up to 20%. For the rest cases, the errors are all below or around 10%.

3.3. Validation of the floater-net system

The final validation cases are related to the whole floater-net system under various wave conditions and combined current and wave conditions. The experiments have also been conducted in Bardestani and Faltinsen (2013), and in the same current-wave flume with the experiments in Section 3.1 and Section 3.2. In this set of experiments, the floater is the same with the one used in Kristiansen (2010), while the weight of the sinker is 1.6 kg. In the experiments under regular waves, the solidity ratio of the net was 0.23. But under combined current and wave condition, the net panel with $S_n = 0.16$ was used. Both of them have been tested in Section 3.2. The net was connected to the floater using strips.

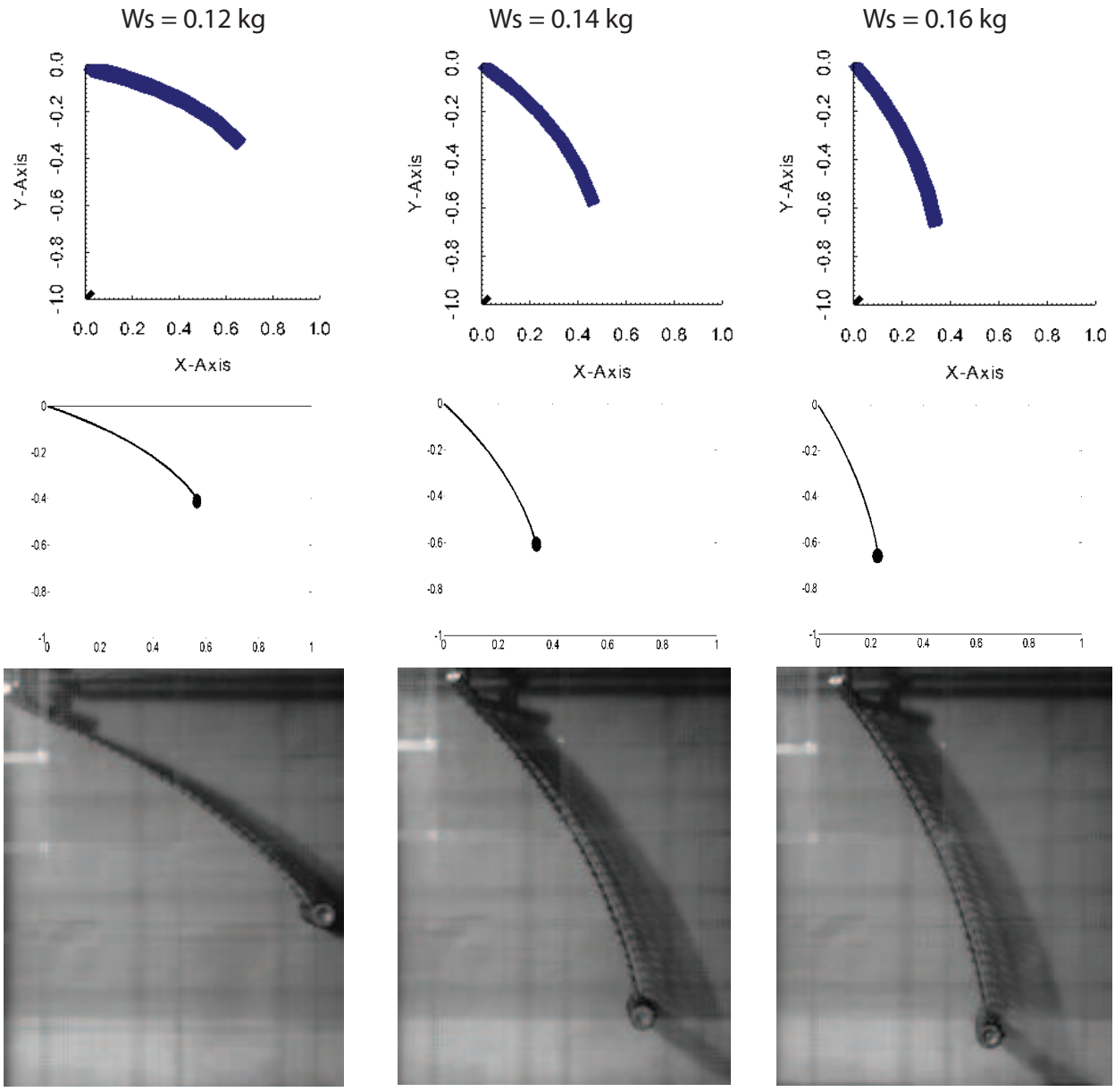

Figure 14: Comparison of the deformation of the net panel with $S_n = 0.19$ and sinker weight $W_S = 0.12$, 0.14 and 0.16 kg. The current velocity $U = 0.2$ m/s. The upper row is the results from the present model. The middle row is the results from the screen type force model in Bardestani and Faltinsen (2013). The lower row is the reproduction of the experimental results from Bardestani and Faltinsen (2013).

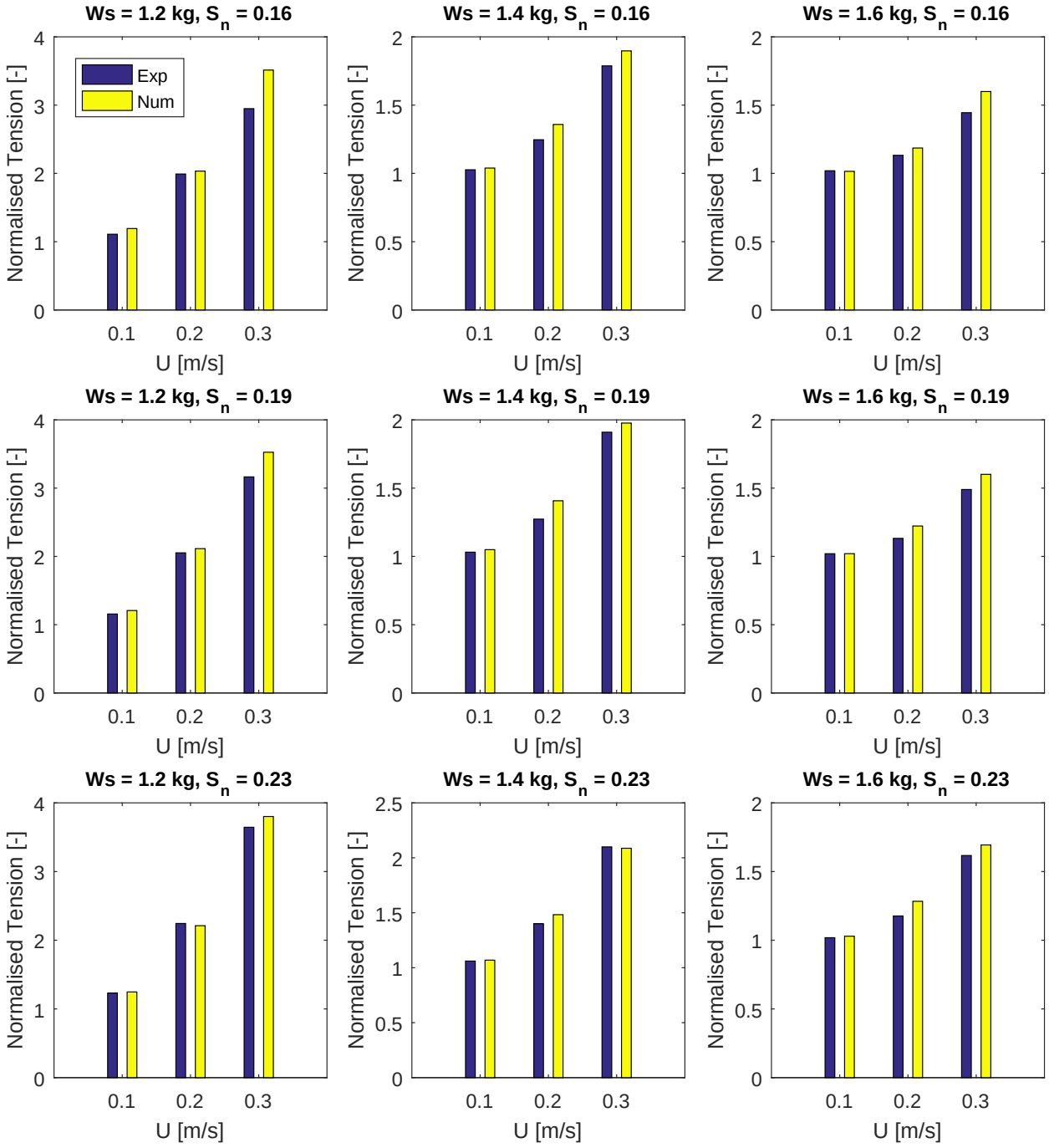

Figure 15: Comparison of the tension forces on the top layer twines of the net panel between the experimental data in Bardestani and Faltinsen (2013) and the present numerical model. The tension force was normalized by the initial tension.

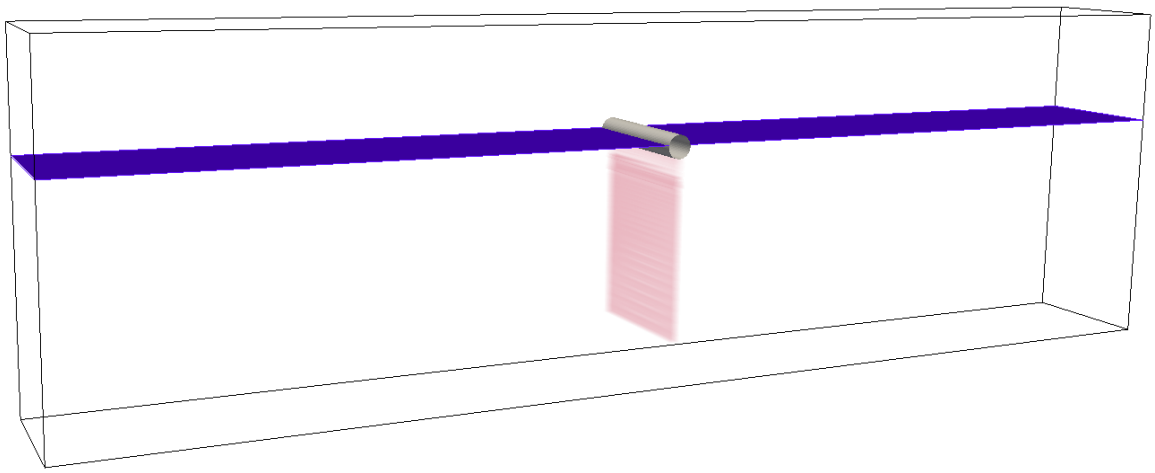

Figure 16: The initial configuration of the numerical model for simulation of floater-net system.

Again we set up our numerical model based on the the experiments, which was a combination of the setup of the numerical model in Section 3.1 and 3.2 A body-fitted mesh was applied in the computational domain, where the floater was described as a boundary patch in the flow domain. The net was modeled as a sheet of porous media, and it was attached on the floater. The numerical wave tank used in this set of simulations is the same with the one used in Section 3.1, while the parameters for the net and sinker system are the same with Section 3.2. A snapshot on the initial configuration of the numerical model is given in Fig. 16.

3.3.1. Snap load of the net under regular wave condition

For the cases with floater-net system under regular wave conditions, the tension force of the net was measured in the experiments. Five force transducers were installed at the top layer of the net, and the average values were reported. A very large snap load was observed for most of the cases. The formulation of the snap load was tightly related to the relative motion between the floater and the sinker, and the characteristics of the net material property. At some specific time in a wave period, due to the relative motion between the floater and the sinker, the distance between them was smaller than at hydrostatic condition. As given by Eq. (36), the compression stiffness of the net material was neglected. This indicated that the net got slack at this time. After that, the floater was moving upwards and the sinker was accelerating downwards. Considering the inertia effect of the sinker, when the net got taut again, very large snap load occurred.

In the present work we numerically reproduced the snap load of the system under five wave conditions, as shown in Table 2. The time series of the snap load under these wave conditions are given in Fig. 17. Several comments are given for the numerical results: (1) In all the cases, at the beginning of the simulation (approximately from 0 - 4 s) before the waves arrived the floater, there still existed periodic cycles for the tension force. The reason is that initially the system was not exactly in equilibrium state. The oscillation period at this stage was related to the natural period of this floating system, as one can see in all the cases the oscillation periods at this stage are the same. (2) There exists two or several peaks within one wave period. This indicated that after the net became taut from slack status for the first time, strong internal force was generated, which is the reason for occurrence of the snap load. This internal force caused the net to get slack again and later produced the second peak. However, the value of the second peak is usually smaller than the first peak, since some of the energy was dissipated between occurrence of the two peaks. (3) The period between two largest peaks is the wave period.

Accurate prediction of this type of snap load is not straightforward. It requires that both the motion of the floater and the sinker should be predicted accurately. Meanwhile, the structural model of the net should reflect the property of the net material precisely. Comparison of the average amplitude of the snap load is

Table 2: The parameters of the selected wave conditions for validation of the floater-net system in regular waves

Wave case no.	1	2	3	4	5
Wave period, T [s]	0.497	0.601	0.672	0.878	1.038
Wave height, H [m]	0.028	0.040	0.050	0.086	0.120

given in Fig. 18. It is seen that the snap load is several times larger than the load at hydrostatic condition, which is about 5 N. Some of the scattering of the experimental data was also observed under the same wave condition.

In Fig. 18 we noted some deviations between the results from the present numerical model and the experimental data. The possible reasons for the deviations are given as follows. In the numerical model, the sinker geometry was not resolved. Therefore, the dynamic response of the sinker and its interaction effects with the net were not modeled. Instead only the mean forces were added to the bottom layer of the net. Since the movement of the sinker contributed significantly to the snap load, this serves as an important reason for the deviation. In addition, the constitutive relationship of the net material used in the present model might be another error source. As mentioned above in Section 2.5, this relation was obtained from the experiments for one specific net, where the coefficients were determined by least-square fitting. However, since the nets used in Lader and Fredheim (2006) and Bardestani and Faltinsen (2013) are different, this set of coefficients used in the numerical model may not precisely reflect the material property of the net used in Bardestani and Faltinsen (2013). Furthermore, the oscillations of the floater-net system at the beginning of the simulations induced some wave radiations. The radiated waves might pollute the incoming waves, which introduced errors. However, the amplitude of the radiated waves were rather small, and should not have significant impact on the final results, especially in rather high wave conditions, e.g. wave case 4 and 5.

3.3.2. Mooring line forces under combined current and wave condition

Another validation case was carried out under combined current and wave condition, where the wave height $H = 0.065$ m, wave period $T = 0.761$ s and the current velocity $U = 0.2$ m/s. In the experiments, the combined current and wave condition was generated by first towing the net panel and the floater towards the wave maker side until a steady state condition was reached. Then the incident regular waves were generated, where the net panel already had an offset before the waves propagated through it.

In the numerical model, exact reproduction of the above experimental setup was not possible, since with a body fitted mesh grid, it was not possible to move the floater towards the wave maker side for a long time until the steady state condition. Therefore, we chose to directly generate the combined current and waves from the wave maker side, based on the high order stream function wave theory in Fenton (1988) with a drift velocity. However, one should note that the wave frequency was changed to the encounter frequency as shown below:

$$\omega_e = \omega - \frac{\omega^2 U}{g} \tag{37}$$

where ω is the wave frequency and ω_e is the encounter frequency.

A snapshot of the floater-net system and the free surface wave is given in Fig. 19. It was observed that within one wave period, the net deformation was largely influenced by the current velocity. On the other hand, the wave has minor influences. This was determined by the magnitude of the wave and current velocities at the position of the net. Especially close to the bottom of he net panel, the current completely dominated the deformation of the net, since the orbital motion of the water particle was significantly reduced at that depth. However, both the current and the wave played important roles on the motion of the floater.

We compared the mooring line forces between the experimental data in Bardestani and Faltinsen (2013) and the present model, and this is given in Fig. 20. It is noticed that the mean value is not zero due to co-existence of the current. Actually the mean mooring line forces is approximately the same with the drag force on the panel under current only condition. The oscillation part is then due to the wave that travels on the current. The experiment and the simulation gave approximately the same mean force on the mooring

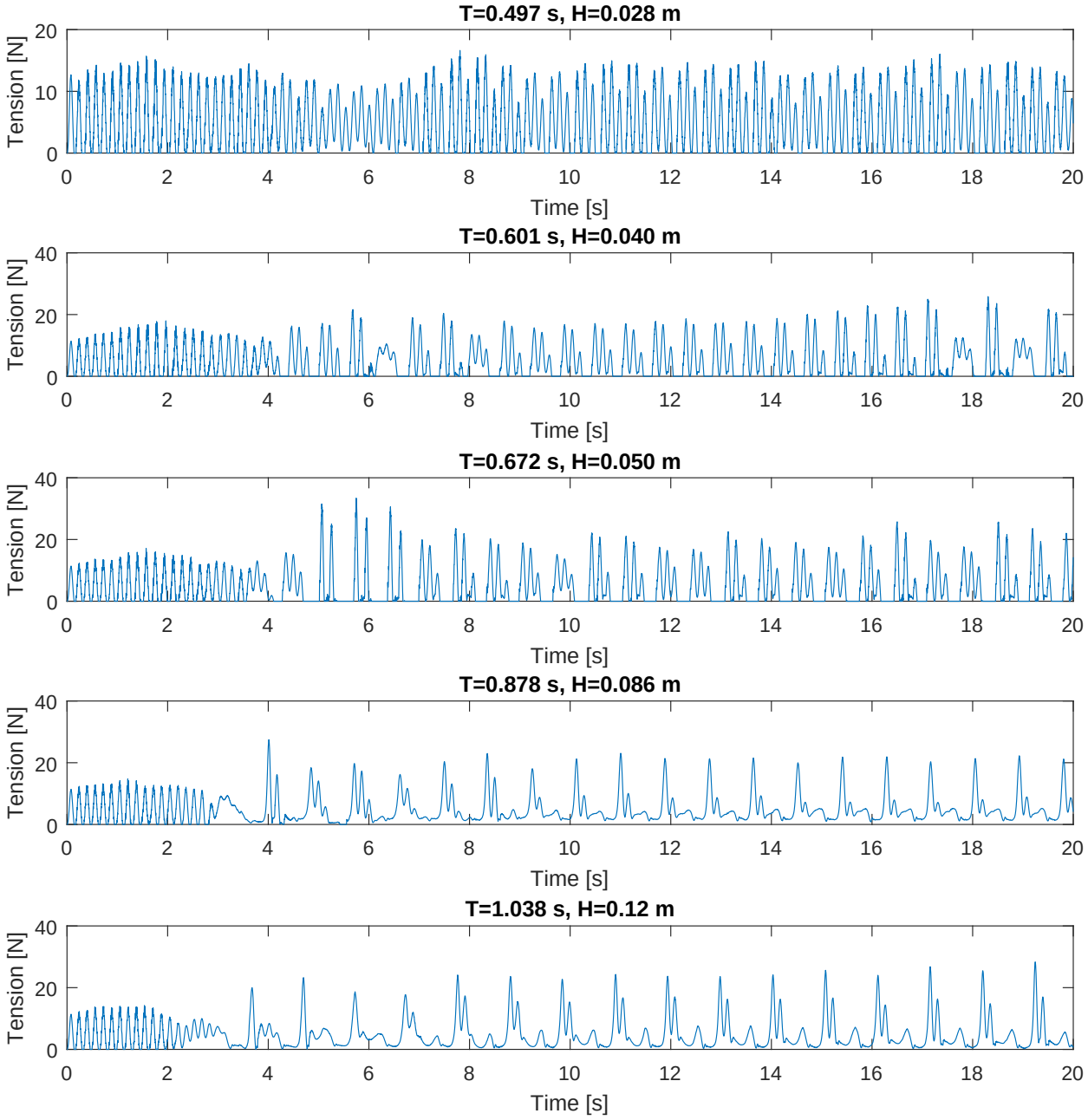

Figure 17: Time series of the tension force from the present numerical model under five wave conditions.

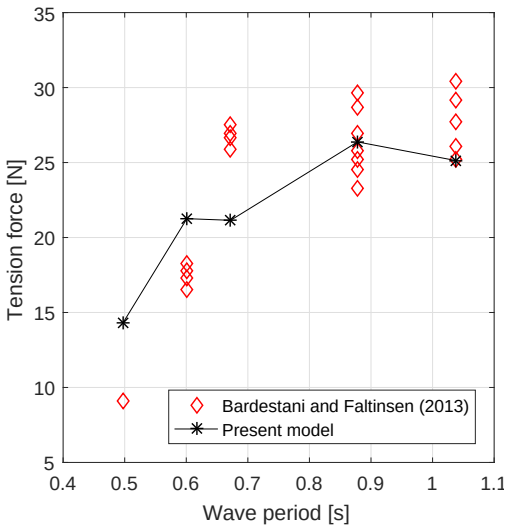

Figure 18: Comparison of the amplitude of the snap load under different wave conditions between the present model and the experiments in Bardestani and Faltinsen (2013).

lines, which are 3.50 N and 3.06 N, respectively. But the oscillation amplitude was underestimated by the present model, and some irregular characteristics were also observed from the numerical result.

4. Conclusions

In the present work a novel numerical model was developed for simulating the responses of floating fish cages in current and waves. The numerical model was developed within the framework of OpenFOAM-3.0.x. In the numerical model the interaction effects between the deformable net cage and the floater motion were fully considered. In order to achieve this, the model couples the hydrodynamic solver for the net cage and the floater, the rigid body motion solver, the structural solver for the net cage, and the mesh motion solver in a segregated manner.

The numerical model was carefully validated against three sets of validations. The first set of validation cases were for floater motion responses in regular waves. Different motion integration methods were applied, and we found that no one is consistently better than the others. It was decided to apply the Adams-Bashforth-Moulton for the following validation cases. The second set of the validation cases were for net cage without floater in steady current. Three net panels with different solidity ratios were applied with three different sinker weights under three current velocities. Therefore totally 27 cases were set up in the validation. We compared the net deformation for three cases, and for all the cases the tension forces were compared. The numerical model gave a very good agreement with the experimental data, which validated the hydrodynamic and structural solver for the net cage.

The final validation cases were related to the whole floater-net system in regular waves and combined current and wave conditions. The snap load of the net produced by the numerical model was presented under different wave conditions, and the amplitudes were compared with the experimental data. Some deviations were found between the present numerical model and the experiments. The possible reasons are related to the neglect of modeling of the sinker, the constitutive relation used in the structural model, and the initial wave diffraction due to non-equilibrium status of the system. One more validation case was also conducted to simulate the floater-net system in combined current and wave condition. The mooring line force was compared with the experimental data. It was found that the mean force agreed well with the experiments, but the amplitude was slightly underestimated.

Future work will be focused on application of the model in 3D cases. In principle the solver we presented in this work can be directly applied in 3D cases, if the floater is treated as a rigid body. However, considering the

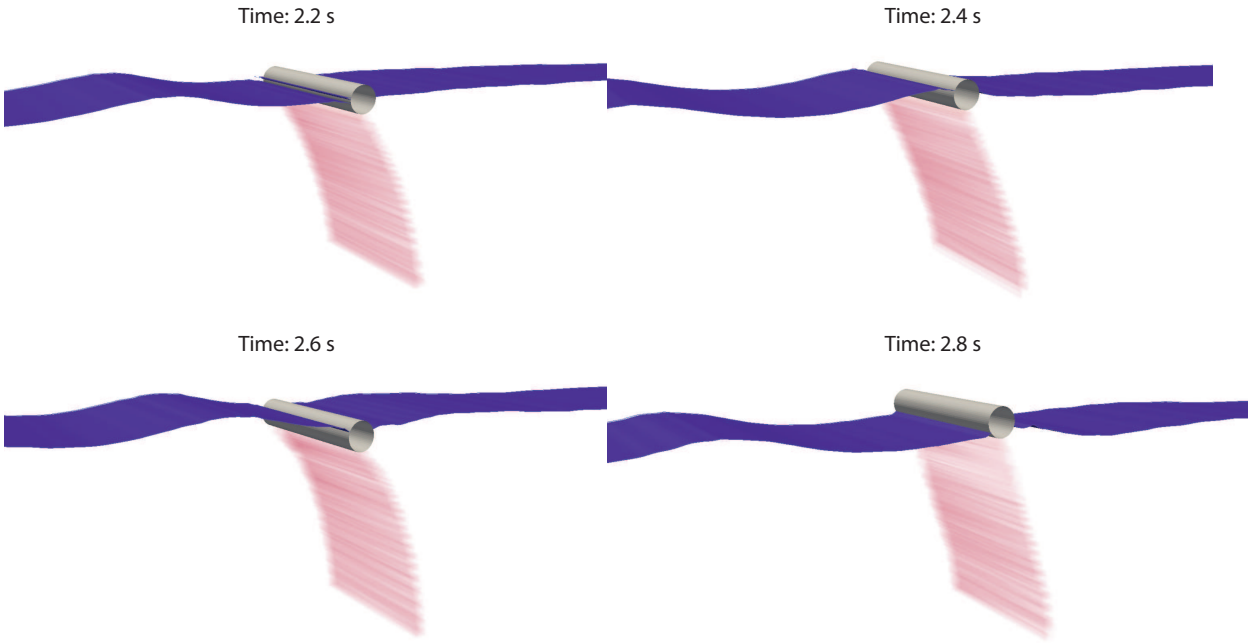

Figure 19: A snapshot on the free surface and the response of floater-net system at different time in combined current and wave condition. The wave period $T = 0.761$ s, wave height $H = 0.065$ m and the current velocity $U = 0.2$ m/s.

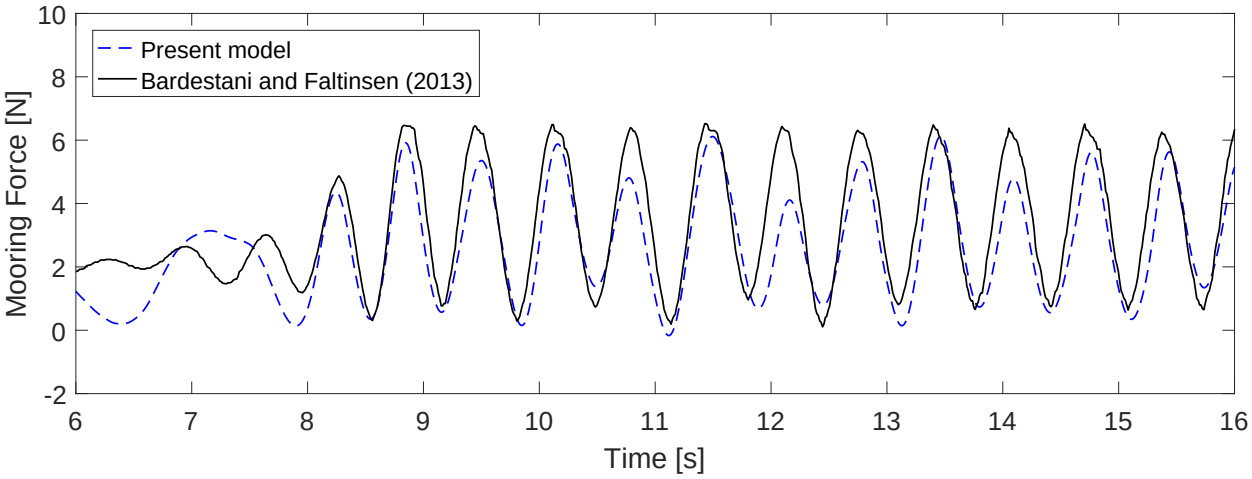

Figure 20: Comparison of the mooring line forces between the present numerical model and the experimental data from Bardestani and Faltinsen (2013) under combined current and wave condition. The current velocity $U = 0.2$ m/s, the solidity ratio $S_n = 0.16$, the wave height $H = 0.065$ m, the wave period $T = 0.761$ s, the sinker weight $Ws = 1.6$ kg.

flexibility of the floater, we will extend our solver by coupling a structural solver, therefore the hydroelastic behavior of the floater could also be considered in the model.

Acknowledgement

Mohsen Bardestani from Norwegian University of Science and Technology is acknowledged for the discussion with the first author on the physics of the snap load. The research was partially supported by FP7-OCEAN-2011 project Innovative multi-purpose offshore platforms: planning, design and operation, MERMAID, 288710, under the call "Ocean of Tomorrow".

Appendix A. Linear solution for motion response of a 2D horizontal cylinder in regular waves

In this section we derive the simple analytic solution for heave and sway motion response of a 2D horizontal cylinder in regular waves. Before derivation, we will clarify the assumptions that are made: (1) The fluid is assumed to be inviscid and irrotational. Therefore, there exists a velocity potential in the domain. (2) The heave and sway motion are assumed to be uncoupled. (3) The floating cylinder oscillates in wave period, and the higher order motion is not considered.

Here we follow the notation used in Newman (1977). Due to assumption of the linearity, the velocity in mode j was written as:

$$U_j(t) = \Re(i\omega\xi_j e^{i\omega t}) \tag{A.1}$$

where ω is the wave frequency, ξ_j is the amplitude of the displacement in mode j.

The floating cylinder is subjected to added mass, damping, restoring and wave force. The added mass and damping forces are given as $a_{jj}\dot{U}_j + b_{jj}U_j$, where a_{jj} and b_{jj} are added mass and damping coefficients in mode j. The restoring force is proportion to the displacement, and expressed as $c_{jj}\xi_j e^{i\omega t}$. The wave excitation force is expressed as AX_j, where A is the wave amplitude and X_j is the complex amplitude of the exciting force in direction j for an incident wave of unit amplitude. Then the motion equation of the floating cylinder is set up as:

$$\xi_j[-\omega^2(m_{jj} + a_{jj}) + i\omega b_{jj} + c_{jj}] = AX_j \tag{A.2}$$

So the response amplitude operator (RAO) was formulated as:

$$\frac{\xi_j}{A} = \frac{|X_j|}{\sqrt{(c_{jj} - \omega^2(m_{jj} + a_{jj}))^2 + \omega^2 b_{jj}^2}} \tag{A.3}$$

The added mass and damping coefficients are given in Faltinsen (1993), where the water depth effect was not accounted for. Regarding the wave exitation force, Newman (1962) derived an analytic solution, where Haskind relation was applied to relate the damping coefficient with the wave excitation force. Hereby the wave force was expressed as $|X_j| = \sqrt{\rho g^2 b_{jj}/\omega}$.

References

Bardestani, M., Faltinsen, O.M., 2013. A two dimensional approximation of a floating fish farm in waves and current with the effect of snap loads, in: Proceedings of the ASME 2013 32nd International Conference on Ocean, Offshore and Arctic Engineering, Nantes, France.

Bi, C., Zhao, Y., Dong, G., Zheng, Y., Gui, F., 2014a. A numerical analysis on the hydrodynamic characteristics of net cages using coupled fluid-structure interaction model. Aquacultural Engineering 59, 1–12. URL: http://linkinghub.elsevier.com/retrieve/pii/S014486091400003Xhttp://www.sciencedirect.com/science/article/pii/S014486091400003X, doi:10.1016/j.aquaeng.2014.01.002.

Bi, C.W., Zhao, Y.P., Dong, G.H., Xu, T.J., Gui, F.K., 2014b. Numerical simulation of the interaction between flow and flexible nets. Journal of Fluids and Structures 45, 180–201. URL: http://linkinghub.elsevier.com/retrieve/pii/S0889974613002594, doi:10.1016/j.jfluidstructs.2013.11.015.

Birdsall, C.K., Langdon, A.B., 2004. Plasma physics via computer simulation. CRC Press.

Chen, H., Christensen, E.D., 2016. Investigations on the porous resistance coefficients for fishing net structures. Journal of Fluids and Structures 65, 76–107. URL: http://www.sciencedirect.com/science/article/pii/S0889974615301687, doi:10.1016/j.jfluidstructs.2016.05.005.

Chow, J.H., Ng, E., 2016. Strongly coupled partitioned six degree-of-freedom rigid body motion solver with Aitken's dynamic under-relaxation. International Journal of Naval Architecture and Ocean Engineering 8, 320–329. URL: http://linkinghub.elsevier.com/retrieve/pii/S2092678216304393, doi:10.1016/j.ijnaoe.2016.04.001.

Devolder, B., Schmitt, P., Rauwoens, P., Elsaesser, B., Troch, P., 2015a. A review of the implicit motion solver algorithm in OpenFOAM to simulate a heaving Buoy. NUTTS conference 2015 : 18th Numerical Towing Tank Symposium , 1–6URL: https://biblio.ugent.be/publication/6954684.

Devolder, B., Schmitt, P., Rauwoens, P., Elsaesser, B., Troch, P., 2015b. A review of the implicit motion solver algorithm in openfoam® to simulate a heaving buoy, in: NUTTS conference 2015: 18th Numerical Towing Tank Symposium, pp. 1–6.

Dullweber, A., Leimkuhler, B., McLachlan, R., 1997. Symplectic splitting methods for rigid body molecular dynamics. The Journal of Chemical Physics 107, 5840. URL: http://scitation.aip.org/content/aip/journal/jcp/107/15/10.1063/1.474310, doi:10.1063/1.474310.

Dunbar, A.J., Craven, B.A., Paterson, E.G., 2015. Development and validation of a tightly coupled CFD/6-DOF solver for simulating floating offshore wind turbine platforms. Ocean Engineering 110, 98–105. URL: http://dx.doi.org/10.1016/j.oceaneng.2015.08.066, doi:10.1016/j.oceaneng.2015.08.066.

Faltinsen, O., 1993. Sea Loads on Ships and Offshore Structures. Cambridge Ocean Technology Series, Cambridge University Press. URL: https://books.google.dk/books?id=qZq4Rs2DZXoC.

Fenton, J., 1988. The numerical solution of steady water wave problems. Computers & Geosciences 14, 357–368. doi:10.1016/0098-3004(88)90066-0.

Förster, C., Wall, W.a., Ramm, E., 2007. Artificial added mass instabilities in sequential staggered coupling of nonlinear structures and incompressible viscous flows. Computer Methods in Applied Mechanics and Engineering 196, 1278–1293. URL: http://linkinghub.elsevier.com/retrieve/pii/S0045782506002544, doi:10.1016/j.cma.2006.09.002.

Fu, S., Xu, Y., Hu, K., Zhong, Q., Li, R., 2014. Experimental Investigation on Hydrodynamics of a Fish Cage Floater-net System in Oscillatory and Steady Flows by Forced Oscillation Tests. Journal of Ship Research 58, 20–29. URL: http://www.ingentaselect.com/rpsv/cgi-bin/cgi?ini=xref{&}body=linker{&}reqdoi=10.5957/JOSR.58.1.130022, doi:10.5957/JOSR.58.1.130022.

Hirt, C., Nichols, B., 1981. Volume of fluid (VOF) method for the dynamics of free boundaries. Journal of Computational Physics 39, 201–225. URL: http://www.sciencedirect.com/science/article/pii/0021999181901455, doi:10.1016/0021-9991(81)90145-5.

Jacobsen, N.G., Fuhrman, D.R., Fredsoe, J., 2012. A wave generation toolbox for the open-source CFD library: OpenFoam (R). INTERNATIONAL JOURNAL FOR NUMERICAL METHODS IN FLUIDS 70, 1073–1088. doi:10.1002/fld.2726.

James, D.F., Truong, Q.S., 1972. Wind load on cylinder with spanwise protrusion. Journal of the Engineering Mechanics Division 98, 1573–1589.

Jensen, B., Jacobsen, N.G., Christensen, E.D., 2014. Investigations on the porous media equations and resistance coefficients for coastal structures. Coastal Engineering 84, 56–72. URL: http://linkinghub.elsevier.com/retrieve/pii/S0378383913001816, doi:10.1016/j.coastaleng.2013.11.004.

Kristiansen, D., 2010. Wave Induced Effects on Floaters of Aquaculture plants. Ph.d. thesis. Norwegian University of Science and Technology.

Kristiansen, T., Faltinsen, O.M., 2012. Modelling of current loads on aquaculture net cages. Journal of Fluids and Structures 34, 218–235. URL: http://linkinghub.elsevier.com/retrieve/pii/S0889974612000783, doi:10.1016/j.jfluidstructs.2012.04.001.

Kristiansen, T., Faltinsen, O.M., 2015. Experimental and numerical study of an aquaculture net cage with floater in waves and current. Journal of Fluids and Structures 54, 1–26. URL: http://linkinghub.elsevier.com/retrieve/pii/S0889974614002114, doi:10.1016/j.jfluidstructs.2014.08.015.

Lader, P.F., Fredheim, A., 2006. Dynamic properties of a flexible net sheet in waves and current-A numerical approach. Aquacultural Engineering 35, 228–238. URL: http://linkinghub.elsevier.com/retrieve/pii/S0144860906000161, doi:10.1016/j.aquaeng.2006.02.002.

Ma, L., Hu, K., Fu, S., Moan, T., Li, R., 2016. A Hybrid Empirical-Numerical Method for Hydroelastic Analysis of a Floater-and-Net System. Journal of Ship Research 60, 14–29. doi:http://dx.doi.org/10.5957/JOSR.60.1.140058, arXiv:/dx.doi.org/10.5957/JOSR.60.1.140058.

Newman, J.N., 1962. The Exciting Forces on Fixed Bodies in Waves. Journal of Ship Research, Society of Naval Architects and Marine Engineers 6, 1–10.

Newman, J.N., 1977. Marine hydrodynamics. MIT press.

Newmark, N.M., 1959. A method of computation for structural dynamics, in: Proc. ASCE, pp. 67–94.

Ong, M.C., Kamath, A., Bihs, H., Afzal, M.S., 2017. Numerical simulation of free-surface waves past two semi-submerged horizontal circular cylinders in tandem. Marine Structures 52, 1–14. URL: http://dx.doi.org/10.1016/j.marstruc.2016.11.002, doi:10.1016/j.marstruc.2016.11.002.

Palm, J., Eskilsson, C., Moura Paredes, G., Bergdahl, L., 2016. Coupled mooring analysis of floating wave energy converters using CFD. International Journal of Marine Energy 16, 83–99. URL: http://dx.doi.org/10.1016/j.ijome.2016.05.003, doi:10.1016/j.ijome.2016.05.003.

Patursson, Ø., Swift, M.R., Tsukrov, I., Simonsen, K., Baldwin, K., Fredriksson, D.W., Celikkol, B., 2010. Development of a porous media model with application to flow through and around a net panel. Ocean Engineering 37, 314–324. URL: http://linkinghub.elsevier.com/retrieve/pii/S0029801809002406, doi:10.1016/j.oceaneng.2009.10.001.

Seng, S., 2012. Slamming And Whipping Analysis Of Ships. Phd thesis. Technical University of Denmark.
Söding, H., 2001. How to integrate free motions of solids in fluids, in: 4th Numerical Towing Tank Symposium, Hamburg.
Xu, T.J., Dong, G.H., Li, Y.C., Guo, W.J., 2014. Numerical study of a self-submersible single-point mooring gravity cage in combined wave-current flow. Applied Ocean Research 48, 66–79. URL: http://dx.doi.org/10.1016/j.apor.2014.07.014, doi:10.1016/j.apor.2014.07.014.
Xu, T.J., Zhao, Y.P., Dong, G.H., Gui, F.K., 2013. Analysis of hydrodynamic behavior of a submersible net cage and mooring system in waves and current. Applied Ocean Research 42, 155–167. URL: http://dx.doi.org/10.1016/j.apor.2013.05.007, doi:10.1016/j.apor.2013.05.007.
Yao, Y., Chen, Y., Zhou, H., Yang, H., 2016. Numerical modeling of current loads on a net cage considering fluidstructure interaction. Journal of Fluids and Structures 62, 350–366. URL: http://linkinghub.elsevier.com/retrieve/pii/S0889974616000116, doi:10.1016/j.jfluidstructs.2016.01.004.
Zhao, Y.P., Bai, X.D., Dong, G.H., Bi, C.W., Gui, F.K., 2015. Numerical analysis of the elastic response of a floating collar in waves. Ocean Engineering 95, 175–182. URL: http://linkinghub.elsevier.com/retrieve/pii/S0029801814004727, doi:10.1016/j.oceaneng.2014.12.015.
Zhao, Y.P., Bi, C.W., Dong, G.H., Gui, F.K., Cui, Y., Guan, C.T., Xu, T.J., 2013. Numerical simulation of the flow around fishing plane nets using the porous media model. Ocean Engineering 62, 25–37. URL: http://linkinghub.elsevier.com/retrieve/pii/S0029801813000243, doi:10.1016/j.oceaneng.2013.01.009.
Zhao, Y.P., Li, Y.C., Dong, G.H., Gui, F.K., Teng, B., 2007. A numerical study on dynamic properties of the gravity cage in combined wave-current flow. Ocean Engineering 34, 2350–2363. URL: http://linkinghub.elsevier.com/retrieve/pii/S0029801807001400, doi:10.1016/j.oceaneng.2007.05.003.

A Applied discretization schemes for the numerical simulations

In this section, the discretization schemes introduced and applied in Chapter 4 and Chapter 5 are presented below. This includes the schemes for different terms in the momentum equation and the transport equation for volume fraction field. Although they contain the same operators, e.g. time derivative operator and divergence operator, they may use different discretization schemes.

The finite volume method was used to discretize the equation on the unstructured mesh. Fig. A.1 gives a definition sketch of finite volume discretization in OpenFOAM. It uses a face addressing system, where in Fig. A.1 the face in-between cell P and cell N is the face of interest. Cell P is the owner of the face and cell N is the neighbor of the face. $\boldsymbol{d}$ is the length vector from the owner to the neighbor, i.e. from P to N. $\boldsymbol{S_f}$ is the face normal vector. The remaining notations are inherited from Chapter 4.

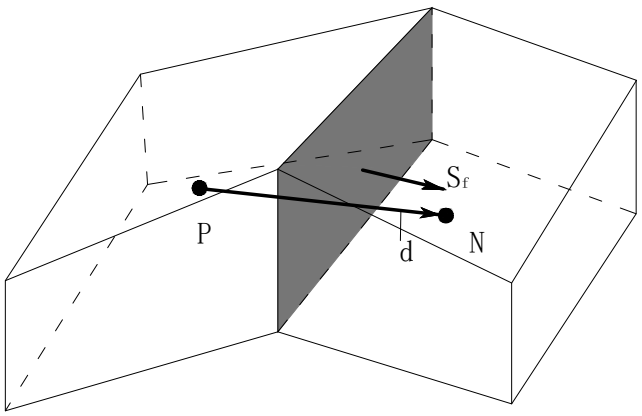

Figure A.1 – A definition sketch for finite volume discretization method in OpenFOAM.

A.1 Momentum equation

The momentum equation in the numerical model is given below in Eq. (A.1):

$$\frac{\partial \rho \boldsymbol{u}}{\partial t} + \nabla \cdot \rho \boldsymbol{u}\boldsymbol{u} - \nabla \cdot [\mu(\nabla \boldsymbol{u})] = -\nabla p - (\boldsymbol{g} \cdot \boldsymbol{x})\nabla \rho + \sigma_T \kappa_\alpha \nabla \alpha \tag{A.1}$$

The finite volume method requires that Eq. (A.1) is satisfied over each control volume, e.g. the owner cell V_P in the integral form:

$$\begin{aligned} &\int_{V_P} \frac{\partial \rho \boldsymbol{u}}{\partial t} \, \mathrm{d}V + \int_{V_P} \nabla \cdot (\rho \boldsymbol{u})\boldsymbol{u} \, \mathrm{d}V - \int_{V_P} \nabla \cdot [\mu(\nabla \boldsymbol{u})] \, \mathrm{d}V = \\ &\int_{V_P} [-\nabla p - (\boldsymbol{g} \cdot \boldsymbol{x})\nabla \rho + \sigma_T \kappa_\alpha \nabla \alpha] \, \mathrm{d}V \end{aligned} \tag{A.2}$$

Eq. (A.2) contains discretization of time derivative operator, divergence operator, gradient operator and Laplace operator. The discretization of them will be examined below in detail.

A.1.1 Time derivative operator

Both backward scheme and the blending scheme between Crank-Nicolson and implicit Euler scheme were applied in the simulation. It was found that in general they produced similar results, but in some particular cases, results from Crank-Nicolson scheme were slightly better. Below the implementations of both schemes in OpenFOAM are introduced.

In order to ease the illustration, we adopt a semi-discretized form where Eq. (A.2) was rewritten as:

$$\frac{\partial}{\partial t} \int_{V_P} \rho \boldsymbol{u} \, \mathrm{d}V + \mathcal{L}(\boldsymbol{u}) = 0 \tag{A.3}$$

where $\mathcal{L}(\boldsymbol{u})$ is the spatial discretization operator at some reference time level.

Backward scheme

Backward scheme in OpenFOAM uses values at current time step and two previous time steps. However, one should keep in mind that the time step is adjustable

based on Courant number limit in the simulation. Therefore, the successive time intervals used in backward differencing scheme may be not the same, and they are denoted as Δt and Δt^o. Expand the dependent variable $\rho\boldsymbol{u}$ at $t-\Delta t$ and $t-\Delta t-\Delta t^o$, namely $(\rho\boldsymbol{u})^o$ and $(\rho\boldsymbol{u})^{oo}$, one can obtain the following expressions:

$$(\rho\boldsymbol{u})^o = (\rho\boldsymbol{u})^n - \Delta t\frac{\partial\rho\boldsymbol{u}}{\partial t} + \frac{\Delta t^2}{2}\frac{\partial^2\rho\boldsymbol{u}}{\partial t^2} + \mathcal{O}(\Delta t^3) \tag{A.4}$$

$$(\rho\boldsymbol{u})^{oo} = (\rho\boldsymbol{u})^n - (\Delta t+\Delta t^o)\frac{\partial\rho\boldsymbol{u}}{\partial t} + \frac{1}{2}(\Delta t+\Delta t^o)^2\frac{\partial^2\rho\boldsymbol{u}}{\partial t^2} + \mathcal{O}(\Delta t^3) \tag{A.5}$$

By some mathematical manipulation, the time derivative term was approximated as:

$$\begin{aligned}\frac{\partial}{\partial t}\int_V \rho\boldsymbol{u}\,\mathrm{d}V = &\left(\frac{1}{\Delta t}+\frac{1}{\Delta t+\Delta t^o}\right)(\rho\boldsymbol{u}V^{cell})^n - \left(\frac{1}{\Delta t}+\frac{1}{\Delta t^o}\right)(\rho\boldsymbol{u}V^{cell})^o + \\ &\left(\frac{\Delta t}{\Delta t^o(\Delta t+\Delta t^o)}\right)(\rho\boldsymbol{u}V^{cell})^{oo}\end{aligned} \tag{A.6}$$

It should be mentioned that the temporal variation of velocity field $\boldsymbol{u}$ was neglected, i.e. $\mathcal{L}(\boldsymbol{u})$ was evaluated implicitly. Hereby the semi-discretization form of Eq. (A.3) reads:

$$\begin{aligned}&\left(\frac{1}{\Delta t}+\frac{1}{\Delta t+\Delta t^o}\right)(\rho\boldsymbol{u}V^{cell})^n - \left(\frac{1}{\Delta t}+\frac{1}{\Delta t^o}\right)(\rho\boldsymbol{u}V^{cell})^o + \\ &\left(\frac{\Delta t}{\Delta t^o(\Delta t+\Delta t^o)}\right)(\rho\boldsymbol{u}V^{cell})^{oo} + \mathcal{L}(\boldsymbol{u}^n) = 0\end{aligned} \tag{A.7}$$

this scheme is fully second order accurate, relatively robust and stable. However, it is not bounded. But this is less important than for the volume fraction field. In addition, although temporal variation of the velocity field was neglected, application of backward scheme with other second order schemes in space will also give a second order accuracy for the whole discretized equation [5].

Blending scheme between Crank-Nicolson and Euler scheme

The implementation of blending scheme between Euler and Crank-Nicolson is not straightforward in OpenFOAM. The off-centered coefficient θ was introduced to quantify the blending, where $\theta = 1$ stands for fully second order Crank-Nicolson

scheme, and $\theta = 0$ stands for the implicit Euler scheme. Presently $\theta = 0.4$ and $\theta = 0.9$ were used in Chapter 4 and Chapter 5. Then the blending coefficient which adjusted the fluxes in the discretized equation was formulated as:

$$\xi = \frac{1}{1+\theta} \tag{A.8}$$

So discretization of Eq. (A.1) using this scheme gave the following expression:

$$\frac{1}{\Delta t}\left((\rho \boldsymbol{u} V^{cell})^n - (\rho \boldsymbol{u} V^{cell})^o\right) + \xi \mathcal{L}(u^n) + (1-\xi)\mathcal{L}(u^o) = 0 \tag{A.9}$$

Eq. (A.9) is the formal formulation of the discretized equation using this scheme. However in OpenFOAM, an alternate formulation was adopted, since the principle to discretize each term in OpenFOAM is that it should be independent with other terms. This will be further explained below. If the final discretized equation was written as:

$$\boldsymbol{A}\boldsymbol{u} = \boldsymbol{b} \tag{A.10}$$

where $\boldsymbol{A}$ is the coefficient matrix and $\boldsymbol{b}$ is the source vector, then the resulted implicit part of the discretization was added to the coefficient matrix $\boldsymbol{A}$ while the explicit part contributed to $\boldsymbol{b}$ vector. Therefore Eq. (A.9) is not convenient for such a procedure, where discretization of the spacial operators (i.e. $\mathcal{L}(\boldsymbol{u})$) and the time derivative operator have mutual influences.

In order to isolate the contributions of $\boldsymbol{A}$ and $\boldsymbol{b}$ from time derivative operator, Eq. (A.9) was written as:

$$\frac{1+\theta}{\Delta t}\left((\rho \boldsymbol{u} V^{cell})^n - (\rho \boldsymbol{u} V^{cell})^o\right) + \mathcal{L}(u^n) + \theta \mathcal{L}(u^o) = 0 \tag{A.11}$$

The term $\mathcal{L}(u^o)$ was treated as a source term, and approximated based on the implicit Euler method:

$$\mathcal{L}(u^o) = -\frac{1}{\Delta t^o}\left((\rho \boldsymbol{u} V^{cell})^o - (\rho \boldsymbol{u} V^{cell})^{oo}\right) \tag{A.12}$$

By the above manipulation, the mutual influences between the time and spacial terms were removed. The contribution from the time derivative term to the

coefficient matrix is:

$$\frac{1+\theta}{\Delta t}(\rho V^{cell})^n \tag{A.13}$$

and it was added to the diagonal of the coefficient matrix $\boldsymbol{A}$. The contribution to the source part is:

$$\left(\frac{(1+\theta)(\rho\boldsymbol{u})^o}{\Delta t} + \frac{\theta((\rho\boldsymbol{u})^o - (\rho\boldsymbol{u})^{oo})}{\Delta t^o}\right) V^{cell} \tag{A.14}$$

and it was added to $\boldsymbol{b}$.

A.1.2 Divergence operator

The convection term $\nabla \cdot \rho\boldsymbol{u}\boldsymbol{u}$ contains a divergence operator. By application of the generalized Gauss theorem, the volume integral was transformed into the surface integral as:

$$\int_{V_P} \nabla \cdot \rho\boldsymbol{u}\boldsymbol{u}\, \mathrm{d}V = \oint_{\partial V} \rho\boldsymbol{u}\boldsymbol{u} \cdot \, \mathrm{d}\boldsymbol{S} = \sum_f \left(\int_f \rho\boldsymbol{u}\boldsymbol{u} \cdot \mathrm{d}\boldsymbol{S}\right) \tag{A.15}$$

where ∂V is the surrounding surface of the cell volume consisting several faces f. By assuming linear variation of the velocity $\boldsymbol{u}$ in the cell volume, the surface integral was simplified as:

$$\int_f \rho\boldsymbol{u}\boldsymbol{u} \cdot \mathrm{d}\boldsymbol{S} \approx \boldsymbol{S}_f \cdot (\rho\boldsymbol{u}\boldsymbol{u})_f \tag{A.16}$$

Hereafter Eq. (A.15) was approximated as:

$$\int_{V_P} \nabla \cdot \rho\boldsymbol{u}\boldsymbol{u}\, \mathrm{d}V \approx \sum_f \boldsymbol{S}_f \cdot (\rho\boldsymbol{u}_f)\boldsymbol{u}_f = \sum_f \Phi\boldsymbol{u}_f \tag{A.17}$$

The interpolated velocity $\boldsymbol{u}_f$ is not straightforward to approximate. It has been observed that with numerical schemes of second or high order accuracy, oscillation may appear. This is the consequence of non-monotone behavior of the applied scheme. The monotonicity requirement for a numerical scheme can be stated as the requirement that no new extrema be created by the numerical scheme, other than those eventually present in the initial condition [4]. However, it has been

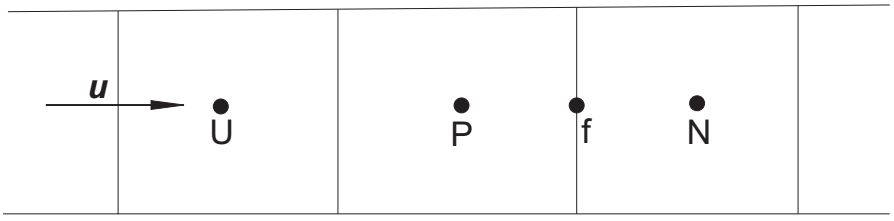

Figure A.2 – One dimensional mesh grid showing the face of interest and its neighboring cells.

demonstrated that all linear monotone schemes for the convection equation are necessarily first order accurate [2]. Therefore, the high-resolution (HR) schemes, namely the schemes of at least (globally) second order accurate without numerical oscillations were introduced. This was realized based on the the concept of limiter, behind which the the basic idea is to control the process of generation of overshoots and undershoots by preventing gradients to exceed certain limits, or to change sign between adjacent points. In this way the gradients were kept within proper bound.

In OpenFOAM the high resolution schemes were implemented within the framework of total variational diminishing (TVD) schemes [3]. In a one dimensional structured grid as shown in Fig. A.2, assume that $\Phi > 0$, except the cell P and cell N, denote the far upstream cell as cell U. If the quantity being transported is ψ, then the interpolated face value using high-resolution scheme is expressed as:

$$\psi_f = \psi_P + \frac{1}{2}\Psi(r_f)(\psi_N - \psi_P) \tag{A.18}$$

where $\Psi(r_f)$ is the limiter function of r_f, the upwind ratio of consecutive gradients expressed as:

$$r_f = \frac{\psi_P - \psi_U}{\psi_N - \psi_P} \tag{A.19}$$

Eq. (A.18) expresses the interpolated face value ψ_f as the sum of a first order upwind term and a correction term. The magnitude of the correction is controlled by the limiter function $\Psi(r_f)$.

In unstructured mesh, the far upstream cell U is unknown, as shown in Fig. A.3. Hereby r_f is not readily available. In [1] an improved expression was proposed for unstructured mesh, where a virtual cell U was determined along the line with cell

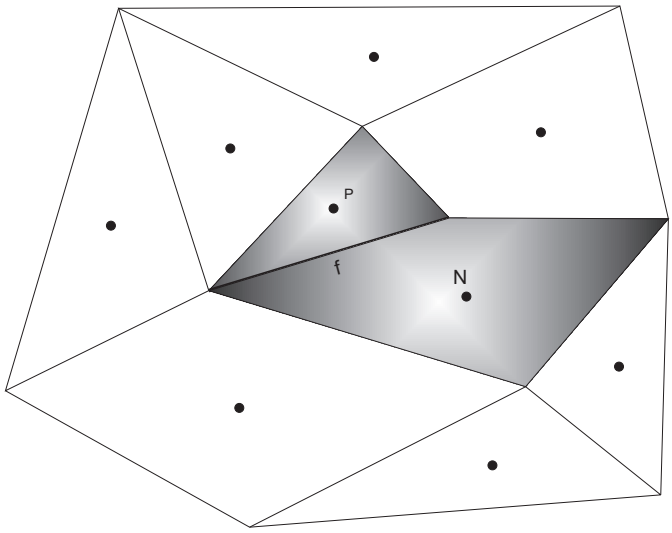

Figure A.3 – Illustration on the unstructured mesh grid and the stencil that can be used for face value interpolation.

P and cell N. Then the gradient ratio r_f is:

$$\begin{aligned} r_f &= \frac{2\nabla\psi_P \cdot \boldsymbol{d}_{PN}}{\psi_N - \psi_P} - 1 \qquad \Phi_f > 0 \\ r_f &= \frac{2\nabla\psi_N \cdot \boldsymbol{d}_{PN}}{\psi_N - \psi_P} - 1 \qquad \Phi_f < 0 \end{aligned} \tag{A.20}$$

In the implementation of HR schemes in OpenFOAM, Eq. (A.18) was slightly changed to:

$$\psi_f = \psi_N + \omega(\psi_P - \psi_N) \tag{A.21}$$

where the relation between the weighting factor ω and the limiter function Ψ is

$$\begin{aligned} \omega &= \omega_{CD}\Psi(r_f) + (1 - \Psi(r_f)) \quad \Phi > 0 \\ \omega &= \omega_{CD}\Psi(r_f) \qquad\qquad\qquad\quad \Phi < 0 \end{aligned} \tag{A.22}$$

where ω_{CD} is the weighting factor for central differencing scheme. In uniform grid, $\omega_{CD} = 1/2$.

A special case is that when the quantity $\boldsymbol{\psi}$ is a vector, just like in Eq. (A.15) where

the velocity is being transported by itself, then Eq. (A.20) was modified as:

$$\begin{aligned} r_f &= \frac{2(\boldsymbol{\psi}_N - \boldsymbol{\psi}_P) \cdot (\nabla \boldsymbol{\psi}_P \cdot \boldsymbol{d}_{PN})}{(\boldsymbol{\psi}_N - \boldsymbol{\psi}_P) \cdot (\boldsymbol{\psi}_N - \boldsymbol{\psi}_P)} - 1 \qquad \Phi > 0 \\ r_f &= \frac{2(\boldsymbol{\psi}_N - \boldsymbol{\psi}_P) \cdot (\nabla \boldsymbol{\psi}_N \cdot \boldsymbol{d}_{PN})}{(\boldsymbol{\psi}_N - \boldsymbol{\psi}_P) \cdot (\boldsymbol{\psi}_N - \boldsymbol{\psi}_P)} - 1 \qquad \Phi < 0 \end{aligned} \tag{A.23}$$

Therefore, as shown in [8], OpenFOAM calculates a single limiter for all the components of the vector based on the direction of most rapidly changing gradient. This results in the strongest limiter being calculated which is most stable but arguably less accurate.

QUICK scheme

In Chapter 4, the quadratic upwind interpolation (QUICK) scheme was used for discretization of the convection term. In OpenFOAM, this scheme was implemented within the framework of TVD-HR scheme. Below the formal definition of QUICK scheme is first introduced, followed by the way how QUICK scheme was implemented in OpenFOAM. Finally a simple proof is given on the equivalence of this implementation to the classic definition of QUICK scheme.

QUICK scheme was first proposed in [7], where two nodes in the upstream direction and one node in the downstream direction were used to express the interpolated face value. Formally for the interpolation scheme itself, it is third accurate. Again if we consider the one dimensional flow in Fig. A.2 for equidistant uniform mesh with positive flux through the face of interest, then the interpolated face value ψ_f is expressed as:

$$\psi_f = \frac{3}{4}\psi_P + \frac{3}{8}\psi_N - \frac{1}{8}\psi_U \tag{A.24}$$

However, as mentioned above in OpenFOAM the QUICK scheme was implemented within the TVD scheme framework. But the limiter for QUICK scheme was not a

function of r_f. Instead it was formulated as:

$$\begin{aligned} \Psi &= \frac{\psi'_f - \psi_P}{\psi_{CD} - \psi_P} \qquad \Phi > 0 \\ \Psi &= \frac{\psi'_f - \psi_N}{\psi_{CD} - \psi_N} \qquad \Phi < 0 \end{aligned} \tag{A.25}$$

where ψ_{CD} is the face interpolation value of ψ based on the central differencing scheme:

$$\psi_{CD} = \omega_{CD}\psi_P + (1 - \omega_{CD})\psi_N \tag{A.26}$$

and ψ'_f was expressed as:

$$\begin{aligned} \psi'_f &= \frac{1}{2}(\psi_{CD} + \psi_P + (1 - \omega_{CD})(\boldsymbol{d}_{PN} \cdot \nabla\psi_P)) \qquad \Phi > 0 \\ \psi'_f &= \frac{1}{2}(\psi_{CD} + \psi_N - \omega_{CD}(\boldsymbol{d}_{PN} \cdot \nabla\psi_N)) \qquad \Phi < 0 \end{aligned} \tag{A.27}$$

Note that here ψ'_f was the quantity used in Eq. (A.27), and ψ_f defined in Eq. (A.24) is the one we need as the interpolated face value. In addition, the limiter function was limited to be between 0 and 2, i.e. upwind and downwind. This indicates that the interpolation is limited to be between the upwind and downwind cell values.

By some mathematical manipulation, one actually can find that Eq. (A.27) is the final expression for ψ_f using QUICK scheme. We again simply demonstrate this in 1D grid as shown in Fig. A.2, where the flux through the face of interest is positive. Given that $\omega_{CD} = 1/2$, then:

$$\psi_{CD} = \frac{1}{2}\psi_P + \frac{1}{2}\psi_N \tag{A.28}$$

By substituting this expression into Eq. (A.25), the limiter function was expressed as:

$$\Psi = \frac{2(\psi'_f - \psi_P)}{\psi_N - \psi_P} \tag{A.29}$$

This gives the weighting factor in Eq. (A.22) as:

$$\omega = \frac{\psi_N - \psi'_f}{\psi_N - \psi_P} \tag{A.30}$$

Therefore, substituting Eq. (A.30) into Eq. (A.21) reads:

$$\psi_f = \psi'_f \tag{A.31}$$

Below we continue to demonstrate that in 1D grid, Eq. (A.27) is equivalent to Eq. (A.24). As shown in [1], the gradient between the quantity ψ at downstream and virtual far upstream node was calculated as:

$$\psi_N - \psi_U = 2\nabla\psi_P \cdot \boldsymbol{d}_{PN} \tag{A.32}$$

Therefore, the inner product between the gradient of ψ_P and the length vector $\boldsymbol{d}_{PN}$ is:

$$\nabla\psi_P \cdot \boldsymbol{d}_{PN} = \frac{1}{2}\psi_N - \frac{1}{2}\psi_U \tag{A.33}$$

Hereafter substituting this relation together with Eq. (A.28) for ψ_{CD} into Eq. (A.27, Eq. (A.24) was obtained.

Since in our case the velocity field is a vector field, we adopted a special version called QUICKV, i.e. the QUICK limiter for the vector field. In this revised formulation, the limiter function Ψ was expressed as:

$$\begin{aligned} \Psi &= \frac{\psi'_f - (\boldsymbol{\psi}_N - \boldsymbol{\psi}_P)\cdot\boldsymbol{\psi}_P}{\psi_{CD} - (\boldsymbol{\psi}_N - \boldsymbol{\psi}_P)\cdot\boldsymbol{\psi}_P} \quad \Phi > 0 \\ \Psi &= \frac{\psi'_f - (\boldsymbol{\psi}_N - \boldsymbol{\psi}_P)\cdot\boldsymbol{\psi}_N}{\psi_{CD} - (\boldsymbol{\psi}_N - \boldsymbol{\psi}_P)\cdot\boldsymbol{\psi}_N} \quad \Phi < 0 \end{aligned} \tag{A.34}$$

where ψ'_f for the vector field were calculated as:

$$\begin{aligned} \psi'_f =& \frac{1}{2}(\psi_{CD} + (\boldsymbol{\psi}_N - \boldsymbol{\psi}_P)\cdot\boldsymbol{\psi}_P + (1-\omega_{CD})((\boldsymbol{\psi}_N - \boldsymbol{\psi}_P)\cdot(\boldsymbol{d}_{PN}\cdot\nabla\boldsymbol{\psi}_P)) \quad \Phi > 0 \\ \psi'_f =& \frac{1}{2}(\psi_{CD} + (\boldsymbol{\psi}_N - \boldsymbol{\psi}_P)\cdot\boldsymbol{\psi}_N - \omega_{CD}((\boldsymbol{\psi}_N - \boldsymbol{\psi}_P)\cdot(\boldsymbol{d}_{PN}\cdot\nabla\boldsymbol{\psi}_N)) \quad \Phi < 0 \end{aligned} \tag{A.35}$$

and ψ_{CD} was written as:

$$\psi_{CD} = (\boldsymbol{\psi}_N - \boldsymbol{\psi}_P) \cdot (\omega_{CD}\boldsymbol{\psi}_P + (1 - \omega_{CD})\boldsymbol{\psi}_N) \tag{A.36}$$

Therefore, the principle for the modification of the limiter function for QUICK scheme is the same with the vector version of the other schemes, namely to use one limiter for all the components based on the direction of most rapidly changing gradient.

It should be mentioned that mostly in the context of finite volume method applied in OpenFOAM, the QUICK scheme is still second order accurate, since the approximation used in Eq. (A.16) is in general second order accurate. Even if Eq. (A.24) was applied for interpolation of $\boldsymbol{u}_f$ as a third order interpolation method, with the single point Gauss integration method, it should still retain second order accurate.

Vanleer scheme

In Chapter 6, QUICK scheme was not used for stability reasons. Due to application of the moving mesh technique, motion of the floater reduced the mesh quality. Under such condition, QUICK scheme has shown some defects and in many cases blew up the simulations. Hereby vanLeer scheme [6] was used to achieve better stability, where the limiter was calculated as:

$$\Psi = \frac{r_f + |r_f|}{1 + |r_f|} \tag{A.37}$$

The limiter should be bounded between 0 and 1.

A.1.3 Surface normal gradient operator

When evaluating surface tension force, pressure and density gradient, the surface normal gradient operator was introduced due to the interpolation and reconstruction procedure as shown in Chapter 4. Linear interpolation was used to discretize these terms:

$$\nabla_f^{\perp}\psi = \frac{\psi_N - \psi_P}{|\boldsymbol{d}_{PN}|} \tag{A.38}$$

Explicit non-orthogonal correction was employed to improve the accuracy.

A.1.4 Laplacian operator

The diffusive term, which contains Laplacian operator, was integrated over the control volume as:

$$\int_{V_P} \nabla \cdot \mu(\nabla \boldsymbol{u}) \, \mathrm{d}V = \sum_f \mu_f \nabla \boldsymbol{u} \cdot \boldsymbol{S}_f \tag{A.39}$$

where the surface normal gradient of $\boldsymbol{u}$ was evaluated as shown in Eq. (A.38). In fully orthogonal mesh we have the following relation:

$$\nabla \boldsymbol{u} \cdot \boldsymbol{S}_f = \frac{\boldsymbol{u}_N - \boldsymbol{u}_P}{|\boldsymbol{d}_{PN}|} |\boldsymbol{S}_f| \tag{A.40}$$

for non-orthogonal mesh, explicit correction was also introduced.

A.2 Transport equation for volume fraction

The standard transport equation for volume fraction α was expressed as:

$$\frac{\partial \alpha}{\partial t} + \nabla \cdot \boldsymbol{u}\alpha = 0 \tag{A.41}$$

In the present work, semi-implicit MULES solver was applied, where a predictor-corrector method was used. Below in this section we give an overview on the different applied schemes in the predictor and corrector step.

A.2.1 Applied schemes in the predictor step

At the predictor stage, Eq. (A.41) was discretized by an implicit bounded operator, i.e. a blending scheme between Crank-Nicolson scheme and Euler scheme for the time derivative term, and first order upwind scheme for the convective scheme. In Chapter 4 the blending coefficient $\theta = 0.4$ was applied, while in Chapter 5 it was changed to $\theta = 0.9$. However, in general the difference is not promising. For convection term, the first order upwind scheme was applied. Therefore, Eq. (A.41) was discretized as:

$$\frac{\alpha_n^{pre} - \alpha_o}{\Delta t} V + \sum_f F_{BD} = 0 \tag{A.42}$$

where α_n^{pre} is the predicted α value at the new time step, F_{BD} is the total bounded flux calculated as:

$$F_{BD} = \phi_{CN}\alpha_{f,n}^{pre} \tag{A.43}$$

where ϕ_{CN} is the Crank-Nicolson volumetric flux:

$$\phi_{CN} = \xi\phi + (1-\xi)\phi_o \tag{A.44}$$

where ϕ_o is the volumetric flux for convection of α field at the previous time step. α was interpolated by upwind scheme as shown below:

$$\begin{aligned} \alpha_f &= \alpha_P \quad \phi_{CN} > 0 \\ \alpha_f &= \alpha_N \quad \phi_{CN} < 0 \end{aligned} \tag{A.45}$$

A.2.2 Applied schemes in the corrector steps

The α_n^{pre} field was further corrected by explicit MULES corrector. The corrector was based on the explicit evaluation of high order flux including contributions from the compressive fluxes. The detailed procedure has been illustrated in Chapter 4. Here we focused on the schemes that have been applied to assemble the high order flux. Since Crank-Nicolson scheme was applied, the Crank-Nicolson off-centered α flux was calculated as:

$$F_{HO,n}^{cor} = \xi F_{HO,n} + (1-\xi)F_{HO,o} \tag{A.46}$$

where $F_{HO,n}^{cor}$ is the flux used at the new time step for the corrector. $F_{HO,n}$ was calculated based on the predicted volume fraction field:

$$F_{HO,n} = \phi\alpha_{f,n}^{pre} + \phi_r\alpha_{f,n}^{pre} \tag{A.47}$$

and $F_{HO,o}$ was calculated based on the volume fraction field at old time step:

$$F_{HO,o} = \phi_o\alpha_{f,o} + \phi_{r,o}\alpha_{f,o} \tag{A.48}$$

The discretization scheme used in the convection term and the compression term in Eq. (A.47) and Eq. (A.48) are different. The TVD scheme with vanLeer limiter was used to interpolate α value to the cell faces for the convection term. The

formulation of the limiter has been given in Eq. (A.37). A special HR scheme was developed in OpenFOAM for the compression term, where the weighting factor in Eq. (A.21) was expressed as:

$$\omega = 1 - \max\{(1 - 4\alpha_P(1 - \alpha_P))^2, (1 - 4\alpha_N(1 - \alpha_N))^2\} \tag{A.49}$$

The limiter should be bounded between 0 and 1.

A.3 References

[1] Darwish, M. S. ; Moukalled, F.: TVD schemes for unstructured grids. In: *International Journal of Heat and Mass Transfer* 46 (2003), Nr. 4, S. 599–611. – ISSN 00179310

[2] Godunov, Sergei K.: A difference method for numerical calculation of discontinuous solutions of the equations of hydrodynamics. In: *Matematicheskii Sbornik* 89 (1959), Nr. 3, S. 271–306

[3] Harten, Ami: High resolution schemes for hyperbolic conservation laws. In: *Journal of computational physics* 49 (1983), Nr. 3, S. 357–393

[4] Hirsch, Charles: *Numerical computation of internal and external flows. volume 1. , fundamentals of computational fluid dynamics*. Amsterdam, Boston, London : Butterworth-Heinemann, 2007. – URL http://opac.inria.fr/record=b1131079. – ISBN 978-0-7506-6594-0

[5] Jasak, Hrvoje: *Error Analysis and Estimation for the Finite Volume Method with Applications to Fluid Flows*, Imperial College, University of London, PhD Thesis, 1996. – 394 S

[6] Leer, Bram van: Towards the ultimate conservative difference scheme. II. Monotonicity and conservation combined in a second-order scheme. In: *Journal of Computational Physics* 14 (1974), Nr. 4, S. 361–370. – URL http://www.sciencedirect.com/science/article/pii/0021999174900199. – ISBN 0021-9991

[7] Leonard, B.P.: A stable and accurate convective modelling procedure based on quadratic upstream interpolation. In: *Computer Methods in Applied Mechanics and Engineering* 19 (1979), Nr. 1, S. 59 – 98. – URL http://www.sciencedirect.com/science/article/pii/0045782579900343. – ISSN 0045-7825

[8] OpenCFD: *OpenFOAM - The Open Source CFD Toolbox - User's Guide*. United Kingdom: OpenCFD Ltd. (Veranst.)

DTU Mechanical Engineering
Section of Fluid Mechanics, Coastal and Maritime Engineering
Technical University of Denmark

Nils Koppels Allé, Bld. 403
DK-2800 Kgs. Lyngby
Denmark
Phone (+45) 4525 1360
Fax (+45) 4588 4325

www.mek.dtu.dk

DCAMM
Danish Center for Applied Mathematics and Mechanics

Nils Koppels Allé, Bld. 404
DK-2800 Kgs. Lyngby
Denmark
Phone (+45) 4525 4250
Fax (+45) 4593 1475
www.dcamm.dk
ISSN: 0903-1685